Processing of Copper Zinc Tin Sulfide Nanocrystal Dispersions for Thin Film Solar Cells

A THESIS

SUBMITTED TO THE FACULTY THE UNIVERSITY OF MINNESOTA

BY

BRYCE ARTHUR WILLIAMS

IN PARTIAL FULFILLMENT OF THE REQUIREMENTS
FOR THE DEGREE OF
DOCTOR OF PHILOSOPHY

Lorraine Francis, Co-Advisor
Eray Aydil, Co-Advisor

June, 2016

Acknowledgments

I would like to thank my advisors Lorraine Francis and Eray Aydil for the opportunity to conduct this exciting research that composes this thesis as well as their invaluable advice and guidance throughout my time at the University of Minnesota. Through their teaching and guidance, I have learned how to conduct thorough and impactful research as well as how to effectively communicate that research through writing and presentation. These lessons will be invaluable to me as I progress in my career. I would like to thank the Industrial Partnership for Research in Interfacial Materials and Engineering (IPRIME) and the NSF Materials Research Science and Engineering Center (MRSEC) at the University of Minnesota for the funding. This work was supported primarily by the National Science Foundation through the University of Minnesota MRSEC under Award Number DMR-1420013. Part of this work was carried out in the College of Science and Engineering Characterization Facility, University of Minnesota, which has received capital equipment funding from the NSF through the UMN MRSEC program under Award Number DMR-1420013. I also want to thank Ross Behling along with Prof Cochran and Bret Ulery along with Prof Narasimhan for guiding me in my earliest research efforts at Iowa State.

I owe much gratitude to Boris Chernormordik for guiding me through CZTS synthesis and characterization as well as his development of novel synthesis techniques which allowed me to further my own research. I would like to thank my collaborators Nancy Trejo and Ankit Mahajan for their contributions to my research as well as Kyle Price and Melissa Johnson for helpful research conversations. Much of the work detailed here was conducted alongside a number of hard-working undergraduate researchers. Without the help of Collin Holgate, Michelle Smeaton, Albert Wu, Eowyn Lucas, and Devon Urness this work would be much less complete. I also want to thank my many group members past and present within the Aydil and Francis research groups.

Much of my success and many of my achievements can also be attributed to my wife Melany. She has provided support for me in so many ways as I traversed the ups and downs of graduate school and was always willing to take up my slack when classes or research became burdening. I look forward to what the future now holds for us and our family. To my parents, your innumerable sacrifices enabled me to find success along my chosen path, and your encouragement to always work at my full potential, even when I felt it was unnecessary, has been a continual source of motivation for me. I do not know where I would be without your help. To my extended family, I appreciate all of the support I have received through the years be it text messages, calls, cards, or just enjoyable company on my off days. To my daughter Lydia, thank you for revealing all the joys of life and offering a glimpse into the future. I hope you find success in all you choose to take on.

To my family for their continued support.

Abstract

A scalable and inexpensive renewable energy source is needed to meet the expected increase in electricity demand throughout the developed and developing world in the next 15 years without contributing further to global warming through CO_2 emissions. Photovoltaics may meet this need but current technologies are less than ideal requiring complex manufacturing processes and/or use of toxic, rare-earth materials. Copper zinc tin sulfide (CZTS) solar cells offer a true "green" alternative based upon non-toxic and abundant elements. Solution-based processes utilizing CZTS nanocrystal dispersions followed by high temperature annealing have received significant research attention due to their compatibility with traditional roll-to-roll coating processes.

In this work, CZTS nanocrystal (5 – 35 nm diameters) dispersions were utilized as a production pathway to form solar absorber layers. Aerosol-based coating methods (aerosol jet printing and ultrasonic spray coating) were optimized for formation of dense, crack-free CZTS nanocrystal coatings. The primary variables underlying determination of coating morphology within the aerosol-coating parameter space were investigated. It was found that the liquid content of the aerosol droplets at the time of substrate impingement play a critical role. Evaporation of the liquid from the aerosol droplets during coating was altered through changes to coating parameters as well as to the CZTS nanocrystal dispersions.

In addition, factors influencing conversion of CZTS nanocrystal coatings into dense, large-grained polycrystalline films suitable for solar cell development during thermal annealing were studied. The roles nanocrystal size, carbon content, sodium uptake, and sulfur pressure were found to have pivotal roles in film microstructure evolution. The effects of these parameters on film morphology, grain growth rates, and chemical makeup were analyzed from SEM images as well as compositional analysis techniques. From these results, a deeper understanding of the interplay between the numerous annealing variables was achieved and improved annealing processes were developed.

Table of Contents

Acknowledgments i
Abstract iv

List of Figures **x**

List of Tables **xviii**

Chapter 1 Introduction **1**
1.1 Solar Cell Technologies 3
1.2 Copper Zinc Tin Sulfide 5
1.3 Thesis Organization 6

Chapter 2 Background Information: Development of CZTS Solar Cells from Nanocrystal Dispersions **9**
2.1 Introduction 9
2.2 CZTS Absorber Layer Formation 10
2.3 CZTS Nanocrystal Synthesis Procedures 12
2.4 CZTS Nanocrystal Dispersion Formulation 13
2.5 CZTS Nanocrystal Coating Formation 14
2.5.1 Nanoparticle Dispersion Coating Methods 14
2.5.2 Cracking During Drying of Nanoparticle Coatings 16
2.6 Annealing of CZTS Nanocrystal Coatings 20
2.6.1 Selenization 21
2.6.2 Sulfidation 23

2.6.3 Effects of Substrates and Alkali Metals on Film Development . . . 24

Chapter 3 Optimization of CZTS Nanocrystal Dispersion Stability 27

3.1 Background and motivation . . . 27

3.2 Experimental . . . 28

3.2.1 Materials . . . 28

3.2.2 Nanocrystal Synthesis . . . 29

3.2.3 Ultrasonication . . . 29

3.2.4 Characterization . . . 29

3.3 Results and Discussion . . . 31

3.3.1 Effect of Alcohol Washing on Ligand Concentration . . . 31

3.3.2 Increasing Ligand Coverage and Dispersion Stability . . . 33

3.3.3 Effect of Ultrasonication on Aggregate Diameter . . . 38

3.4 Conclusion . . . 40

Chapter 4 Formation of CZTS Nanocrystal Coatings *via* Aerosol Jet Printing and Compaction 42

4.1 Introduction . . . 42

4.2 Experimental . . . 43

4.2.1 Materials . . . 43

4.2.2 Nanocrystal Dispersions . . . 43

4.2.3 Aerosol Jet Printing . . . 44

4.2.4 Compaction by Weighted Roller . . . 46

4.2.5 Compaction by Hydraulic Press . . . 47

4.3 Results and Discussion . . . 50

4.3.1 Aerosol Jet Printing . . . 50

4.3.2 Compaction by Weighted Roller . . . 56

4.3.3 Compaction by Hydraulic Press . . . 56

4.3.4 Thermal Annealing of the Aerosol Jet Printed CZTS Nanocrystal Coatings . . . 60

4.4 Conclusion 62

Chapter 5 Effect of Nanocrsytal Size on Microstructure Development During Annealing of CZTS Nanocrystal Coatings 65

5.1 Introduction 65
5.2 Experimental Section 67
5.2.1 Materials 67
5.2.2 Nanocrystals 67
5.2.3 Alteration of CZTS nanocrystal dispersion carbon content 68
5.2.4 Deposition and annealing of CZTS nanocrystal coatings 69
5.2.5 Characterization 70
5.3 Results 71
5.3.1 Effect of Sulfur Vapor Pressure and Thermal Annealing Time . . . 71
5.3.2 Effect of Nanocrystal Size and Carbon Content 78
5.4 Summary and Conclusions 85

Chapter 6 Effect of NaOH on Microstructure Development During Annealing of Ultrasonic Spray Coated Copper Zinc Tin Sulfide Nanocrystals 89

6.1 Introduction 89
6.2 Experimental 91
6.2.1 Materials 91
6.2.2 Nanocrystal Synthesis 91
6.2.3 CZTS Nanocrystal Coating Formation 92
6.2.4 Annealing of CZTS Nanocrystal Coatings 93
6.2.5 Characterization 94
6.2.6 Simulation Setup for Droplet Evaporation 95
6.3 Results and Discussion 97
6.3.1 Spray Coating of CZTS Nanocrystal Dispersions 97
6.3.2 The Effects of Na Addition and Sulfur Pressure During Annealing . 102
6.4 Conclusion 110

Chapter 7 Intense Pulsed Light Annealing of CZTS Nanocrystal Coatings 113
7.1 Introduction . . . 113
7.2 Experimental details . . . 115
7.2.1 Synthesis of CZTS Nanocrystals . . . 115
7.2.2 Preparation of CZTS Nanocrystal Coatings . . . 115
7.2.3 Intense Pulsed Light and Thermal Annealing . . . 116
7.2.4 Characterization . . . 118
7.2.5 Simulation of IPL Annealing of CZTS Nanocrystal Coatings . . . 119
7.3 Results and Discussion . . . 122
7.3.1 IPL Annealing of CZTS Nanocrystal Coatings on Mo-Coated SLG 122
7.3.2 CZTS Decomposition and Blister Formation Mechanism . . . 126
7.4 Origin of High Density Cracking . . . 135
7.4.1 IPL Annealing of CZTS Nanocrystal Coatings on Molybdenum Foil 140
7.5 Outlook for CZTS Grain Growth During IPL Annealing . . . 143
7.6 Conclusion . . . 145

Chapter 8 Future Directions 147

Bibliography 149

Appendix A Effect of CZTS Nanocrystal Size on Coating Microstructure Using Ultrasonic Spray Coating, Aerosol Jet Printing, and Dropcasting Methods 162
A.1 Dropcasting . . . 162
A.2 Ultrasonic Spray Coating . . . 163
A.3 Aerosol Jet Printing . . . 164

Appendix B Liquid Selenium Enhanced Sintering During Intense Pulsed Light Annealing of Cu_2ZnSnS_4 Nanocrystal Coatings 166
B.1 Introduction . . . 166
B.2 Materials and Methods . . . 167

B.3 Results and Discussion 168
B.4 Outlook 169

List of Figures

Figure 1.1 Cumulative past and predicted future net electricity generation by year for OCED and non-OCED countries. 2

Figure 1.2 (a) Plot of cumulative installed PV capacity from 2008 to 2014 based upon region.(b) Graph of technology distribution of installed PV systems from 1980 to 2014. 4

Figure 2.1 Diagram illustrating the four primary process steps comprising nanocrystal synthesis, dispersion formulation, nanocrystal coating formation, and polycrystalline film development. 11

Figure 2.2 Schematic of a typical device structure for a CZTS solar cell. . . 11

Figure 2.3 Common coating processes used to form nanoparticle coatings. . 15

Figure 2.4 Time-lapse optical images extracted from a high-speed video of a CZTS nanocrystal (5 nm) coating cracking during during drying. 18

Figure 2.5 Illustrations of the phases of drying and cracking. 18

Figure 2.6 Illustrations of two common CZTS nanocrystal coating annealing procedures: (a) tube furnace utilizing a graphite boxand (b) sealed quartz ampules. 21

Figure 2.7 Illustration of the typical film morphology after selenization of CZTS nanocrystal coatings. 23

Figure 2.8 Illustration depicting (a) normal- and (b) abnormal-grain growth during annealing of CZTS nanocrystal coatings. 25

Figure 3.1 (a) Schematic of washing procedure used to purify CZTS nanocrystals after synthesis. Process was repeated up to 4 times to study effects on dispersion stability. (b) Illustration of ATR-FTIR spectroscopy of CZTS nanocrystals cast from dispersion. 30

Figure 3.2 (a) ATR-FTIR spectra from CZTS nanocrystal dispersions after drying that had been washed 1, 2, and 3 times after synthesis. (b) Depictions of the Chemical structures of octadecene, oleic acid, and oleyelamine, the primary solvents and ligands used in CZTS nanocrystal synthesis. 32

Figure 3.3 Plot of average aggregate diameter as measured by DLS as function of the number of dispersion washing cycles. 34
Figure 3.4 (a) Full and (b) zoomed ATR-FTIR spectra of CZTS nanocrystals cast from toluene dispersions containing 0, 10^{-4}, 10^{-3}, 5×10^{-3}, and 10^{-2} volume fraction free oleic acid. 36
Figure 3.5 Illustration of oleic acid associating with the surface of a CZTS nanocrystal showing the loss of the C=O vibration at 1710 cm^{-1} after the oleate complex is formed. 36
Figure 3.6 (a) ATR-FTIR spectra of CZTS nanocrystal coatings with no added oleic acid and with up to 10^{-2} vol frac of oleic acid. (b) Illustration of the effects of large oleic acid volume fractions on the FTIR sampling volume during analysis of CZTS nanocrystals. 37
Figure 3.7 ATR-FTIR spectra of CZTS nanocrystal coatings with no added oleic acid, 10^{-4}, and 10^{-3} vol frac where no sampling volume effects due to excess oleic acid were observed. (b) Average relative aggregate diameter, as measured by DLS, in CZTS nanocrystal dispersions with added oleic acid volume fractions from 10^{-4} to 10^{-1}. 39
Figure 3.8 (a) Plot of the effect of sonication time on aggregate diameter in CZTS nanocrystal dispersions with added oleic acid and with 10^{-4} volume fraction oleic acid. (b) ATR-FTIR spectra of CZTS nanocrystal coatings with no added oleic acid and with added oleic acid after 0, 15, and 30 minutes of sonication. 39

Figure 4.1 Schematic of the aerosol jet printing system used for coating substrates with CZTS nanocrystals. 45
Figure 4.2 Schematic illustrations of roller-based compaction setup 48
Figure 4.3 Schematic illustrations of the two methods used to compress the nanocrystal coatings in the hydraulic press. 50
Figure 4.4 SEM images of isolated lines printed from 2 weight percent dispersions of 5 nm CZTS nanocrystals. 52
Figure 4.5 Illustrations of the aerosol drying process and the mechanisms that lead to various coating morphologies at various carrier gas flow rates, Q_{CG}, and focusing ratios. 53
Figure 4.6 SEM images showing the effect of roller compaction pressure on the densification of aerosol jet printed CZTS coatings. 57

Figure 4.7 SEM images of aerosol jet printed coatings from a 2 weight percent 5 nm CZTS nanocrystal dispersion (a and d) before and after compaction using a hydraulic press at (b and e) 200 MPa pressure, and (c and f) at 800 MPa. 58
Figure 4.8 Optical images showing the effects of mild annealing on CZTS nanocrystal coatings after compaction and TGA results showing weight loss in aerosol jet printed coatings during a mild annealing treatment. 59
Figure 4.9 SEM images of CZTS nanocrystal coatings, compacted using different methods and compaction pressures, before and after annealing for one hour at 600 °C with 1 mg of solid sulfur (~50 Torr evaporated) in a evacuated quartz ampule 63
Figure 4.10 XRD and Raman spectra of annealed CZTS nanocrystal coatings with various initial densities. 64

Figure 5.1 Schematic of coating and annealing procedures using 5 and 35 nm CZTS nanocrystals dispersions. 70
Figure 5.2 SEM images of coatings prior to annealing. (a) and (b) are planar and cross-sectional images of a coating composed of 5 nm CZTS nanocrystals and formed by AJP followed by compaction. (c) and (d) are planar and cross-sectional images of a coating composed of 35 nm CZTS nanocrystals and formed by dropcasting. 71
Figure 5.3 SEM images of 5 nm CZTS nanocrystal coatings after annealing at 600 °C for one hour with sulfur vapor pressures of 50 and 500 Torr. 73
Figure 5.4 Surface coverage of abnormal grains as a function of annealing time for coatings composed of 5 nm CZTS nanocrystals. The coatings were annealed at 600 °C in the 50 and 500 Torr of sulfur vapor pressure. 74
Figure 5.5 Carbon concentration (at%) and copper-to-sum-of-zinc-and-tin ratio (Cu/(Zn+Sn)) as determined from EDS, as a function of annealing time for coatings composed of 5 nm CZTS nanocrystals. The coatings were annealed at 600 °C in (a) 50 Torr and (b) 500 Torr sulfur. 75
Figure 5.6 XRD and Raman spectra of CZTS films produced by annealing 5 nm CZTS nanocrystal coatings at 600 °C in the presence of (a,b) 50 Torr and (c,d) 500 Torr of sulfur for 10, 30, and 60 minutes. . 76

Figure 5.7 SEM images of 35 nm CZTS nanocrystal coatings after annealing at 600 °C for one hour with sulfur vapor pressures of 50 and 500 Torr. 77
Figure 5.8 Carbon concentration (at%) and copper-to-sum-of-zinc-and-tin ratio (Cu/(Zn+Sn)) as determined from EDS, as a function of annealing time for coatings composed of 35 nm CZTS nanocrystals. Coatings were annealed at 600 °C in (a) 50 Torr and (b) 500 Torr of sulfur. 79
Figure 5.9 XRD and Raman spectra of CZTS films produced by annealing 35 nm CZTS nanocrystal coatings at 600 °C in the presence of (a,b) 50 Torr and (c,d) 500 Torr of sulfur for 10, 30, and 60 minutes. 80
Figure 5.10 SEM images of CZTS nanocrystal coatings after annealing for 60 minutes at 600 °C in (a and c) 50 Torr and (b and d) 500 Torr of sulfur. The coatings were composed of (a and b) 5 nm or (c and d) 35 nm CZTS nanocrystals. 81
Figure 5.11 SEM images of 5 nm CZTS nanocrystal coatings from (a,c) as-synthesized nanocrystals and (b,d) a nanocrystal dispersion washed to remove surface-attached ligands after annealing at 600 °C for 60 minutes with sulfur pressure of 500 Torr). 82
Figure 5.12 (a) XRD patterns and (b) Raman spectra of 5 nm CZTS nanocrystal coatings produced from a nanocrystal dispersion washed four successive times after annealing for 60 minutes at 600 °C with a sulfur vapor pressure of 500 Torr. 83
Figure 5.13 SEM images of 35 CZTS nanocrystal coatings with (a,b) no added polystyrene added polystyrene masses of (c,d) 0.035 mg, (e,f) 0.070 mg, (g,h) 0.175 mg, and (i,j) 0.350 mg after annealing at 600 °C for 60 minutes with a sulfur pressure of 500 Torr (10 mg of sulfur powder loaded into the ampule). 87
Figure 5.14 (a) XRD patterns and (b) Raman spectra of 35 nm CZTS nanocrystal coatings with varying amounts of polystyrene (PS) added to the dispersion after annealing for 60 minutes at 600 °C with a sulfur vapor pressure of 500 Torr. 88
Figure 5.15 Plot of the fractional surface area coverage of abnormal grains versus carbon content of 35 nm CZTS nanocrystal coatings annealed at 600 °C with a sulfur pressure of 500 Torr. 88

Figure 6.1 (a) Schematic illustration of ultrasonic spray coating setup and sample parameter ranges. (b) Photograph of ultrasonic spray coating apparatus used for CZTS nanocrystal coating creation. 93

Figure 6.2 Photograph of CZTS nanocrystal coating after annealing using "hot-loading" method. 94
Figure 6.3 (a) Illustration showing process used to create NaOH coated tubes for annealing experiments. (b) Illustration showing orientation of NaOH-rich region above CZTS nanocrystal coating as used during annealing. 95
Figure 6.4 (a) Probability and (b) cumulative probability density plots for droplet sizes produced by ultrasonic spray coating nozzle with water and toluene. 98
Figure 6.5 SEM images of CZTS nanocrystal coatings formed by ultrasonic spray deposition using 3 passes from 5 weight percent nanocrystals dispersed in (a,c) pure toluene and (b,d) 70 volume percent toluene/30 volume percent cyclohexanone dispersions. 99
Figure 6.6 Plot of the normalized aerosol droplet radius as a function of time for pure toluene droplets and for a binary liquid droplets comprising 30 volume percent cyclohexanone and balance toluene. . . . 101
Figure 6.7 SEM images of CZTS nanocrystal coatings formed by ultrasonic spray deposition from a 10 weight percent CZTS nanocrystal dispersion using (a) 3, (b) 6, and (c) 9 coating passes. 103
Figure 6.8 Plan view SEM images of coatings comprised of 15 nm CZTS nanocrystals after annealing at 600 °C for 1.25 hours with (a-c) no NaOH,(d-f) 0.1 μmol, and (g-i) 1 μmol NaOH. 105
Figure 6.9 Cross-sectional SEM images of 15 nm CZTS nanocrystal coatings after annealing at 600 °C for 1.25 hours with (a-c) no NaOH,(d-f) 0.1 μmol, and (g-i) 1 μmol NaOH. 105
Figure 6.10 (a-c) XRD patterns and (d-f) Raman spectra of 15 nm CZTS nanocrystal coatings annealed at 150, 225, and 300 Torr of sulfur with no added NaOH, 0.1 μmol NaOH, and 1 μmol NaOH. . . . 106
Figure 6.11 Plot of abnormal grain coverage percent for coatings annealed with no NaOH, 0.1 μmol NaOH, and 1 μmol NaOH for 15 nm CZTS nanocrystal coatings. 107
Figure 6.12 Plan view SEM images of coatings comprised of 20 nm CZTS nanocrystals after annealing at 600 °C for 1.25 hours with (a-c) no NaOH,(d-f) 0.1 μmol, and (g-i) 1 μmol NaOH. 108
Figure 6.13 Cross-sectional SEM images of 20 nm CZTS nanocrystal coatings after annealing at 600 °C for 1.25 hours with (a-c) no NaOH,(d-f) 0.1 μmol, and (g-i) 1 μmol NaOH. 108

Figure 6.14 (a-c) XRD patterns and (d-f) Raman spectra of 15 nm CZTS nanocrystal coatings annealed at 150, 225, and 300 Torr of sulfur with no added NaOH, 0.1 μmol NaOH, and 1 μmol NaOH. . . . 109
Figure 6.15 Plot of abnormal grain coverage percent for coatings annealed with no NaOH, 0.1 μmol NaOH, and 1 μmol NaOH for 20 nm CZTS nanocrystal coatings 111

Figure 7.1 SEM images of as-coated CZTS nanocrystal coating on Mo-coated SLG substrate. 117
Figure 7.2 Schematic graph of energy output of IPL annealing operation. $\dot{Q}$ is energy output in watts, t_{flash} is length of flash period, and t_{period} is the flash period of flashes. 117
Figure 7.3 Photographs of (a) sulfur powder placed beside a CZTS nanocrystal coating on Mo foil prior to annealing, and (b) CZTS nanocrystal coating sealed in quartz ampoule after IPL annealing showing vaporization and subsequent condensation of the sulfur powder. 118
Figure 7.4 Summary schematic for setup for FEM of IPL annealing of CZTS nanocrystal coatings. 121
Figure 7.5 Graph of curve fit for absorption of xenon flash lamp spectrum by a single grain CZTS layer. 123
Figure 7.6 SEM images of CZTS nanocrystal coatings on Mo-coated SLG substrates after IPL annealing at flash energy densities ranging between 3.9 and 11.6 J/cm^2 for 1 and 10 flashes. 124
Figure 7.7 Photograph of quartz ampule with residue deposited from CZTS nanocrystal coating during IPL annealing at 11.6 J/cm^2 for 10 flashes. 125
Figure 7.8 XRD patterns of CZTS nanocrystal coatings on Mo-coated SLG substrates before and after IPL annealing at flash energy densities ranging between 3.9 and 11.6 J/cm^2 for (a) 1 and (b) 10 flashes. . 126
Figure 7.9 SEM image and summary of EDS results from a CZTS nanocrystal coating on a Mo-SLG substrate annealed at 9.0 J/cm^2 for 10 flashes. 126
Figure 7.10 SEM image and summary of EDS results from a CZTS nanocrystal coating on a Mo-SLG substrate annealed at 11.6 J/cm^2 for 10 flashes. 127
Figure 7.11 Representative Raman spectra from IPL annealed CZTS nanocrystal coatings on Mo-coated SLG substrates at varying energy densities for (a) 1 flash and (b) 10 flashes. 128

Figure 7.12 Plot of linear crack density of CZTS nanocrystal coatings on Mo-coated SLG after IPL annealing as a function of cumulative energy density. 129
Figure 7.13 SEM image of blistered region of CZTS nanocrystal coating after IPL annealing at 9.0 J/cm^2 for 10 flashes. Center of blister shows small nanocrystal deposits. 130
Figure 7.14 Summary of the analysis, using confocal Raman microscopy and imaging, of the Mo-CZTS interfacial region in a blister formed on the nanocrystal coating post IPL annealing with ten 9.0 J/cm^2 flashes. 131
Figure 7.15 A schematic illustration of the proposed blister formation mechanism. CZTS decomposition at the CZTS-Mo interface during IPL annealing generates gases; blistering is caused by these product gases as they leave the film. 132
Figure 7.16 SEM images of CZTS nanocrystal coatings after thermal annealing in a conventional furnace at 600 °C for 1 hour with and without 1 mg of sulfur loaded into the ampule (50 Torr sulfur vapor pressure). 133
Figure 7.17 (a) XRD patterns and (b) Raman spectra for CZTS nanocrystal coatings on Mo-SLG substrates corresponding to Figure 4 for non-IPL-treated and IPL-treated CZTS coatings after thermal annealing. 134
Figure 7.18 SEM images of a CZTS nanocrystal coating on quartz after IPL annealing with ten 9.0 J/cm^2 flashes at (a) low and (b) high magnification, showing lack of blistering but presence of high density cracking. 136
Figure 7.19 (a) XRD pattern and (b) Raman spectrum for CZTS nanocrystal coating on quartz substrate after IPL annealing at 9.0 J/cm^2 for 10 flashes. 136
Figure 7.20 Simulated temporal variation of CZTS films and bottom of substrate using Mo-SLG and Mo foil substrates. 137
Figure 7.21 Spatial variation of the temperature in the x-z plane at different times. 140
Figure 7.22 SEM images of CZTS nanocrystal coatings on (b & d) Mo foil and (a & c) Mo-coated SLG after IPL annealing with (a & b) one 9.0 J/cm^2 flash and (c & d) ten 11.6 J/cm^2 flashes. 142

Figure 7.23 SEM images of CZTS nanocrystal coatings on Mo foil after IPL annealing at an energy density of 11.6 J/cm^2 without sulfur for (a,b) 10 flashes, (c,d) 35 flashes, and (e,f) 50 flashes and with 1 mg of sulfur loaded into the ampule for (g,h) 10 flashes, (i,j) 35 flashes, and (k,l) 50 flashes. 143
Figure 7.24 XRD patterns and Raman spectra of CZTS nanocrystal coatings on molybdenum foil substrates after IPL annealing at 11.6 J/cm^2 for 10, 35, and 50 flashes (a) with no additional sulfur and (b) 1 mg of sulfur in the quartz ampule. 144
Figure 7.25 SEM images of CZTS nanocrystal coating on Mo foil after IPL annealing in sulfur with 400 flashes at an energy density of 11.7 J/cm^2. Annealing was conducted with 10 mg of sulfur loaded into the annealing ampule. 145
Figure 7.26 (a) XRD pattern and (b) Raman spectrum for CZTS nanocrystal coating on Mo foil after IPL annealing at 11.6 J/cm^2 for 400 flashes. 145

Figure A.1 SEM images of CZTS nanocrystal coatings formed by dropcasting CZTS nanocrystal dispersions containing (a,b) 5 and (c,d) 35 nm diameter nanocrystals. 163
Figure A.2 SEM images of CZTS nanocrystal coatings formed by ultrasonic spray coating CZTS nanocrystal dispersions containing (a-d) 5 and (e-h) 15 nm nanocrystals formed with 3 coating passes and 6 coating passes. 164
Figure A.3 SEM images of CZTS nanocrystal coatings formed aerosol jet printing followed by compaction *via* hydraulic press at 800 MPa for 15 seconds using (a,b) 5 nm and (c,d) 35 nm CZTS nanocrystal dispersions. 165

Figure B.1 (a) XRD pattern and (b) Raman spectrum for CZTS nanocrystal coating on quartz substrate after IPL annealing at 9.0 J/cm^2 for 10 flashes. 168
Figure B.2 (a) XRD pattern and (b) Raman spectrum for CZTS nanocrystal coating on quartz substrate after IPL annealing at 9.0 J/cm^2 for 10 flashes. 169
Figure B.3 Photographs of CZTS nanocrystal coatings on Mo foil after deposition of 70 μL of Se-containing ethanethiol and ethlyenediamine solution on top of coating. A significant amount of residual carbon was as the solution dried. 169

List of Tables

7.1 Thermal properties used for development of finite element model. 122
7.2 Summary of EDS results from IPL annealed CZTS nanocrystal coatings on Mo-SLG substrates at various energies and flashes. 127

Chapter 1

Introduction

As the economies of developing countries mature, electricity demand is forecasted to grow quickly. As their gross domestic product (GDP) increases, they will be able to expand their utility infrastructures. The worldwide net electricity generation (*i.e.*, electricity produced after subtracting the amount required to operate the generating stations) was approximately 2.5 terawatt (TW) in 2010 and is expected to rise to 4.4 TW by 2040.[1] The majority of this growth is going to occur in developing countries as shown in Figure 1.1a which shows past and predicted net electricity generation in countries belonging to the Organization for Economic Co-Operation and Development (OCED) and non-OCED member countries.[1] The OCED is largely composed of developed nations while non-OCED members are largely developing countries. To meet this increased demand, developing nations are currently relying on high CO_2-emitting sources, such as coal and natural gas, for electricity generation.[2] This is worrying on a global scale due to the role of rising atmospheric CO_2 concentration plays in global warming.[3] Electricity generation from abundant solar energy provides an ideal alternative for these developing regions which during their development can bypass traditional carbon-based electricity sources.

Solar cells use suitable semiconducting materials to generate electrical current upon light absorption, are ideal candidates for harnessing solar energy. At the beginning of the century, global photovoltaic (PV) installations were slow to take hold outside markets such as Germany, where public policies encouraged installation through tax incentives and other

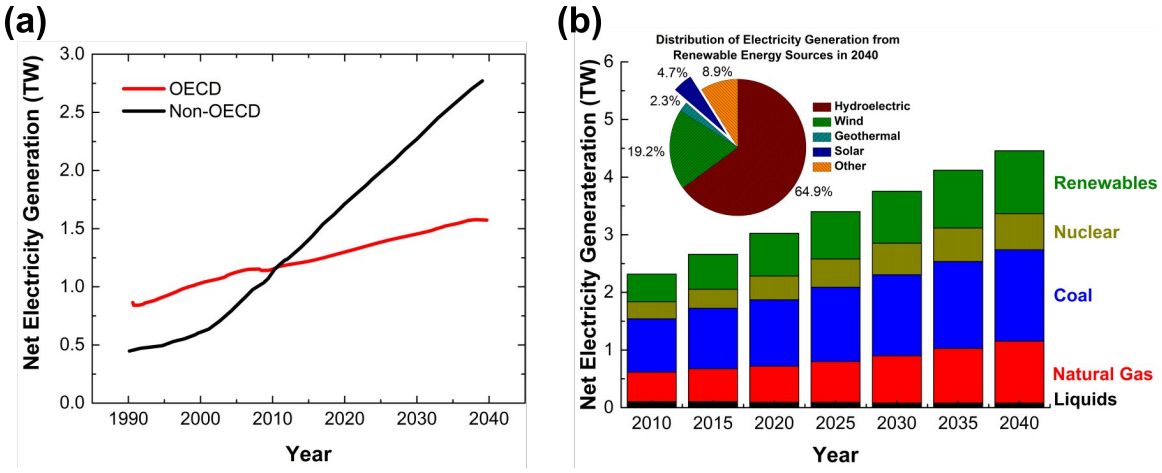

Figure 1.1 Cumulative past and predicted future net electricity generation by year for OCED and non-OCED countries.[1]

programs.[4] Installation and operating costs have been seen as the primary factor preventing wide spread of PV. Grid-parity (*i.e.*, equivalent cost per kWh over the installed lifespan) with public utilities, mainly produced from carbon-rich coal and natural gas in the U.S., has been a general goal for renewable energy sources. Electricity generated *via* wind and hydroelectric are capable of producing electricity at a cost comparable to coal power plants[5] but require specific geographical and climatic conditions. For photovoltaics, grid-parity has been achieved in six states (Hawaii, Florida, Alaska, New Mexico, New York, and California) within the U.S. with high solar irradiance and/or high utility prices when local and federal subsidies are considered.[6] PV is also becoming wide spread in more locations worldwide with recent decreases in PV module and installation costs as well as increases in solar cell efficiency. Over the last 5 years, the reduced cost in comparison to public utilities has lead to a large increases in PV installations across the world as shown in Figure 1.2a. While price is no longer the primary stumbling block to further PV installation, continued cost reductions could bring the price of PV well-below that of traditional carbon-dependent power sources.

1.1 Solar Cell Technologies

Silicon solar cells, in monocrystalline (m-Si) and polycrystalline (p-Si) forms, have an overwhelming majority of the solar cell market when compared to other technologies, as shown in Figure 1.2b which plots the market shares of different solar cell technologies. Recently, improvements in efficiency and economies of scale have led to increases in silicon's market dominance. The manufacturing of silicon solar cells has benefited from the improvements in efficiency and technological advances made during pursuits to improve fabrication of integrated circuits for computer processors and memory.[7] Even though it currently dominates the PV market, silicon is not the most suitable material for solar cells due to its indirect bandgap and, consequently, low absorption coefficient. To overcome its shortcomings, silicon absorber layers in solar cells must be relatively thick ($\gtrsim 400$ μm),[7] producing large and heavy modules. In spite of its shortcomings, the efficiency of silicon solar cells has risen from 15%, achieved in the 1960's, to the current record efficiency of 25.6 % in 2014, which has allowed the material to maintain its leading status.[7,8]

Manufacturing monocrystalline silicon solar cells requires significant capital and operating costs due to the batch-based cell fabrication and module integration processes. Highly efficient cells also require a high material purity, necessitating clean room production environments with high overhead costs.[10] In addition, the limitations of silicon result in rigid solar cell modules that limit installation techniques and require the use metal framing for installation. Because of these issues, alternative solar cell materials that allow for simplified manufacturing processes and more adaptable installation paradigms may increase PV penetration as well as reduce module and installation costs.

Thin film solar cells are the prime candidate to proceed silicon solar cells in the marketplace. Both CdTe and CIGS are direct bandgap semiconductors and possess high absorption coefficients allowing for thin absorber layers (~1 μm) capable of absorbing the full solar spectrum.[10] With the benefit of thin absorber layers, devices can be fabricated on flexible substrates, which may reduce manufacturing costs by allowing for roll-to-roll continuous production and for simplifying installation with no need for metal framing. Additionally, deployment of thin film solar cell modules is associated with a much lower level of carbon

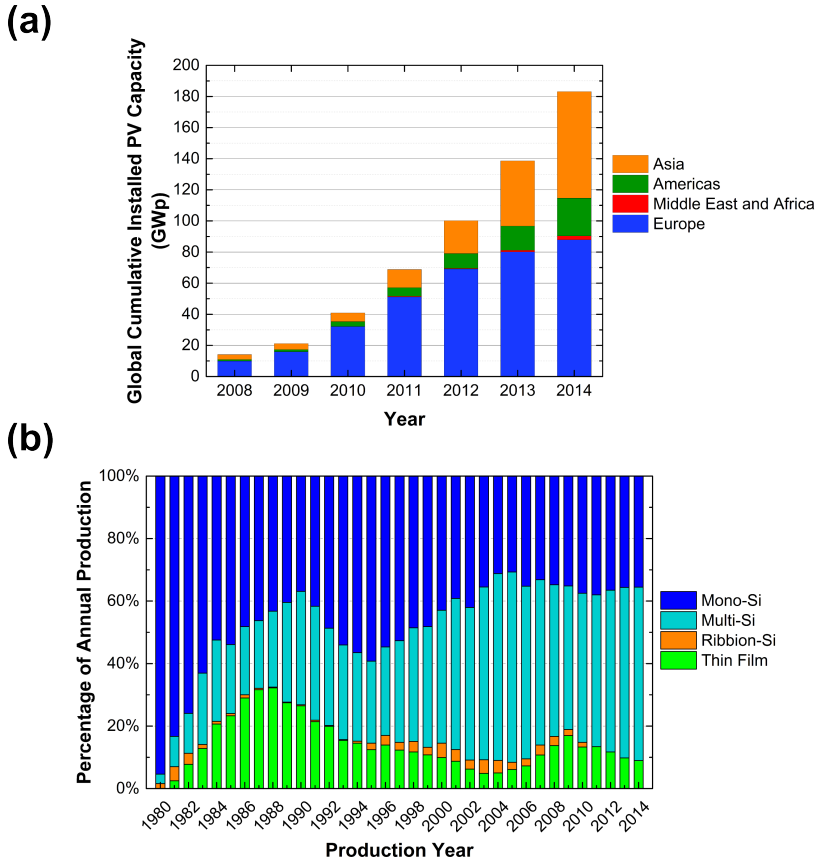

Figure 1.2 (a) Plot of cumulative installed PV capacity from 2008 to 2014 based upon region.[9] (b) Graph of technology distribution of installed PV systems from 1980 to 2014.[9]

emissions (14 and 27 g CO_2-equivalent per kWh for CdTe and CIGS, respectively[11]) than silicon solar cell deployment (45 g CO_2-equivalent per kW[12]), primarily due to the large energy input required to process high-purity silicon.[10]

The benefits of CdTe and CIGS are dampened by their reliance on toxic (Cd and In) and rare-earth elements (In, Ga, and Te), increasing their manufacturing and raw material costs. It has been suggested that the toxicity risks associated with Cd in CdTe solar cells is overstated,[13] but concerns remain nonetheless. The limited abundancy of Te, Ga, and In are more significant factors limiting the potential of CdTe and CIGS solar cells. Due to their scarcity and use in other applications, these metals have been classified as critical

metals by both United States and European Union governmental agencies.[14,15] The current supply bases of Te, In, and Ga are not capable of scaling to terawatts (TW) of installed PV capacity.[16,17] The scarcity concerns could be alleviated by implementation of robust recycling systems, but would require cooperation from many governmental and industrial partners.[18,19] Furthermore, it is in developing regions where a reduction in carbon emissions through use of PV would be most beneficial especially considering the low GDP per capita in regions with high solar irrandiance.[20] However, robust PV recycling programs would be difficult to implement given that electronic waste recycling in these regions has resulted in substantial health and environmental hazards.[21,22] Development of solar cells based upon environmentally-friendly and earth-abundant materials would be able to meet these substantial challenges faced by the current thin film technologies.

1.2 Copper Zinc Tin Sulfide

Copper zinc tin sulfide (Cu_2ZnSnS_4, CZTS) is an emerging thin film solar cell material that is unencumbered by the inherent disadvantages of CdTe and CIGS. CZTS is composed of non-toxic, earth-abundant elements making it a true "green" material for solar cell use. In addition, it possesses a high absorption coefficient (10^4 cm^{-1} for visible wavelengths[23] and a tunable bandgap (1 - 1.5 eV) through alloying CZTS with Se to form $Cu_2ZnSn(Se_{1-x}S_x)_4$ (CZTSSe).[24] Friedlmeier *et al.* reported device efficiencies of 2.3% and 0.6% for CZTS and CZTSSe devices, respectively, in 1997 which were both champion devices at the time.[25] These early films were formed *via* thermal evaporation of binary sulfides in vacuum, a process that has more recently been used to make a 8.6% efficient CZTS device.[26] Since these initial efforts, a multitude of processes have been developed to form CZTS absorber layers with solution-based approaches (namely coatings from molecular-precursor solutions and nanocrystal dispersions) receiving a significant amount of attention due to their attractive compatibility with large-scale, roll-to-roll manufacturing processes.

1.3 Thesis Organization

In Chapter 2, background concerning solar absorber layer formation using CZTS nanocrystal dispersions is discussed. The process steps are broken into sections: synthesis, dispersion formulation, coating, and annealing. The primary processing stumbling blocks of nanoparticle coating cracking, lack of continuous ammenable coating procedures, and incomplete film formation during annealing are introduced and discussed in detail. In addition, the tools and procedures common in the field are presented along with their advantages and drawbacks.

Chapter 3 looks at optimization of CZTS nanocrystal dispersion formulations to achieve consistent and stable dispersions across all synthesis batches. Ligands, namely oleylamine and oleic acid, attach to the CZTS nanocrystals during the hot injection synthesis. The ligand coverage level is critical for synthesis consistency but has not been studied sufficiently. An understanding of these properties in CZTS nanocrystal toluene dispersions was developed through use of dynamic light scattering and attenuated total reflection Fourier-transform infrared spectroscopy. Specifically, the effects of post-synthesis processing and dilution on dispersion stability were studied with these results informing an optimized processing conditions.

In Chapter 4 coating method utilizing aerosol jet printing (AJP) and compaction *via* weighted roller and hydraulic press is described. These steps are amenable to continuous roll-to-roll production. The effects of AJP coating parameters on the printed coating morphology are investigated and an ideal morphology is determined within the available parameter space. The coatings formed by AJP are continuous but have a high porosity unsuitable for further processing into polycrystalline films. To increase the coating density, two compaction systems were used: a weighted roller and a hydraulic press. Compaction by weighted roller increased coating density by rearranging the nanocrystal agglomerates formed during AJP but did not deform the agglomerates. Compaction by hydraulic press produced qualitatively dense nanocrystal coatings comparable to nanocrystal coatings produced by other methods such as dropcasting or spin coating. Higher compaction pressures (> 500 MPa) reduced isolated pores caused by incomplete consolidation. CZTS nanocrystal

coatings with different initial densities were annealed in a high temperature furnace at a sulfur vapor pressure of 50 Torr. The post-annealing film microstructure was found to depend heavily on the initial coating density. This chapter has been published as B. A. Williams, A. Mahajan, M. A. Smeaton, C. S. Holgate, E. S. Aydil, and L. F. Francis, "Formation of Copper Zinc Tin Sulfide Thin Films from Colloidal Nanocrystal Dispersions *via* Aerosol-Jet Printing and Compaction," ACS Appl. Mater. Interfaces. **2015**, 7, 11526.

Chapter 5 delves further into the factors that affect microstructure development during annealing of CZTS nanocrystal coatings. The 5 nm nanocrystals coatings were formed by AJP followed by compaction by hydraulic press and the 35 nm nanocrystals coatings were formed by dropcasting on molybdenum-coated soda lime glass (Mo-coated SLG). Annealing was conducted with 50 and 500 Torr of sulfur at 600 °C for 10, 30, and 60 minutes. Two different film growth mechanisms were identified, abnormal and normal grain growth. Abnormal grain growth was the prominent growth mechanism in 5 nm CZTS nanocrystal coatings where large CZTS grains grew above the nanocrystal coating and consumed the underlying coating. Normal grain growth is the growth mechanism in 35 nm CZTS nanocrystal coatings where the nanocrystal coating was directly converted into a polycrystalline film within the initial boundaries defined by the coating. In addition to nanocrystal size, the concentration of carbon plays a significant role determining the growth mechanism. When carbon concentration is decreased in 5 nm nanocrystal coatings, abnormal grain growth is ceases and normal grain growth is significantly slowed. Adding carbon to 35 nm CZTS nanocrystals with the addition of polystyrene leads to enhancement of abnormal grain growth. This work has been prepared for submission as B. A. Williams, M. A. Smeaton, N. D. Trejo, L. F. Francis, and E. S. Aydil, "Influence of nanocrystal size during annealing of copper zinc tin sulfide nanocrystal coatings."

Chapter 6 looks at the use of ultrasonic spray coating (USC) to form dense CZTS nanocrystal coatings and the effects of NaOH on film microstructure development during annealing. Coatings formed *via* USC from pure toluene dispersions contain surface craters and have non-uniform coating thickness. The addition of cyclohexanone (30 volume percent) eliminates these craters and the coating thickness becomes more uniform. The coating microstructure improves due to the lower evaporation rate of the aerosol droplets during

transport to the substrate. The droplets impinge on the substrate with a more uniform liquid content, improving coating consolidation uniformity. These coatings were then used to study the effects of Na addition on microstructure development during thermal annealing. Different amounts of aqueous NaOH (total NaOH amounts of 0.1 and 1 μmol)were dried in the glass annealing ampules prior to annealing. It was found that both 0.1 and 1 umol of NaOH enhanced grain growth rates and substrate coverage.

Chapter 7 is on intense pulsed light annealing (IPL) of CZTS nanocrystal coatings. IPL utilizes a xenon flash lamp to produce a broadband emission spectrum ranging from near-IR to ultraviolet quickly heat materials that absorb in the relevant wavelength range. Its application for annealing of CZTS nanocrystals coating has not been extensively studied although the Xe lamp spectrum overlaps well with the absorption of CZTS. IPL annealing of ~35 nm CZTS nanocrystal coatings on Mo-coated SLG substrates lead to crack formation with the crack severity and density depending on the pulse (light) intensity and the number of lamp flashes. Raman spectroscopy of nanocrystal remnants at the Mo-CZTS interface helped determine that low density cracking was caused by CZTS decomposition at the this interface. High density cracking was linked to the thermal stress generated during repeated flashes of the xenon flash lamp. Finite element simulations provided insight into the spatiotemporal evolution of the temperature in the CZTS film and substrates and revealed the presence of severe temperature gradients during flashes and rapid cooling after flashes. It was proposed that replacing the Mo-coated SLG with a high thermal diffusivity substrate, such as a metal foil, would reduce and eliminate these detrimental thermal stress events. IPL annealing was conducted with molybdenum foil subtrates to evaluate this proposal. Under the same annealing conditions used with Mo-coated SLG, the CZTS coatings on Mo foil exhibited neither high nor low density cracking. At longer annealing times, coatings on Mo foil did show low density cracking but this was eliminated by the addition solid sulfur to the annealing ampule to counteract CZTS decomposition. This work has been prepared for submission as B. A. Williams, M. A. Smeaton, C. S. Holgate, N. D. Trejo, L. F. Francis, and E. S. Aydil, “Intense pulsed light annealing of copper zinc tin sulfide nanocrystal coatings.”

Chapter 2

Background Information: Development of CZTS Solar Cells from Nanocrystal Dispersions

2.1 Introduction

Development of CZTS solar cells followed shortly after the first reports of the photovoltaic effect in CZTS in 1988.[24] The CZTS absorber layers used in the earliest devices were formed *via* sulfidation (*i.e.*, annealing at high temperatures in the presence of sulfur vapor) of vacuum-deposited metal (Cu-Zn-Sn) layers and achieved power conversion efficiencies of 2.3%.[25] Since that time, sulfidation of a precursor film has been the primary technique used to form CZTS absorber layers for solar cells, but the precursor film deposition approaches have evolved and expanded. The majority of these methods can be divided into two categories: vacuum-based (chemical vapor, physical vapor deposition, and co-evaporation) and solution-based (electro-deposited layers, chemical bath deposition, and molecular and nanocrystal "inks"). Recently, solution based techniques have been the primary formation method as solar cells developed from vacuum-based techniques have stalled at a maximum efficiencies of approximately 9%.[8,27,28]

Solution-based techniques utilizing CZTSSe inks offer the potential to decrease solar

cell production costs by enabling roll-to-roll production using flexible substrates and traditional large-scale coating technologies. Efficiencies of 12.6%[29] and 9.0%[30] using molecular-precursor solutions and nanocrystal dispersions, respectively, have been achieved, surpassing those achieved through vacuum-based techniques. These high-efficiency devices have been formed utilizing CZTS alloyed with Se to form $Cu_2ZnSn(S_{1-x}Se_x)_4$. These films will be referred to as CZTSSe and CZTSe films depending on the extent of substitution. The CZTS nanocrystal dispersion approach is particularly interesting due to the freedom to tune the dispersion makeup and separate the coating formation from the CZTS phase formation. This separation is not possible with the molecular precursor-based approaches.

2.2 CZTS Absorber Layer Formation

Figure 2.1 illustrates the four processing steps necessary to form CZTS absorber layers from nanocrystal dispersions. First, CZTS nanocrystals are synthesized using a variety of techniques. The general synthesis categories and a few specific synthesis procedures are discussed in the following section. After synthesis, the nanocrystals are incorporated into a well-stabilized dispersion using organic or polar solvents depending on the synthesis procedure. The dispersions are then used to form dense nanocrystal coatings ranging from 1 - 3 μm in thickness. The nanocrystal coatings are annealed in a chalcogenide (S or Se) atmosphere at high temperatures (> 550 °C) to induce growth of large CZTS grains to form a polycrystalline film, a common and necessary feature of high-efficiency solar cells. After annealing, the CZTS absorber layer is integrated processed into a solar cell with deposition of additional films (*e.g.*, CdS, ZnO, etc.) on top of the CZTS layer.

Figure 2.2 is a schematic of a completed CZTS solar cell. The structure resembles that commonly used for CIGS solar cells.[31] A molybdenum-coated soda lime glass (Mo-coated SLG) substrate acts as the back electrical contact as well as providing structural rigidity to the device. Molybdenum possesses a suitable band alignment with CZTS providing limited resistance to hole transport at the Mo:CZTS interface.[32] On top of the Mo-coated SLG is the CZTS absorber layer which is a polycrystalline film with a thickness of 0.5 to 1.5 μm. A

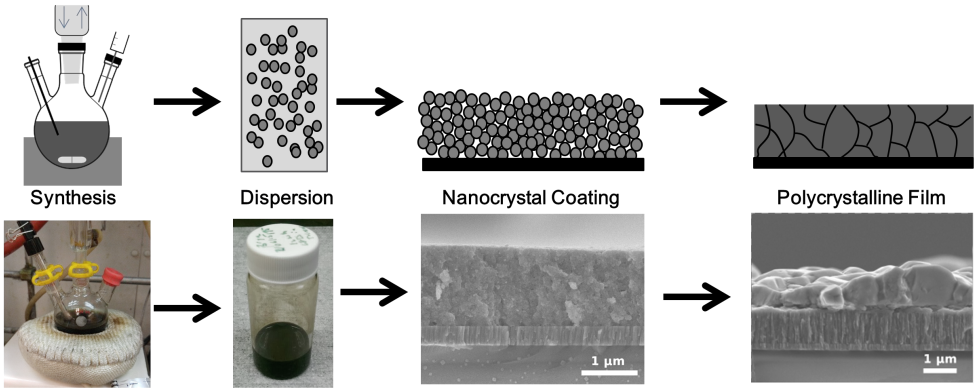

Figure 2.1 Illustration of the four primary process steps to form CZTS absorber layers comprising nanocrystal synthesis, dispersion formulation, nanocrystal coating formation, and polycrystalline film development. Each processing system requires optimization and coherence with proceeding and preceding operations.

thin (~50 nm) CdS layer is deposited above the CZTS absorber layer forming a *p*-*n* junction with the *p*-type CZTS and is generally created using chemical bath deposition.[33,34] A zinc oxide:aluminum-doped zinc oxide (ZnO:Al-ZnO) transparent conducting layer is deposited on top of the CdS to allow charge transport to the top electrode. An anti-reflective layer is sometimes used to reduce reflective efficiency losses, but is often not used in laboratory devices. During processing of the absorber layer, the effects of the microstructure, morphology, and chemical composition of the CZTS layer on the deposition efficiency and function of the subsequent layers must be considered to create a highly efficient solar cell.

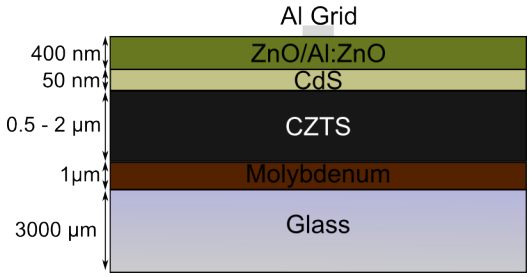

Figure 2.2 Schematic of a typical device structure for a CZTS solar cell.

2.3 CZTS Nanocrystal Synthesis Procedures

Research in the synthesis of CZTS and CZTSSe nanocrystals has been burgeoning as many researchers recognize the advantages of a solution-based approach. A variety of nanocrystal synthesis methods have been developed including heat-up,[35,36] hot-injection,[37,38] mechanochemical,[39–41] and microwave reactions.[42,43] From these methods, hot-injection reactions have become popular due to their relatively short synthesis times, simple experimental protocols, and consistent yields.[44] It is important to note that CZTS has two room temperature stable crystal forms: kesterite and wurtzite.[45] Most nanocrystal synthesis methods produce the kesterite phase with a minority generating wurtzite nanocrystals.[46,47] In most cases, annealing of wurtzite CZTS nanocrystals produces the slightly more stable kesterite phase.[48,49] Further discussion here is focused on development of kesterite nanocrystals and films.

Hot-injection synthesis of CZTS relies upon decomposition of precursor molecules in a coordinating-solvent such as oleylamine (OLA),[50,51] oleic acid[52] or triphenylphosphine oxide (TOPO)[53,54] with TOPO primarily used to from pure selenium CZTSe nanocrystals. The precursor molecules are commonly metal salts including metal chlorides,[55] acetates,[38] and acetylacetonates.[37,38] In a typical synthesis procedure, the precursor molecules are dissolved in a long-chain organic coordinating solvent and heated to the desired reaction temperature. Olyelamine is injected into the precursor solution and held at the reaction temperature for as little as 10 minutes or for as long as 20 hours.[54,56] It has been reported that the reaction temperature and the choice of coordinating ligand affect the size and shape of the nanocrystals formed.[52,56–58] Collord *et al.* saw small changes in nanocrystal size with constant reaction times of 10 minutes to 24 hours, indicating nanocrystals form quickly during hot injection reactions. However, they did observe changes in elemental stoichiometry with reaction time, supporting the choice of extended reaction times used in other works.[56]

In a slightly different synthesis procedure, precursor molecules containing sulfur in the form of metal dithiocarbamate compounds are dissolved in oleic acid solutions and then injected into hot oleylamine[52] or have room temperature oleylamine injected into them.[59] This reaction relies upon thermal decomposition of the precursor molecules rather than nucle-

ation due to precursor supersaturation as in the previous methods. The thermal decomposition-based reaction is utilized here to form 5 - 35 nm CZTS nanocrystals from copper (II) diethyldithocarbmate, zinc (II) diethyldithiocarbmate, and tin (IV) diehtyldithiocarbmate precursors. CZTS nanocrystals formed using this method will be considered from this point forward, although the following information is applicable to nanocrystals formed by other methods.

2.4 CZTS Nanocrystal Dispersion Formulation

After synthesis, the nanocrystals are suspended in the reactant solution with unreacted species and reaction by-products as well as long carbon chain organic solvents that are unsuitable for subsequent coating operations due to their high boiling points. To remove these undesired components and disperse the nanocrystals in a more suitable liquid for coating operations, the reactant solution is commonly "washed" *via* dilution with an alcohol which causes the sterically stabilized nanocrystals to sediment which is further prompted by centrifugation of the solution.[37,38,59] After centrifugation, the supernatant is decanted, leaving the CZTS nanocrystals. This process may be repeated multiple times by re-dispersing the nanocrystals in a suitable liquid and repeating the alcohol washing procedure.

After washing, the final dispersing liquid used depends on the coating application. For coating operations requiring low viscosity dispersions, toluene,[60] hexane,[61] or other low viscosity organic solvents are used. On the other hand, high viscosity and highly-loaded (> 0.1 g/mL) 1-hexanethiol pastes are commonly used for doctorblading.[30,50] In some cases, it is desired to re-disperse the sterically-stabilized nanocrystals in polar solvents, most commonly water, through ligand exchanges. Aqueous dispersions are appealing because they reduce the dispersion's inherent toxicity and alleviate the environmental concerns associated with some organic solvents. This can be accomplished by extended stirring of a two-phase liquid mixture with one phase being the CZTS dispersion and the other being formamide with a sulfur ion source (such as K_2S or Na_2S).[62,63] Another approach uses excess 5-amino-1-pentonal as both the exchange phase and capping liquid, although the final nanocrystals

dispersed poorly in some polar solvents.[36]

2.5 CZTS Nanocrystal Coating Formation

After a stable dispersion is formed, a suitable coating operation must be used to create CZTS nanocrystal coatings.To serve as effective solar absorber layers after annealing, a dense, crack-free CZTS nanocrystal coating is required. This is to prevent insufficient film thickness, which would limit absorption efficiency, and prevent short-circuits caused by film voids.

2.5.1 Nanoparticle Dispersion Coating Methods

Figure 2.3 illustrates five common laboratory-scale coating methods used in processing of nanoparticle dispersions for solar absorber layers. Dropcasting, spin-coating, and doctor-blading are the most commonly used coating methods in the field. During dropcasting, a precise volume of a low viscosity nanoparticle dispersion with a low particle loading (~8 - 30 mg/ml) is deposited onto to a substrate. A metal frame that acts as a "well" for the dispersions defines the coating area and thickness. The use of a metal frame also acts to improve the coating thickness uniformity according to reports on similar particle-based coating operations.[64] At times, the evaporation rate is slowed by placing an inverted funnel over the coating during drying.[60] This aids in crack prevention and coating uniformity by slowing stress development and allowing time for particle diffusion.[65] While similar in process fundamentals to large-scale coating techniques such as slot coating, dropcasting may be difficult to scale to large scale production due extended drying times.

In doctor blading, a highly-loaded (> 0.1 g/ml) dispersion, generally in 1-hexanethiol, is spread across a substrate with a coating area defined by either a metal frame or scotch tape.[39,66–68] For this process to be successful, it is generally desired that the dispersion forms a moldable "paste" that can be forcibly spread within the coating area. High viscosity dispersing liquids achieve this rheological desire but usually also have high boiling points, making them difficult to remove from the coating even after high temperature atmospheric

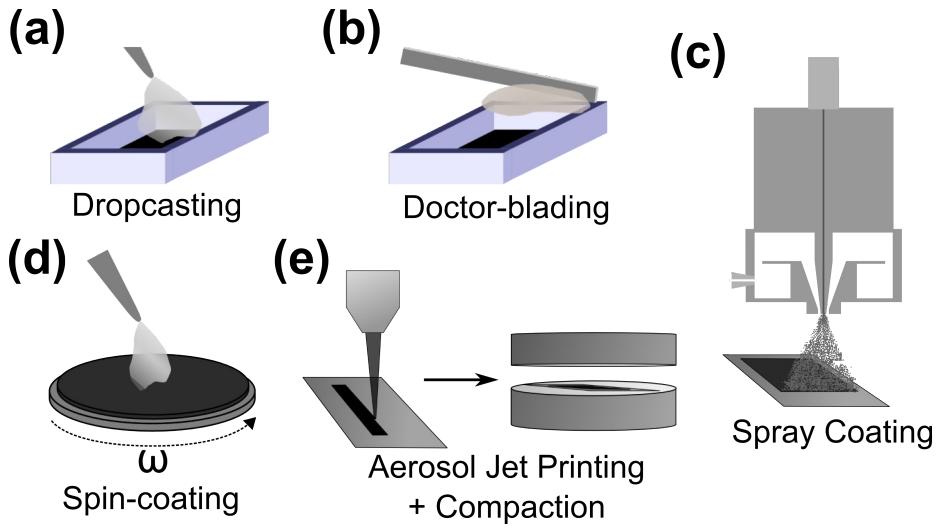

Figure 2.3 Common coating processes used to form nanoparticle coatings.

annealing.[66,69] Additionally, the highly-viscous dispersions present processing challenges relating to transport and ink pumpability.

Spin-coating is commonly used for creating thin (< 100 nm) and uniform coatings. In this technique, a substrate is mounted to a spinning axis through a vacuum seal. A small amount of dispersion or coating solution is deposited into the center of the substrate which is then spun at a constant angular velocity. The thickness of the coating depends on the volume of dispersion deposited, the dispersion rheology, and the angular velocity used. By applying multiple layers, a thicker coating can be constructed although intermediate treatments may be required to prevent redispersion or dissolution of previous layers.[37,51,70] Spin-coating is inherently a batch process that is difficult to cost-effectively scale to large production volumes. In addition, a significant portion of the deposited ink is ejected from the substrate during coating and is usually not recoverable. This is a significant issue with high-cost ink like those used for solar absorber layers.

Both ultrasonic spray coating and aerosol jet printing, shown in Figures 2.3c,e, respectively, are aerosol-based coating methods that have recently found use in absorber layer processing. Additionally, conventional pneumatic spray coating has been reported by a number of groups to create solar absorber layers.[71–74] In conventional spray coating, the

nanoparticle dispersion is pumped to a the nozzle of the spray gun. The nozzle, or air cap, is designed to mix the incoming liquid with high-pressure air atomizing the dispersion into an aerosol with droplet sizes decreasing at higher air pressures.[75] Ultrasonic spray coating is similar in general operation to pneumatic spray coating but relies upon mechanical rather than pneumatic atomization to generate the aerosol. The dispersion is pumped into the spray nozzle to an atomizing tip which vibrates at a frequency ranging from 20 to 180 kHz with higher frequencies generating smaller aerosol droplets.[76] The rapid vibrations cause standing waves to form on the nozzle tip which in turn eject aerosol droplets. After ejection, the aerosol is focused into a dense stream using high-pressure air.

Aerosol jet printing (AJP) is a recent evolution of spray coating. The defining advantage of aerosol jet printing is the ability to print narrow ($\geq$ 15 μm), high aspect-ratio lines with few material or solution restrictions. AJP has received significant attention in printed electronic applications while use in other applications is rapidly expanding. With AJP, aerosol generation occurs in a ultrasonication water bath separated from the nozzle. This process creates a finer aerosol than produced in conventional or ultrasonic spray coating with droplets ranging from 3 - 10 μm in diameter. The aerosol is transported from the atomization vessel to the printing nozzle with a nitrogen carrier gas. At the nozzle tip, the aerosol is focused by a separate sheath gas. This additional flow propels the aerosol rapidly onto the substrate. Coatings and patterns are formed through translation of the nozzle or stage during printing. Both aerosol jet printing and ultrasonic spray coating are discussed in further detail in Chapters 4 and 6, respectively.

2.5.2 Cracking During Drying of Nanoparticle Coatings

Figure 2.4 exemplifies the major challenge faced in formation of thick crack-free nanoparticle coatings. Here, a 5 nm CZTS nanocrystal tolune-based dispersion was dropcasted onto a silicon substrate within a 250 μm thick metal frame and the coating was recorded with a high-speed camera as it dried in atmospheric conditions. The coating underwent non-uniform drying, a common occurrence during drying of particle-based coatings,[65,77–79] where a drying front progresses from left to the right in the images (*i.e.*, from lighter to

darker color). As the interface, or drying front, progresses across the coating, cracks are initiated in the wet (dark region) and grow in size as the surrounding area dries. The "mud cracking" pattern in the dried coating is caused by relaxation of the biaxial stress developed during drying through cracking.[80,81] It is clear from these images that cracks develop while the film is wet and progress as the film dries in agreement with observations by others.[82,83] These cracks are common across many applications involving coating of nanoparticle dispersions.[84–86] It is a particularly significant problem in the processing of nanocrystal dispersions for solar cells since this application requires thick and dense coatings, properties that are at odds with each other in crack prevention.

A schematic detailing the three drying phases of a particle-based coating is illustrated in Figure 2.5a. Drying is initiated after the dispersion is deposited onto the substrate. As drying time increases, the liquid level is decreased and the dispersed particles began to aggregate and form a loose particle network. Due to the use of the metal frame to define the coating area, a drying front develops that initiates at the center of the coating and progresses outward. At this front, air begins to invade the now condensed particle network as the liquid level recedes below the coating surface.

Crack development during the drying of particulate coatings has been extensively studied[65,83,87,88] but exact causes and contributing factors for crack development are still debated. Figure 2.5b illustrates the generally accepted process of crack formation during the air invasion phase of drying. As the liquid recedes into the particle matrix, liquid menisci form between neighboring particles. The liquid menisci a negative radius of curvature relative to the air leading to a pressure drop, referred to as capillary pressure, across the interface in accordance with the Young-Laplace equation.[89] This capillary pressure, p_{cap}, has a general relationship of

$$p_{cap} = -\phi \frac{2\gamma}{d} \tag{2.1}$$

where ϕ is a system dependent "suction" factor, γ is surface tension, and d is the primary particle size.[77] The pressure difference induced by the menisci creates a cumulative com-

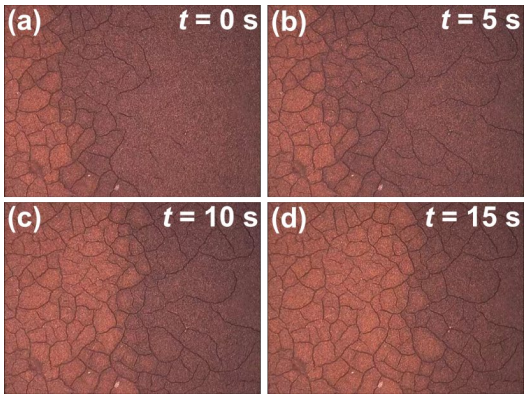

Figure 2.4 Time lapse optical images extracted from a high-speed video of a CZTS nanocrystal (5 nm) coating cracking during during drying. Cracks are approximately 10 μm. Scalebar is absent due to the limitations of acquisition camera.

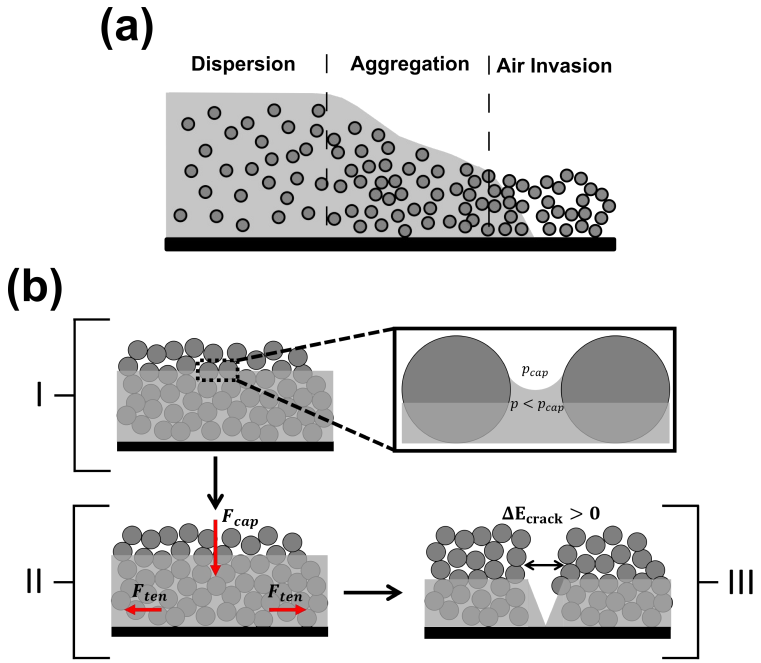

Figure 2.5 (a) Schematic illustration of overall drying process with particle dispersions. (b) Schematic illustration of stress generation and crack formation during air invasion phase of drying with particle-based coating.

pressive force on the particle network in all directions. If the coating is unrestrained during drying, this compressive force would act in all directions and the coating would shrink isotropically.[90] Since the particle network is adhered to the substrate laterally, movement is limited in the transverse direction. In response to this constraint, a tensile stress develops parallel to the substrate. A crack may develop if the energy released through stress relaxation by cracking is greater than that required to create the newly exposed crack surface area (*i.e.*, $\Delta E_{\text{crack}} > 0$).

The maximum stress sustained before cracking is dependent on numerous liquid, dispersion, and film properties including shear modulus, film thickness, initial strain, and liquid viscosity as detailed by Russel *et al.*[83] The exact details of these relationships are beyond the scope of this analysis, but some general trends and conclusions are useful for designing and conducting experiments. Two critical values can be defined from the relationships, critical capillary pressure and critical cracking thickness (CCT). With fixed film properties, a particle-based coating has an inherent critical capillary pressure. If the capillary pressure from the liquid menisci is below the critical capillary pressure, the film will not crack as the energy relieved through crack formation is less than that required for crack surface formation. Similarly, if the film thickness is below the CCT, the film will not crack. The CCT is often used to determine the relative film stress with a large CCT indicating a lower stress or higher fracture toughness.[65,77,78,91–95]

Several strategies have been used to prevent cracking while coating nanoparticle dispersions during production of solar absorber layers. In one strategy, polymer binders are added to the nanocrystal dispersion to increase the coating's fracture resistance, increasing its maximum sustainable stress.[65] While this approach produces crack-free films, resulting solar cells suffer from low power conversion efficiencies due to residual carbon layers formed from decomposition of the polymeric binders.[66,96] Another strategy is to build the film up to the desired thickness using multiple, individually coated, layers where each layer is thinner than the CCT.[85,91,97,98] Mild thermal annealing or chemical treatment may be required to prevent redispersion of previous layers before the next layer is applied. Increasing the coating's drying time by manipulating the evaporation rate has proven beneficial in avoiding cracking, by slowing stress development and allowing for diffusional rearrangement of the

nanoparticles into more robust particle networks.[37,60]

2.6 Annealing of CZTS Nanocrystal Coatings

Solar cells constructed from unnannealed nanocrystal coatings suffer from low power conversion efficiencies likely caused by surface defects along the grain boundaries, poor conductivity due to high porosity, and high electrical resistance from insulating carbon ligands.[71,98] These detrimental properties may be alleviated by annealing the nanocrystal coatings at high temperatures.[99,100] In the case of CZTS, optimized annealing procedures transforms coatings into dense, polycrystalline films composed of large-grained (1-3 μm) CZTS.[30] This technique is not unique to CZTS as CIGS and CIS solar cells processed from nanocrystal dispersions are also subjected annealing to induce grain growth.[68] Annealing conditions for successful conversion of a CZTS nanocrystal coating are rather strenuous due morphological influences on device efficiency and the material's susceptibility to de-composition at high temperatures.[101] To prevent decomposition and enhance grain growth rates, annealing is conducted at high temperatures in the presence of either sulfur vapor, called sulfidation, for formation of CZTS films or selenium vapor, called selenization, to form CZTSSe films.

Figure 2.6 shows two common annealing setups used to isolate the CZTS coating and provide an appreciable chalcogenide vapor pressure during annealing: (a) sealed graphite boxes[30,102–104] and (b) quartz ampules.[60,105–107] In the former, the CZTS nanocrystal coatings are sealed in a graphite box with a known mass of solid selenium or sulfur to provide the chalcogenide atmosphere when heated. The box is then placed in an isolated, evacuated furnace with an inert purge gas (*e.g.*, Ar, N_2, etc.) to remove the selenium or sulfur vapor that diffuses through the semi-permeable graphite box.[108] The continuous loss of vapor makes measurement and even estimation of the selenium/sulfur vapor pressure within the box difficult. It has been reported that use of the same graphite box for multiple annealing operations leads to adsorption of gas species on the box surface, which may have an affect on reproducibility of annealing results.[109]

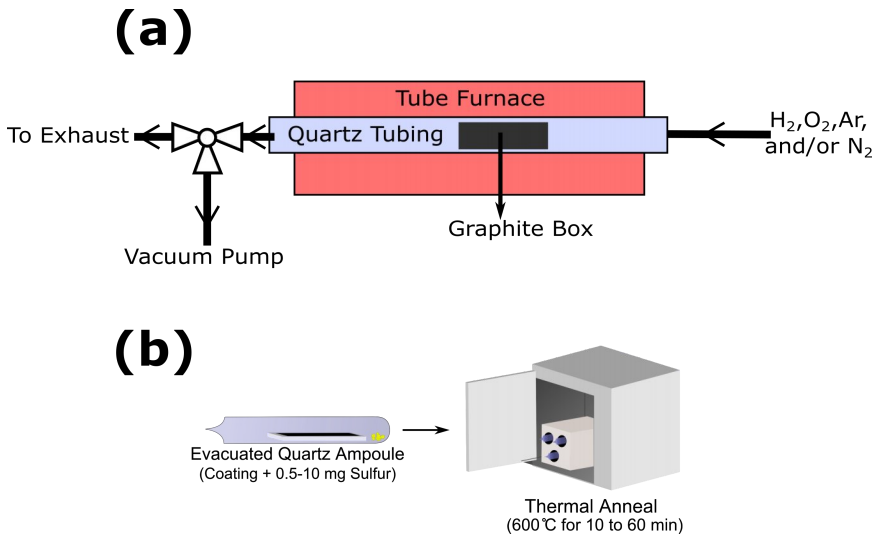

Figure 2.6 Illustrations of two common CZTS nanocrystal coating annealing procedures: (a) tube furnace utilizing a graphite box[108] and (b) sealed quartz ampules.

Quartz ampules are an appealing alternative to graphite boxes for isolation of the CZTS coatings during annealing. CZTS nanocrystal coatings are placed in cylindrical quartz tubes along with a mass of solid chalcogenide. The tubes are evacuated (~10^{-6} Torr) and then flame-sealed to form individual annealing ampules. The ampules are then placed in a high temperature furnace to anneal the CZTS coatings. Since the ampules have a known internal volume, the chalcogenide vapor pressure within the ampules can be calculated from the initial solid mass.[60,106] Additionally, the relatively inexpensive ampules are disposed of after one use, removing any the possible effects of adsorbed species associated with multiple use containers.

2.6.1 Selenization

Selenization is the predominant annealing method for transforming CZTS nanocrystal coatings into polycrystalline films. Miskin *et al.* reported a record efficiency of 9.6% for a CZTSSe solar cell produced by selenization of a CZTS nanocrystal coating.[30] They used a graphite box setup similar to that shown in Figure 2.6a and annealed in a Se atmosphere for

20 minutes at 550°C. The popularity of selenization may be related to the lower volatility of selenium compared to sulfur,[60] which results in better vapor containment within the loosely sealed graphite boxes. Nevertheless, selenization has proved effective in solar cell device fabrication and will likely remain the leading annealing procedure unless the performance of sulfurized CZTS devices improves.

Curiously, pure sulfide CZTS nanocrystal coatings produce superior film morphologies during selenization compared to pure selenide CZTSe nanocrystal coatings. In the pursuit of $CuIn(S,Se)_2$ films from nanoparticle coatings, Guo *et al.* reported enhanced grain growth during selenization with $CuInS_2$ nanocrystals compared to $CuInSe_2$ nanocrystals.[110] They attributed this behavior to the additional reactive driving force provided by the sulfide to selenide reaction which is absent during selenization of pure selenide $CuInSe_2$. Later reports by Guo *et al.* found that mixed chalcogenide CZTSSe nanoparticles with initial Se content up to ~75% of the total chalcogenide content (*i.e.*, $Cu_2ZnSnS_1Se_3$) grew rapidly during selenization, a result contrary to the reaction-driven enhancement hypothesis.[111] Riha *et al.* proposed that Se provides faster vapor-transport compared to S during annealing of CZTS nanocrystal coatings, rather than providing additional driving force.[112] In addition to the increased rate of grain growth, the replacement of S with Se within the nanocrystals grains may aid in porosity reduction since this replacement reaction results in a 14.6% increase in the crystal unit volume.[110]

CZTSSe films formed by selenization of nanocrystal coatings share a general film morphology like that illustrated in Figure 2.7. The films have a bilayer structure comprising a bottom layer of fine-grained CZTSSe and a top layer of large (1 - 5 μm) CZTSSe grains.[30,113] The evolution of this bilayer structure during selenization was analyzed by Mainz *et al.* through *in-situ* energy dispersive X-ray diffraction and electron microscopy.[102] They reported the formation of copper selenide on the surface of the nanocrystal coating which evolved into CZTSSe while the underlying nanocrystal coating was slowly selenized producing a small increase in average grain size. The presence of the fine grain layer has seemingly no detrimental effect on electrical properties,[103] but does limit the thickness of the large grained absorber layer since not all CZTS material is incorporated into the primary absorbing layer.

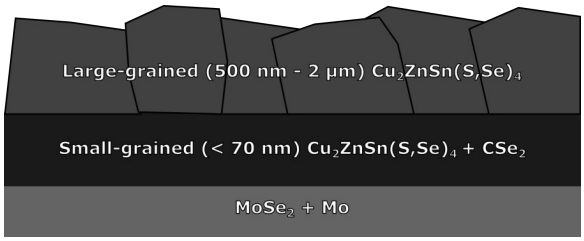

Figure 2.7 Illustration of the typical film morphology after selenization of CZTS nanocrystal coatings. Large-grained CZTSSe lies above a "fine-grain" layer composed of CZTS/CZTSSe nanocrystals that contains a high concentration of C, Zn, and Se.[102] The fine-grain layer undergoes little to no grain growth but experiences sintering.

2.6.2 Sulfidation

In contrast to selenization, sulfidation of CZTS nanocrystal coatings has received little research attention resulting in a dearth of process optimization and understanding. CZTSSe devices formed through selenization have higher reported device efficiencies than CZTS devices produced by sulfidation which may be due to inherent material properties or simply the lack of research volume on sulfidation.[44] sulfidation retains the CZTS phase which has a slightly more suitable bandgap for solar devices (1.5 eV for CZTS[24] vs. 1.0 eV for CZTSe[114]).[23,115] In addition, selenium is toxic in significant doses making sulfidation more attractive for large production volumes. For these reasons, pursuit of a pure sulfide process to form CZTS solar cells from nanocrystal coatings is worthwhile.

sulfidation is conducted in the same manner as selenization. The majority of reports detail use of graphite boxes and tube furnaces to isolate the nanocrystal coatings in a sulfur-rich atmosphere.[53,60,116,117] Early attempts at sulfidation produced films with high porosity and small grain sizes resulting in low device efficiencies (< 2%).[116,117] Improvements have been achieved through optimization of the sulfur atmosphere conditions[60] and by altering the surface-attached ligands.[53] By exchanging the original oleylamine ligand for a triphenylphosphate ligand, Kim *et al.* enhanced CZTS grain growth with formation of up to 3 µm CZTS grains.[53] This resulted in solar cells with an efficiency of 3.6%.

Chernomordik *et al.* showed that sulfur vapor pressure, annealing temperature, and substrate choice all have substantial effects on CZTS grain growth rates.[60] Additionally, they

explicitly identified and defined a distinction between normal grain growth and abnormal grain growth. Normal grain growth is characterized by direct transformation of the nanocrystal coating into a large grained film as nanocrystals neck, sinter, and grow. Conversely, abnormal grain growth is characterized by bimodal grain size distribution as CZTS grain growth above the top surface of the nanocrystal coating *via* consumption of the underlying coating as growth progresses. The two mechanisms can exist and operate together as the CZTS film microstructure evolves. Figure 2.8 illustrates growth in both of these scenarios. It was found that increasing the sulfur vapor pressure and increasing the annealing temperature independently increased both abnormal and normal CZTS grain growth rates. It was determined that abnormal and normal grain growth processes are compete with each other with one dominating over the other depending on the annealing conditions. Chernormodik *et al.* also reported enhanced grain growth with the use of substrates containing alkali-metals, an observation discussed in further detail in the following section.

2.6.3 Effects of Substrates and Alkali Metals on Film Development

Traditionally, molybdenum-coated soda lime glass (Mo-coated SLG) has been the substrate of choice for CZTS device development, initially due to the material's popularity and success in CIGS device development as well as the suitable work function of Mo with CZTS.[32,118] In CIGS research, it was identified that alkali metals, common impurities within SLG, enhanced grain growth and improved electrical properties.[119–123] Recently, similar effects have been observed in CZTS thin films. Johnson *et al.*[106] and Chernomordik *et al.*[60] reported superior CZTS film morphologies when annealing was conducted on SLG substrates than on fused quartz substrates, which have low alkali metal content.

These effects rely upon the diffusion of alkali metals from the substrate into the coating or precursor film which limits control of the alkali metal uptake. To address this, extrinsic methods to incorporate alkali-metals into CZTS films prior to or during annealing have been developed. Johnson *et al.* introduced alkali metals through vapor transport of NaOH/KOH deposited on the interior of annealing ampules prior to annealing.[124] Yang *et al.* placed bare SLG on top of a CZTS nanocrystal coating to increase sodium incorporation.[125] A variety

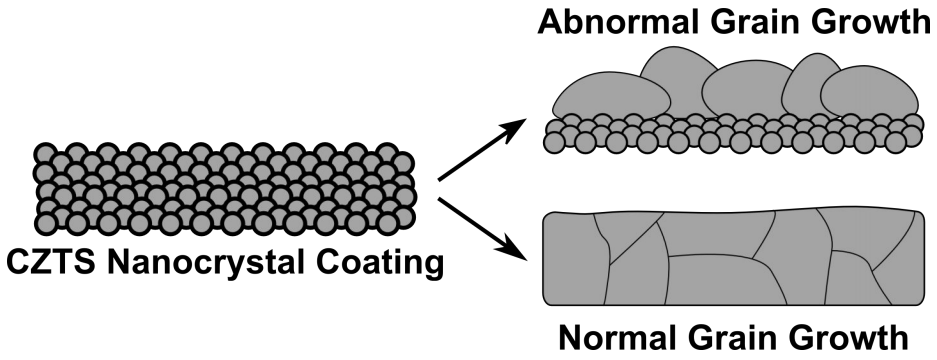

Figure 2.8 Illustration depicting (a) normal- and (b) abnormal-grain growth during annealing of CZTS nanocrystal coatings.

of other methods to enhance sodium concentration have been reported including soaking of precursor coatings in aqueous sodium solutions,[53,68] sputtered layers of NaF,[126,127] and synthesis of CZTS nanocrystals with internally incorporated Na.[128]

There is no clear consensus on how alkali metals aid the microstructure development during annealing of CZTS nanocrystal coatings. A number of plausible hypotheses have been proposed but lack direct experimental evidence. Sutter-Fella *et al.* suggested a liquid phase of Na_2Se_x is formed on the surface of the nanocrystal coating during selenization.[127] The hypothesis is based upon the Na-Se phase diagram and morphology development similarities with work on CIGS where experimental evidence of Na_2Se_x has been reported.[119,129] The melting point of Na-Se compounds range from 258 °C for $NaSe_3$ to 876 °C for Na_2Se[130] which is within the range of temperatures used for selenization (~500 - 600 °C). Similar melting points are reported for Na-S phases[131] which would extend this operating mechanism to sulfidation as well. Johnson *et al.* hypothesized that alkali metals would segregate to CZTS grain boundaries and affect the local melting point, enhancing grain growth.[124]

In addition to the effects on microstructure development, alkali metals have beneficial effects on the electrical properties of CZTS films by increasing minority carrier lifetimes and carrier concentrations.[126–128,132–134] These improvements are attributed to defect passivation causing a reduction in non-radiative recombination. Maeda *et al.* calculated energies required for sodium and potassium substitution within a CZTS lattice as well as the migra-

tion energies to vacancies at interstitial sites in the lattice.[135] They found that sodium and potassium have low migration energies to copper and zinc vacancies (*i.e.*, Na_{Zn} and Na_{Cu}) A correlation of copper-deficiency and increased sodium concentration was observed by Xie *et al.* in CZTSSe absorber layers after post-annealing low temperature treatments, indicating possible Na_{Cu} substitutions.[136] More work is necessary to determine the underlying mechanisms for the experimentally observed physical and electrical effects alkali metals have on CZTS films.

Chapter 3

Optimization of CZTS Nanocrystal Dispersion Stability

3.1 Background and motivation

The benefits of using CZTS nanocrystal dispersions to form CZTS solar cells become apparent at large production volumes. Successful scale-up of laboratory procedures requires a high degree of material and process consistency. When dispersions are involved, special attention must be given the to the dispersion composition and stability. Any batch-to-batch variations may complicate downstream processing and require expensive process tuning for every unique batch. Additionally, it may be impractical to utilize dispersions soon after synthesis and they may have to be stored for significant periods of time before use, requiring long-term dispersion stability. With sterically-stabilized dispersions, a thorough knowledge of the ligand coverage dynamics throughout the various processing stages is critical to achieving consistent dispersion properties.

The roles of oleylamine and oleic acid, popular choices for coordinating ligands and solvents, during hot injection reactions have been studied by a number of researchers.[46,56–58,137] However, their roles in stabilization of the subsequent dispersion has been studied less even though they are the primary steric stabilization sources. Many of the reports pertaining to ligand dynamics in nanocrystal inks pertain to replacement of long chain carbon lig-

ands with either shorter chain ligands (*e.g.*, pyridine,[138] hexanethiol,[23,50] ethylenediamine[99] among others) or simpler molecular stabilizing ligands (metal molecular chalcogenides[139] or simple chalcogen ion ligands[62,140]). These *in-situ* ligand exchanges rely upon mixing of a two-phase mixture leading to extract of the nanocrystals to the polar phase as surface ligands are replaced. In some cases, complete ligand exchange is not achievable,[62,141] possibly indicating more complicated ligand dynamics than generally assumed.

Here, a comprehensive examination of the effects of common post-synthesis cleaning and processing procedures on CZTS nanocrystal dispersion stability was conducted. First, the effects of alcohol washing (*i.e.*, addition of alcohol and forced sedimentation *via* centrifugation followed by redispersion in toluene) on ligand coverage and aggregation were studied by attenuated total reflection Fourier-transform infrared spectroscopy (ATR-FTIR) and dynamic light scattering (DLS), respectively. Successive washing cycles reduced the number of ligands attached to the CZTS nanocrystals causing a decrease in dispersion stability. The efficiency of adding surface ligands by addition of free oleic acid into the CZTS nanocrystal dispersions as well as the effects of ultrasonication were analyzed. These results were used to inform post-synthesis processing procedures and dispersion formulation.

3.2 Experimental

3.2.1 Materials

Metal diethyldithiocarbamate precursors used for nanocrystal synthesis were synthesized as described by Chernomordik *et al.*[52] Octadecene (technical grade, 90%), oleic acid (technical grade, 90%), oleylamine (technical grade, 70%), and toluene (HPLC grade, 99%) were purchased from Sigma Aldrich. Reagent alcohol (histological grade, 90% ethyl alcohol, 5% methyl alcohol, 5% butyl alcohol) was purchased from Fisher Scientific.

3.2.2 Nanocrystal Synthesis

After synthesis, the solution was washed as illustrated in Figure 3.1a. The reaction solution was poured into equal volumes into two centrifuge tubes. Reagent alcohol was added to each tube at a 1:1 volume ratio to the original reaction solution. This mixture was stirred and then centrifuged at 4000 RPM for 10 minutes, sedimenting the nanocrystals. After centrifugation, the supernatant was decanted leaving only the solid nanocrystals. The nanocrystals were then redispersed in 6 ml of neat toluene and subjected to ultrasonication to break up nanocrystal aggregates. To further clean the nanocrystals, the washing procedure (*i.e.*, addition of reagent alcohol, centrifugation, and redisperse in toluene) was repeated up to 4 times.

3.2.3 Ultrasonication

Ultrasonication was conducted with a Branson 2510 water bath sonicator. For sonication, CZTS nanocrystal dispersions were deposited into 20 ml glass scintillation vials. The vials were suspended above in the sonicator water bath by attaching them with laboratory clamps. The lower half of the vial was submerged into the water bath at a depth of approximately 1 cm. The sonicator was then set for the desired sonication time ranging from 10 to 120 minutes.

3.2.4 Characterization

X-ray diffraction (XRD) was conducted on the synthesized CZTS nanocrystals using a Cu Kα source with a Bruker D8 Discover equipped with a Hi-Star 2D area detector. Raman specroscopy was conducted with a Witec Alpha300R confocal Raman microscope using an Ar ion laser (514.5 nm wavelength), a UHTS300 spectrometer, and a DV401 CCD detector.

Attenuated total reflection Fourier transform infrared (ATR-FTIR) spectroscopy was conducted on a Nicolet Magna-IR Spectrometer 550, a mercury cadmium telluride detector (cutoff frequencey of 400 cm^{-1}), and a KBr beamsplitter. A schematic of the ATR-FTIR analysis procedure is shown in Figure 3.1b. First, 200 µl of a 8 mg/ml CZTS nanocrystal

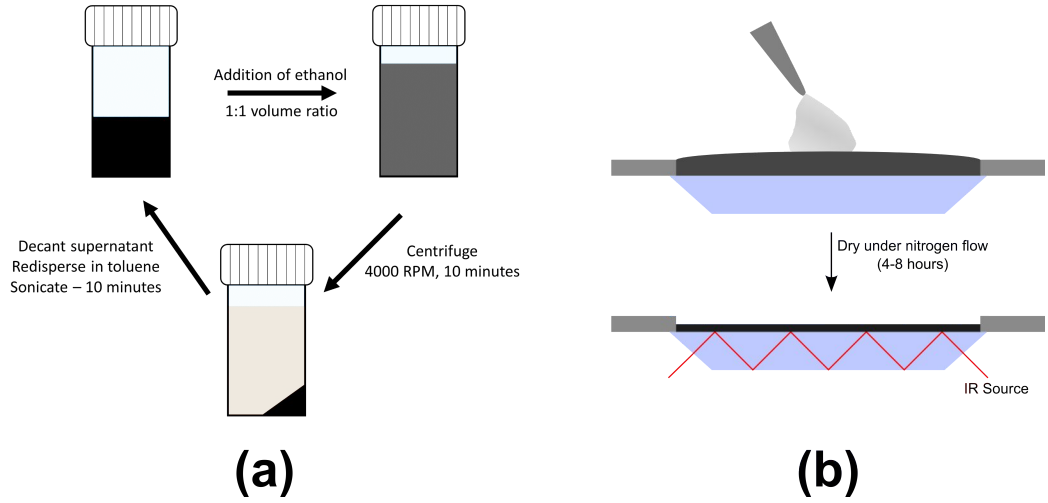

Figure 3.1 (a) Schematic of washing procedure used to purify CZTS nanocrystals after synthesis. Process was repeated up to 4 times to study effects on dispersion stability. (b) Illustration of ATR-FTIR spectroscopy of CZTS nanocrystals cast from dispersion. Dispersion was pipetted onto ATR crystal and then allowed to dry until no signal from toluene was observed in spectra, usually 4 - 8 hours depending on dispersion formulation. ATR-FTIR spectra were then obtained from the dry CZTS nanocrystals coating.

dispersion was deposited across the full width and length of the ATR crystal (area of 5 cm^2). The dispersion was then dried for 4-8 hours. The drying time was determined by acquiring temporal FTIR spectra until the absorption from liquid toluene was no longer detectable. The final coating thickness (~500 nm) is assumed to be greater than the penetration length within the CZTS nanocrystal coating of the source IR source. Sample scans were conducted over a frequency range of 400 to 4000 cm^{-1} with a resolution of 2 cm^{-1}. To reduce data noise, 100 spectra were collected over 60 seconds and integrated to improve the signal-to-noise ratio.

Dynamic light scattering (DLS) was conducted on a Brookhaven ZetaPALS Zeta Potential Analyzer and particle size was determined using ZetaPlus Particle Sizing Software (Version 4.16). For analysis, 8 mg/ml CZTS nanocrystal dispersions were diluted to 0.1 mg/ml to form translucent dispersions. To determine particle size, the viscosity (0.558 centipoise) and refractive index (1.489) of neat toluene were used as the relevant solvent

properties. The real and imaginary refractive indices of CZTS were set to 2.73 and 2.50, respectively.[142] DLS spectra were collected at 25 °C using a wavelength of 657.0 nm at a 90° incident angle. For each analysis, 5 independent runs of 45 seconds were completed. The individual hydrodynamic diameters determined from the independent runs were averaged to provide a single data point for each dispersion. A log-normal size distribution was assumed in all cases.

3.3 Results and Discussion

3.3.1 Effect of Alcohol Washing on Ligand Concentration

Figure 3.2a shows an ATR-FTIR spectra of 5 nm CZTS nanocrystal dispersions that had been washed by alcohol addition 1, 2, and 3 times after synthesis. The first significant peak at 3000 cm^{-1} corresponds to a C-H(sp^2) stretch while the peaks at 2956, 2924, and 2854 cm^{-1} correspond to characteristic stretches of C-H(sp^3).[143] The absorptions peaks are due to the by hydrocarbons present during CZTS nanocrystal synthesis: oleylamine, oleic acid, and octadecene. The structures of these compounds are shown in Figure 3.2b. Each contains 18 carbons and one carbon-carbon double bond. Oleic acid contains a carboxylic acid group on the 18^{th} carbon whereas oleylamine contains an amine group at the same location. After each washing cycle, the absorption intensity of C-H characteristic peak decreased by 95% after the third wash compared to the intensity after the first wash. The absorption intensity is related to the concentration of the absorbing compound in the sample volume.[143] Thus, the hydrocarbon concentration within the nanocrystal coating is decreasing with each washing cycle.

To understand the decrease in carbon concentration with washing, a discussion of the role hydrocarbon species play in the hot-injection reaction is necessary. Due to its high boiling point and the absence of any reactive groups, octadecene functions as a reaction medium. Oleic acid serves as a coordinating ligand likely forming metal-oleate complexes during injection, as observed in other nanocrystal reaction systems. Metal-oleate complexes have high diffusion coefficients and allow for rapid nanocrystal formation.[144] Olyelamine

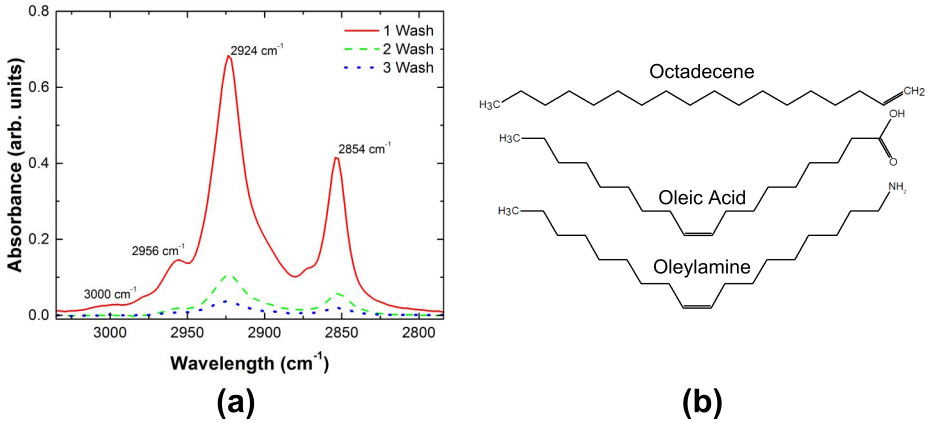

Figure 3.2 (a) ATR-FTIR spectra from CZTS nanocrystal dispersions after drying that had been washed 1, 2, and 3 times after synthesis. (b) Depictions of the Chemical structures of octadecene, oleic acid, and oleyelamine, the primary solvents and ligands used in CZTS nanocrystal synthesis.

plays numerous roles in hot-injection nanocrystal reactions acting as a solvent, ligand, and reducing agent.[145] In the thermalolysis reaction used here, it also acts as a decomposition initiator. In the presence of oleylamine, the diethyldithocarbamate complexes rapidly decompose at temperatures well below their individual decomposition temperatures.[52,59,146,147] After the reaction, oleylamine and oleic acid serve as surface-attached ligands that stabilize the nanocrystals when dispersed in non-polar liquids.[52]

Two mechanisms may be responsible for the reduction in carbon concentration in the nanocrystal coatings during washing. The first is that unattached, free hydrocarbon species are diluted and removed during the washing cycles. For this to be true, the washing cycles would be seemingly ineffective at removing free, unattached hydrocarbons which is unlikely due to the high miscibility of toluene with each hydrocarbon used in the reaction. The second more likely possibility is that each washing cycle removes a portion of the surface-attached ligands from the CZTS nanocrystal surfaces. Both oleylamine and oleic acid have been shown to act as ligands for the CZTS nanocrystals.[59] The surface-attached ligands likely establish an equilibrium with free, unattached species in the dispersing liquid. During the washing cycles, the free ligands present in the liquid are removed and neat toluene is reintroduced. Surface-attached ligands then desorb from the nanocrystal surfaces and a

new equilibrium, with a lower overall ligand concentration, is established. Repeating this process lowers the total surface ligand concentration with each washing cycle.

Dynamic light scattering was conducted on 5 nm CZTS nanocrystal dispersions washed for 1, 2, and 3 cycles to determine the effects on aggregation. Figure 3.3 plots the aggregate diameter calculated assuming a log-normal distribution from DLS as a function of washing cycles. The initial average aggregate diameter is 243 nm before washing. The aggregate diameter increases to 397 nm and 2.43 μm after the second and third washing cycles, respectively. It is important to note that the measured aggregate sizes may be inflated relative to their actual size in the dispersion because the dispersions were diluted with toluene to form translucent dispersions for DLS analysis. Since the dilution volume was held constant during sample preparation, the measured aggregate sizes can be used to infer differences in dispersion stability in the undiluted dispersions as well. The increase in aggregate size agrees well with the qualitatively observed effects of repeated alcohol washing cycles on dispersion stability.

From these results, it is apparent that the decrease in hydrocarbon concentration observed in Figure 3.1a is due to removal of carbon ligands from the surface of the CZTS nanocrystals, causing aggregation and decreasing dispersion stability. Removal of unreacted species and reaction by-products is required but is achieved at the expense of dispersion stability. Understanding the dynamics of ligand attachment to the CZTS nanocrystals in the dispersion is critical to producing a stable CZTS nanocrystal dispersion for development of CZTS solar cells.

3.3.2 Increasing Ligand Coverage and Dispersion Stability

Ligand attachment is assumed to behave as a reversible equilibrium process described by

$$\mathrm{N} + \mathrm{L} \rightleftharpoons \mathrm{NL} \tag{R1}$$

where N is an unoccupied attachment site on the surface of a CZTS nanocrystal, L is a free ligand (oleic acid or oleylamine) within the dispersing ligand, and NL is the ligand-

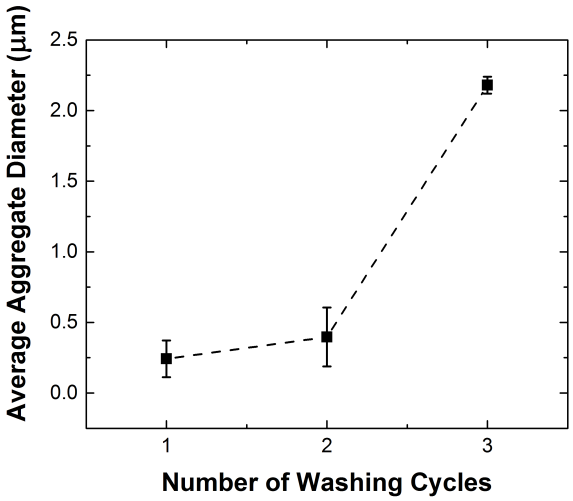

Figure 3.3 Plot of average aggregate diameter as measured by DLS as function of the number of dispersion washing cycles.

nanocrystal surface complex formed when ligands attach to the CZTS nanocrystal. The equilibrium concentrations of each species is described by

$$K_{eq} = \frac{[NL]_{eq}}{[N]_{eq}[L]_{eq}} \tag{R2}$$

where K_{eq} is the equilibrium constant and $[i]_{eq}$ with $i = $ NL, N, or L represents the concentration of species i in the dispersion at equilibrium.

Reaction 1 describes the removal of carbon from the nanocrystal coatings with repeated washings. After the supernatant is decanted following centrifugation and fresh toluene is added, [L] is initially 0 which forces the attachment to reverse, causing NL complexes into N + L to dissociate until the equilibrium is reestablished in accordance with Reaction 2. With this disassociation, a decrease in dispersion stability occurs as the steric stabilization forces on the nanocrystal surfaces are reduced. If the ligand dynamics do behave according to Reaction 1, introduction of free ligand to the dispersion should prompt reattachment of ligands and increase dispersion stability.

Figure 3.4a shows FTIR spectra of CZTS nanocrystals cast from dispersions subjected to two wash cycles and then dispersed in toluene with added free oleic acid at volume frac-

tions (vol frac) ranging from 0 to 10^{-2}. The peaks characteristic of C-H vibrations are present at wavelengths from 3000 to 2800 cm^{-1}. The intensity of these peaks increase with increasing oleic acid volume fraction indicating the added oleic acid is present in the nanocrystal coating after drying. In addition to the hydrocarbon peaks, a strong peak at ~1710 cm^{-1}, characteristic of C=O, is present and increases in intensity with oleic acid volume fraction.

Figure 3.4b shows a zoomed in plot of the C=O characteristic peak for each of the oleic acid volume fractions. With no added OA, there is no peak present at 1710 cm^{-1}. With the addition of a small amount of oleic acid to the dispersion (10^{-4} volume fraction), the intensity increases to 0.10. The intensity increases with an oleic acid volume fraction of 10^{-3} to 0.41 and to 0.56 at a volume fraction of 10^{-2}.

As expected, the concentration of both C-H (3000 - 2800 cm^{-1}) and C=0 (1710 cm^{-1}) increase at higher oleic acid volume fractions. However, the concentrations of the two species do not seem to increase linearly as would be expected if all oleic acid remained free in the dispersing liquid. Oleic acid attaches to the CZTS nanocrystal surface through formation of an oleate-metal complex as illustrated in Figure 3.5.[148,149] This results in the loss of the C=O vibration at 1710 cm^{-1} in any oleic acid molecules that attach to CZTS nanocrystals. However, C-H characteristic absorption peaks do not differ between free and attached oleic acid. By subtracting a pure oleic acid spectra from the nanocrystal spectra in Figure 3.4, the contribution to the C-H absorption peaks from free oleic acid can be removed, leaving only the absorption from hydrocarbons attached to the CZTS nanocrystals.[150] This allows analysis of the effects of oleic acid addition on ligand attachment without free oleic acid contributions.

Figure 3.6a shows the ATR-FTIR spectra of CZTS nanocrystals cast from toluene dispersions containing varying amounts of oleic acid. In these spectra, the contribution from free oleic acid has been removed from the hydrocarbon peaks through linear subtraction of a pure oleic acid spectra from the CZTS nanocrystal spectra. Before subtraction, the intensity trend of the C-H absorption peaks followed that of the oleic acid volume fraction (*i.e.*, lowest with no added free oleic acid and highest with 10^{-2} oleic acid vol frac). After subtraction, the intensity trend no longer strictly follows the oleic acid volume fraction. The intensity of the peak at 2924 cm^{-1} with the no oleic acid peak is 0.1 and increases to a maxi-

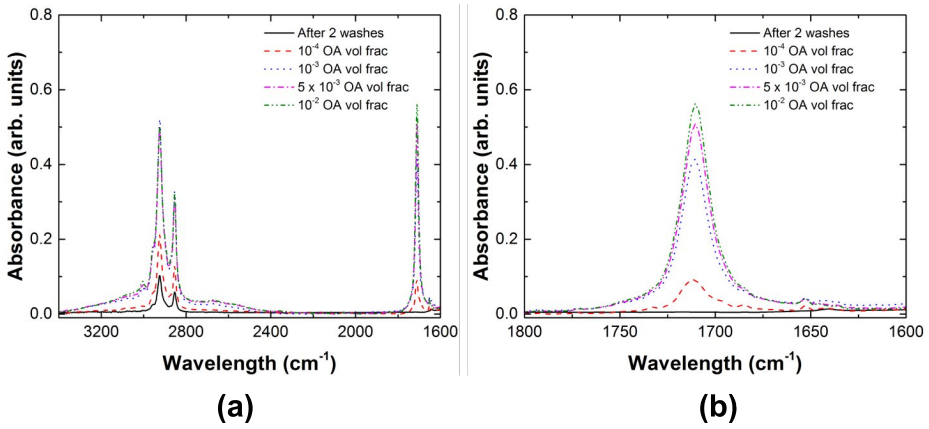

Figure 3.4 (a) Full and (b) zoomed ATR-FTIR spectra of CZTS nanocrystals cast from toluene dispersions containing 0, 10^{-4}, 10^{-3}, 5×10^{-3}, and 10^{-2} volume fraction free oleic acid.

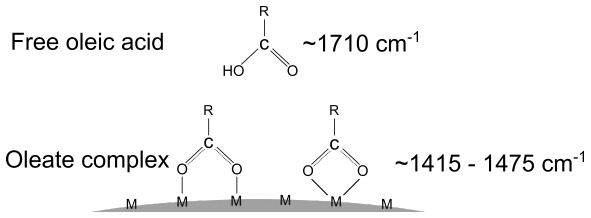

Figure 3.5 Illustration of oleic acid associating with the surface of a CZTS nanocrystal showing the loss of the C=O vibration at 1710 cm^{-1} after the oleate complex is formed.

mum of 0.25 with 10^{-3} oleic acid volume fraction. The intensity decreases to 0.15 and 0.13 at oleic acid volume fractions of 5×10^{-3} and 10^{-4}, respectively. The decrease in intensity indicates a decrease in hydrocarbon concentration which is surprising since carbon could only be added to the dispersions with the addition more oleic acid.

Figure 3.6b illustrates a possible mechanism for the carbon concentration trend observed at higher oleic acid volume fractions. With no added oleic acid, the CZTS nanocrystals contain a minimal amount of carbon ligands. Adding a small volume fraction of oleic acid (10^{-4}), increases the ligand coverage on the surface of the nanocrystals, indicated by the border thickness around the nanocrystals in Figure 3.6b. At high volume fractions, the nanocrystal surfaces are saturated with ligands and addition of more oleic acid increases the volume of free oleic acid. The higher volume of oleic acid in the "dry" coating induces

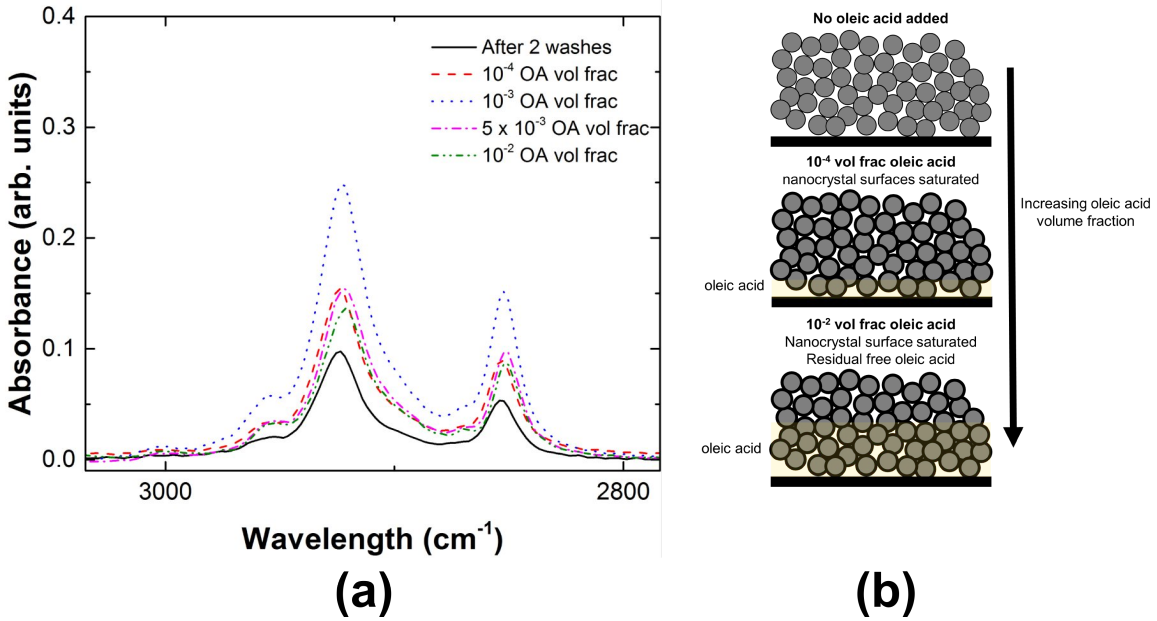

Figure 3.6 (a) ATR-FTIR spectra of CZTS nanocrystal coatings with no added oleic acid and with up to 10^{-2} vol frac of oleic acid. (b) Illustration of the effects of large oleic acid volume fractions on the FTIR sampling volume during analysis of CZTS nanocrystals.

a change in the volume sampled during ATR-FTIR. At the surface of the ATR crystal, the IR source encounters nanocrystals within an oleic acid medium rather than air medium. This would reduce the IR penetration length and subsequently the number of nanocrystal surface area sampled.

Figure 3.7a replots the spectra from Figure 3.6a, omitting the higher oleic acid volume fractions for clarity. Within this range of oleic acid volume fraction, theres a steady increase in surface-attached ligand concentration. The stabilization due to added oleic acid is further evidenced by a decrease in aggregation as determined by DLS analysis. Figure 3.7b plots the average aggregate diameter determined from log-normal number distributions calculated from DLS results of 5 nm CZTS nanocrystal dispersions with added oleic acid. The diameters are normalized by the initial dispersion aggregate diameter (D_0) before addition of oleic acid. At the lowest volume fraction (10^{-4}), the aggregate diameter sharply decreases to half of the original aggregate size. Further increases in oleic acid volume fraction pro-

duce no significant decrease in aggregate size. From this analysis, the CZTS nanocrystal dispersing liquid utilized following synthesis was modified to toluene with 10^{-4} volume fraction oleic acid to increase dispersion stability and provide consistent ligand coverage between synthesis batches.

3.3.3 Effect of Ultrasonication on Aggregate Diameter

Ultrasonication, usually conducted in water bath sonicators, is commonly used to improve dispersion stability presumably by breaking up aggregate.[60,62] Figure 3.8a shows the effect of sonication time on the relative aggregate diameter of 5 nm CZTS nanocrystal dispersions with no added oleic acid (represented by ●) and with 10^{-4} oleic acid volume fraction (represented by ■) determined by DLS analysis. Before sonication, the neat (no added oleic acid) dispersion had an average aggregate diameter of 684 nm which is used as the basis value for D_0 for both the neat and oleic acid dispersion relative aggregate diameters. With the addition of oleic acid, the aggregate diameter is reduced to 424 nm (0.62 relative diameter) indicating the strong dispersing effects of oleic acid even in the absence of sonication. Without added oleic acid, sonication has little effect on the aggregate diameter with the relative diameter reduced to 0.88 after two hours of sonication. In the presence of oleic acid, there is a sharp decrease in relative aggregate size to 0.28 after sonicating for 20 minutes. Further sonication did not reduce the measured aggregate size. From the DLS results, sonicating does help disperse the nanocrystals in the presence of oleic acid and achieves its maximum benefit after approximately 20 minutes. Sonication without excess free ligand does little to break up CZTS nanocrystal aggregates likely due to inadequately passivated surfaces (*i.e.*, low ligand coverage).

Figure 3.8b shows ATR-FTIR spectra of 5 nm CZTS nanocrystal coatings cast from dispersions containing no added oleic acid and containing 10^{-4} volume fraction oleic acid. All contributions from free oleic acid have been subtracted. In agreement with the DLS results, the addition of free oleic acid with no sonication increases ligand coverage evidenced by the increase the hydrocarbon absorption intensity (0.13 with no oleic acid and 0.29 with 10^{-4} oleic acid volume fraction using the characteristic peak centered at 2924 cm^{-1}). After

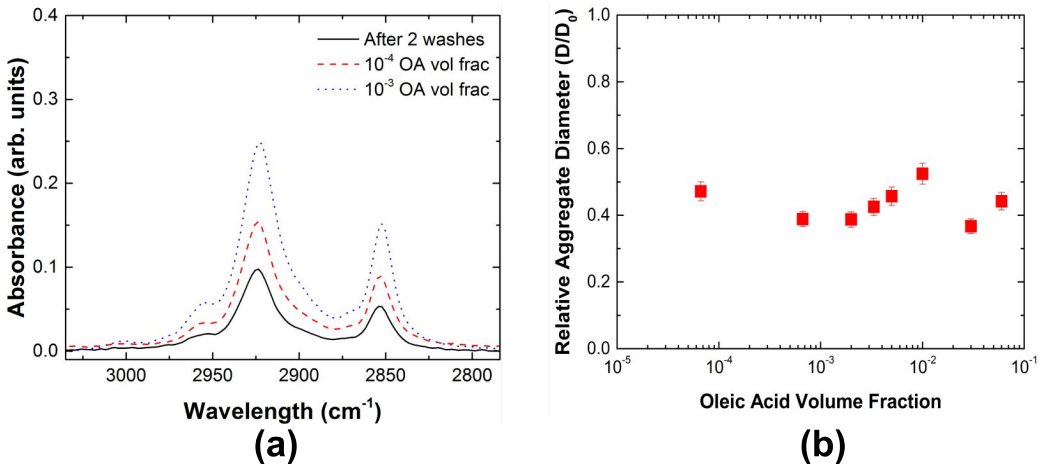

Figure 3.7 ATR-FTIR spectra of CZTS nanocrystal coatings with no added oleic acid, 10^{-4}, and 10^{-3} vol frac where no sampling volume effects due to excess oleic acid were observed. (b) Average relative aggregate diameter, as measured by DLS, in CZTS nanocrystal dispersions with added oleic acid volume fractions from 10^{-4} to 10^{-1}. Relative aggregate diameter is the measured aggregate diameter divided by the initial aggregate diameter measured before oleic acid addition.

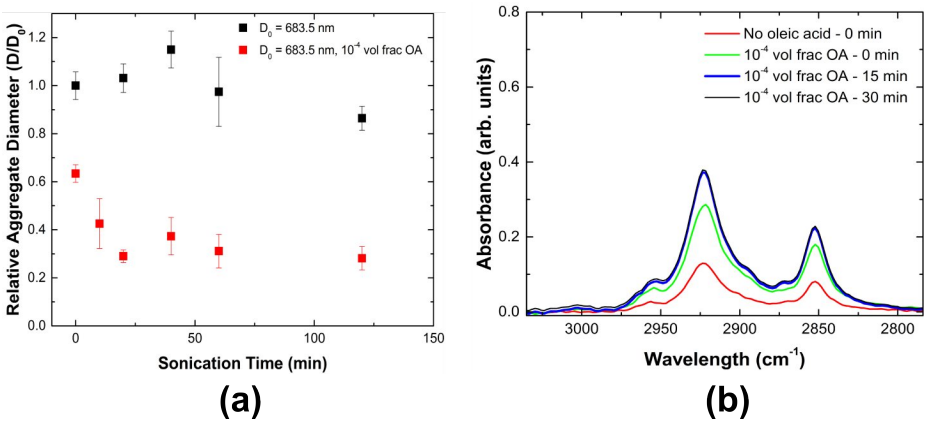

Figure 3.8 (a) Plot of the effect of sonication time on aggregate diameter in CZTS nanocrystal dispersions (●) with no added oleic acid and (■) with 10^{-4} volume fraction oleic acid. (b) ATR-FTIR spectra of CZTS nanocrystal coatings with no added oleic acid and with added oleic acid after 0, 15, and 30 minutes of sonication.

15 minutes of sonication, the 2924 cm^{-1} peak intensity increases to 0.38 and remains at that approximate value. Initially, the CZTS nanocrystal surfaces are ligand poor and readily adsorb free oleic acid without mechanical agitation, reducing aggregation. With agitation, aggregates are broken up and more nanocrystal surfaces are exposed to the excess free oleic acid in the dispersing liquid, leading to increased ligand attachment and coverage.

3.4 Conclusion

Reliable production of stable CZTS nanocrystal dispersions is critical to providing a successful platform to produce CZTS solar cells. The effects of post-synthesis processing on dispersion properties was studied. It was found that washing through addition of alcohol followed by forced sedimentation by centrifugation and redispersion in toluene affected the concentration of surface-attached stabilizing ligands. ATR-FTIR showed a reduction in intensity of the characteristic hydrocarbon peaks present in the 2875 to 2825 cm^{-1} wavelength range. Sepecifically, the intensity of the peak related to a C-H vibration at 2924 cm^{-1} was reduced by 95 % from the first to third washing cycle. Along with the reduction in intensity, each washing cycle decreased dispersion stability and caused an increase in aggregate size, as determined by DLS analysis. The decrease in hydrocarbon concentration and increase in aggregation was caused by the removal of surface ligands stabilizing the nanocrystal dispersions.

Through addition of free oleic acid at volume fractions ranging from 10^{-4} to 10^{-2} to the toluene CZTS nanocrystal dispersions, the hydrocarbon concentration of the nanocrystals could be adjusted back to pre-washing levels. In the oleic acid volume fraction range of 10^{-4} to 10^{-3}, ATR-FTIR analysis revealed an increase in surface-attached ligand coverage. Increases in oleic acid volume fraction beyond 10^{-3} saturates the CZTS nanocrystal surfaces with carbon ligands and results in a high volume of residual free oleic acid that alters the ATR-FTIR sampling environment, causing the spectra obtained under these conditions unsuitable for comparison to other samples. In addition to the increased ligand coverage, nanocrystal aggregate size was found to decrease with the addition of oleic acid to the disper-

sions. A volume fraction of 10^{-4} reduced the aggregate size by approximately 50%. Higher oleic acid volume fractions produced no further deceases in aggregate size. It was determined that an oleic acid volume fraction of 10^{-4} provided the best balance of dispersion stabilization and residual oleic acid after drying.

The effect of ultrasonication time on nanocrystal ligand coverage and aggregate size was also studied. Addition of oleic acid to the dispersion without mechanical agitation resulted in an increase in ligand coverage and decreased aggregate size as determined by ATR-FTIR and DLS, respectively. Sonication for up to 30 minutes produced small increases in ligand coverage and decreased aggregate size, but further sonication times resulted in no changes in either property. From these results, the effect of post-synthesis processing on dispersion quality has been established. These results allowed development of improved washing procedures and CZTS nanocrystal dispersion formulations.

Chapter 4

Formation of CZTS Nanocrystal Coatings *via* Aerosol Jet Printing and Compaction*

4.1 Introduction

There are several difficulties that complicate large-scale continuous production of films from nanocrystal dispersions. Cracking of nanocrystal coatings during drying and long drying times are two important issues that must be addressed.[84–86] Nanocrystal coatings crack to relieve capillary stresses during drying.[65] Moreover, stresses can build due to constrained shrinkage during annealing: films shrink when dispersion stabilizing ligands desorb or decompose during heating. Because of these effects, it is difficult to deposit micron-thick coatings from dispersions of nanocrystals with sizes < 10 nm in a single step and within the constraints of solar cell manufacturing requirements.

In this chapter, a general method to create dense micron-thick, crack-free coatings is demonstrated with CZTS nanocrystals. Additionally, the CZTS nanocrystal coatings can be annealed to form polycrystalline CZTS films with microstructure suitable for solar cells. The approach to forming polycrystalline films comprises three steps, aerosol jet printing

*Portions of this work have been published as B. A. Williams, A. Mahajan, M. A. Smeaton, C. S. Holgate, E. S. Aydil, and L. F. Francis, "Formation of Copper Zinc Tin Sulfide Thin Films from Colloidal Nanocrystal Dispersions *via* Aerosol-Jet Printing and Compaction," ACS Appl. Mater. Interfaces. **2015**, 7, 11526.

(AJP) from dispersions of CZTS in toluene, densification by compression, and annealing in sulfur vapor. AJP (or spray deposition) combined with the compaction step can be used with nanoparticles other than CZTS, particularly when a high throughput continuous process is required to form dense nanoparticle coatings. Combining these steps with post annealing can produce a wide range of inorganic polycrystalline films.

4.2 Experimental

4.2.1 Materials

Metal diethyldithiocarbamate precursors used for nanocrystal synthesis were synthesized as described by Chernomordik *et al.*[52] Octadecene (technical grade, 90%), oleic acid (technical grade, 90%), oleylamine (technical grade, 70%), and toluene (HPLC grade, 99%) were purchased from Sigma Aldrich. Reagent alcohol (histological grade, 90% ethyl alcohol, 5% methyl alcohol, 5% butyl alcohol) and acetone (HPLC grade, 99.5%) were purchased from Fisher Scientific. Isopropyl alcohol (histological grade, 99.5%) was purchased from Macron Fine Chemicals. Silicon (test grade), fused quartz polished plates, Kapton, and soda lime glass substrates were purchased from Silicon Quest International, GM Associates, American Durafilm, and Valley Design Corporation, respectively. Solid sulfur (99.999%) was purchased from Cerac, Inc.

4.2.2 Nanocrystal Dispersions

Copper zinc tin sulfide (Cu_2ZnSnS_4) nanocrystals were synthesized *via* the hot-injection method from metal diethyldithiocarbamate precursors in a similar manner as described as described in Section 3.2.2. Following synthesis, the nanocrystals were dispersed in a 5 ml solution of oleic acid (10^{-4} volume fraction) in toluene. Before use, the nanocrystal dispersion was diluted with toluene and oleic acid solution to produce a 1-5 weight percent (wt%) CZTS dispersion. The average diameters of the CZTS nanocrystals used in this study were between 4 and 5 nm as determined from the width of the (112) x-ray diffraction peak

using the Scherrer equation. This 1 nm range is due to variations between numerous batches used in the study.

4.2.3 Aerosol Jet Printing

Aerosol jet printing is a direct-write method for patterning functional materials on substrates for a variety of applications, such as printed electronics,[151–153] solar cell metalization,[154] and organic photovoltaics.[155] Figure 4.1 shows a schematic of the AJP process. An aerosol mist composed of ~1-5 μm dispersing liquid (toluene) droplets containing the nanocrystals is created by agitating the ink in an ultrasonic atomizer with adjustable wave amplitude. The vial containing the ink is immersed in a cooling water bath to maintain a constant temperature. The aerosol is transported from the ultrasonic atomization vial to the jet nozzle by a carrier gas, typically dry nitrogen. At the nozzle, the aerosol stream is focused by a second nitrogen gas flow (the sheath gas), forming a high-speed jet with a velocity between 20 to 70 m/s depending on the sheath and the carrier gas flow rates. The focusing ratio, F_R, relates these two flow rates and is defined as

$$F_R = \frac{Q_{SG}}{Q_{CG}} \tag{4.1}$$

where Q_{SG} and Q_{CG} are the sheath and the carrier gas flow rates, respectively.[156] Substrates are coated by placing them on an x-y translation stage below the nozzle in the path of the aerosol jet. By rastering the stage and partially overlapping consecutive lines, coatings can be formed from the individual ~200 μm wide lines. AJP is utilized here as a small-scale analog to a spray deposition system that would create large area coatings more effectively.

Substrates, including silicon (used as-purchased with native SiO_2 layer), quartz, Kapton, and molybdenum-coated soda lime glass (~500 nm molybdenum layer formed by sputter deposition) were cleaned with isopropyl alcohol and acetone under ultrasonic sonication and dried using flowing nitrogen before use. After cleaning, the substrates were coated with CZTS nanocrystals using a commercial aerosol jet printer with an ultrasonic atomizer (Aerosol Jet 200, Optomec Inc.). The ultrasonic atomizer produces droplets with diameters

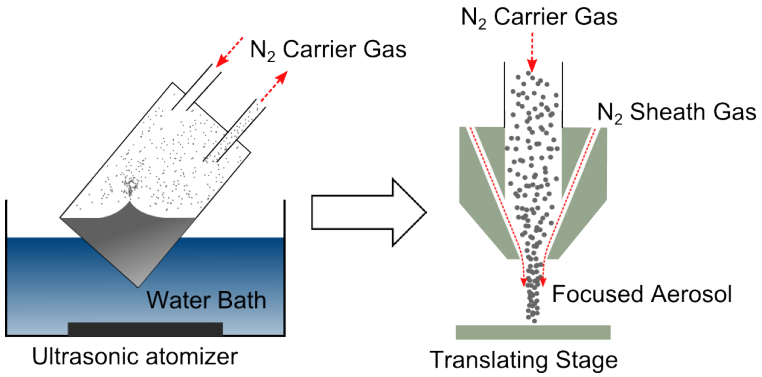

Figure 4.1 Schematic of the aerosol jet printing system used for coating substrates with CZTS nanocrystals.

in the 1-5 µm range as reported by Optomec Inc. The vial containing the CZTS ink was immersed in a bath maintained at 19 °C with recirculating water. Dry nitrogen gas (HP grade, 99.998%) was used as the carrier and sheath gases. Carrier and sheath gas flow rates were varied between 18-24 and 18-72 standard cubic centimeters per minute (sccm), respectively. The current supplied to the ultrasonic atomizer (U_A) was varied between 0.31 and 0.45 mA through the control system. Both 150 µm and 200 µm diameter nozzles were used. CZTS coatings are formed by rastering the stage to create 40 lines (each 11 mm long) with a center-to-center separation of 0.05 mm at a nozzle separation distance (end of nozzle to top of substrate) of 0.5 cm. Stage translation speeds (u_s) were varied from 1 to 8 mm/s.

Thermogravimetric analysis (Perkin-Elmer TG/DTA 6300) was carried out on the material exiting the aerosol jet printer at carrier gas flow rate of 20 sccm and sheath gas flow rate of 36 sccm. A CZTS nanocrystal coating was created inside an aluminum TGA sample pan by rastering a 150 µm nozzle over a 3 × 3 mm^2 area with ten consecutive passes. During analysis the temperature was ramped at 15 °C per minute from 25 to 140 °C and held at 140 °C for 15 minutes under a nitrogen gas purge before naturally cooling.

4.2.4 Compaction by Weighted Roller

Two compression methods, a weighted roller and a hydraulic press, were used for compacting the coatings. In compaction by the weighted roller, the nanocrystal coatings were compressed by passing them through a nip formed between a 1 cm diameter glass cylinder and a smooth glass plate mounted onto a raised metal platform. A schematic of the roller compression setup is shown in Figure 4.2 accompanied by a full description of the apparatus setup and operation. Compaction pressures were adjusted by altering the weight loaded onto a steel platform suspended from the axle through the glass cylinder underneath the compaction platform (see Figure 4.2b). Compaction pressure varied from 8 to 43 MPa by altering the weight suspended from the glass cylinder from 0.3 to 1.5 kg. The coated substrate was fixed on top of a polyethylene terephthalate (PET) film using a double-sided tape. A thin sheet of Kapton was placed over the coating to prevent the coating from sticking to the glass roller and to avoid subsequent delamination. The coated substrate was passed underneath the weighted roller by pulling the PET film at a steady rate (~0.2 cm/s): *i.e.*, the total compression time was approximately 5 seconds for the 1 cm long CZTS coating.

Figure 4.2a shows a photograph of the roller compression system utilized to compress CZTS nanocrystal coatings. Figure 4.2b is a schematic of the roller system illustrating its setup and operation. The roller system is mounted on a stainless steel platform with independently adjustable length legs to allow for a level compacting surface. Two stainless steel pillars are attached to the top surface of the platform and extend upwards 4 cm. Between the pillars, a smooth glass cylinder (1 cm diameter and 2 cm length), which acts as the compacting surface, is suspend by an axle that extends from its center through cutouts in the opposing steel pillars. The cutouts allow for the cylinder to remain horizontal stationary but free to move vertically during compression. A smooth glass plate is mounted onto the stainless steel platform directly below the glass cylinder. Coatings are compressed at the nip formed between the glass plate and cylinder. A second smaller stainless steel platform is suspended below the compaction surface by rigid steel wires wrapped over the extended ends of glass cylinder's axle. The suspended platform allows the addition of weights to increase the compaction force of the glass cylinder, as illustrated with the addition of a 0.5

kg mass to the platform in Figure 4.2b.

Figure 4.2c shows a detailed view of the setup used to compress CZTS nanocrystal coatings by the weighted roller on top of the glass plate. The coating was printed by AJP on a silicon substrate and then taped on to a PET film. Following, a Kapton cover layer was laid on top of the coating. The coating, sandwiched between the substrate and the Kapton layer, was compressed by pulling on the PET film and moving it underneath the roller. The Kapton cover layer and PET were removed after compression leaving the compressed coating on the substrate for further processing steps or characterization. The compaction pressure was calculated using the contact arc length between the coating and the roller as shown in Figure 4.2d, which does not show the Kapton layer and the PET for clarity. In Figure 4.2d, $\bar{S}$ is the contact length, R is the roller radius, H_0 is the initial coating thickness, and H_1 is the compressed coating thickness, and Θ is the contact angle. The contact angle was calculated from

$$\Theta = \sin^{-1}\left(\frac{\sqrt{R^2 - (R - [H_0 - H_1])^2}}{R}\right) \tag{4.2}$$

and the compression pressure, P_c, from

$$P_c = \frac{m}{R \times \Theta * W} \tag{4.3}$$

where m is the mass loading, and W is the width of the coating in the direction parallel to the cylinder axis.

4.2.5 Compaction by Hydraulic Press

A hydraulic press (Carver AutoPellet 3887) was used to compress the CZTS nanocrystals at pressures higher than 50 MPa. The load used during compression ranged from 450 to 5440 kg, corresponding to compaction pressures of 100 MPa to 1 GPa based on the coating area. Due to deformation of the cover layer during compression, contact between

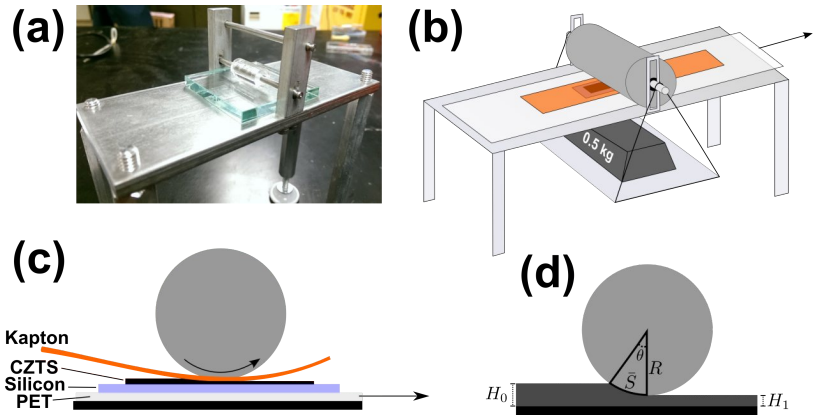

Figure 4.2 (a) Photograph of the roller compaction system used to compress CZTS nanocrystal coatings. (b) Schematic of roller compaction system setup and use. (c) Detailed schematic of materials and operation of roller compaction system. (d) Illustration of the variable definitions for compaction pressure calculation based on pre- and post-compaction thicknesses (H_0, H_1), roller radius (R), contact angle (Θ), and contact arc ($\bar{S}$).

the cover layer and coating substrate occurred outside of the coating increasing the effective contact area and decreasing the actual compaction pressure by up to a factor of 2. For this reason, the calculated pressures may not represent the true compaction pressures but are used as references to analyze the effect of increasing compaction load.

Coatings were compressed using two different methods. In the first method, the CZTS coatings were printed on to Kapton and then transferred onto a silicon substrate by placing the coated Kapton on top of the silicon with the CZTS coating facing the silicon. The nanocrystal coating, now sandwiched between the Kapton and the silicon substrate, was compressed for 60 seconds at the desired pressure. After compression, the Kapton layer was peeled from the nanocrystal coating, releasing and leaving the CZTS nanocrystals on top of the silicon substrate. This approach with the sacrificial Kapton layer was ineffective when molybdenum-coated soda lime glass (Mo-coated SLG) substrates were used instead of silicon: the nanocrystals peeled with the Kapton layer and CZTS coating delaminated. To eliminate delamination from Mo-coated SLG substrates a second hydraulic compression method was developed. In the second method, CZTS coating was printed on Mo-coated SLG instead of Kapton and then heated on a hot plate for 10 minutes at temperatures ranging

from 100 to 140 °C. This mild heat treatment was found to increase adhesion to the substrate if the annealing temperature was > 120 °C. The heat-treated coatings were then compressed with a Kapton cover layer on top of the CZTS nanocrystals with no coating delamination, resulting in intact, compressed CZTS coatings even on Mo-coated SLG.

Schematic illustrations of the two methods used for hydraulic press compression of the CZTS coatings are shown in Figure 4.3. In one method shown in Figure 4.3a, the coating was printed on a sacrificial Kapton layer, which was then placed under the hydraulic press. Before compression, a piece of silicon wafer larger than the Kapton piece with the coating was placed on the coating with the polished side facing the nanocrystals. During compression, the CZTS nanocrystals stuck to this silicon wafer and the coating was transferred from the Kapton onto the silicon. In the second method shown in Figure 4.3b, the nanocrystal coating was printed onto molybdenum-coated soda lime glass (Mo-SLG) and then heated on a hot plate for 10 minutes at 140 °C. This improved the adhesion of the coating to the substrate. Following, the coating on Mo-SLG was placed under the hydraulic press with a Kapton layer placed on top of it and compressed at the desired pressure. After compression, the coating remained adhered to the Mo-SLG substrate and did not delaminate.

The pressure produced during hydraulic press compaction, P_c, with mass loading, M,was calculated from

$$P_c = \frac{M}{A} \tag{4.4}$$

where A is the coating area, as shown in Figure 4.3c. This area is likely smaller than the actual contact area due to deformation of the Kapton cover layer and the coating substrate during compression. The deformation of the cover layer causes contact with the substrate outside of the coating area. This is evidenced by the impression of the coating substrate on the Kapton cover layer after compression by hydraulic press. Thus, the actual compaction pressure may be lower by a factor of 2 based on the non-coated substrate area than the calculated value.

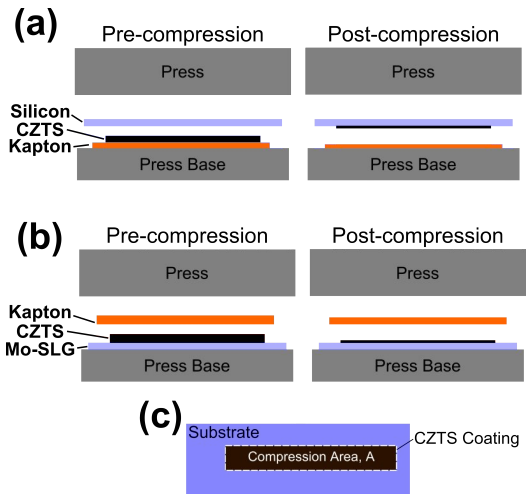

Figure 4.3 Schematic illustrations of the two methods used to compress the nanocrystal coatings in the hydraulic press: (a) the method where the nanocrystal coating is compressed and transferred from a sacrificial Kapton layer to the substrate and (b) the method where the nanocrystal coating is fixed onto the substrate using mild annealing at 140 °C. (c) A schematic illustration identifying the compression area, A, used to calculate the compaction pressure.

4.3 Results and Discussion

4.3.1 Aerosol Jet Printing

Figure 4.4 shows CZTS nanocrystal lines created by AJP using carrier gas flow rates of 18 and 24 sccm with focusing ratios of 1, 2, and 4. A single line for each condition is shown to illustrate the effects of these parameters on coating density, morphology and width. (To make continuous coatings partially overlapping lines are printed.) All lines in Figure 4.4 were printed from a 2 wt% CZTS dispersion in toluene with an atomizer current of 0.38 mA, while the stage was moved under a 150 µm diameter nozzle in a single pass at 4 mm/s. Using 18 sccm of carrier gas flow at a focusing ratio of 1 creates a ~288 µm wide line. Higher magnification SEM images show that this line comprises nanocrystal agglomerates with sizes ranging from 0.2 µm to 1 µm (Figure 4.4b). Increasing the focusing ratio to 2 and 4 decreases the line width to 244 µm and 145 µm, respectively, without substantial change in the microstructure of the coating: the lines still comprise 0.2-1 µm

nanocrystal agglomerates. When the carrier gas flow is increased to 24 sccm, nanocrystal agglomerates no longer appear in the center of the printed line but are limited to the line's outer edges. A cracked nanocrystal coating is formed at the center where the aerosol jet impinges on the substrate. Increasing the focusing ratio from 1 to 4 at a carrier gas flow rate of 24 sccm produces no significant changes in the coating line width, hinting that the jet diameter and fluid dynamics are irrelevant in determining the printed line width under these conditions. This observation suggests that the line width is dictated by liquid spreading after deposition.[156] Indeed, all coatings deposited at high carrier gas flow rates are cracked, consistent with the printed line having high liquid content at the time of deposition.

The systematic study of the aerosol jet printing parameters shown in Figure 4.4 revealed three types of coating morphologies: (1) discontinuous low-coverage coatings consisting of sparse nanocrystal agglomerates (*e.g.*, Figures 4.4a and 4.4b); (2) continuous high-coverage coatings, also consisting of nanocrystal agglomerates (*e.g.*, Figures 4.4i and 4.4j) and (3) cracked coatings (*e.g.*, Figures 4.4c and 4.4d, 4.4g and 4.4h, or 4.4k and 4.4l).

Figure 4.5 shows a schematic of the proposed mechanisms that result in these three morphologies. A key parameter that determines the coating morphology is the aerosol transport time,

$$\tau_T = \frac{A_x L}{Q_{CG}} \tag{4.5}$$

where A_x and L are the cross-sectional area and length of the tubing that carries the aerosol from the atomization vessel to the nozzle, respectively.

The volume fraction of the solvent in the aerosol droplet when it lands on the substrate is determined by the evaporation rate and the time it takes for the aerosol droplets to travel from the atomization vessel to the nozzle, the aerosol transport time (τ_T). As the aerosol is generated in the atomization vessel, CZTS nanocrystals become entrained in the aerosol droplets at a concentration assumed to be equal to that of the bulk dispersion. At low carrier gas flow rates (Q_{CG}=18 sccm and τ_T= 5.2 s, Figure 4.5a), the aerosol transport time is long and a significant fraction of the solvent in the mist droplets evaporates before the

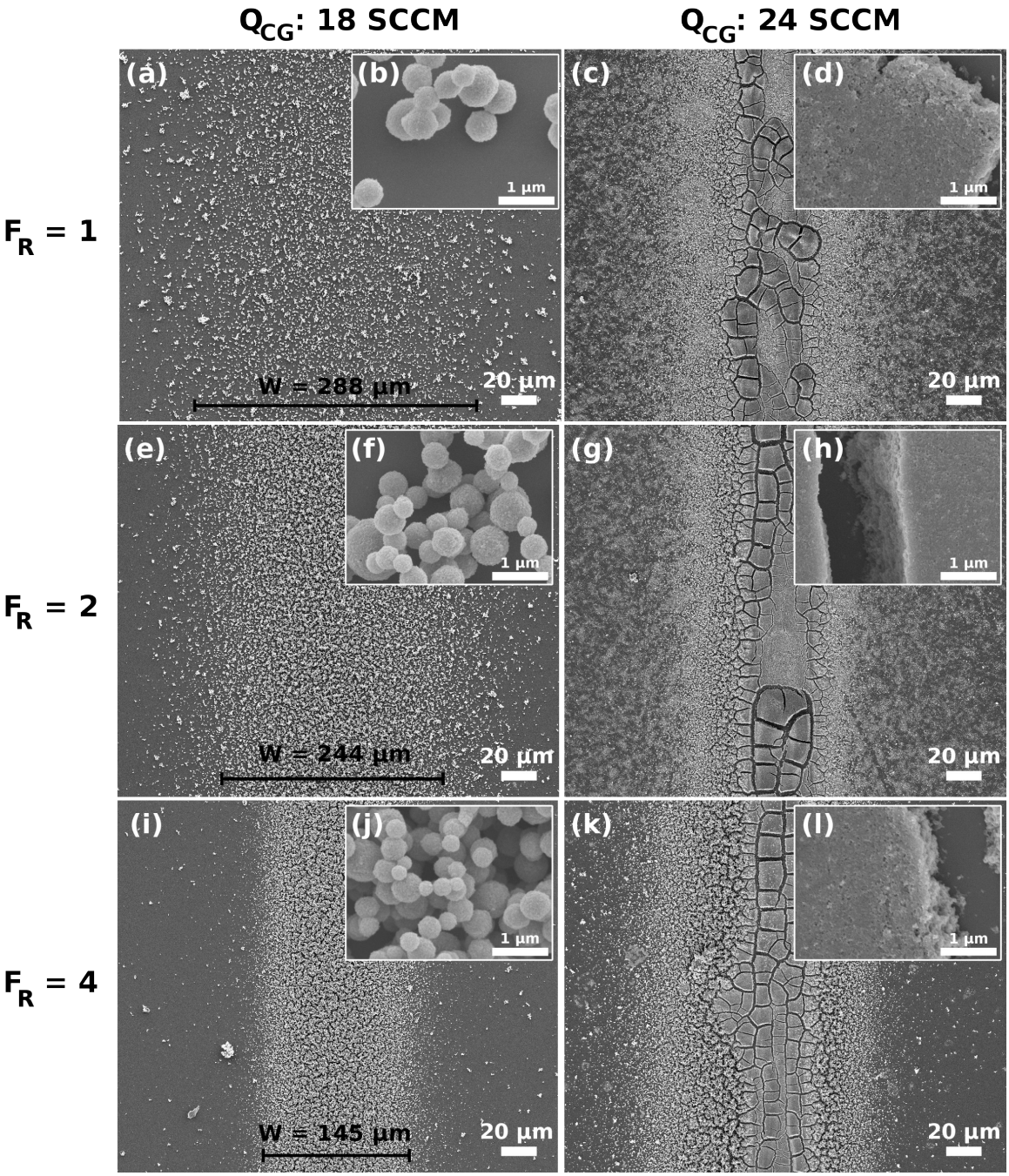

Figure 4.4 SEM images of isolated lines printed from 2 wt% dispersions of 5 nm CZTS nanocrystals. Coatings were printed on silicon substrates using carrier gas flow rates (Q_{CG}) of 18 sccm (a-b, e-f, i-j) and 24 sccm (c-d, g-h, k-l) with focusing ratios (F_R) of 1 (a-d), 2 (e-h), and 4 (i-l). Coatings were printed using a 150 µm nozzle at a stage speed u_s = 4 mm/s and atomization current U_A = 0.38 mA.

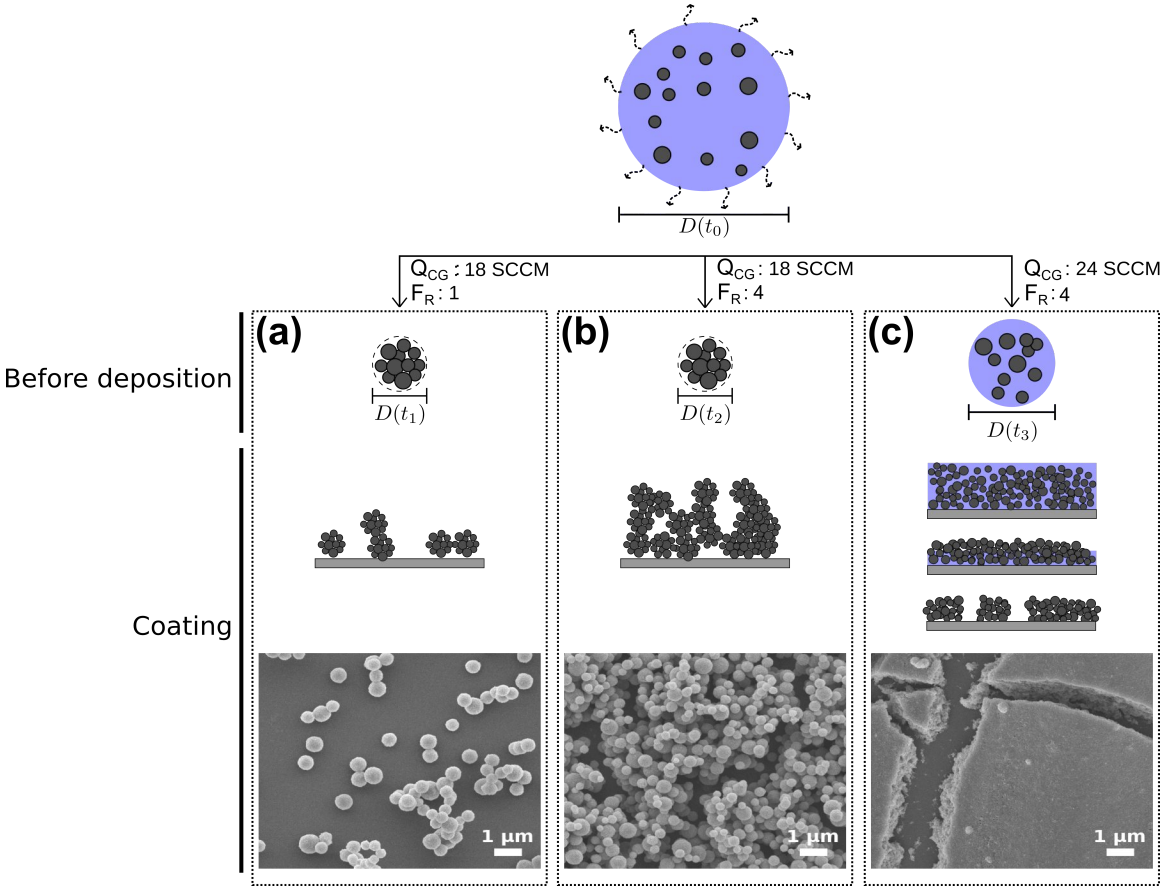

Figure 4.5 Illustrations of the aerosol drying process and the mechanisms that lead to various coating morphologies at various carrier gas flow rates, Q_{CG}, and focusing ratios. Upon atomization at $t = t_0$, a typical aerosolized nanocrystal dispersion droplet with an initial diameter $D(t_0)$ is transported by the carrier gas to the substrate. Transport times are inversely related to Q_{CG} so that $t_1 = t_2 > t_3$ in panels a through c. When Q_{CG} is 18 sccm (panels a and b), agglomerates form because the transport time is much longer that the time for solvent to evaporate. When Q_{CG} is 18 sccm and focusing ratio is 1, a sparse coating of agglomerates are deposited on the substrate. Increasing the focusing ratio to 4 produces a coating with higher coverage by these agglomerates. When the Q_{CG} is 24 sccm (panel c), agglomerates do not form because the transport time is too short for solvent to evaporate. Consequently, the nanocrystal dispersion droplet with diameter $D(t_3)$ arrives at the substrate surface with significant amount of solvent. The liquid droplets with the nanocrystals coalesce after impinging the substrate, forming a wet dispersion coating, which then cracks upon drying.

droplets reach the substrate. As the solvent evaporates and the nanocrystal concentration rises, the nanocrystals agglomerate within the droplet (Figures 4.5a and 4.5b). The periphery of the agglomerates comprising 5 nm CZTS nanocrystals appears smooth and densely packed when examined with SEM (resolution ≥ 8 nm). Moreover, the agglomerates appear spherical, suggesting that nearly all or a significant fraction of the solvent has evaporated such that the aerosol of dispersion droplets has been transformed into an aerosol of spherical agglomerates with very low liquid content.[157] Thus, the agglomerates are nearly dry when they reach the substrate (Figures 4.5a and 4.5b). In this study, agglomerates formed when the carrier gas flow rate was ≤ 20 sccm corresponding to $\tau_T \geq 4.6$ seconds. Werner *et al.* have also reported similar coating morphologies during aerosol jet printing of silver nanoparticles. Werner *et al.* used a tube heater to heat the aerosol as it traveled towards the substrate.[152] In Werner's work, solvent evaporation upon heating also formed an aerosol of agglomerates with very low liquid content. In our work, the morphology consisting of the agglomerates was observed even without heating.

At the lowest focusing ratio (F_R = 1) and with low carrier gas flow rates (Q_{CG} = 18 sccm), the nanocrystal agglomerates sparsely coat the substrate and form a wide line as shown in Figure 4.4a and 4.5a. Increasing the focusing ratio to 4 (Figures 4.4i and 4.5b) while maintaining the carrier gas flow rate at 18 sccm results in a narrower line because focusing the jet while keeping the material flow rate constant increases the agglomerate flux to the substrate as illustrated in Figure 4.4a, 4.4e and 4.4i. As a consequence, coverage of the substrate with nanocrystal agglomerates also increases. Thus, increasing the focusing ratio results in a continuous, albeit porous, line of nanocrystal agglomerates.

Increasing the carrier gas flow rate to 24 sccm while keeping the focusing ratio at 3 results in nanocrystal coatings with significant cracking (Figure 4.5c). At 24 sccm, the transport time, τ_T = 3.9 s, is evidently shorter than the time it takes the solvent to evaporate. Thus, the dispersion droplets are solvent laden as they impinge on the substrate and coalesce to form a wet coating. The coating does not seem to densify fully based on the porous morphology at the cracked edges indicating a low solvent volume fraction upon aerosol impingement at the substrate. Nevertheless, this coating develops stresses while drying and eventually cracks to relax these stresses.

The balance between the evaporation time to form agglomerates and the transit time is additionally influenced by the dispersion properties, especially the properties of the dispersing liquid. The addition of co-solvents, a common practice in aerosol jet printing,[156] or the use of a different dispersing liquid may reduce or accelerate the evaporation rate depending on the volatility of the dispersing liquid(s) relative to toluene. The change in the evaporation rate would be expected to shift the ranges of the absolute carrier gas flow rates where each distinct morphology is observed but not to affect the morphology trends with increasing carrier gas flow rate. Knowledge of the evaporation time to form CZTS nanocrystal agglomerates from the aerosol droplets would provide a predictive parameter for coating morphology, which could be adjusted for different dispersing liquids. However, calculating the evaporation time is complicated and requires modeling of the changes in the toluene partial pressure during AJP as well as the nontrivial effects of agglomerate formation on the evaporation rate. While such modeling is outside the scope of the present study, further research exploring the effects of these factors may lead to a coating process map to predict morphology based upon the ratio of the evaporation and transit times.

Of the three distinct morphologies shown in Figure 4.5, the continuous coating of agglomerates (Figure 4.5b) appears most suitable as a precursor for forming thin polycrystalline films for solar cells. The morphology with sparse coverage of agglomerates (Figure 4.5a) is clearly undesirable and so is the cracked coating in Figure 4.5c. However, the morphology in Figure 4.5b, while free of cracks, is very porous. Annealing this film may result in a film with many voids. To reduce the porosity, the films were compressed using two approaches, compression using a weighted roller and compression using a hydraulic press. A similar approach was used by Halme *et al.* to produce dense TiO_2 nanoparticle coatings from agglomerates formed during spray deposition on to a heated substrate.[158] For the compression studies, the coatings were prepared by aerosol jet printing using 5 nm CZTS nanocrystal dispersions in toluene and rastering the aerosol beam to cover a 10 mm $\times$ 4 mm area.

4.3.2 Compaction by Weighted Roller

Figure 4.6 shows a CZTS nanocrystal coating before (Figure 4.6a) and after (Figure 4.6b and 4.6c) compaction by a weighted roller at 25 MPa (1.5 kg mass loading). There is a clear decrease in the porosity and surface roughness of the coating after compaction. The extent of compaction, α, was determined from the average coating thickness before and after compaction using

$$\alpha = \frac{H_I}{H_F} \tag{4.6}$$

where H_I and H_F are the initial (pre-compaction) and final (post-compaction) coating thicknesses, respectively. Figure 4.6d shows that, within the range studied, α is independent of compaction pressure. This indicates that the nanocrystal coating compacts into a dense agglomerate network readily and this dense agglomerate network resists further consolidation and deformation. Additionally, there is no indication of agglomerate deformation at pressures accessible with the roller system (< 45 MPa). Further decreases in porosity appears to require agglomerate deformation, which may be observed at the higher compaction pressures afforded by a hydraulic press.

4.3.3 Compaction by Hydraulic Press

Figure 4.7 shows an as-printed nanocrystal coating (Figures 4.7a and 4.7d) and coatings compacted at 200 MPa (Figures 4.7b and 4.7e) and 800 MPa (Figures 4.7c and 4.7f) using a hydraulic press. The compressed coatings were printed on Kapton and transferred onto silicon substrates. The nanocrystal coating compacted at 200 MPa is clearly compressed and the agglomerates have been flattened and deformed. The boundaries between the compressed agglomerates are still visible because the particles have not been compressed enough to form an entirely continuous coating. Increasing the pressure to 800 MPa deforms the agglomerates further and the coating densifies significantly. The boundaries between the agglomerates are no longer visible in much of the coating. Occasional but infrequent

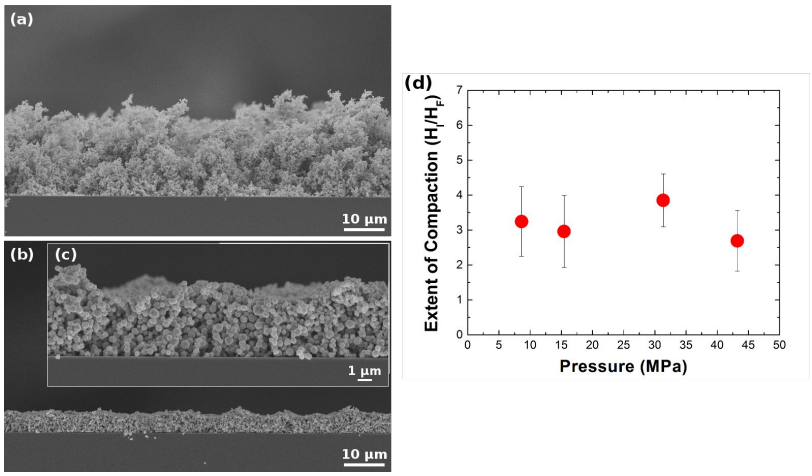

Figure 4.6 An aerosol jet printed CZTS coating from a 2 weight percent dispersion (a) before and (b,c) after compaction by a weighted roller at 44 MPa. Coatings were printed onto silicon substrates using a 150 µm nozzle, carrier gas flow rate Q_{CG} = 20 sccm, focusing ratio F_R = 3, stage speed u_s = 8 mm/s, and atomization current U_A = 0.38 mA. (d) Extent of compaction (initial coating thickness divided by final thickness) as a function of the compaction pressure.

voids (*e.g.*, on the left edge of Figure 4.7c) are visible. These voids were also reported by Halme *et al.* in compaction of TiO_2 agglomerates who thought that these voids formed in regions where there is not enough material to fill the voids between the agglomerates as they deform. The voids observed in this study are much smaller than the ~1-3 µm voids observed by Halme *et al.*[158]

The effect of mild annealing prior to compaction was investigated to improve adhesion to the coating substrate, particularly to molybdenum-coated substrates commonly used for CZTS solar cells. Figure 4.8a-d show optical images of CZTS nanocrystal coatings on Mo-coated SLG substrates before (Figure 4.8a) and after compression by hydraulic press at 800 MPa following mild annealing at 100 °C (Figures 4.8b and 4.8c) and at 120 °C (Figure 4.8d). The as-printed coating completely covers the substrate and has a brown color. After mild annealing and compaction, the coatings appear darker. Mild annealing at 100 °C for 10 minutes does not prevent delamination (Figures 4.8b and 4.8c). The coating remains at the boundaries of the coating area, but CZTS nanocrystals at the center of the substrate peel and stick to the Kapton cover slip as indicted with labels for the CZTS coating (C) and molybde-

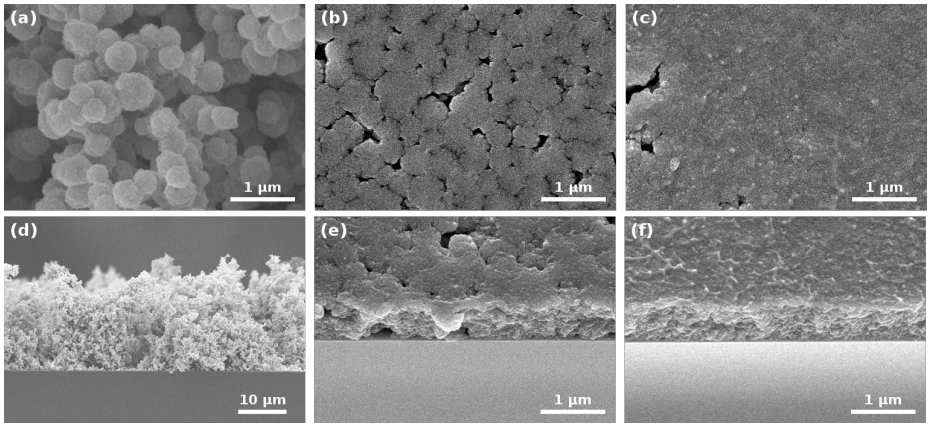

Figure 4.7 SEM images of aerosol jet printed coatings from a 2 wt% 5 nm CZTS nanocrystal dispersion (a and d) before and after compaction using a hydraulic press at (b and e) 200 MPa pressure, and (c and f) at 800 MPa. Coatings were printed on Kapton substrates using a 200 µm nozzle, carrier gas flow rate Q_{CG} = 20 sccm, focusing ratio F_R = 2.5, stage speed u_s = 4 mm/s, and atomization current U_A = 0.41 mA. At low compression pressures, 200 MPa, agglomerates deform, but the coating remains porous. Increasing loading to 800 MPa (c,f) deforms the agglomerates even more and forms a dense nanocrystal coating. While there are still voids in the coating, these voids are limited in size and density.

num (Mo) in Figure 4.8b,c. Increasing the annealing temperature above 120°C (Figure 4.8d) eliminates delamination, producing dense coatings on Mo-coated SLG substrates. Figure 4.8e shows a SEM image of a CZTS nanocrystal coating on Mo-coated quartz substrate after annealing at 140 °C followed by compression at 800 MPa. Interestingly, CZTS coatings compressed without annealing (Figure 4.7c and 4.7f) appear to have higher coating density and fewer voids than coatings compressed after mild annealing at 120-140 °C even when the compression pressures are the same. In addition to increasing coating adhesion, mild annealing increases the agglomerates' yield strength and resistance to deformation.

To understand the reason behind this observation, the CZTS nanocrystal agglomerates were studied using thermogravimetric analysis (TGA). Figure 4.8f displays the weight of the CZTS agglomerates and their temperature versus heating time. In this experiment, the agglomerates were heated to 140 °C at 15 °C/minute and held at 140 °C for 15 minutes. During the analysis time, the CZTS agglomerates show a steady, linear weight loss for approximately 10 minutes. The total weight loss is 0.2 mg and corresponds to approximately

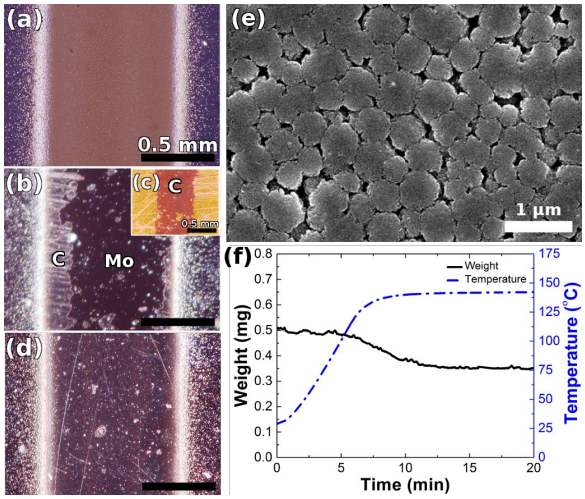

Figure 4.8 Optical images of CZTS nanocrystal coatings on Mo-coated SLG substrates formed *via* AJP (a) before and (b) after compression by a hydraulic press at 800 MPa following mild annealing (b and c) at 100 °C and (d) at 120 °C for 10 minutes. Panel c shows that heating at or below 100 °C did not prevent coating delamination and sticking to the Kapton cover layer: the coating, region labeled as "C" at left edge of panel b, remains at the edges of the Mo-coated SLG substrate but is peeled off the substrate at center of the line which is attached to the Kapton (region labeled as "C" in center of panel c). Mild annealing treatments at or above 120 °C prevented delamination. Panel (e) shows an SEM image of a coating compressed at 800 MPa after annealing at 140 °C for 10 minutes. (f) TGA data from CZTS agglomerates heated to and held at 140 °C for 40 minutes. Significant weight loss occurs at approximately 5 minutes into analysis corresponding to a temperature of 110 °C.

30% of the original weight. The onset of the weight loss corresponds to the normal boiling point of toluene (110 °C) and the reduction in weight is attributed to the evaporation of residual toluene trapped in the space between the CZTS nanocrystals within the agglomerates, likely still solvating and physically bound to the ligands surrounding the nanocrystals. This trapped toluene solvating the ligands is believed to have a lubricating effect during the compaction of the CZTS agglomerates. Presence of this toluene between the nanocrystals and the substrate weakens adhesion. Desorbing the residual toluene allows the coating to adhere better to the substrate. The agglomerates without the residual toluene (*e.g.*, coatings after mild annealing) do not deform as much as the agglomerates with residual toluene but they still deform enough to increase the coating density.

4.3.4 Thermal Annealing of the Aerosol Jet Printed CZTS Nanocrystal Coatings

Nanocrystal coatings prepared using the different approaches discussed above were annealed in sulfur vapor to transform them into polycrystalline thin films. Each coating has a distinct pre-anneal coating density that affects the final film morphology. The effect of coating density on the annealed film morphology is shown in Figure 4.9. Specifically, Figures 4.9a-d show the SEM images of a CZTS film (Figures 4.9b,d) made by annealing an as-printed nanocrystal coating without any compaction (Figures 4.9a,c). Figures 4.9e,h show the SEM images of a CZTS film (Figures 4.9f,h) made by annealing a nanocrystal coating compacted at 25 MPa using the weighted roller (Figures 4.9e,g). Figures 4.9i-l show the SEM images of a CZTS film (Figures 4.9j,l) by annealing a nanocrystal coating compacted at 800 MPa using the hydraulic press (Figures 4.9i,k). Raman spectroscopy and XRD were also conducted on the annealed films and are shown in Figure 4.10. The kesterite CZTS structure exhibits a major Raman peak at 336-338 cm^{-1}. We attribute the variations in major peak location to laser heating during data collection as reported by Valakh *et al.*[159] and Caballero *et al.*[160] Peaks at Raman shifts of 378 and 404 cm^{-1} in the annealed as-printed sample are attributed to MoS_2. Because the structure is porous, sulfur reaches the Mo readily and sulfidizes it rapidly. These coatings were printed by AJP (Q_{CG} = 20 sccm, F_R = 1.8, u_s = 1 mm/s, U_A = 0.49 mA, 150 μm diameter nozzle) from a 5 nm CZTS nanocrystal dispersion (5 wt% in toluene) on Mo-coated SLG substrates. Under these printing conditions, nanocrystal agglomerates form during aerosol transport and coat the substrate with complete coverage as shown in Figure 4.5b. All coatings were pre-annealed at 140 °C for 10 minutes. Two of the coatings were then compacted by weighted roller and hydraulic press. All three coatings were annealed for one hour at 600 °C in 50 Torr of sulfur.[60]

Prior to annealing, the as-printed coating comprises sub-micron agglomerates that form a disordered porous coating. When this coating is annealed, 0.3-1 μm CZTS crystals form (*e.g.,* Figure 4.9d) but the resulting film is discontinuous with some nanocrystal agglomerates, unaltered by annealing, interspersed in between the larger 0.3-1 μm grains. The coverage of large grains on the substrate is low with significant empty spaces between them

(Figure 4.9b). In addition to these empty spaces there are large voids between the large grains even in locations where the grain density is high.

Annealing the coating that was compacted using a weighted roller at 25 MPa produces a denser film with fewer voids (Figure 4.9h) though careful inspection of SEMs from different locations still show occasional voids as large as 100 nm. Grains near the film surface are noticeably larger (> 500 nm) than the grains closer to the substrate (< 300 nm; Figures 4.9f,h). The large grains have an aerial density of 42 grains per 100 μm^2 This microstructure is reminiscent of the bimodal size distribution and abnormal grain growth that has been observed recently during annealing of dropcast nanocrystal coatings.[60]

The coating compressed by hydraulic press at 800 MPa (Figure 4.9i) shows the highest initial coating density of the three coatings. Occasionally holes on the surface (0.1-1 μm) of the pre-annealed coating can be seen. It is not clear if these voids are confined to the surface of the film or extend to the substrate, though the cross sectional SEMs look dense. After annealing, the hydraulic pressed coatings form the densest polycrystalline films. The annealed film is 0.4 to 1 μm thick and consists of 1 to 5 μm CZTS grains (Figures 4.9j,l). The large grains span the entire thickness of the film, a microstructure well-suited for solar cells similar to densely packed large-grained films that has led to high efficiency devices.[29,30]

CZTS and CZTSSe films with large grains (> 1 μm) have been shown to provide the highest solar cell efficiencies independent of the synthesis approach.[28–30,50] It has been difficult to achieve large-grained CZTS films by annealing nanocrystal coatings in sulfur vapor.[116,161] Nevertheless, Kim *et al.* was able to produce polycrystalline CZTS films by annealing trioctylphosphine oxide capped CZTS nanocrystals.[53] Chen *et al.* achieved similar films by annealing oxide nanoparticles.[162] These films by Kim *et al.* and Chen *et al.* resulted in 3.6% and 1.47% efficient solar cells, respectively. These efficiencies are lower than the highest efficiencies achieved (9.0%) in solar cells made by annealing CZTS nanocrystal coatings in selenium to form polycrystalline CZTSSe films.[30] This efficiency discrepancy is likely in part due to the large open current voltage deficits in CZTS devices as compared to CZTSSe devices and reflect the differences in defect concentrations in these two different types of films.[126] Suboptimal film morphologies may also be responsible for low efficiencies in CZTS solar cells made by annealing nanocrystal coatings, especially

since much higher (8.4%) efficiencies have been demonstrated in solar cells that employ CZTS films synthesized using vacuum-based process.[28] Further film growth optimization studies may be able to provide insight into improving the efficiency of CZTS solar cells from nanocrystal coatings.

4.4 Conclusion

Aerosol jet printing from nanocrystal dispersions followed by mechanical compaction is a promising approach for producing nanocrystal coatings in a continuous-amenable process. An additional annealing procedure can produce polycrystalline thin films from these coatings. This approach is general but demonstrated here for the specific case of forming CZTS thin films from CZTS nanocrystal dispersions. The coating morphology depends on the ratio of the aerosol transport and evaporation times, which can be manipulated *via* the carrier gas flow rate. When evaporation is fast compared to aerosol transport time, the aerosol mist droplets dry substantially in flight to the substrate to form nanocrystal agglomerates. These agglomerates impinge on the substrate with little solvent content. The resulting coatings are crack-free but porous. When the aerosol transport time is short, nanocrystal dispersion droplets arrive at the substrate with higher solvent content and coalesce to form wet coatings, which crack upon drying. Porous nanocrystal agglomerate coatings formed by aerosol jet printing can be converted to dense, crack-free nanocrystal coatings through compaction. High temperature annealing of these compacted films in sulfur vapor showed that the thin film microstructure depends on the pre-annealing coating morphology, specifically, the coating density. High density coatings formed *via* compaction at high pressures can be annealed in sulfur to form dense polycrystalline films comprised of large 1-5 μm grains. In contrast, less dense films result in a porous film microstructure. Optimization of the approaches described herein and careful balancing of the factors that determine the coating and thin film morphology may lead to a continuous roll-to-roll process for the production of thin microcrystalline films suitable for solar cells.

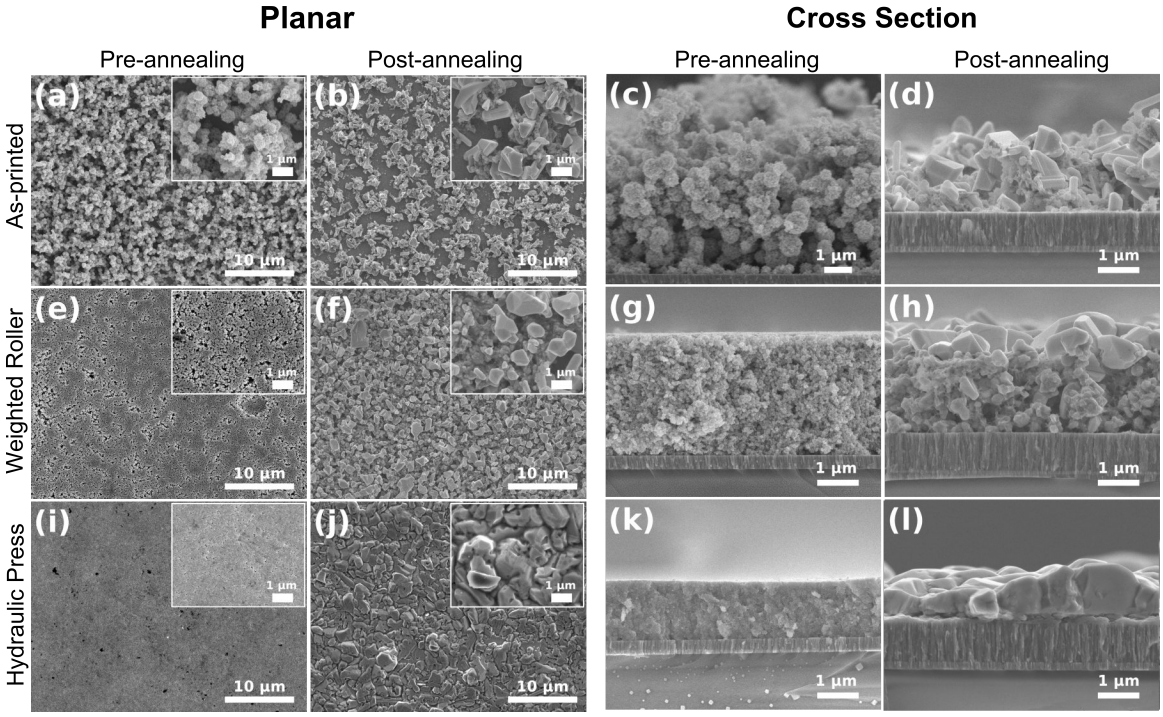

Figure 4.9 SEM images of CZTS nanocrystal coatings, compacted using different methods and compaction pressures, before and after annealing for one hour at 600 °C with 1 mg of solid sulfur (~50 Torr evaporated) in a evacuated quartz ampule; panels (a-d), show the SEMs of a coating that was not compacted prior to annealing (a,c) before and (b,d) after annealing; panels (e-h) show the SEM images of a coating that was compacted using a weighted roller at 25 MPa (e,g) before and (f, h) after annealing; panels (i-l) show the SEM images of a coating compressed using hydraulic press at 800 MPa (i, k) before and (j, l) after annealing. Higher magnification planar SEM images are shown in the insets. All coatings were formed by AJP onto Mo-coated SLG substrates from a 5 wt% 5 nm CZTS nanocrystal dispersion in toluene with a 150 µm diameter nozzle, Q_{CG} = 20 sccm, F_R = 2.5, u_s = 1 mm/s, and U_A = 0.45 mA.

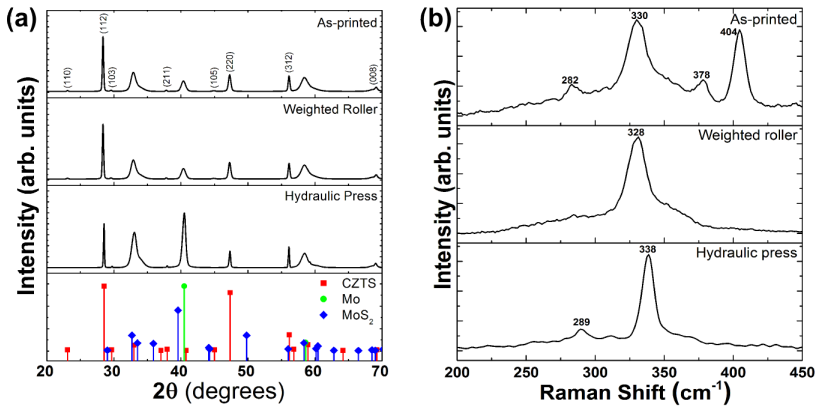

Figure 4.10 (a) XRD patterns and (b) Raman spectra from the as-printed and compressed coatings after annealing in 50 Torr of sulfur at 600 °C. The data are for films shown in the SEMs of Figure 4.9. XRD patterns match the expected powder diffraction pattern for CZTS (shown in the bottom panel in (a).

Chapter 5

Effect of Nanocrsytal Size on Microstructure Development During Annealing of CZTS Nanocrystal Coatings

5.1 Introduction

The highest performing CZTSSe nanocrystal-based devices have a common film morphology characterized by a dense monolayer of large CZTSSe grains (500 nm to 2 μm).[29,30] This morphology is generally achieved by thermally annealing nanocrystal coatings in the presence of sulfur or selenium vapor (hereafter referred to as sulfidation or selenization) at temperatures greater than 500 °C for up to 2 hours. However, after annealing in Se vapor, a bilayer film composed of a fine grained, carbon-rich layer below a large grained CZTSSe film is also formed and is commonly thought to limit the solar cell performance[102,113,132] though Wu *et al.*[103] analyzed the chemical and electronic properties of the fine grain layer in such a film and asserted that the layer imparted no detrimental effects on device performance. Ideally, however, complete conversion of the nanocrystal coating into a polycrystalline film is desired to improve the absorption efficiency.[103,113] Furthermore, attempts to

prevent or reduce the thickness of the carbon-rich layer while increasing the large grain layer thickness have had middling success.[30,35] By contrast, it has been shown that when CZTS nanocrystals coatings on soda-lime glass substrates are sulfidized, this carbon-rich layer does not form provided that the annealing time is sufficiently long.[60,107] This allows optimization of the absorber layer thickness without the complications imparted by a fine grain layer.

Chernomordik *et al.* studied the effect of sulfur pressure and substrate on film microstructure development during sulfidation of coatings comprised of ~25 nm CZTS nanocrystals.[60] They found that the grain growth rate was enhanced by high sulfur pressures and by substrates containing alkali metals, such as soda-lime glass, in agreement with other work on CZTS grain growth.[124,163] However Chernomordik et al. did not address the effects of nanocrystal size or the effects of coating carbon content on the microstructure development although they hypothesized that carbon may affect the film microstructure. Tiong *et al.*[69] reported on the effects of carbon remaining in the film from residual solvent used to disperse the CZTS nanocrystals. They reported that CZTS grain growth rate decreased with increasing carbon content in the nanocrystal coating, and a fine grain layer at the substrate-film interface was observed in all CZTS films. These experiments were conducted at constant sulfidation conditions. The mechanisms hypothesized in these studies suggest that there must be strong coupling between the effects of nanocrystal size, carbon content and sulfur pressure. Moreover, it is difficult to decouple these effects. For example carbon is removed from the film by sulfur and hence sulfur pressure is expected to influence the carbon content of the coating during annealing. The surface-to-volume ratio of the nanocrystal increase with decreasing size such that more carbon in the form of dispersion stabilizing ligands is expected to remain in the coatings. To examine these issues we conducted a systematic study of the effects of these variables on microstructure development. Herein, we describe the effects of carbon concentration, sulfur pressure, and nanocrystal size on CZTS grain growth during sulfidation of CZTS nanocrystal coatings. We find that the carbon concentration in the nanocrystal coating dictates the growth mechanism. When the carbon concentration in the coatings is low (~15 - 20 at.%) the nanocrystals get bigger via normal grain growth in which the average grain size increases uniformly in the coating. When the

carbon concentration in the coating is high (≥35 at.%) nanocrystals exhibit abnormal grain growth in which large CZTS grains form on the coating surface and consume the underlying nanocrystal layer as they grow. As-coated, 5 nm nanocrystal coatings were found to have a higher inherent carbon concentration from surface-attached stabilizing ligands compared to 35 nm nanocrystal coatings. Increasing the sulfur vapor pressure enhances both abnormal and normal grain growth rates. From the combined effects of nanocrystal size, carbon content, and annealing sulfur pressure a growth mechanism is proposed.

5.2 Experimental Section

5.2.1 Materials

Metal diethyldithiocarbamate precursors used for synthesis of 5 and 35 nm CZTS nanocrystals were produced as described by Chernomordik *et al.*[52] Octadecene (technical grade, 90%), oleic acid (technical grade, 90%), oleylamine (technical grade, 70%), and toluene (HPLC grade, 99%) were purchased from Sigma Aldrich. Reagent alcohol (histological grade, 90% ethyl alcohol, 5% methyl alcohol, 5% butyl alcohol) and acetone (HPLC grade, 99.5%) were purchased from Fisher Scientific. Isopropyl alcohol (histological grade, 99.5%) was purchased from Macron Fine Chemicals. Polystyrene (230,000 MW) was purchased from Sigma-Aldrich. Soda lime glass substrates were purchased from Valley Design Corporation. Solid sulfur (99.999%) was purchased from Cerac, Inc. Molybdenum-coated soda lime glass (Mo-coated SLG) was purchased from DASSTECH.

5.2.2 Nanocrystals

CZTS nanocrystals with an average diameter of 35 nm were synthesized by injection of the precursors into a hot coordinating solvent, as described by Chernomordik *et al.*[52] but with slight modification. Briefly, copper (II) diethyldithiocarbamate (54 mg), zinc (II) diethyldithiocarbamate (28 mg), and tin (IV) diethyldithiocarbamate (53.6 mg) were dissolved in 5 ml of oleic acid in a 15 ml round bottom flask. Separately, 10 ml of oleylamine

was poured into a 100 ml round bottom flask. Both flasks were heated to 60 °C at which point the solutions were degassed under vacuum and then purged with nitrogen. The degas-purge cycle was repeated three times. The flasks were then placed under nitrogen flow for the duration of the reaction. The precursor solution was heated to 140 °C to ensure dissolution of all precursors before cooling to 100 °C. The flask containing oleylamine was heated to 340 °C. Upon reaching 340 °C, the precursor-oleic acid solution was quickly injected into the oleylamine using a needle and a syringe. The reaction was allowed to proceed at 340 °C for 10 minutes after which the solution was cooled to room temperature. After cooling, reagent alcohol was added to the reaction solution at a 1:1 volume ratio before centrifuging at 4000 rpm for 10 minutes to sediment the CZTS nanocrystals. Following, the supernatant was discarded and the nanocrystals were redisperesed into 2 ml of a toluene and oleic acid (10^{-4} volume fraction) solution. The alcohol washing procedure was repeated two more times to remove reaction byproducts and unreacted species. After the final washing, the nanocrystals were dispersed in 1.5 ml of a toluene and oleic acid (10^{-4} volume fraction) solution, forming an approximately 30 mg/ml dispersion for coating use.

Synthesis of the 5 nm CZTS nanocrystals has been previously described in Section 3.2.2. The 5 nm nanocrystals were dispersed in 1.5 ml of a toluene and oleic acid (10^{-4} volume fraction) solution, forming an approximately 30 mg/ml dispersion for coating use. Particle size was measured by Scherrer's equation using the full-width at half maximum of the CZTS diffraction peak at 28.5°.

5.2.3 Alteration of CZTS nanocrystal dispersion carbon content

To reduce the carbon content of 5 nm CZTS nanocrystal coatings, carbon ligands attached to the nanocrystal surface (mainly oleylamine and oleic acid[59]) were removed by repeated washing with alcohol followed by redispersion in toluene.After synthesis, the nanocrystal dispersion was diluted with reagent alcohol at a 1:1 volume ratio. The resulting solution was centrifuged at 4000 rpm for 5 minutes. The supernatant was discarded and 1.5 ml of toluene was added to the vial before redispersing the nanocrystals through ultrasonication for 10 minutes. This procedure was repeated three times. The as-produced dispersion

was unstable and the nanocrystals sedimented out of the dispersion within 5 minutes after sonication, indicating loss of stabilizing ligands. In spite of the decreased stability, these nanocrystal dispersions could be used to form coatings by aerosol jet printing successfully.

To increase the carbon content of 35 nm CZTS nanocrystal coatings, polystyrene was added to dispersions of 35 nm CZTS nanocrystals. A polystyrene-containing toluene solution was created by dissolving 100 mg of polystyrene beads in 1 ml of toluene. A specified volume of this solution replaced the same volume of the toluene/oleic acid solution during redispersing of the nanocrystals after synthesis (i.e. 75 μL of toluene-polystyrene solution mixed with 1.425 ml of toluene-oleic acid solution in place of 1.5 ml of toluene-oleic acid solution). After polystyrene addition, the dispersion was subjected to ultrasonication for 20 minutes before use. Polystyrene is expected to be well-mixed within the solution due to its high solubility in toluene and the absence of noticeable effects on dispersion stability is consistent with this expectation.

5.2.4 Deposition and annealing of CZTS nanocrystal coatings

Figure 5.1 is a schematic of the coating and annealing process used to form polycrystalline CZTS films from dispersions of 5 and 35 nm nanocrystals. Forming crack-free nanocrystal coatings from 5 nm CZTS nanocrystal dispersions using conventional coating techniques is difficult. To overcome this difficulty we formed the nanocrystal films, as described in our previous publication, by aerosol jet printing a porous coating and then compacting it with a hydraulic press. in the manner described in Section 4.2.3 Coatings cast from 35 nm CZTS nanocrystals did not exhibit the same cracking susceptibility during traditional wet coating, likely due to lower coating stress generated during drying.[79] Thus, coatings comprising 35 nm CZTS nanocrystals could be dropcast from a nanocrystal dispersion onto a Mo-SLG substrate without cracking as described by Chernomordik *et al.*[60] The coating area defined by a metal frame was 155 mm^2.

Figure 5.2 displays planar and cross-sectional scanning electron microscopy (SEM) images of typical coatings produced from 5 nm (Figures 5.2a and 5.2b) and 35 nm (Figures 5.2c and 5.2d) CZTS nanocrystal dispersions. The density and thickness of the coatings

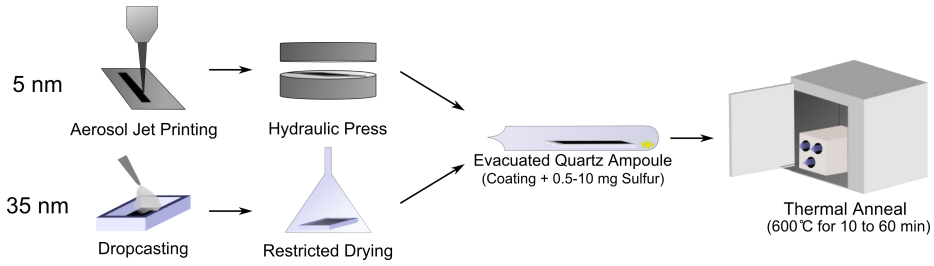

Figure 5.1 A schematic of the coating and annealing procedures to make polycrystalline CZTS films from CZTS nanocrystal dispersions. Coatings composed of 5 nm CZTS nanocrystal are formed by aerosol jet printing from dispersions in toluene followed by compaction to increase coating density. Coatings composed of 35 nm CZTS nanocrystals are formed by dropcasting from dispersions in toluene onto a substrate masked by a frame followed by drying under restricted airflow. Coatings are sealed in evacuated quartz ampules with 1 to 10 mg of sulfur and annealed in a furnace at 600 °C for up to 60 minutes.

appear similar between the two coatings. Individual nanocrystals are discernible in the 35 nm nanocrystal coating images but not in the 5 nm coating due to the resolution limit of the SEM (> 8 nm).

Procedures for annealing the CZTS nanocrystal coatings has been described elsewhere.[60,107] A schematic of the annealing procedure is shown in Figure 5.1. Briefly, substrates coated with nanocrystals were placed in quartz tubes with 1 to 10 mg of solid sulfur. The tubes were evacuated to 10^{-6} Torr and flame sealed to form ampules. Following, the ampules were placed in a furnace that had been preheated for 3 hours to 600 °C. After the desired annealing time (10, 30, or 60 minutes), the furnace was turned off and the furnace door was opened to allow the ampules to cool to room temperature. The cooling rate was such that the furnace temperature reached 350 °C after 3 hours. Finally, the ampules were removed from the furnace and fractured to remove the substrates with annealed coatings.

5.2.5 Characterization

The nanocrystal coatings were imaged before and after annealing using a JEOL 6500 field-emission scanning electron microscope (SEM). Abnormal grain surface coverage was determined using ImageJ (NIH) image analysis software. A Thermo-Noran Vantage energy

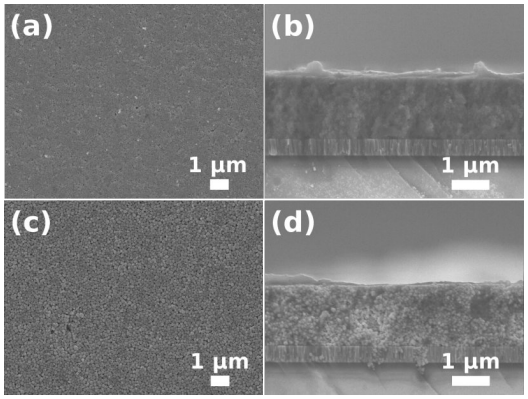

Figure 5.2 SEM images of coatings prior to annealing. (a) and (b) are planar and cross-sectional images of a coating composed of 5 nm CZTS nanocrystals and formed by AJP followed by compaction. (c) and (d) are planar and cross-sectional images of a coating composed of 35 nm CZTS nanocrystals and formed by dropcasting.

dispersive X-ray spectrometer (EDS) was used to determine the elemental composition of the films before and after annealing in sulfur. X-ray diffraction (XRD) was conducted using a Bruker D8 Discover system comprising a Co Kα source and a VÅNTEC-500 2D area detector. XRD patterns were converted to Cu Kα source format using analysis software (JADE, Materials Data Incorporated). Raman spectroscopy was conducted using a Witec Alpha300R confocal Raman microscope equipped with a 532 nm wavelength source, a DV401 CCD detector, and a UHTS300 spectrometer. The Raman spectra were collected with an 1800 lines/mm grating, providing a spectral resolution of 0.02 cm^{-1}. Attenuated total reflection Fourier transform infrared (ATR-FTIR) spectroscopy was conducted on a Nicolet Magna-IR 550 spectrometer with a germanium ATR crystal and KBr optics.

5.3 Results

5.3.1 Effect of Sulfur Vapor Pressure and Thermal Annealing Time

Figures 5.3a and 5.3d displays the SEM images of 5 nm CZTS nanocrystal coatings after annealing in 50 Torr of sulfur at 600 °C for 10 minutes. Large (1-2 µm) CZTS grains

appear on the surface of the nanocrystal coating. This microstructure is similar to that reported by Chernomordik *et al.*[60] during annealing of 25 nm CZTS nanocrystals on quartz substrates. In that work, the large grains that formed on top of the film were referred to as the abnormal grains and the underlying small grains, as the normal grains. We adopt the same terminology here for consistency. When the annealing duration is increased to 30 minutes (Figures 5.3b and 5.3e) and 60 minutes (Figures 5.3c and 5.3f), the abnormal grains increase in size and coverage (i.e., number of abnormal grains per unit area increases). When the sulfur pressure is increased to 500 Torr, grains grow faster, reaching as large as > 3 μm after only 10 minutes. We still observe both abnormal and normal grain growth as we did at lower sulfur pressure

A striking difference between the coatings annealed at 50 and 500 Torr of sulfur is the abnormal grain surface coverage at 10 and 30 minutes: compare for example Figure 5.3a to 5.3g and Figure 5.3b to 5.3h. The abnormal grain surface coverage was quantified for each of the films in Figure 3 and is plotted as a function of annealing time in Figure 5.4. After annealing in 50 Torr of sulfur pressure for 10 minutes, only 8% of the coating surface is covered with abnormal grains whose sizes vary between 1 μm and 3 μm. The coverage increases to 37% and 96% after 30 and 60 minutes, respectively. When the sulfur pressure is increased to 500 Torr, grain growth rate increases significantly and even 10 minutes of annealing covers 83% of the surface with abnormal grains. The abnormal grain surface coverage increases gradually after this initial rapid growth. Although the coating annealed at 500 Torr has greater surface coverage at 10 minutes than the film annealed for the same amount of time at 50 Torr, bot films are nearly completely covered with abnormal grains (~96% coverage) after 60 minutes. Films formed in 500 Torr of sulfur exhibit thicker abnormal grains (average thickness of ~750 nm, Figures 5.3j, 5.3k and 5.3l) than the films formed in 50 Torr of sulfur (average thickness of ~520 nm, Figures 5.3d, 5.3e and 5.3f). Correspondingly, the films formed in 500 Torr of sulfur end up with a thinner fine-grained layer beneath the abnormal grains than the film annealed in 50 Torr of sulfur. Compare for example Figures 5.3d-5.3f with Figures 5.3j-5.3l.

When the elemental composition of these films were analyzed using EDS, we found that the carbon concentration in the film decreases with increasing annealing time and with

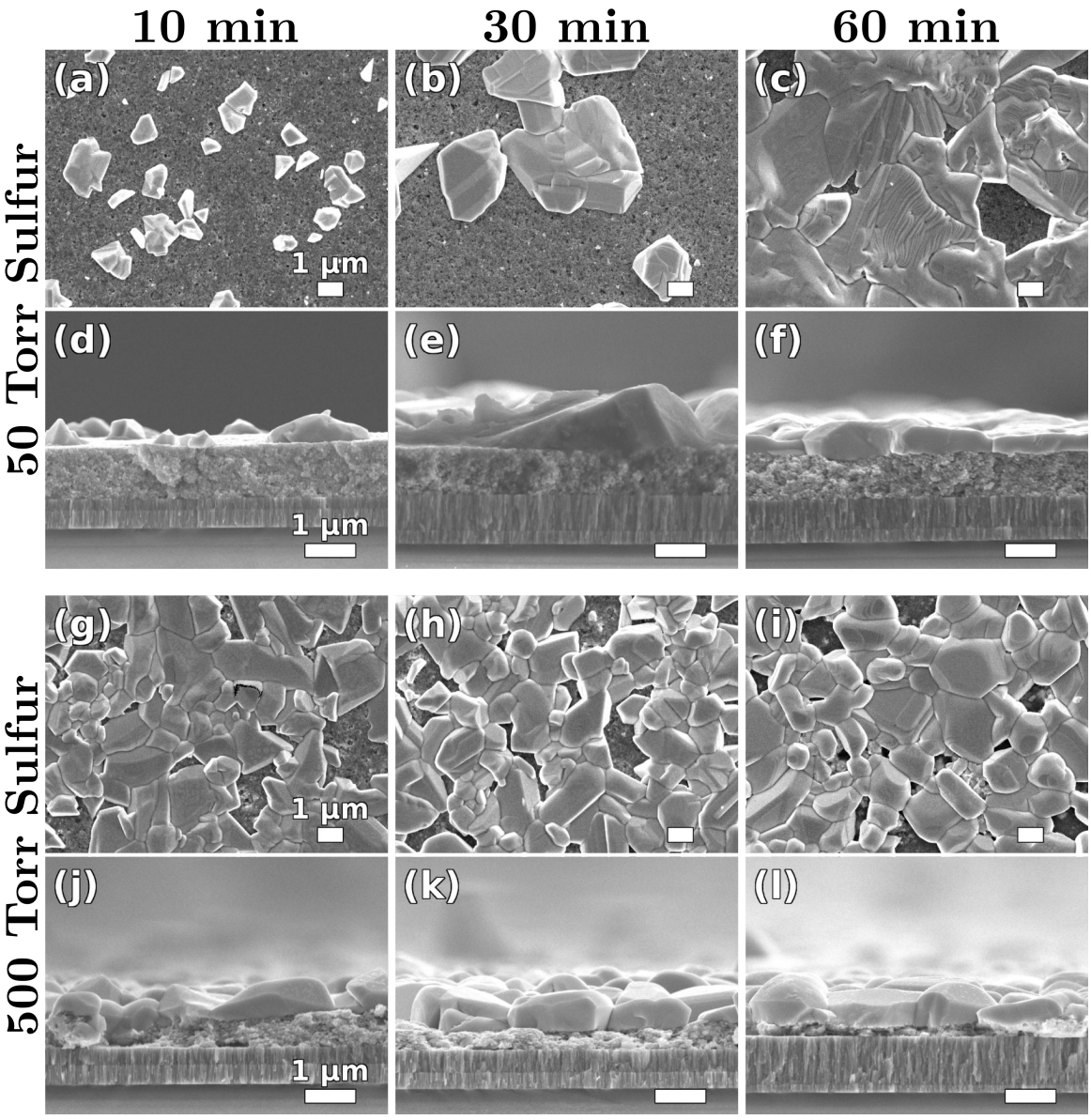

Figure 5.3 (a-f) SEM images CZTS coatings composed of 5 nm diameter CZTS nanocrystals after annealing at 600 °C for (a,d) 10 minutes, (b,e) 30 minutes, and (c,f) 60 minutes in evacuated quartz ampules with 1 mg of sulfur (50 Torr sulfur pressure). (g-l) SEM images CZTS coatings composed of 5 nm diameter CZTS nanocrystals after annealing at 600 °C for (g,j) 10 minutes, (h,k) 30 minutes, and (i,l) 60 minutes in evacuated quartz ampules with 10 mg of sulfur (500 Torr sulfur pressure).

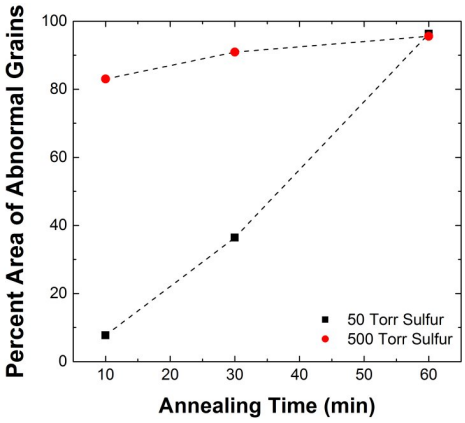

Figure 5.4 Surface coverage of abnormal grains as a function of annealing time for coatings composed of 5 nm CZTS nanocrystals. The coatings were annealed at 600 °C in the 50 and 500 Torr of sulfur vapor pressure.

increasing sulfur pressure. Figure 5.5 shows the carbon concentration and the Cu/[Zn+Sn] ratio in the fine-grained layer that forms during annealing of coatings composed of 5 nm CZTS nanocrystals. Initially, the carbon concentration in this coating was 45 at% but decreased to 26 at% after annealing in 50 Torr of sulfur for 60 minutes. In contrast, carbon concentration decreased from 53 at% to 12 at% after the same nanocrystal coatings were annealed in 500 Torr of sulfur for 60 minutes. Clearly more carbon is removed at higher sulfur pressure. (The absolute values of the carbon concentrations are subject to errors due to the inaccuracies of EDS measurements for low atomic number elements. Only the trends of the relative values have significance).[164] When the annealing is conducted in 50 Torr of sulfur, the fine-grained CZTS layer is slightly copper poor (Cu/[Zn+Sn] ≈ 0.95) for all annealing times, indicating no significant change in stoichiometry during annealing. The 5 nm CZTS nanocrystal coatings annealed at 500 Torr started slightly copper-rich (Cu/[Zn+Sn] ≈ 1.05) and remained so throughout annealing, as shown in Figure 5.5b. After annealing, XRD patterns and Raman spectra of the films exhibited the expected peaks characteristic of kesterite CZTS, as shown in Figure 5.6 of the Supplemental Information. Increases in the average grain size with annealing time is also evident in narrowing of the full width at half maximum (FWHM) of the (112) CZTS diffraction peak at ~28.5°.

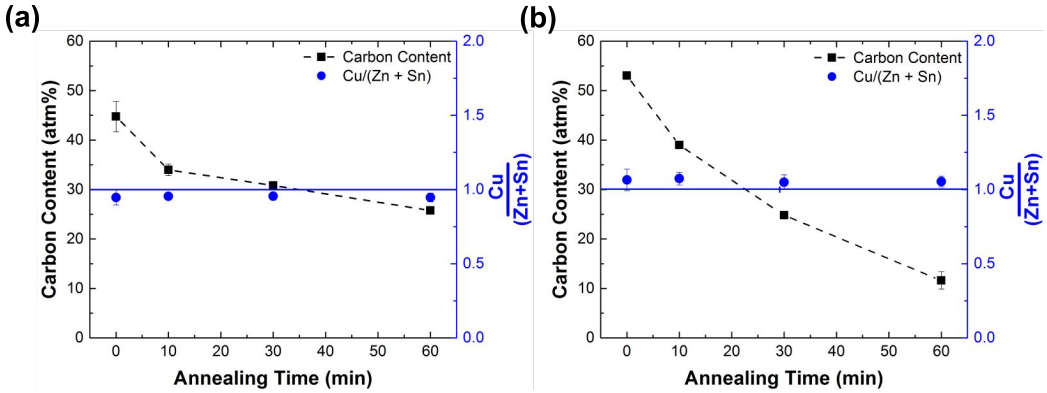

Figure 5.5 Carbon concentration (at%) and copper-to-sum-of-zinc-and-tin ratio (Cu/(Zn+Sn)) as determined from EDS, as a function of annealing time for coatings composed of 5 nm CZTS nanocrystals. The coatings were annealed at 600 °C in (a) 50 Torr and (b) 500 Torr sulfur.

Figure 5.7 displays the SEM images of CZTS coatings cast from a dispersion of 35 nm nanocrystals after they were annealed in sulfur at 600 oC. The film microstructure before (Figures 5.2c and 5.2d) and after annealing in 50 Torr of sulfur for 10 minutes (Figures 5.7a and 5.7d) appear nearly the same except for a few small abnormal grains (*e.g.,* left side of Figure 5.7d). When the annealing time is extended to 30 and 60 minutes, the size and number density of the abnormal grains increases but this increase is much slower and less pronounced than the growth observed with coatings composed of 5 nm CZTS nanocrystals under the same conditions. Increasing the sulfur pressure to 500 Torr and annealing for 10 minutes transforms the 35 nm nanocrystals into a polycrystalline film with grain sizes between 100-300 nm. Few isolated abnormal surface grains are present (top of Figure 5.7j) but the polycrystalline film appears to develop primarily through the growth of normal grains. The normal grains continue to grow with increasing annealing time, reaching approximately 700 nm and 1.5 µm after 30 and 60 minutes, respectively. The size and number density of the abnormal grains do not change with annealing time, indicating a loss of driving force for abnormal grain growth after the first 10 minutes. In fact, scarcity of abnormal grains even after 10 minutes indicate that the driving force to grow abnormal grains has been significantly reduced compared to the coatings formed with 5 nm nanocrystals. The thickness of the CZTS film decreases gradually with annealing time, likely a result of film densification

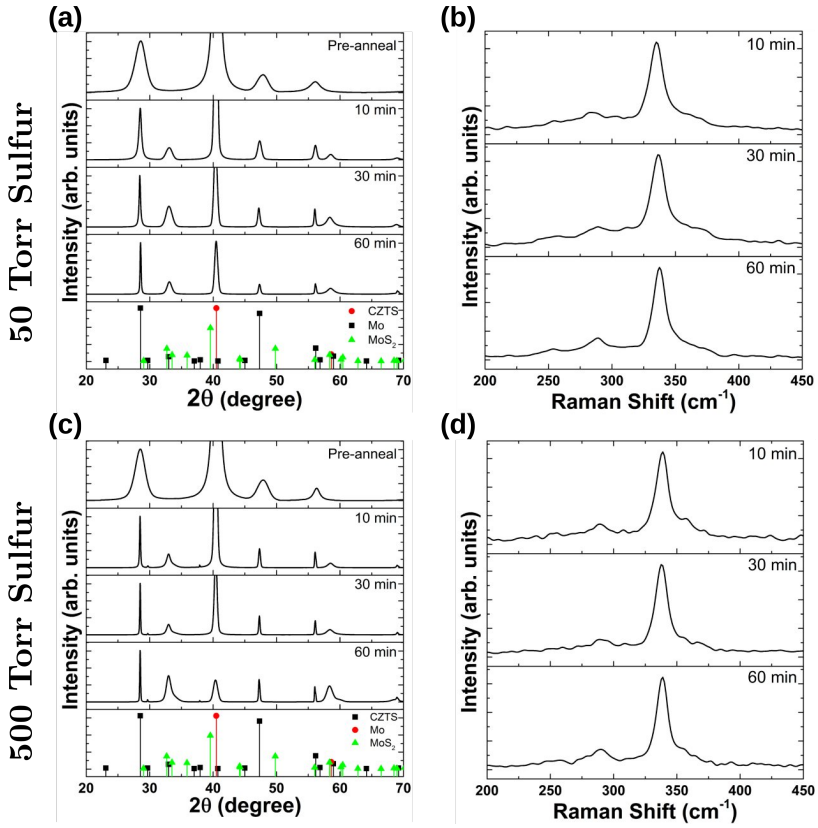

Figure 5.6 XRD and Raman spectra of CZTS films produced by annealing 5 nm CZTS nanocrystal coatings at 600 °C in the presence of (a,b) 50 Torr and (c,d) 500 Torr of sulfur for 10, 30, and 60 minutes.

due to sintering.

Figures 5.8a and 5.8b show the annealing time dependence of carbon concentration and the (Cu/[Zn+Sn]) ratio, as determined from EDS, for CZTS films formed by annealing 35 nm nanocrystal coatings with 50 Torr and 500 Torr of sulfur pressure, respectively. Compared to 5 nm CZTS nanocrystal coatings, the 35 nm nanocrystal coatings have significantly lower initial carbon content (~17 at% for 35 nm and ~50 at% for 5 nm coatings). The carbon concentration in these coatings appear to decrease with annealing time although a definitive conclusion is made difficult because of the variability inherent in EDS measurements of carbon. After annealing, XRD patterns and Raman spectra of the 35 nm CZTS

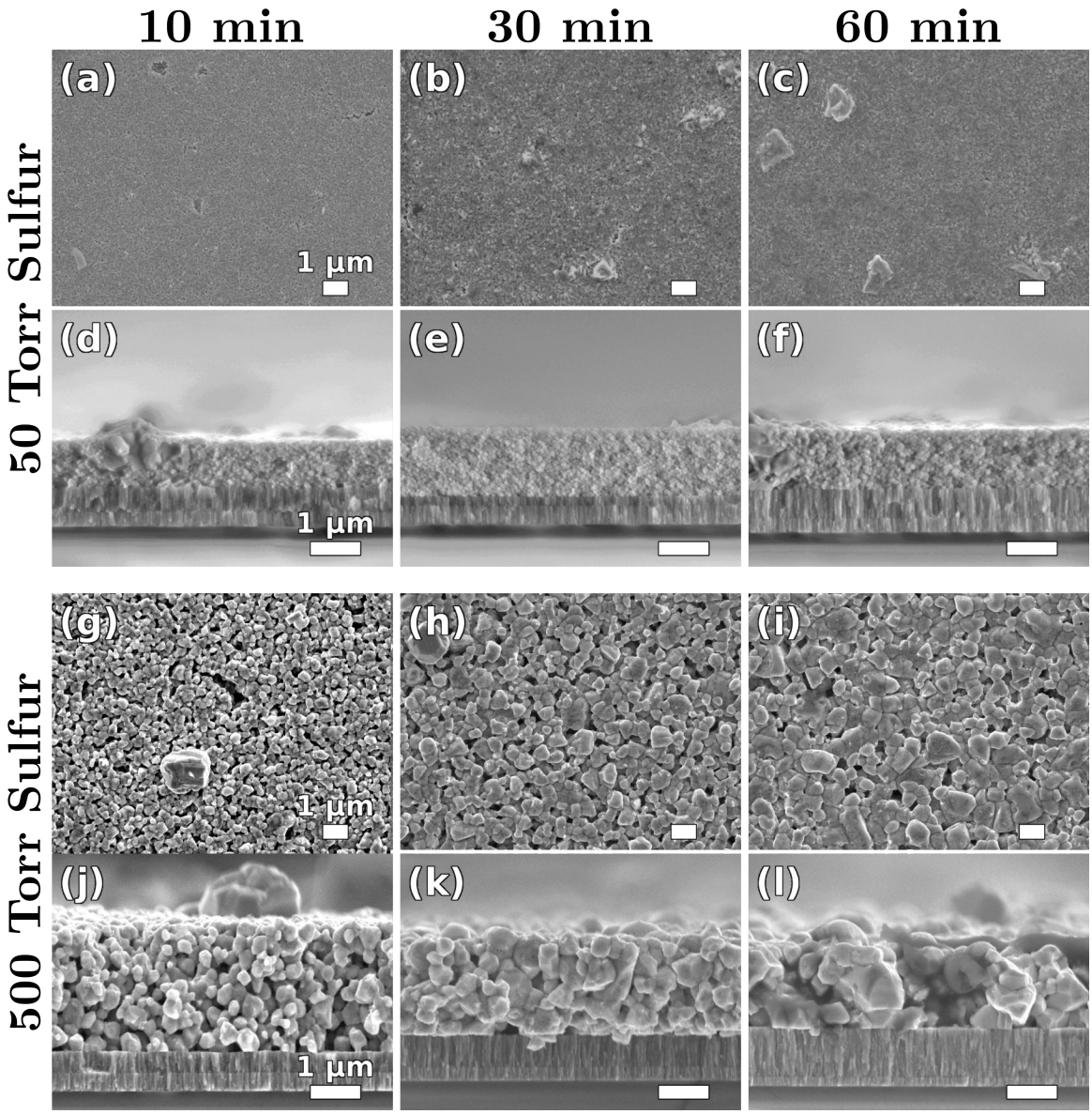

Figure 5.7 (a-f) SEM images CZTS coatings composed of 35 nm diameter CZTS nanocrystals after annealing at 600 °C for (a,d) 10 minutes, (b,e) 30 minutes, and (c,f) 60 minutes in evacuated quartz ampules with 1 mg of sulfur (50 Torr sulfur pressure). (g-l) SEM images CZTS coatings composed of 35 nm diameter CZTS nanocrystals after annealing at 600 °C for (g,j) 10 minutes, (h,k) 30 minutes, and (i,l) 60 minutes in evacuated quartz ampules with 10 mg of sulfur (500 Torr sulfur pressure).

nanocrystal coatings show the expected kesterite CZTS peaks indicating that CZTS phase is retained after annealing as shown in Figure 5.9

5.3.2 Effect of Nanocrystal Size and Carbon Content

It had been suggested that carbon concentration in the coatings may affect the microstructure evolution during annealing in sulfur.[69,165] This is a plausible suggestion. For example, carbon containing ligands in the CZTS nanocrystal coatings may be limiting the grain growth by acting as a barrier between neighboring nanocrystals and reducing sulfur vapor access to the interior of the coating: this effect is expected to depend on the amount of ligands and carbon in the coatings. The difference in carbon concentration could contribute to the differences in microstructure when coatings composed of different size nanocrystals are annealed in sulfur. Unfortunately, it is nearly impossible to completely deconvolute the effects of carbon concentration in the coatings from the effects of nanocrystal size. The carbon concentration in the coatings and the CZTS nanocrystal size are inherently linked because the amount of ligands in the coating depends on the nanocrystal surface area.

Figure 5.10 is a side-by-side comparison of the SEMs of films formed by annealing coatings composed of 5 nm nanocrystals (Figures 5.10a and b) with films formed by annealing coatings composed of 35 nm nanocrystals (Figures 5.10c and d) for one hour in 50 (Figures 5.10a and c) and 500 Torr (Figures 5.10b and d) of sulfur, respectively. When annealing is conducted at 50 Torr (Figures 5.10a and c), large (~1-5 μm), many abnormal CZTS grains are formed from the 5 nm CZTS nanocrystal coatings while only a few abnormal grains are formed from the 35 nm nanocrystals. Increasing the sulfur pressure from 50 Torr to 500 Torr has very little effect on the final morphology of the films formed by annealing coatings composed of 5 nm CZTS nanocrystals (compare Figures 5.10a and 5.10b), while increasing the sulfur vapor pressure increases normal grain growth dramatically in coatings composed of 35 nm CZTS nanocrystals: the 35 nm nanocrystals neck sinter and grow to as large as 0.5 – 2 μm large grains within the bulk of the coating (compare Figures 5.10c and 5.10d).

The differences observed in Figure 5.10 could be either due to the nanocrystal size or due to the differences in carbon concentration in the coatings cast from 5 nm and 35 nm

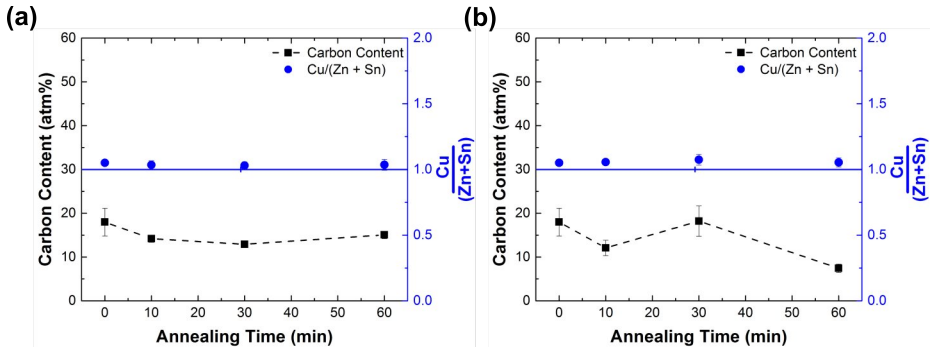

Figure 5.8 Carbon concentration (at%) and copper-to-sum-of-zinc-and-tin ratio (Cu/(Zn+Sn)) as determined from EDS, as a function of annealing time for coatings composed of 35 nm CZTS nanocrystals. Coatings were annealed at 600 °C in (a) 50 Torr and (b) 500 Torr of sulfur.

nanocrystals. Figures 5.5 and 5.8 show that the initial carbon concentration in coatings cast from 5 nm and 35 nm nanocrystal coatings differ considerably. To deconvolute the effects of nanocrystal size from the effects of carbon concentration, we manipulated the carbon content in the coatings while keeping the nanocrystal size constant. Specifically, we decreased the carbon concentration in coatings composed of 5 nm CZTS nanocrystals by subjecting the nanocrystal dispersions to additional washing steps during dispersion formulation to reduce the oleate ligand coverage.

Figure 5.11 displays the SEM images of 5 nm CZTS nanocrystal coatings with different carbon concentrations after annealing at 600 °C for 60 minutes in 500 Torr of sulfur. The films shown in Figures 5.11a and 5.11c were obtained by annealing coatings where the carbon concentration was unaltered while the films shown in Figures 5.11b and 5.11d were obtained by annealing coatings where the carbon concentration in the coating was reduced through repeated washings of the nanocrystals with ethanol followed by dispersion in toluene. The effect of these successive washing-dispersion cycles on ligand coverage was quantified using ATR-FTIR spectroscopy and it was found that the washing-redispersing cycles decreased the carbon concentration in the nanocrystal coatings. Specifically, the C-H stretching absorptions at 2853, 2923, and 2956 cm^{-1} decreased with each redispersion cycle, as shown in Chapter 3. After annealing, the coating with lower carbon concentration exhibited significantly fewer and smaller abnormal grains (Figures 5.11b and 5.11d) than

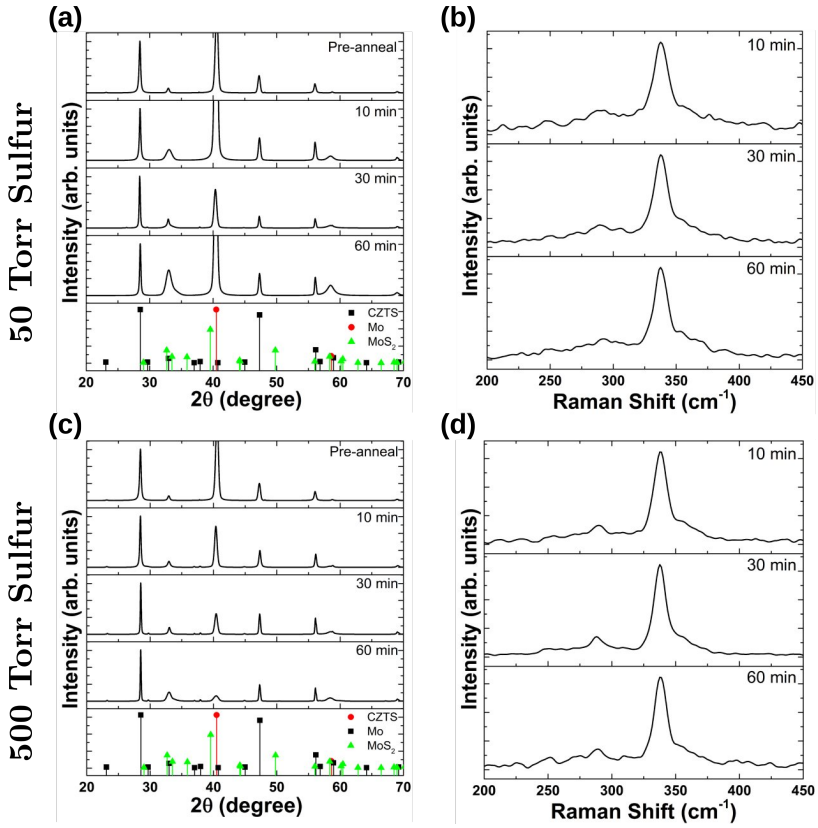

Figure 5.9 XRD and Raman spectra of CZTS films produced by annealing 35 nm CZTS nanocrystal coatings at 600 °C in the presence of (a,b) 50 Torr and (c,d) 500 Torr of sulfur for 10, 30, and 60 minutes.

the coating with the higher carbon concentration (Figures 5.11a and 5.11c). The average grain size in the coating with the reduced carbon concentration increases from 4.8 nm to 20, 27, and 41 nm after 10, 30, and 60 minutes of annealing. These grain sizes were determined using the Scherrer's equation and the width of the (112) XRD peak. XRD patterns and Raman spectra for these films are shown in Figure 5.12.

We also increased the carbon concentration in 35 nm nanocrystal coatings, by adding polystyrene to the nanocrystal dispersion before coating the substrates. Figure 5.13 displays SEM images of an (a.b) unaltered 35 nm CZTS nanocrystal coating and 35 nm CZTS nanocrystal coatings with different masses of polystyrene added (c,d - 0.035 mg; e,f - 0.07

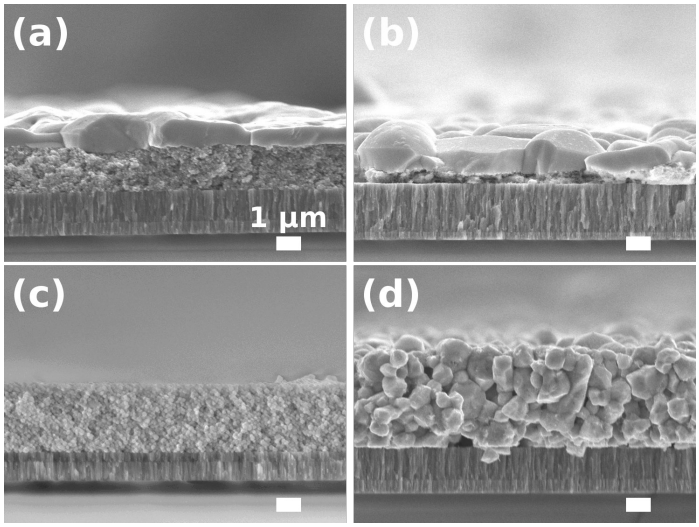

Figure 5.10 SEM images of CZTS nanocrystal coatings after annealing for 60 minutes at 600 °C in (a and c) 50 Torr and (b and d) 500 Torr of sulfur. The coatings were composed of (a and b) 5 nm or (c and d) 35 nm CZTS nanocrystals.

mg; g,h - 0.175 mg; i,j - 0.350 mg) after annealing for 60 minutes with a sulfur pressure of 500 Torr. XRD and Raman show all films conform to results expected of kesterite CZTS as shown in Figure 5.14. Figure 5.13 shows that addition of a small amount (0.035 g) of polystyrene leads to the formation of large abnormal grains during annealing. This is in distinct contrast to coatings annealed without any polystyrene, where normal grain growth dominates. Increasing the mass of polystyrene added to the coating beyond this small amount decreases both abnormal and normal grain growth, in agreement with the observations of Tiong *et al.*[69] where increasing carbon content by increasing the amount of residual dispersing liquid retained in the coating after drying through use of higher boiling point dispersing liquids.

Figure 5.15 shows the effect of carbon content on the microstructure of films formed by annealing coatings cast from 35 nm CZTS nanocrystals in 500 Torr of sulfur at 600 °C for 60 minutes. Specifically, Figure 5.15 shows abnormal grain surface coverage versus the initial carbon concentration in the coating as determined by EDS. The initial carbon concentration was controlled by varying the mass of the polystyrene added to the dispersion used to cast

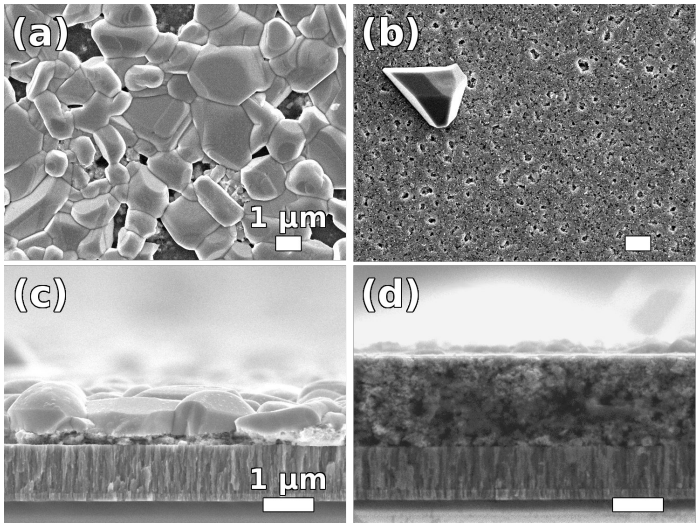

Figure 5.11 SEM images of coatings composed of 5 nm CZTS nanocrystals after annealing at 600 °C for 60 minutes in 500 Torr of sulfur (10 mg of sulfur added to ampule). In (a and c) the coatings were made from as-synthesized nanocrystals while in (b and d) the nanocrystal were washed four times to reduce the coverage of ligands attached to their surfaces (*i.e.,* sedimented by addition of alcohol and redispersed in toluene): The washing reduces the ligand coverage and thus the carbon concentration in the coatings. (a) and (b) are the plan views while (c) and (d) are the cross sectional images.

the coatings. The coating with no polystyrene added undergoes normal grain growth and has an abnormal grain surface coverage < 0.1%. Addition of polystyrene to the nanocrystal coatings increases the initial carbon concentration which in turn prompts abnormal grain growth. Further increases in the carbon concentration gradually decreases abnormal grain growth. The abnormal grain surface coverage reaches a minimum value of ~20% at an initial carbon concentration of 60 at% (0.25 mg of PS added).

The reduction of abnormal grain growth at high carbon concentrations, as observed with 35 nm CZTS nanocrystals above, has been reported previously by Tiong *et al.*[69] and the decrease was attributed to the formation of carbon barrier layers between nanocrystals that require removal through reaction with sulfur before grain growth can occur. In the mechanism proposed by Tiong *et al.*, abnormal grain growth was explained by preferential removal of carbon surrounding the nanocrystals located at the coating surface over other

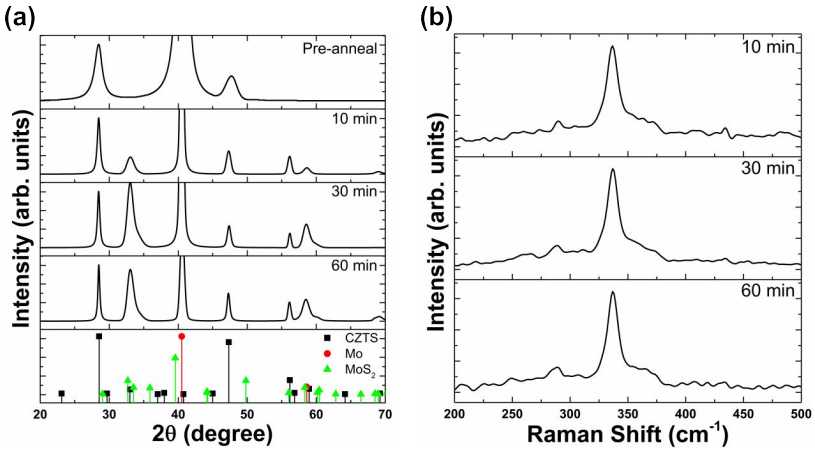

Figure 5.12 (a) XRD patterns and (b) Raman spectra of 5 nm CZTS nanocrystal coatings produced from a nanocrystal dispersion washed four successive times after annealing for 60 minutes at 600 °C with a sulfur vapor pressure of 500 Torr.

regions deeper in the coating. Removal of carbon at the surface was proposed to lead to abnormal grain growth and the effectiveness of this removal is reduced at higher carbon concentrations. Diffusion barrier formation likely plays a role in the reduction of abnormal grain growth rates at high carbon concentrations but the data in Figures 5.11 and 5.13, particularly at low carbon concentrations, suggest that the role of carbon in microstructure development during CZTS nanocrystal annealing is more complex. Clearly, small concentrations of carbon leads to a dramatic change from normal grain growth to abnormal grain growth.

It is apparent that there is an intricate interplay amongst sulfur vapor pressure, carbon concentration and nanocrystal size on CZTS microstructure development. Sulfur vapor pressure increases both normal and abnormal grain growth rates though it does not appear to significantly influence the balance between normal and abnormal grain growth mechanisms. For example, an order of magnitude change in sulfur pressure did not change the dominant growth mechanism in 5 nm CZTS nanocrystal coatings (Figure 5.3) which exhibited dominant abnormal grain growth at both 50 and 500 Torr of Sulfur. Similarly, normal grain growth remained the dominant growth mechanism in 35 nm CZTS nanocrystal coatings (Figure 5.7) when the sulfur pressure was increased from 50 Torr to 500 Torr.

On the other hand, CZTS nanocrystal size and the carbon concentration in the films do affect and alter the growth mechanism, changing it from normal grain growth dominated to abnormal grain growth dominated and vice versa. Figures 5.11 and 5.13 show conclusively that decreasing the carbon concentration in the coatings can shut down the abnormal grain growth while increasing the carbon concentration can switch the dominant mechanism from normal grain growth to abnormal grain growth. Through replacement of oleylamine ligands for formamide ligands, Huang *et al.*[165] convert the growth mechanism in ~5-6 nm CZTS nanocrystal coatings from abnormal grain growth with the carbon-rich oleylamine-capped nanocrystals to normal grain growth with the carbon-poor formamide-capped nanocrystals. These results also support the prominent effect carbon content has on microstructure determination.

CZTS nanocrystal size affects the microstructure development in two ways. First, nanocrystal size determines the carbon concentration in the coating because smaller nanocrystals provide more surface area for ligand attachment per volume of CZTS. Second, nanocrystal size determines the total surface energy of the films: larger this energy, greater the driving force for grain growth. These effects are coupled and difficult to deconvolute but experiments with 5 nm and 35 nm nanocrystals where we have change the carbon concentration offer some conclusions and partially decouple these two effects. It appears that nanocrystal size affects the rate of abnormal grain growth even if the films have similar carbon concentrations. When the carbon concentration is sufficiently high abnormal grain growth is observed with coatings cast from both nanocrystal sizes (5 nm – Figures 5.3i and 5.3l; 35 nm – Figures 5.13g,h), but the growth is faster for coatings composed of 5 nm nanocrystals under otherwise identical annealing conditions (at 600 °C for 60 minutes in 500 Torr). The carbon concentrations in these 5 nm and 35 nm coatings were both approximately 45 at%. Furthermore, even the abnormal grain growth rate while annealing coatings composed of 5 nm nanocrystals coatings in 50 Torr of sulfur (Figures 5.3c and 5.3f) is higher than that while annealing coatings composed of 35 nm nanocrystals at 500 Torr of sulfur (Figures 5.7b and 5.7d). The higher abnormal grain growth rate of smaller nanocrystals is attributed (i) to the increased driving force due to larger nanocrystal surface area and hence total surface energy, and (ii) to increased cation diffusion rate to the abnormal grains from the underlying

nanocrystal coating through the boundaries between the nanocrystals. The larger surface area in 5 nm nanocrystal coatings (factor of 7 greater than that of a 35 nm CZTS nanocrystal coating of equal CZTS mass) provides more grain boundary area for diffusion, increasing the flux of Cu, Zn, and Sn to the coating surface, enhancing the abnormal grain growth rate.

5.4 Summary and Conclusions

Coatings comprising 5 and 35 nm CZTS nanocrystals were annealed at 600 °C for 10, 30, and 60 minutes in the presence of 50 and 500 Torr sulfur pressure. During annealing, 5 nm CZTS nanocrystal coatings developed large abnormal grains on the film surface that grew in size with increased annealing time at 50 Torr sulfur pressure. Increasing the sulfur pressure to 500 Torr enhanced the abnormal grain growth rate such that large 2-5 μm grains formed after 10 minutes of annealing. At a sulfur pressure of 50 Torr, 35 nm CZTS nanocrystal coatings produced only a small increase in average grain size, which was accompanied by formation of few small abnormal grains. Increasing the sulfur pressure to 500 Torr enhanced normal grain growth and the nanocrystal coating was converted into a dense polycrystalline film comprising 1-2 μm CZTS grains. Grain growth during annealing of 35 nm CZTS nanocrystal coatings was found to be slower than that of 5 nm nanocrystal coatings and was dominated by normal grain growth, in contrast to the abnormal grain growth observed in 5 nm CZTS nanocrystal coatings.

Through EDS measurements, it was found that prior to annealing 5 nm CZTS nanocrystals coatings contained significantly more carbon than 35 nm CZTS nanocrystal coatings, a potential factor in microstructure development differences. Removal of carbon ligands from the surface of the 5 nm CZTS nanocrystals by successive cleaning followed by redispersion prior to coating reduced both the abnormal grain growth rate and abnormal grain density during annealing. Addition of polystyrene to 35 nm CZTS nanocrystal coatings to increase the carbon concentration switched the grain growth mechanism from normal-dominated to abnormal-dominated grain growth during annealing. The size and density of the abnormal grains decreased as the amount of polystyrene added increased. Abnormal

grain growth rates were found to be higher in 5 nm nanocrystal coatings compared to 35 nm nanocrystal coatings at similar carbon concentrations. The smaller CZTS nanocrystals provide more grain boundary area for diffusion, leading to higher elemental flux of metallic elements composing CZTS through the coating to the film surface, increasing the abnormal grain growth rate.

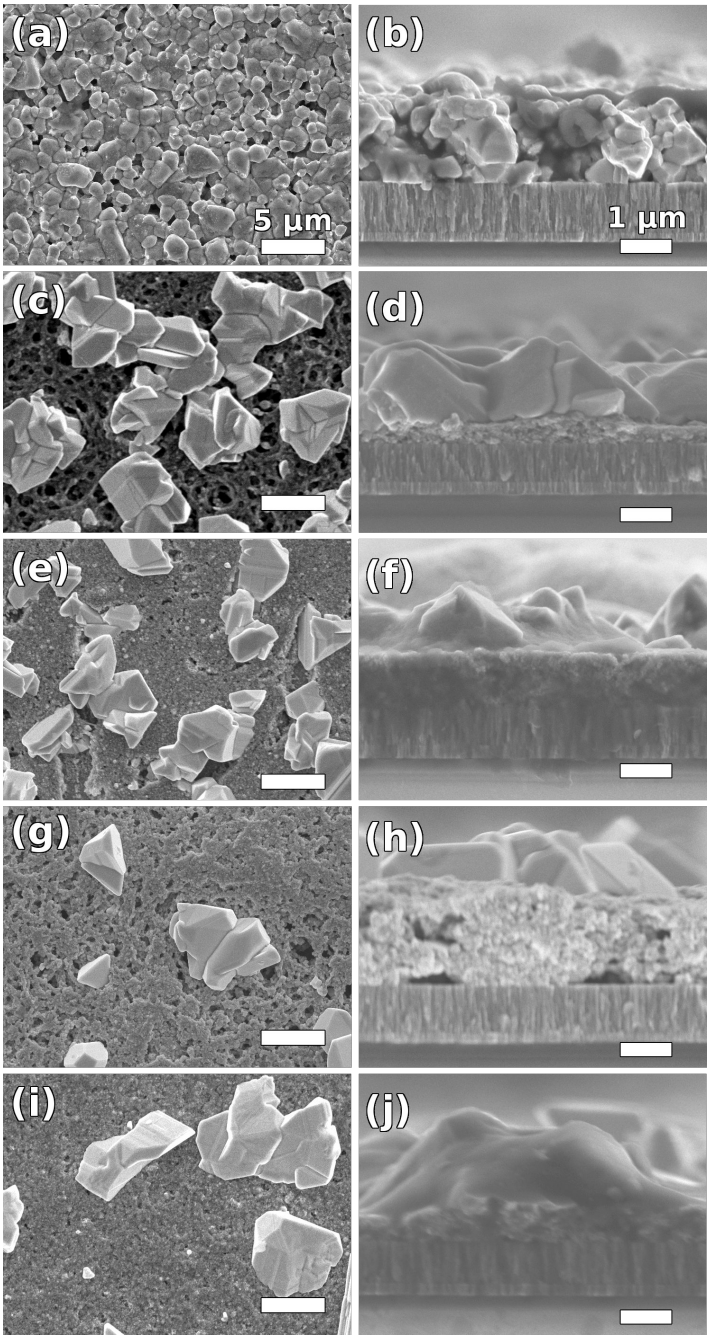

Figure 5.13 SEM images of 35 CZTS nanocrystal coatings with (a,b) no added polystyrene added polystyrene masses of (c,d) 0.035 mg, (e,f) 0.070 mg, (g,h) 0.175 mg, and (i,j) 0.350 mg after annealing at 600 °C for 60 minutes with a sulfur pressure of 500 Torr (10 mg of sulfur powder loaded into the ampule).

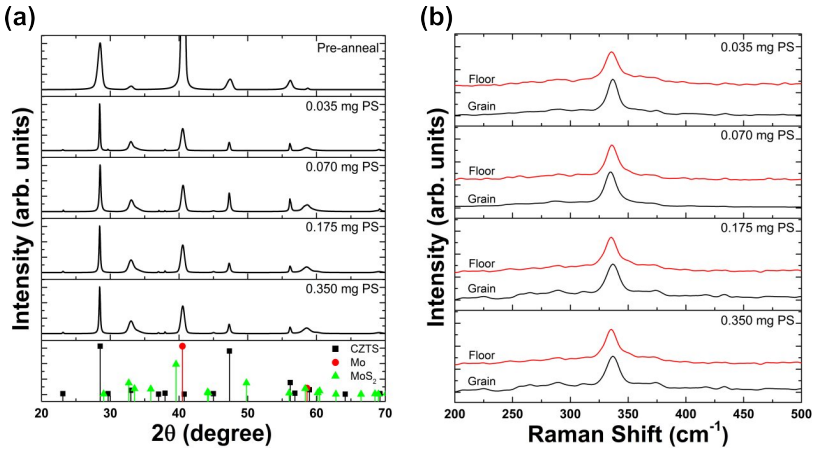

Figure 5.14 (a) XRD patterns and (b) Raman spectra of 35 nm CZTS nanocrystal coatings with varying amounts of polystyrene (PS) added to the dispersion after annealing for 60 minutes at 600 °C with a sulfur vapor pressure of 500 Torr. Labeled mass in figures is expected total PS mass added to coating.

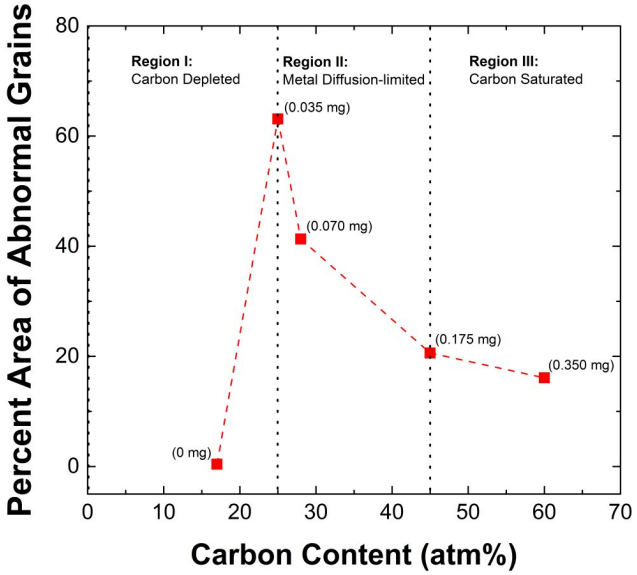

Figure 5.15 Fractional surface coverage of abnormal grains versus carbon concentration in coatings composed of 35 nm CZTS nanocrystals after annealing at 600 °C for 60 minutes in 500 Torr of sulfur. Varying amounts of polystyrene were added to the nanocrystal dispersions before coating to increase the carbon concentration in the coatings. The mass of polystyrene added to the coatings is indicated in parentheses beside each data point.

Chapter 6

Effect of NaOH on Microstructure Development During Annealing of Ultrasonic Spray Coated Copper Zinc Tin Sulfide Nanocrystals

6.1 Introduction

Formation of nanocrystal coatings for solar absorber layers has traditionally been conducted through processes that are difficult to scale directly to large production volumes such as dip-coating,[38,166] blade-coating,[30,68] drop-casting,[60,167] and spin-coating.[168,169] Work on spray coating of CZTS or other solar materials such as copper indium gallium diselenide (CIGS) nanocrystal dispersions have been reported.[72,107,170,171] In some cases, heated substrates or inert atmospheres have been necessary for successful coating formation and could possibly complicate process scale-up. Successful spray coating at ambient conditions without any additional drying steps may enable low-cost solution-processing for producing CZTS solar cells from nanocrystal dispersions.

Regardless of the method used to form the CZTS nanocrystal coatings, they must be annealed into dense large-grained films to achieve high solar cell efficiencies. This is tra-

ditionally accomplished in high temperature (> 550 °C) furnaces with an overpressure of S or Se. During this process, alkali-metals have been shown to enhance CZTS grain growth, film morphology, and electrical properties.[124,128,132,163,172] However, incorporation of these alkali metals (i.e. Na and K) and their beneficial effects are largely uncontrolled because their concentration in the CZTS films during and after annealing is determined by their diffusion rate from the soda lime glass (SLG) substrate into the CZTS film: this diffusion rate depends sensitively on the concentration of these impurities in the SLG substrate as well as the microstructure and therefore the sputtering conditions of the Mo electrode deposited on the SLG.[106,163]

To provide more consistent and reproducible results, various methods have been developed to deliberately and controllably incorporate alkali metals into the films during annealing.[124,132,173,174] Johnson *et al.* dried aqueous NaOH solutions at varying but controlled concentrations inside quartz tubes which were then used as annealing ampules during sulfidation of copper-zinc-tin metal alloy films to form CZTS.[124] It was found that Na from the walls of the ampules could be transported to the films via vapor during sulfidation and improved film morphology: specifically, they showed that the average grain size depended on the amount of NaOH added to the ampules and could be controllably tuned. This simple method provides control over the Na incorporation into the film and does not require pre-annealing processing of the CZTS precursor films. The effects of this process on the film microstructure development during annealing of CZTS nanocrystal coatings has not been fully investigated, but it has the potential to enhance grain growth rates and reduce required annealing times to achieve dense polycrystalline films.

Herein, we utilize ultrasonic spray coating to form CZTS nanocrystal coatings from nanocrystal dispersions in pure toluene and in a mixture of toluene and cyclohexanone (30 vol%), a cosolvent. Compared to the pure toluene dispersions, use of the cosolvent reduced the coating surface roughness and improved large-scale coating uniformity. The improvements in coating microstructure were linked to the effects of the cyclohexanone addition on both aerosol droplet evaporation rates and nanocrystal coating saturation during spray coating . In addition, we investigated the effect of NaOH incorporation and sulfur pressure on microstructure evolution during annealing of these ultrasonic spray-coated CZTS nano-

crystal coatings. Without Na addition, coatings formed from smaller nanocrystals (15 nm) formed large abnormal grains on top of the nanocrystal coating upon annealing in S, while no substantial grain growth was observed when the coating comprised larger nanocrystals (20 nm). When Na was added to the annealing ampoule, grain growth rates increased for both large and small nanocrystal coatings.

6.2 Experimental

6.2.1 Materials

Metal diethyldithiocarbamate (dedc) precursors used for synthesis of 15 nm and 20 nm CZTS nanocrystals were prepared following the procedure described by Chernomordik *et al.*[52] Oleic acid (technical grade, 90%), oleylamine (technical grade, 70%), and toluene (HPLC grade, 99%) were purchased from Sigma Aldrich. Cyclohexanone was purchased from Fisher Scientific (Certified ACS, 99.99%). Reagent alcohol (histological grade, 90% ethyl alcohol, 5% methyl alcohol, 5% butyl alcohol) and acetone (HPLC grade, 99.5%) were purchased from Fisher Scientific. Isopropyl alcohol (histological grade, 99.5%) was purchased from Macron Fine Chemicals. Molybdenum-coated soda lime glass (Mo-coated SLG) was purchased from DASSTECH.

6.2.2 Nanocrystal Synthesis

CZTS nanocrystals were synthesized as described by Chernomordik *et al.* with some modifications.[52] $Cu(dedc)_2$ (108 mg), $Zn(dedc)_2$ (54.0 mg), and $Sn(dedc)_4$ (106.8 mg) were dissolved in 10 ml of oleic acid within a 15 ml round bottom flask. Additionally, 20 ml of oleylamine was poured into two 100 ml round bottom flask (10 ml oleylamine each). The three round bottom flasks were attached to separate valves on a Schlenk line. The flasks were placed on heating mantles and fitted with thermocouples to allow temperature control. All flasks were heated to 60 °C and degassed to 50 Torr before being purged with pure nitrogen. The degas-purge cycle was repeated three times. The flasks remained under

nitrogen flow for the remainder of the reaction. The oleic acid-precursor solution was heated to 140 °C to ensure precursor dissolution. The two oleylamine flasks were heated to 290, 300, or 320 °C for synthesis of 10, 15, or 20 nm CZTS nanocrystals, respectively. When the oleylamine reached the desired reaction temperature, 5 ml of the oleic acid-precursor solution was injected into each of the oleylamine-containing flasks. The reacting solutions were kept at the injection temperature for 10 minutes. After 10 minutes, the heating mantles were removed from underneath the flasks and the solutions were allowed to cool to room temperature, which took approximately 15 minutes. The solutions were washed with three cycles of successive reagent alcohol dilution, sedimentation by centrifuge, and redispersion in toluene. After the final washing cycle, the nanocrystals were dispersed in 1 ml of toluene with 10^{-4} volume fraction oleic acid or a solution of 0.3 ml cyclohexanone and 0.7 ml of toluene containing 10^{-4} volume fraction of oleic acid. The dispersions were sonicated for 30 minutes prior to coating.

6.2.3 CZTS Nanocrystal Coating Formation

Ultrasonic spray coating was conducted with a 120 kHz Sono-tek Accumist spray nozzle set to constant power amplitude of 3.4 W. A schematic of the spray coating setup and parameter ranges are shown in Figure 6.1 along with a digital photograph of the coating apparatus ad was attached to a metal arm above a stationary coating stage. The nozzle was positioned such that the tip was 4 in above the substrate. The arm could be translated along the x-axis at a variable speed but this was maintained at 2.5 mm/s for this work. A syringe pump was used to transport the CZTS dispersion to the nozzle at a constant flow rate of 0.025 ml/min through 1.5 feet of Teflon tubing (0.038 in inner diameter). An in-house nitrogen gas line was attached to the nozzle to provide focusing flow at 4.5 psi.

During coating, the Mo-coated SLG substrates (6 mm $\times$ 10 mm) were aligned below the spray nozzle in a horizontal path. To begin coating, the syringe pump and translation motor were turned on and set to 0.025 ml/min and 0.1 in/s, respectively. The translation motor and syringe pump were stopped after the last substrate was coated. The nozzle was then returned back to the starting position. To produce thick coatings, multiple coating

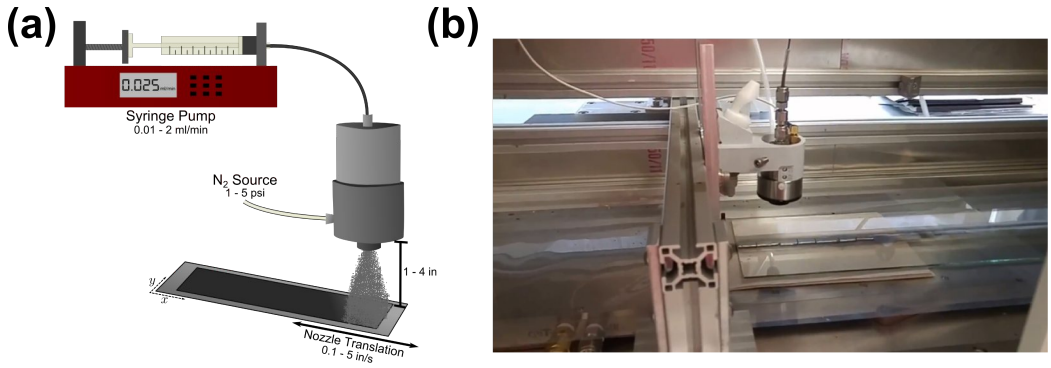

Figure 6.1 (a) Schematic illustration of ultrasonic spray coating setup and sample parameter ranges. (b) Photograph of ultrasonic spray coating apparatus used for CZTS nanocrystal coating creation.

passes were conducted. The period between coating passes was approximately 70 ± 10 – 15 seconds depending on the number of substrates coated in each pass.

6.2.4 Annealing of CZTS Nanocrystal Coatings

The annealing procedure for CZTS nanocrystal coatings has been described elsewhere.[60,107] Briefly, the CZTS nanocrystals coatings were placed in quartz tubes along with the desired mass of solid sulfur (3 to 6 mg depening on the desired sulfur pressure). The tubes were evacuated and flame-sealed to form annealing ampules. In initial experiments, ampules were placed into a preheated furnace at 600 °C.[60] Using this procedure, non-uniform films were produced, as shown in Figure 6.2, likely due to sulfur condensation on the nanocrystal coating during the fast temperature transient the tube experiences when placed into the hot furnace. This is similar to that observed by Chernomordik *et al.* during selenization of CZTS nanocrystal coatings.[175] An alternative heating procedure was developed to avoid sulfur condensation. The ampules were placed in the furnace at room temperature and the furnace was then heated slowly. Specifically, the temperature was ramped to 175 °C for 30 minutes,then to 275 °C for 30 minutes, and finally to 600 °C and held there for 1.25 hours. After, the furnace was turned off and allowed to cool naturally to room temperature with the furnace door closed.

In some cases, known concentration and volume of NaOH solution (and this known

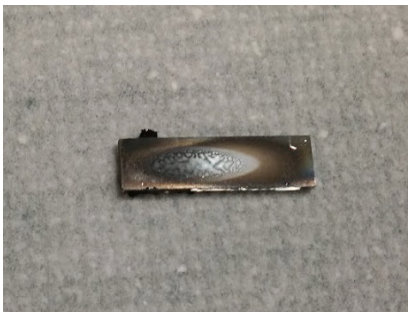

Figure 6.2 Photograph of CZTS nanocrystal coating after annealing using "hot-loading" method where furnace was preheated to 600 °C before inserting the annealing ampule with the coating. The plume region is likely caused by sulfur condensation on the thick Mo-coated SLG substrate due to uneven heating.

total moles) was dried in the ampules to coat the interior walls with NaOH before annealing. The procedure was modified from that reported by Johnson *et al.*[124] Aqueous NaOH solutions with varying molarities were deposited into quartz tubes. One milliliter of the desired solution was deposited into each tube. The total amount of NaOH added was either 0.1 or 1 μmol depending on the solution concentration. The tubes were dried in an oven at 115 °C for a minimum of 4 hours to ensure complete water evaporation. During drying the tubes were placed at a slight angle (~5°) from horizontal, as illustrated in Figure 6.3a. This resulted in a NaOH-rich region inside the tube covering approximately one-half of the tube circumference and extended approximately 1 in from the end of the 7' tube. After drying, the substrates with the CZTS coating were placed in the ampules (one per ampule) which were then sealed as described previously. For annealing, the coating on the substrate was oriented within the ampule such that the NaOH-rich area was situated directly above the nanocrystal coating, as illustrated in Figure S3b, to ensure consistent and reproducible Na exposure.

6.2.5 Characterization

Coatings produced *via* ultrasonic spray coating were imaged before and after annealing using a JEOL 6500 field-emission scanning electron microscope (SEM). The thickness

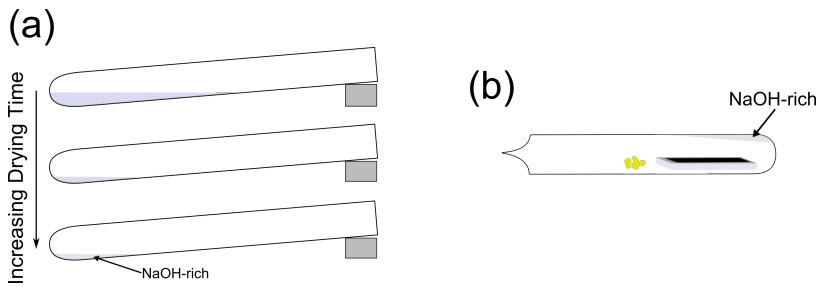

Figure 6.3 (a) Illustration showing process used to create NaOH coated tubes for annealing experiments. First, 1 ml of an aqueous NaOH solution is added to the tube with a total NaOH content of 0.1 or 1 µmol. After, the tube laid horizontally at a slight angle to concentrate the NaOH in the lower end of the ampule. (b) Illustration showing orientation of NaOH-rich region above CZTS nanocrystal coating as used during annealing.

of the coatings prior to annealing and the abnormal CZTS grain coverage area after annealing films were determined from SEM images using particle analysis functions of the ImageJ (NIH) image analysis software[176] obtained through the Fiji distribution.[177] A Thermo-Noran Vantage energy dispersive X-ray spectrometer was used to conduct energy dispersive X-ray spectroscopy (EDS) of the coatings and the annealed films. X-ray diffraction (XRD) was conducted on a Bruker D8 Discover system equipped with a Co Kα source and a VÅNTEC-500 2D area detector. The Co Kα XRD patterns were converted to Cu Kα patterns using the analysis software JADE (Materials Data Incorporated). A Witec Alpha300R confocal Raman microscope with a 532 nm wavelength excitation source was used for Raman spectroscopy. The microscope was connected to a DV401 CCD detector, and a UHTS300 spectrometer. Spectra were collected with an 1800 lines/mm grating that resulted in a spectral resolution of 0.02 cm^{-1}.

6.2.6 Simulation Setup for Droplet Evaporation

The evaporation of aerosol droplets was simulated using the model developed by Ravindran and Davis.[178] In this model, the CZTS nanocrystals and evaporative cooling effects were ignored and the droplets were assumed to be pure liquid at 293 K and 1 atm. Additionally, the solvent mixture is assumed to behave as an ideal solution and the mixture

within the droplets are assumed to be well-mixed at all times. The solvent concentration in the vapor phase outside of droplet is assumed to be dilute with diffusion acting as the sole transport mechanism. Under these assumptions, the change in size (radius, r) of an aerosol droplet with time (t) is given by

The change in size of an aerosol droplet at time t is given by

$$\frac{dU}{dt} = 2\left[\phi_{13} x_1 V_1 + \phi_{23}\left(1 - x_1\right) V_2\right] \tag{6.1}$$

where $U = \left(r/r_0\right)^2$, $\phi_{13} = \left(D_{13} p_1^0\right)/RT$, and $\phi_{23} = \left(D_{23} p_2^0\right)/RT$. In these expressions, r is the aerosol droplet diameter at time t, r_0 is the initial aerosol droplet radius, D_{i3} is the diffusion coefficient of species i (*e.g.*, $i = 1$ for toluene and $i = 2$ for cyclohexanone) with subscript 3 indicating air at standard temperature and pressure (STP), p_i^0 is the partial pressure of species i at STP, x_1 is the liquid molar fraction of toluene in the droplet, V_i is the molar volume of species i, R is the ideal gas constant, and T is the temperature. The liquid molar composition (x_1) inside of the aerosol droplet at time t is given by

$$\frac{dx_1}{dt} = \frac{3}{U}\left(\phi_{23} - \phi_{13}\right)\left[\left(V_1 - V_2\right) x_1 + V_2\right]\left(x_1 - x_1^2\right). \tag{6.2}$$

Pairing Equations 6.1 and 6.2 forms a pair of coupled nonlinear partial differential equations fully describing the droplet size and composition evolution with time. Equations 6.1 and 6.2 were solved using the ODE solver function ode45 included in Matlab (ver. 2014a). The initial droplet sizes at $t = 0$ were determined from measurements reported by the nozzle manufacturer using water as the atomization liquid. The droplet sizes were scaled to representative sizes for toluene and cyclohexanone using the property scaling of the capillary wave droplet size equation,[179]

$$\bar{D}_M = 0.34\left(\frac{\pi^3 \sigma}{\rho f^2}\right)^{\frac{1}{3}} \tag{6.3}$$

where σ is the liquid surface tension (28.52 and 34.4 mN/m for toluene and cyclohexanone, respectively), ρ is the liquid density (0.87 and 0.95 g/ml for toluene and cyclohexanone, respectively), and f is the atomization frequency (120 kHz). The ratio of toluene droplet radius and cyclohexanone droplet radius to water droplet, calculated using Equation 6.3, are 0.76 and 0.79, respectively. Although the physical liquid properties differ, the resulting predicted effects on aerosol droplet size are similar between toluene and cyclohexanone. For this reason, we assumed that toluene and mixtures of toluene and cyclohexanone form the same size droplets during ultrasonic atomization. The lognormal droplet size distribution produced by the 120 kHz spray nozzle with water is shown in Figure 6.4 as given by the nozzle manufacturer. The mean radius and standard deviation of the droplet distribution were calculated to be 12 μm and 8 μm, respectively. Accounting surface tension and density differences between water and toluene/cyclohexanone mixtures scales the expected mean droplet radius to 8 μm and standard deviation to 6 μm assuming that the geometric standard deviation remains constant from liquid to liquid. The calculated log-normal droplet size distribution for toluene is shown in Figure 6.4. For drying analysis, the drying time was calculated for droplet sizes at the distribution mean (8 μm) and one standard deviation above and below the mean (±3 μm). The vapor pressures of toluene and cyclohexanone were obtained from Besley *et al.*[180] and the NIOSH Pocket Guide to Chemical Hazards,[181] respectively. Diffusion coefficients for toluene and cyclohexanone were obtained from Erbil *et al.*[182] and Uchiyama *et al.*,[183] respectively.

6.3 Results and Discussion

6.3.1 Spray Coating of CZTS Nanocrystal Dispersions

Effect of Co-Dispersing Liquids on Coating Morphology

Figure 6.5 shows CZTS nanocrystal coatings produced *via* ultrasonic spray coating with three coating passes using 5 wt% 10 nm average diameter CZTS nanocrystals dispersed in (Figures 6.5a and 6.5c) toluene with oleic acid (10^{-4} volume fraction) and (Figures 6.5b

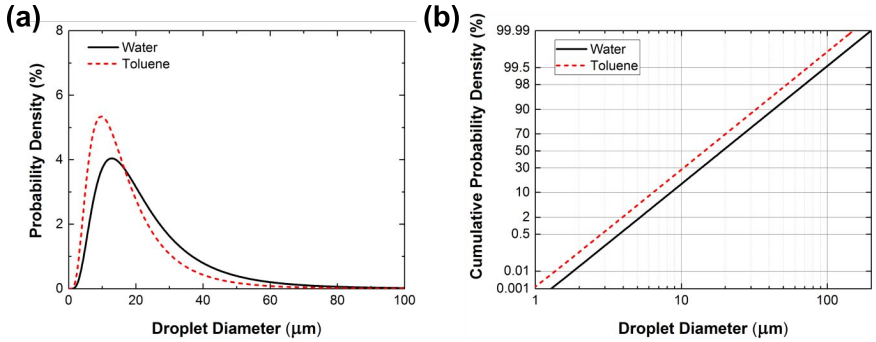

Figure 6.4 (a) Probability and (b) cumulative probability density plots for droplet sizes produced by ultrasonic spray coating nozzle with water and toluene.

and 6.5d) a solution of 30 vol% cyclohexanone and toluene with oleic acid (10^{-4} volume fraction). When pure toluene is used, large regions (> 10 μm diameter) of the coating are noticeably thinner than their surroundings (Figures 6.5a and 6.5c). Cross sectional images show a sharp variation in coating thickness in these regions decreasing from 2 μm to < 200 nm. These non-uniformities would be problematic for solar applications due to the likelihood of incomplete surface coverage after annealing which may end up in electrical short circuits. Dispersing the nanocrystals in a solution of 30 vol% cyclohexanone in toluene with the same CZTS nanocrystal loading improves the coating uniformity significantly (Figure 6.5b and 6.5d). No large non-uniformities are visible in the planar SEM image. More significantly, cross-sectional images reveal a more uniform coating thickness (varying from 800 nm to 1.2 μm) compared to coatings formed from pure toluene dispersions.

The improvement in coating uniformity with the addition of cyclohexanone is substantial and we attribute this to the lowering of the evaporation rate during the droplet's flight from the nozzle where it is generated to the substrate. Indeed, previous research has shown that the liquid content of the aerosol droplets at the moment they impinge on the substrate is a significant factor in determining coating morphology during aerosol-based coating operations like aerosol jet printing and spray deposition.[107,152] Aerosol evaporation and transport is difficult to study systematically during ultrasonic spray coating because aerosol generation, evaporation and deposition are coupled and occur simultaneously on similar time scales. Independent manipulation of the evaporation rate using coating variables such as

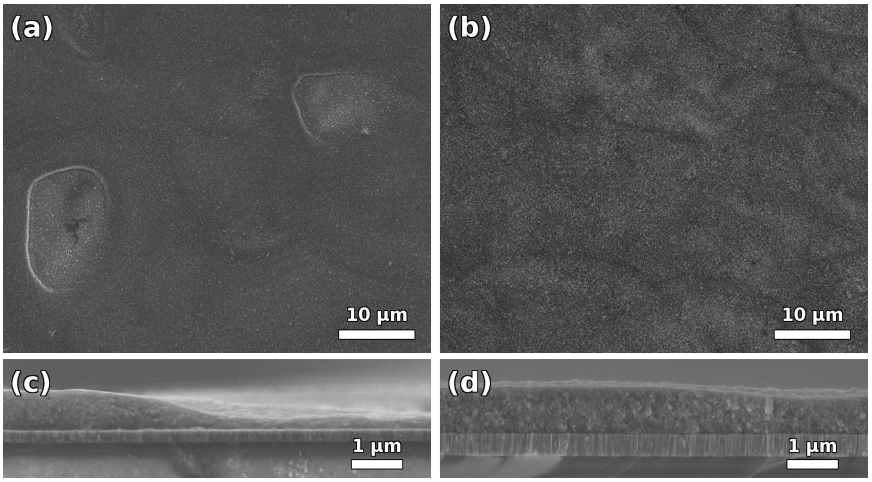

Figure 6.5 SEM images of CZTS nanocrystal coatings formed by ultrasonic spray coating using 3 passes at a stage speed of 0.1 in/s and liquid flow rate of 0.025 ml/min from 5 wt% nanocrystals dispersed in (a,c) pure toluene and (b,d) 70 vol% toluene/30 vol% cyclohexanone.

air and liquid flow rates is not possible because of their simultaneous effects on atomization, aerosol focusing, coating width, and liquid content. Rather than manipulating coating parameters to tune coating morphology, changing the dispersion liquid composition allows for tuning of aerosol droplet evaporation rates without requiring changes to the ultrasonic spray coating parameters. Including cyclohexanone in the dispersing liquid, a less volatile solvent than toluene, reduces droplet evaporation rate and results in aerosol droplets with higher liquid content. This in turn improves the uniformity.

The distribution of droplet sizes produced by the spray nozzle is a critical factor in determining the aerosol droplet liquid content upon impingement. The aerosol droplets undergo continuous evaporation from their surfaces while they traverse the 4 cm distance from nozzle to the substrate. The evaporation rate increases with decreasing droplet size in accordance with the Kelvin equation. If there is a wide droplet size distribution, the droplets may arrive at the substrate with significantly different liquid content and form coating non-uniformities like those seen in Figures 6.5a and 6.5c. From the droplet distributions shown in Figure 6.4, the expected toluene droplet distribution is quite wide. Approximately 10% of the droplets are smaller than 6.5 µm while another 10% are bigger than 30 µm. The

evaporation rates experienced by these droplets varies substantially. Since the liquid content at the time of impingement is the critical factor in coating formation, it is important to analyze the effects on drying dynamics imparted by changes to the dispersing liquid.

A simplified evaporation model using liquid-only aerosol droplets was utilized to help describe the mechanism behind the morphological differences observed in 6.5. Figure 6.6 shows the change in the normalized aerosol droplet radius ($(r/r_0)^2$) as a function of drying time for pure toluene droplets and binary liquid droplets comprising cyclohexanone (30 vol%) and toluene. The plot depicts the evaporation of droplet with mean radius ($\bar{r}_{0,M} = 8$ µm) as a function of time. The plot also shows the same for droplet sizes up to 3 µm (1/2 of the standard deviation) above and below the mean radius.

A toluene droplet with mean size evaporates completely within 0.03 s. At this point in time, the droplets that started their flight with diameters one standard deviation above the mean still have radii approximately 77% of their initial value [$(r/r_0)^2 \approxeq 0.6$ from Figure 6.6], indicating a significant variation in the liquid content of droplets with CZTS nanocrystals at this end of the distribution. With 30 vol% cyclohexanone, the drying time for the mean initial diameter is tripled to 0.09 s. The cyclohexanone-toluene droplets that started their flight with diameters one standard deviation above the mean distribution would have radii approximately 54% of their initial value [$(r/r_0)^2 \approxeq 0.3$ from Figure 6.6]. If these droplets contained nanocrystals this reduction in size would mean less liquid content when they strike the substrate surface compared to the liquid content of aeresols created with toluene only.

The insights provided by Figure 6.6 and discussion above suggests a mechanism for the coating thickness non-uniformities shown in Figure 6.5. When dispersions are in toluene, the majority of the liquid in the aerosol droplets evaporates rapidly and consequently, they reach at the substrate with low liquid content. However, the droplet size distribution is wide and the larger droplets are slow to evaporate compared to the mean sized droplets. These larger droplets contain enough liquid, upon impinging the substrate, that they redisperse the already deposited nanocrystals leading to the formation of a liquid depression. These regions then dry to form the thin, non-uniform circular regions observed in Figures 6.5a and 6.5c. The reason for the thickness non-uniformities is the wide distribution of the liq-

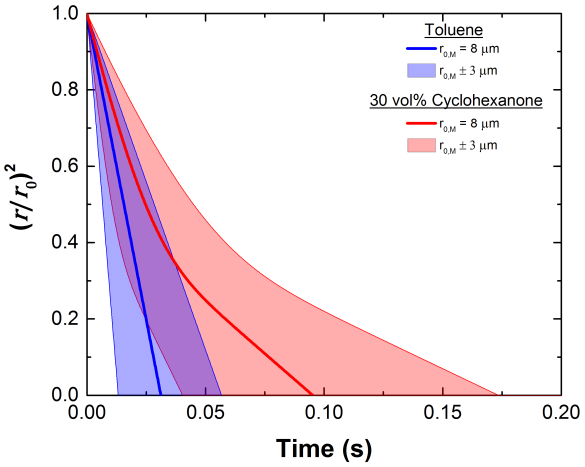

Figure 6.6 Plot of the normalized aerosol droplet radius as a function of time for pure toluene droplets, depicted in blue, and for a binary liquid droplets comprising cyclohexanone (30 vol%) and toluene, depicted in red. For both liquids, the temporal evolution of the mean droplet size during drying is represented by the solid line. In both cases, the mean initial droplet radius is 8 µm. The shaded regions depict drying of aerosol droplets with initial radius of 8 µm ± 3 µm.

uid fraction of the aerosol droplets. The evaporation rate decreases with the addition of cyclohexanone to the dispersion. Cyclohexanone is less volatile than toluene: their normal boiling points are 155 °C and 110 °C, respectively. The lower volatility of cyclohexanone results in a more uniform liquid content of the droplets across the entire size distribution. This reduces the tendency for the formation of the valleys observed in coatings formed from dispersions in toluene alone. The resulting film is smoother and more uniform. Bose *et al.*[184] found similar effects during ultrasonic spray coating of films from polymer solutions: more uniform polymer film formed when cyclohexanone was used as the solvent compared to toluene. The surface tensions of cyclohexanone and toluene are similar Consequently, we conclude that the droplet evaporation rate differences between toluene and cyclohexanone and toluene mixtures is the key factor that determines the differences in coating morphology and uniformity. In both the polymer solutions and nanoparticle dispersions, the liquid content of the impinging droplets is a critical factor in the formation of a uniform coating.

Addition of less volatile cyclohexanone also increases the saturation state of the nanocrystal coating after deposition, which should also help improve thickness uniformity while

reducing the cratering displayed in Figure 1. There is evidence in literature that cratering is reduced in granular beds when the granular bed is slightly wet. For example, Zhang *et al.*[185] analyzed the formation of impact craters formed by oil droplets impinging on a wet granular bed of soda-lime glass beads (90 μm diameter) at different saturation levels. They reported a decrease in crater size and depth as the granular bed was slightly saturated compared to a dry granular bed. Although difficult to measure, we expect the coatings formed from nanocrystals carried in cyclohexanone/toluene droplets to have a higher saturation than coatings formed from nanocrystals carried in toluene droplets. The increased saturation may aid in reduction of impact craters and surface non-uniformities observed in Figure 6.5.

Tuning CZTS Nanocrystal Coating Thickness

Figure 6.7a-c shows cross-sectional SEM images of CZTS nanocrystal coatings formed by ultrasonic spraying using 3, 6, and 9 coating passes. The coating thickness increases from 2.1 μm to 3.6 μm and to 4.4 μm for the 3-, 6-, and 9-pass coatings, respectively (Figure 6.7d). As expected, the coating thickness increases with the number of coating layers, but the average thickness deposited per pass appear to decrease as more layers are applied to the coating. The decrease in average layer thickness is surprising since the liquid flow rate and the flux of CZTS nanocrystals impinging on the substrate are expected to remain from pass to pass. This apparent decrease in average thickness deposited per pass may be due to increased densification during subsequent coating passes or due to variations in the dispersion flow rate supplied by the syringe pump.

6.3.2 The Effects of Na Addition and Sulfur Pressure During Annealing

Successful coating formation is just one step required to form a CZTS solar absorber layer. A dense polycrystalline film is required to create high efficiency solar cells. CZTS nanocrystal coatings may be converted into these polycrystalline films through high temperature annealing in the presence of S or Se vapor. To achieve a large scale roll-to-roll CZTS absorber layer production platform annealing must be conducted quickly and con-

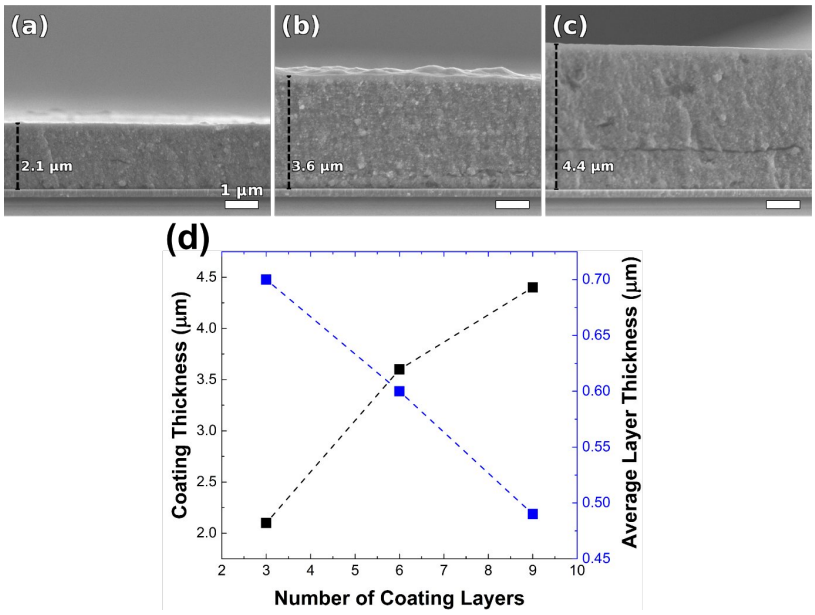

Figure 6.7 SEM images of CZTS nanocrystal coatings formed by ultrasonic spray coating from a 10 wt% CZTS nanocrystal dispersion using (a) 3, (b) 6, and (c) 9 coating passes. Coatings were conducted using standard coating parameters. (d) Plot of total coating thickness and average coating layer thickness (*i.e.*, thickness of each individual coating pass averaged over all coating passes) plotted against the number of coating layers, or passes.

sistently. To this end, we investigated the effect of NaOH exposure and sulfur pressure on microstructure development during annealing of CZTS nanocrystal coatings formed by ultrasonic spray-coating.

Figure 6.8 shows a matrix of SEM images of coatings spray deposited from dispersions of 15 nm CZTS nanocrystal after they were annealed at 600 °C for 1.25 hours with 3 mg (150 Torr), 4.5 mg (225 Torr), and 6 mg (300 Torr), sulfur (columns of SEMs in Figure 6.8) with no NaOH, 0.1 µmol NaOH, and 1 µmol NaOH added to the annealing ampule (rows of SEMs in Figure 6.8). Cross-sectional images, Raman spectra, and XRD patterns of the annealed coatings are shown in Figures 6.9, 6.10a-c, and 6.10d-f, respectively. Prior to annealing, the CZTS nanocrystals had an average nanocrystal size of 15 nm as determined by Scherrer's equation from the FWHM of the (112) XRD peak at 2□=28.5°. All coatings undergo abnormal grain growth with large CZTS grains forming on top of the CZTS

nanocrystal coating as observed in previous reports.[60,69,107,165] Recently, we have shown that abnormal grain growth is promoted by high carbon concentration inherent in coatings comprised of smaller (< 25 nm) CZTS nanocrystals: these small nanocrystals have high surface area and proportionately more ligands are trapped in the coatings as compared to larger nanocrystals (see Chapter 5).

The film area covered by abnormal grains after annealing is affected by both sulfur pressure and NaOH amount. Figure 6.11 shows the abnormal grain coverage versus sulfur pressure for different amounts of NaOH added to the ampule during annealing. With no NaOH addition and a sulfur pressure of 150 Torr, large (~2 μm in diameter) isolated abnormal CZTS grains grow on top of the CZTS nanocrystal coating layer and cover 36% of the film. The abnormal grain aerial coverage increases to 75% and 92% when the sulfur pressure is increased to 225 and 300 Torr, respectively. At highest sulfur pressures, the abnormal grains are no longer isolated and grain boundaries begin to form between most of the neighboring grains though some gaps still remain between these polycrystalline islands. With the addition of 0.1 μmol and 1 μmol of NaOH to the ampule, the growth rate of abnormal grains and the rate of consumption of the fine grain layer are significantly increased compared to the coatings annealed without NaOH. Additionally, with the addition of NaOH to the annealing ampules planar growth is enhanced at all sulfur pressures. The aerial coverage of abnormal grains approaches 100% (Figure 6.11) of the coating area even at the lowest sulfur pressure of 150 Torr for both NaOH amounts.

For 15 nm CZTS nanocrystal coatings annealed with NaOH, the sulfur pressure has little effect on the film morphology or abnormal grain area coverage in the range 150 to 300 Torr. The grain growth enhancement due to NaOH addition eclipses the effects of sulfur pressure on the grain growth and the film morphology. This is clearly the case for one hour of annealing but it is possible that differences in microstructure development due to sulfur pressure could be observed at shorter annealing times. Nevertheless, the addition of 0.1-1 μmol of NaOH to the ampule converts the CZTS nanocrystal coatings into continuous polycrystalline films.

In some of the cross-sectional SEM images a thin fine-grain layer is visible underneath the abnormal grains (Figure 6.9). EDS analysis of this fine-grain layer in films annealed in

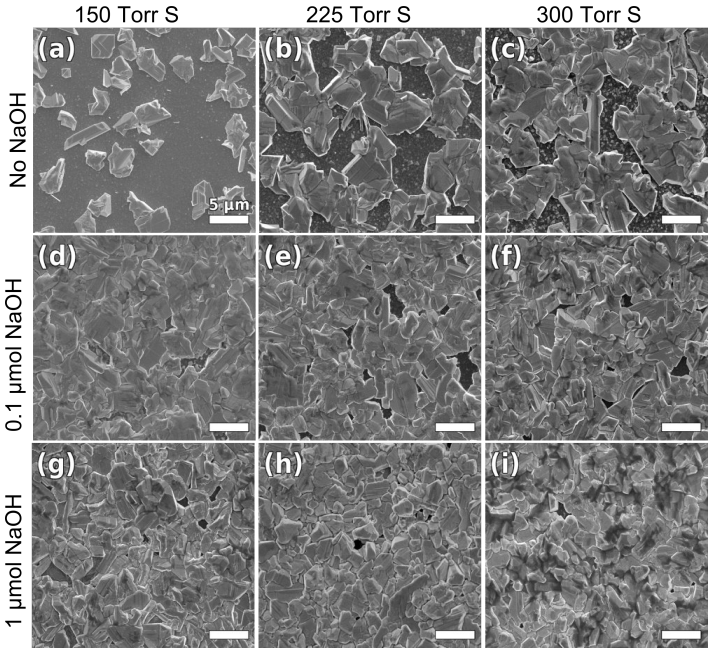

Figure 6.8 Plan view SEM images of coatings comprised of 15 nm CZTS nanocrystals after annealing at 600 °C for 1.25 hours with (a-c) no NaOH,(d-f) 0.1 µmol, and (g-i) 1 µmol NaOH, coated on the quartz tube at sulfur pressures of (a, d, g) 150 Torr, (b, e, h) 225 Torr, and (c, f, j) 300 Torr corresponding to 3, 4.5, and 6 mg of solid sulfur loaded into the ampule, respectively.

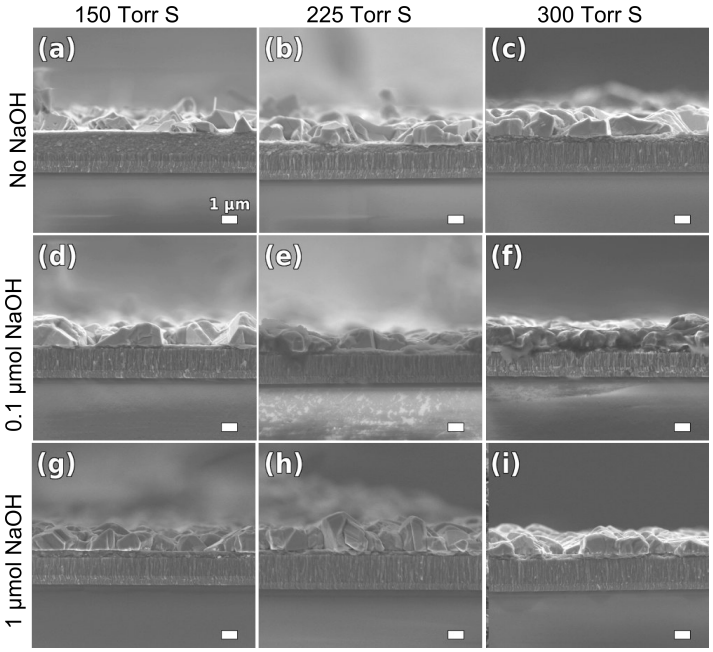

Figure 6.9 Cross-sectional SEM images of 15 nm CZTS nanocrystal coatings after annealing at 600 °C for 1.25 hours with (a-c) no NaOH,(d-f) 0.1 µmol, and (g-i) 1 µmol NaOH, coated on the quartz tube at sulfur pressures of (a, d, g) 150 Torr, (b, e, h) 225 Torr, and (c, f, j) 300 Torr corresponding to 3, 4.5, and 6 mg of solid sulfur loaded into the ampule, respectively.

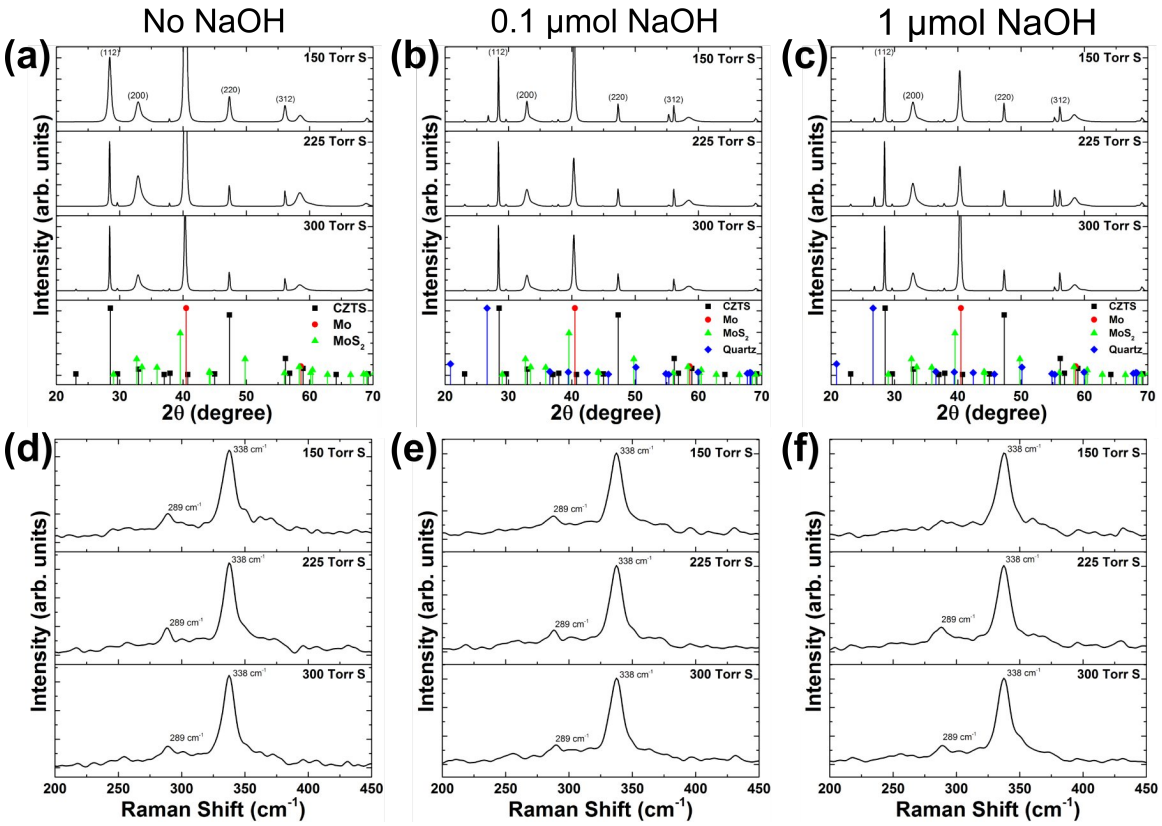

Figure 6.10 (a-c) XRD patterns and (d-f) Raman spectra of 15 nm CZTS nanocrystal coatings annealed at 150, 225, and 300 Torr of sulfur with no added NaOH, 0.1 µmol NaOH, and 1 µmol NaOH, corresponding to films shown in Figures 6.8 and 6.9

300 Torr sulfur and without NaOH (Figure 6.9c). showed that this layer is contains ~30 at% carbon and ~44 at% S (we caution that Mo peak interferes with S). The Cu, Zn, and Sn concentrations in this layer are 12, 7, and 7 at%, respectively. The ratios of these concentrations approximately match to the expected stoichiometry of CZTS though the fine grain layer is somewhat Cu-poor while the large grains are stoichiometric. The fine-grain layer thickness of approximately 200 – 300 nm in these films is similar to that seen in CZTSSe films formed by selenization of CZTS nanocrystal coatings[30] and in other sulfidation work.[165] in films annealed with NaOH the fine grain layer is completely covered with abnormal grains and could not be analyzed by EDS.

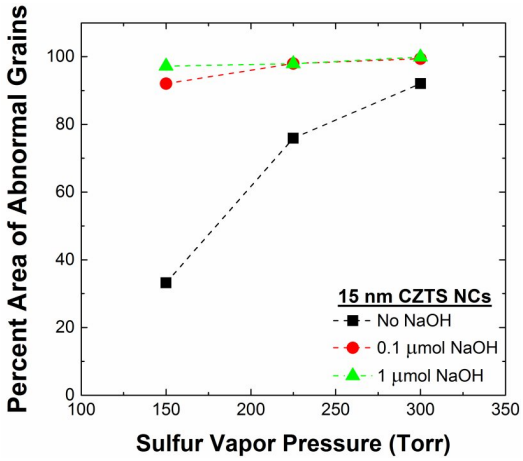

Figure 6.11 Plot of abnormal grain coverage percent for coatings annealed with no NaOH, 0.1 µmol NaOH, and 1 µmol NaOH for 15 nm CZTS nanocrystal coatings annealed at sulfur pressures of 150, 225, and 300 Torr.

Figure 6.12 shows plan view SEM images of coatings comprised of 20 nm CZTS nanocrystals after they were annealed at 600 °C for 1.25 hr with 3 mg, (150 Torr) 4.5 mg (225 Torr), and 6 mg (300 Torr) sulfur (columns of SEMs in Figure 6.12) with no NaOH, 0.1 µmol NaOH, and 1 µmol NaOH added to the annealing ampule (rows of SEMs in Figure 6.12). Cross-sectional images, Raman spectra, and XRD patterns of the coatings are shown in Figures 6.13, 6.14a-c, and 6.14d-f, respectively. There is no discernible grain growth at any sulfur pressure without added NaOH (Figure 6.12a-c). This is expected since previous work found higher sulfur pressures (~500 Torr) were required to induce grain growth when coatings are composed of large (> 20 nm) CZTS nanocrystals with a low concentrations of alkali metals present during growth.[60] In this case, it is likely that the relatively thick (~ 1 µm) Mo layer prevents significant diffusion of Na, resulting in negligible grain growth.

When NaOH is added to the annealing ampule, abnormal grains grow on the surface of the nanocrystal coatings at all sulfur pressures. Figure 6.15 shows abnormal grain coverage versus sulfur pressure after 20 nm CZTS nanocrystal coatings are annealed at 600 °C for one hour with 0.1 and 1 µmol of NaOH present in the ampule. The trend in abnormal grain coverage with sulfur pressure is similar for both NaOH amounts but the abnormal grain

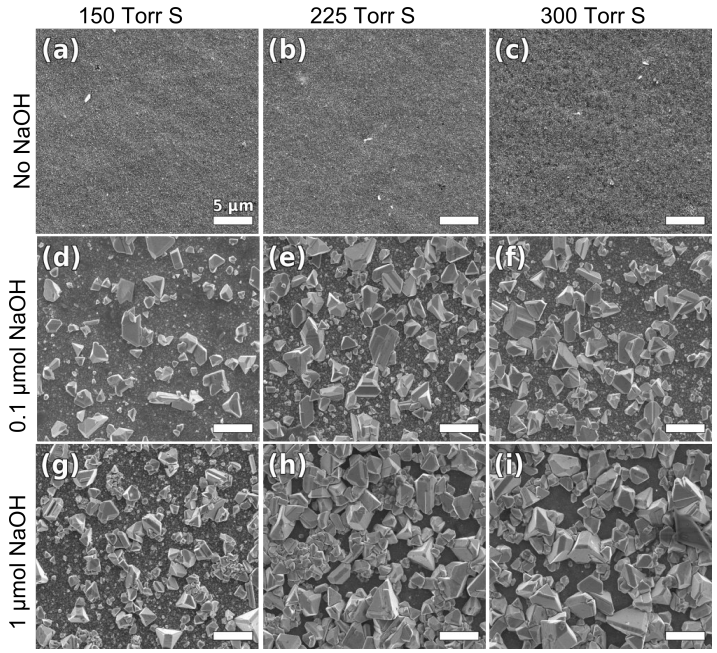

Figure 6.12 Plan view SEM images of coatings comprised of 20 nm CZTS nanocrystals after annealing at 600 °C for 1.25 hours with (a-c) no NaOH,(d-f) 0.1 µmol, and (g-i) 1 µmol NaOH, coated on the quartz tube at sulfur pressures of (a, d, g) 150 Torr, (b, e, h) 225 Torr, and (c, f, j) 300 Torr corresponding to 3, 4.5, and 6 mg of solid sulfur loaded into the ampule, respectively.

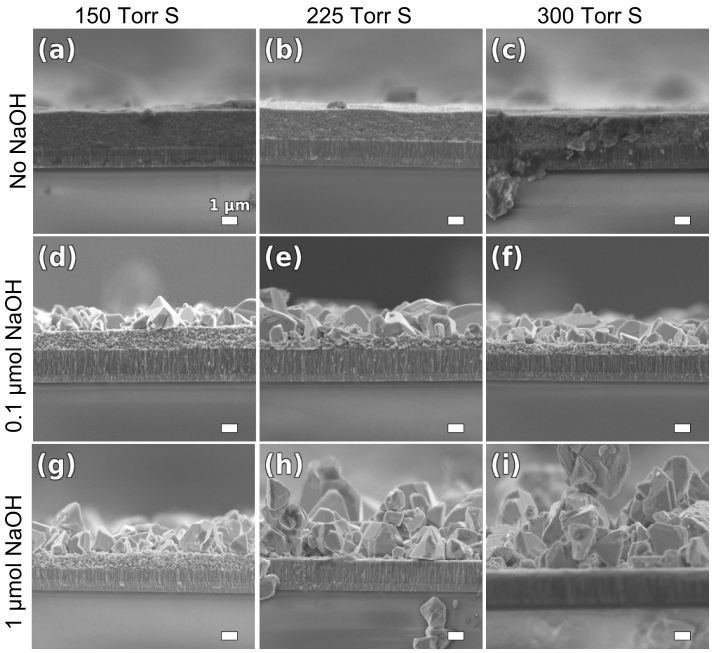

Figure 6.13 Cross-sectional SEM images of 20 nm CZTS nanocrystal coatings after annealing at 600 °C for 1.25 hours with (a-c) no NaOH,(d-f) 0.1 µmol, and (g-i) 1 µmol NaOH, coated on the quartz tube at sulfur pressures of (a, d, g) 150 Torr, (b, e, h) 225 Torr, and (c, f, j) 300 Torr corresponding to 3, 4.5, and 6 mg of solid sulfur loaded into the ampule, respectively.

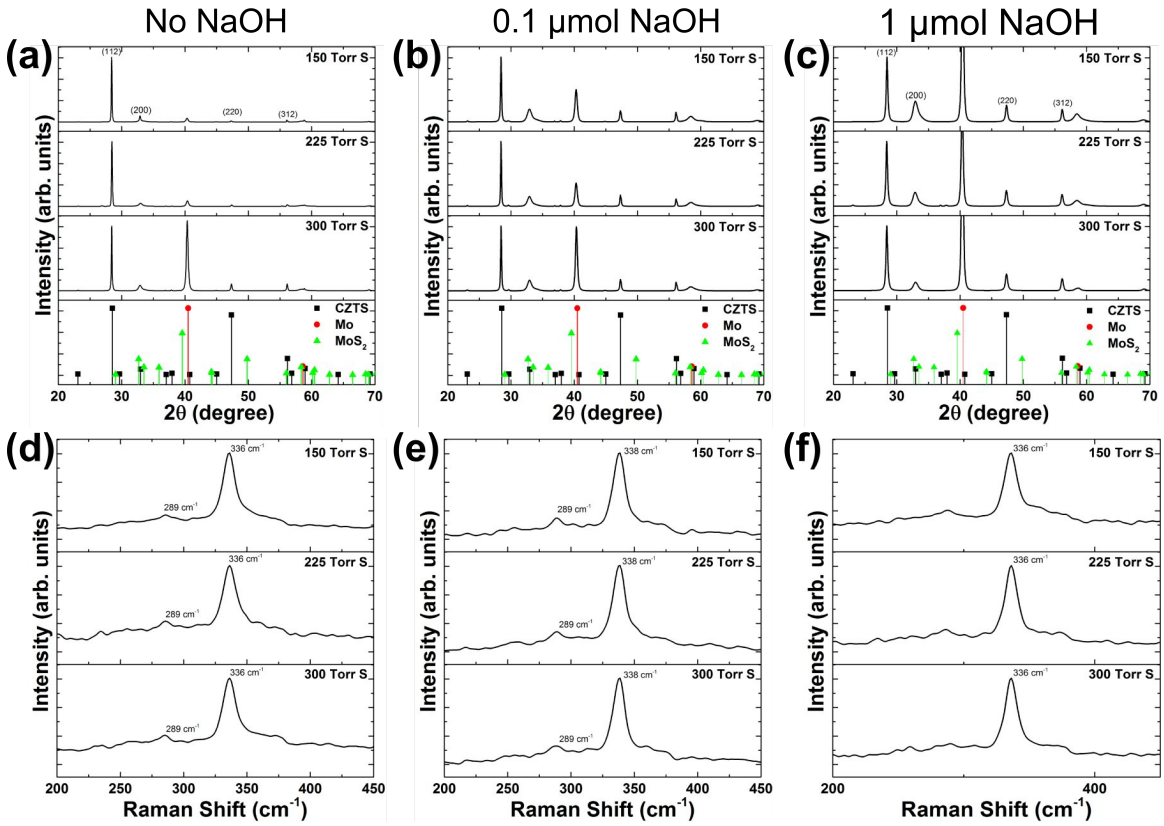

Figure 6.14 (a-c) XRD patterns and (d-f) Raman spectra of 20 nm CZTS nanocrystal coatings annealed at 150, 225, and 300 Torr of sulfur with no added NaOH, 0.1 µmol NaOH, and 1 µmol NaOH, corresponding to films shown in Figures 6.12 and 6.13

coverage with 1 µmol of NaOH is higher at all sulfur pressures. At a sulfur pressure of 150 Torr, abnormal grains grow above the nanocrystal coating resulting in 46% and 58% coverage with 0.1 and 1 µmol of NaOH, respectively. Increasing the sulfur pressure to 225 Torr leads to an increase of approximately ~30% higher abnormal grain coverage at both NaOH levels. At the highest sulfur pressure of 300 Torr, the abnormal grain coverage for the two Na levels converge to ~80%. The cross-sectional SEM of the film annealed with 1 µmol of NaOH (Figure 6.13) show that the abnormal grains have completely consumed the underlying nanocrystal coating. EDS of the gaps between abnormal grains of the films in Figure 6.12i indicates these regions are composed entirely of Mo or S with no evidence

of residual coating. With 0.1 μmol of NaOH, the fine grain layer is preserved through all sulfur pressures.

There are a number of differences between the films produced by annealing coatings comprised of 15 and 20 nm CZTS nanocrystals (Figures 6.8 and 6.12, respectively). When no NaOH is added to the ampule during annealing, the coatings comprised of 15 nm CZTS nanocrystals (Figure 6.8a,d) exhibited abnormal grain growth while the 20 nm CZTS crystals show no growth. Due to the similarity with the alkali-metal free sulfidation results reported by Chernomordik *et al.*,[60] it is assumed that the Mo-coated SLG substrates used here impart little to no alkali metals to the CZTS layer. This distinct change is related to the decrease in abnormal grain driving force due to the decreased carbon content in the 20 nm CZTS nanocrystal coatings (see Chapter 5). Additionally, normal grain growth may be occurring in these films but at a slow rate due to the low sulfur pressure which has been found to greatly influence normal grain growth rates (see Chapter 5).

When the coatings are annealed with 0.1 or 1 μmol of NaOH coated on the ampule (15 nm - Figure 6.8c-d; 20 nm - Figure 6.12c-d), bilayer films with abnormal grains growing above the original nanocrystal coating with both nanocrystal sizes. However, the rate of growth and grain sizes are larger with 15 nm CZTS nanocrystal coatings. The additional Na supplied through the gas phase, likely in the form of NaS_2,[124] provides an additional abnormal grain driving force. It is clear that the 15 nm CZTS nanocrystal coatings respond more effectively to NaOH addition and form films more suitable for solar cell development than those formed from 20 nm CZTS nanocrystal coatings.

6.4 Conclusion

Ultrasonic spray coating was used to form CZTS nanocrystal coatings from pure toluene and a solution of toluene with cyclohexanone (30 vol%) dispersions containing 10 nm CZTS nanocrystals. It was found that coatings spray coated from the pure toluene dispersions had regular surface non-uniformities (*i.e.*, large ~10 μm craters) that disappeared when cyclohexanone was added to the dispersion. A model for pure liquid droplet evaporation was

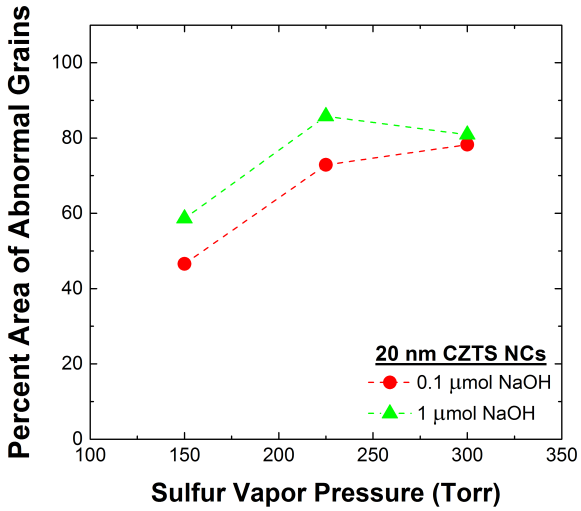

Figure 6.15 Abnormal grain coverage (% area) as a function of sulfur pressure for coatings annealed with no NaOH, 0.1 µmol NaOH, and 1 µmol NaOH. The initial coatings were comprised of 20 nm CZTS nanocrystals.

developed to analyze the effects of cyclohexanone addition on droplet liquid content. Cyclohexanone addition extended droplet drying time and resulted in a more uniform liquid content across the droplet size distribution which would likely help to prevent non-uniformities. Additionally, the lower volatility cyclohexanone may aid in reducing crater size by increasing the amount of residual liquid within the coating.

These optimized spray coating conditions were used to form coatings from 15 and 20 nm CZTS nanocrystal dispersions on Mo-coated SLG substrates. The effects of NaOH addition to the annealing ampules used during high temperature annealing of the coatings was investigated. The coatings were annealed at 600 °C with no added NaOH and with 0.1 and 1 µmol of NaOH added to the annealing ampule in sulfur pressures of 150, 225, and 300 Torr. When annealed with no NaOH, 15 nm CZTS nanocrystals coatings developed large, abnormal CZTS grains on their surfaces that increased in size with sulfur pressure. The growth was enhanced with both 0.1 and 1 µmol of NaOH added to the annealing ampules with the abnormal grains covering 100% of the coating area. No substantial difference in morphology was observed between coatings annealed at different sulfur pressures probably

due to the overshadowing effects of the NaOH addition. On the other hand, 20 nm CZTS nanocrystal coatings showed no significant signs of growth with no NaOH, likely due to a higher carbon content that acts to prevent grain growth. When 20 nm CZTS nanocrystals were annealed with NaOH exposure, abnormal grain growth was observed and increased with increasing sulfur pressure. With 1 μmol of NaOH and a sulfur pressure of 300 Torr, the 20 nm nanocrystal coating was converted completely into a large grain film but only reached ~80% area coverage. It was concluded that NaOH acts to enhance the rate of abnormal grain growth in both 15 and 20 nm nanocrystal coatings. With 15 nm nanocrystals, the enhanced growth produces a dense, continuous polycrystalline film suitable for solar device development.

Chapter 7

Intense Pulsed Light Annealing of CZTS Nanocrystal Coatings

7.1 Introduction

A variety of methods have been used to form precursor CZTS coatings that are subsequently annealed to make CZTSSe absorber layers: these methods include physical vapor deposition,[106,186] chemical vapor deposition,[187] electro-deposition,[188] and coatings cast from molecular precursor inks[29,189] and nanocrystal dispersions.[30,60] All these methods require post-deposition annealing at 500 - 600 °C to form large-grained (1 to 3 μm) polycrystalline CZTSSe films, which have been shown to lead to high efficiency solar cells. High temperature (> 500 °C) furnaces are commonly used for annealing with films isolated in graphite boxes or glass ampules in a sulfur or selenium containing atmosphere for durations ranging from 15 minutes to several hours.[30,60,190] At the laboratory scale, these annealing procedures provide precise control of temperatures and atmospheric conditions. However, furnace annealing is not ideal at large production volumes due to long annealing times and difficulties that arise when adapting to continuous roll-to-roll production.

Two alternative methods, rapid thermal annealing (RTA)[191,192] and intense pulsed light (IPL) annealing,[193] have been proposed and explored to anneal CZTSSe and other thin film solar cell absorber layers. A typical RTA system employs halogen lamps to rapidly heat the

absorber layer at with rates up to 10 °C/s,[191] decreasing the total heating time and the amount of energy used compared to annealing in resistively-heated furnaces. Heating during RTA is non-selective; that is the absorber layer, the substrate, and anything in thermal contact with the substrate are all heated. Because of this, achieving high heating rates requires small volumes which limits the use of RTA at large production scales, although roll-to-roll compatible RTA equipment with processing speeds approaching 4 cm/min have been reported for sintering silver nanoparticles.[194]

Intense pulsed light (IPL), also known as photonic sintering, is a selective heating process wherein a high intensity broadband xenon flash lamp is used to heat materials that absorb radiation emitted by the lamp. Since the emission spectrum of the xenon flash lamp covers ultraviolet to near-infrared a long list of films absorbing in this region can be heated selectively when deposited on transparent substrates. Selectivity can also be achieved on opaque substrates when the film is optically thick and absorbs most of the light emitted by the lamp before it reaches the substrate. Selective heating with IPL has been used to successfully anneal and sinter printed silver lines on thermally sensitive materials without substrate damage.[194,195] IPL has also been used for annealing thin films of cadmium sulfide (CdS)[196] and CZTS[193] in solar cells, as well as CdS,[197] cadmium telluride,[198] and copper indium gallium diselenide[199,200] coatings. The spatiotemporal variation of temperature during IPL annealing of solar absorber layers has been reported in some of these cases[196] but the effect of various IPL and coating parameters on temperature development remains understudied.

Herein, we investigated the effects of flash energy density (3.9 to 11.6 J/cm^2) and number of flashes (1 - 400) on the morphology and chemical composition of thin films formed by intense pulsed light annealing of CZTS nanocrystal coatings on three different types of substrates: molybdenum-coated soda lime glass (Mo-coated SLG), quartz, and molybdenum foil (Mo foil). The experimental variations of the film morphology and composition as a function of the IPL parameters were understood by visualizing the spatial and temporal variation of the coating and substrate temperatures with the aid of a two-dimensional heat transport model. Based on experiments and simulations we set conditions for limiting coating microstructure damage and decomposition during IPL annealing of CZTS nanocrystal coatings.

7.2 Experimental details

7.2.1 Synthesis of CZTS Nanocrystals

CZTS nanocrystals were synthesized as described in Section 5.2.2 and were 35 nm in diameter as determined from the width of the (112) x-ray diffraction peak of kesterite CZTS using Scherrer's equation. The nanocrystals were dispersed in a solution of toluene and oleic acid (10^{-4} volume fraction) to form ~30 mg/ml CZTS nanocrystal dispersions.

7.2.2 Preparation of CZTS Nanocrystal Coatings

Substrates were molybdenum-coated soda lime glass (SLG) (2×0.1 cm, Valley Design Corp.), polished quartz ($2 \times 2 \times 0.15$ cm, GM Associates), or molybdenum foil ($1 \times 2.8 \times 0.05$ cm, Goodfellow). The Mo-coated SLG substrates were made by DC sputtering 400 nm thick molybdenum onto SLG from a Mo target (99.95%) in a flow of 20 sccm argon. The Mo film consisted of 250 nm and 150 nm top and bottom layers deposited at 2 mTorr and 5 mTorr sputter pressure, respectively.

Prior to use, all substrates were cleaned by ultrasonication first in isopropyl alcohol (histological grade, Macron) and then acetone (HPLC grade, Fisher Scientific) for 10 minutes each before drying under flowing nitrogen. CZTS nanocrystal coating was drop-cast into a 250 μm deep well with an interior area of 160 mm^2 formed by placing a 250 μm thick stainless steel frame in the center of the substrate. The frame was attached to the substrate with binder clips.[60] The CZTS nanocrystal dispersion (70 μL, 30 mg/ml) was dispensed into this shallow well with a pipette and allowed to spread, filling the coating area. The entire substrate was covered by a funnel to slow the evaporation rate, and the wet coatings were allowed to dry for approximately 4 hours. After drying, the coatings were fractured into three equal sections for annealing under different conditions. This procedure was used for Mo-coated SLG and quartz substrates. Figure 7.1 shows SEM images of a typical CZTS nanocrystal coating formed *via* dropcasting in this manner. Nanocrystal coatings on Mo foils were produced in a similar manner but the stainless steel frame was secured to the foil using nail polish (CBI Dist. Corp.) instead of binder clips. This prevented the CZTS

nanocrystal dispersion from leaking out of the coating area. After allowing the polish to dry, CZTS nanocrystal dispersion (70 μL, 30 mg/ml) was dispensed into the center of the frame and allowed to spread. After the coating dried, the frame was pried gently from the Mo foil and residual polish was removed with acetone to prevent contamination during annealing.

7.2.3 Intense Pulsed Light and Thermal Annealing

Intense pulsed light annealing was conducted using a Sinteron 2010 (Xenon Corp) equipped with a 10" xenon u-shaped lamp. The flash energy density was determined from the manufacturer provided calibration that related the lamp voltage settings to power. The cumulative energy density during an individual flash with a duration of 3.5 ms was varied between 3.9 J/cm^2 and 11.6 J/cm^2 by adjusting the voltage between 1900 and 3000 volts. The reported energy density is based on the area of the lamp window (275 cm^2) and cumulative energy density. The flash duration and flash period were maintained at 3.5 ms and 2.31 s, respectively, for all annealing experiments. The number of flashes used during annealing ranged from a single flash to as many as 400. Figure 7.2 shows a schematic depicting a typical annealing experiment consisting of 5 flashes defining the flash duration and period.

Prior to annealing, CZTS coatings on Mo-coated SLG, quartz, or Mo foil were placed in quartz tubes which were evacuated to 10^{-6} Torr and flame sealed to form ampules. The ampule containing the CZTS coating was placed ~1.5 in below the xenon lamp. In some experiments, 1 to 10 mg of sulfur powder (99.999%, Cerac, Inc) was also included in the quartz tubes and sealed along with the coatings. When 1 mg of sulfur was used for annealing, the sulfur powder was placed onto a bare section of the substrate besides the CZTS coating as shown in Figure 7.3a. A small volume of toluene was dropped onto the sulfur powder to keep it from blowing off the Mo foil during handling. The toluene was allowed to partially dry before placing the coating in the quartz tube for evacuation. The rest of the toluene evaporates during tube evacuation. The sulfur powder vaporizes during IPL annealing and condenses on the quartz ampule after the last flash as shown in Figure 7.3b. When more than 1 mg of sulfur was used, the sulfur powder was placed in the quartz tube near the substrate but not on the substrate. In this arrangement, the sulfur is not in direct contact

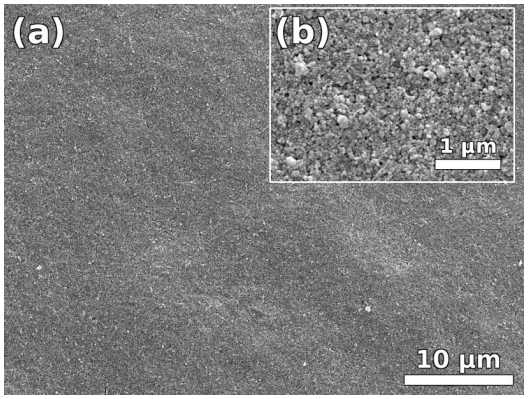

Figure 7.1 SEM images of as-coated CZTS nanocrystal coating on Mo-coated SLG substrate.

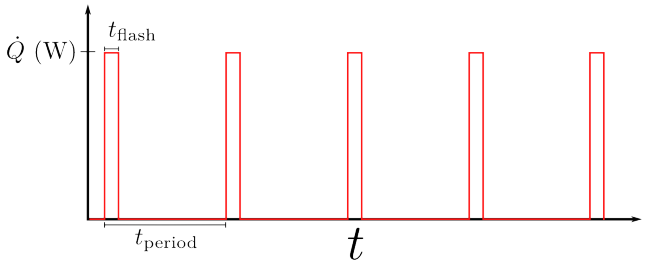

Figure 7.2 Schematic graph of energy output of IPL annealing operation. $\dot{Q}$ is energy output in watts, t_{flash} is length of flash period, and t_{period} is the flash period of flashes.

with the hot substrate but still could be vaporized when > 50 flashes were used (*i.e.*, sulfur also absorbs the radiation emitted by the lamp). After annealing, the ampule was removed from the lamp enclosure and allowed to cool before removing the coating by fracturing the ampule.

For comparison, we also annealed coatings thermally using a conventional furnace (Barnstead Thermolyne 1400). Coating preparation for thermal annealing experiments was similar to that for IPL annealing experiments. CZTS coatings on Mo-coated SLG substrates were placed in quartz tubes with 1 mg of sulfur and flame sealed after evacuation to 10^{-6} Torr. Prior to annealing, an alumina block with three slots sized for the quartz ampules was preheated in a furnace for 3 hours at 600 °C. The quartz ampules were quickly inserted into the slots of the alumina block inside of the preheated furnace to begin annealing. The fur-

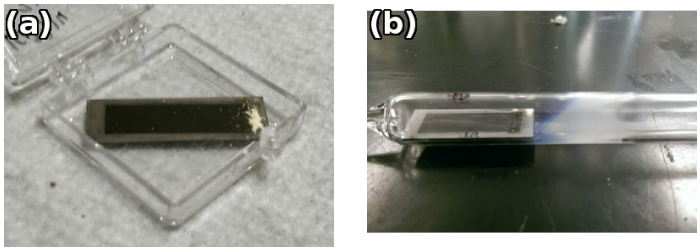

Figure 7.3 Photographs of (a) sulfur powder placed beside a CZTS nanocrystal coating on Mo foil prior to annealing, and (b) CZTS nanocrystal coating sealed in quartz ampoule after IPL annealing showing vaporization and subsequent condensation of the sulfur powder.

nace temperature was held at 600 °C for one hour after which the furnace was turned off and allowed to cool naturally with the furnace door closed. The cooling rate was such that after 3 hours the temperature had dropped to 350 °C.[60] After cooling to room temperature, the ampules were taken out of the furnace and the substrates with the coatings were removed by fracturing the ampules.

7.2.4 Characterization

CZTS coatings were characterized using a suite of techniques before and after annealing. The coatings were imaged with a JEOL-6500 field emission scanning electron microscope (SEM). Energy dispersive x-ray spectroscopy (EDS) was conducted with a Thermo-Noran Vantage energy dispersive x-ray spectrometer. X-ray diffraction was collected using a Bruker D8 Discover diffractometer equipped with a Co Kα source and a VÅNTEC-500 2D-area detector. A 0.8 mm beam collimator was used for collection of all XRD patterns. The XRD patterns were converted to Cu Kα source format using analysis software (JADE, Materials Data Incorporated). Raman scattering spectra were collected using a Witec Alpha300R confocal Raman microscope equipped with a 532 nm wavelength source, a DV401 CCD detector, and a UHTS300 spectrometer. The spectra were collected with an 1800 lines/mm grating, providing a spectral resolution of 0.02 cm^{-1}.

Crack densities of IPL annealed coatings were determined from the SEM images. Horizontal lines (2 pixel width) with a spacing of 100 pixels (image spatial distance of 1.8 μm)

were placed across 1280 × 980 pixel resolution images (coating area of 450 μm^2). The average linear crack density was determined from the number of cracks that intersect these lines (*i.e.*, number of intersections/length of the line).

7.2.5 Simulation of IPL Annealing of CZTS Nanocrystal Coatings

The heat transfer equations describing the IPL annealing of CZTS nanocrystal coatings, were solved using a heat transfer model within the COMSOL software package (version 4.4). The model geometry and FEM mesh were constructed using the built-in features of COMSOL. Two model substrate configurations were used for simulations. The first comprised, from top to bottom, a 3 μm CZTS coating (modeled as a continuous layer of CZTS), a 1 μm thick Mo layer, and a 1 mm thick SLG substrate. The second configuration comprised a 3 μm CZTS coating on a 500 μm thick molybdenum foil substrate. Upon these geometries, the generated mesh elements were graded in size ranging from 0.25 μm in the CZTS layer to 5 μm at the bottom of the substrate. A flash energy density of 11.6 J/cm^2, flash duration of 3.5 ms, and flash period of 2.31 s were used to simulate heating from 10 lamp flashes during IPL annealing. The total simulation time was 45 seconds to observing cooling behavior after annealing was completed. To accurately model the rapid transient heating during each flash, the simulation time-steps during flashes were set to 0.1 ms; time steps were increased to 50 ms when the flash was off.

Heat Transport Modeling of IPL Annealing

We constructed a model of heat transport during IPL annealing to determine the spatiotemporal evolution of the CZTS coating and substrate temperature. The two-dimensional (2-D) transient differential energy balance equations were solved using the finite element method (FEM). Figures 7.4a and 7.4b illustrate the model, the equations and the boundary conditions. Specifically, two different substrate and coating configurations were studied. The first configuration was a CZTS nanocrystal coating cast on a Mo-coated SLG substrate. The second configuration was a CZTS nanocrystal coating cast on Mo foil (Figure 7.4c). The spatiotemporal evolution of the temperatures of the substrate and its overlayers were

determined by solving the heat equation in 2-D,

$$\rho_i C_i \frac{\partial T_i}{\partial t} = k_i \vec{\nabla}^2 T_i + \dot{\Theta}_i \tag{7.1}$$

where i denotes the properties of material i (e.g., i=CZTS or Mo or SLG), ρ_i is the density, C is heat capacity, T is the temperature, k is the thermal conductivity, and $\dot{\Theta}_i$ is the heat generation rate per unit volume. The boundary conditions at the bottom of the substrate and at the top of the nanocrystal coating are constructed by assuming that the convective and conductive heat losses are negligible and that radiation is the sole energy loss mechanism. These are good assumptions because the thermal contact area between the substrate and surrounding quartz ampule is very small and the substrate is in vacuum. On all surfaces the heat flux is assumed to be radiative and given by

$$J_{\text{rad},i} = \varepsilon_i \sigma \left(T_i^4 - T_s^4 \right) \tag{7.2}$$

where ε is the thermal emissivity of material i, σ is the Stefan-Boltzmann constant, and T_s, is taken to be 298 K. The temperature and the heat flux are continuous across all interfaces (*i.e.*, between substrate and CZTS coating, between substrate and Mo, etc.). The xenon flash lamp emission spectrum is assumed to reach the quartz ampule with a wavelength-dependent energy density of J_{Xe} (W/m^2). After passing through the quartz ampule walls, the intensity is reduced to J_{Qz} due to absorption and reflection from the quartz ampule. These loses are incorporated into the model as a reduction to the total energy density per flash such that

$$J_{\text{Qz}} = T_{\text{QZ}} J_{\text{Xe}} \tag{7.3}$$

where T_{QZ} is the wavelength-dependent transmissivity of quartz. The photons with energy exceeding the band gap of CZTS are absorbed upon reaching the CZTS coating because the

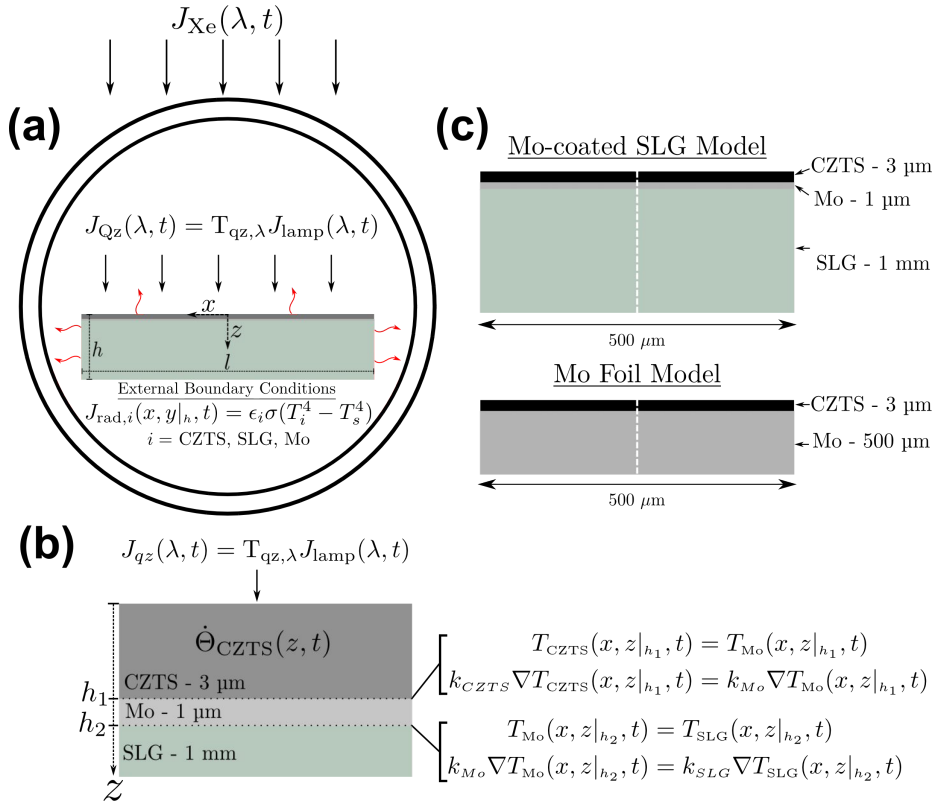

Figure 7.4 (a) Summary schematic for setup for FEM of IPL annealing of CZTS nanocrystal coatings. (b) Detailed schematic showing heat generation in CZTS layer according to Equation 7.4 and inter-material boundary conditions for temperature and heat flux continuity. (c) Illustrations of geometries used for FEM simulations of intense pulsed light annealing of CZTS coatings on Mo-coated SLG and Mo foil substrates.

optical density of CZTS is large enough to absorb the entire spectrum above the band gap of CZTS (*i.e.*, $\dot{\Theta}_i = 0$ except for i = CZTS). The angle of incidence is taken to be normal to the CZTS surface. Within the CZTS layer, the light is absorbed according to Beer's law and heat is generated at distance, z, from the CZTS surface according to

$$\dot{\Theta}_{\mathrm{CZTS}} = I_{\mathrm{Qz}} \int_0^{\infty} \left[1 - \mathrm{R}\left(\lambda\right)\right] j_{\mathrm{Qz}}\left(\lambda\right) \alpha\left(\lambda\right) e^{-\alpha(\lambda)z} d\lambda \tag{7.4}$$

where I_{Qz} is the total energy density, λ is the wavelength, R is the reflectivity of CZTS, j_{Qz} is

the normalized wavelength-dependent irradiance, and α is the CZTS absorption coefficient. The transmissivity of quartz was taken as that reported by Beder *et al.*[201] The wavelength length-dependent absorption properties of CZTS were estimated from absorption spectra and absorption coefficients reported by Levcenko *et al.*[142] and Cheng *et al.*,[202] respectively. Table 7.1 summarizes the thermal and optical properties used in the simulations. MATLAB (v2014A, MathWorks) was used to find a curve fit based for the numerical integration of Equation 7.4. The fit profile and equation is shown in Figure 7.5. The final equation has an R^2 value of 0.99 indicating an accurate representation of the overall absorption equation.

Table 7.1 Thermal properties used for development of finite element model.

Material	Density (kg/m^3)	Heat Capacity (J/kg K)	Thermal Conductivity (W/m K)	Thermal Diffusivity (10^{-6} m^2/s)	Emissivity	Absorption Coefficient (cm^{-1})
CZTS	4,560	885	2	0.5	1	Refs. [142] & [202]
Molybdenum	10,280	250	138	55	0.18	–
Soda lime glass	2,440	720	1.05	0.6	1	–

7.3 Results and Discussion

7.3.1 IPL Annealing of CZTS Nanocrystal Coatings on Mo-Coated SLG

During IPL annealing, CZTS nanocrystal coatings crack with varying crack densities. Figure 7.6 with SEM images of coatings cast from 35 nm diameter CZTS nanocrystals after IPL annealing at energy densities ranging from 3.9 to 11.6 J/cm^2 for 1 and 10 flashes. The flash duration was 3.5 ms and flash period was 2.31 s for all coatings. When CZTS nanocrystal coatings are annealed with a single flash at an energy density of 3.9 J/cm^2, there are no discernible changes compared to the SEMs of coatings prior to annealing (Figure 7.1). As the energy density of the single flash increases, cracks begin to develop in the coatings and increase in width while maintaining the same crack density. With 10 flashes, cracks are apparent even at the lowest energy density (3.9 J/cm^2). Increasing the flash energy density to 9.0 J/cm^2 causes “blisters”, areas of raised coating, throughout the coating surface (Figure

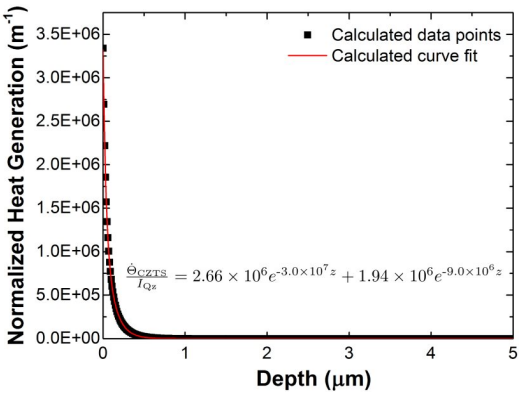

Figure 7.5 Graph of curve fit for absorption of xenon flash lamp spectrum by a single grain CZTS layer found by integration of Equation 7.4. The plotted equation provides total heat generation normalized by total heating power per unit area ($\dot{\Theta}/I_{Qz}$). Depth, z, is distance from exposed CZTS surface.

7.6k,l). In some cases, blisters are connected by cracks as if the cracks have originated from the blisters. At the highest energy density (11.6 J/cm^2), the nanocrystal coating is no longer continuous but has formed isolated islands surrounded by bright, textured areas that do not resemble the original Mo surface. Additionally, the appearance of these islands is accompanied by deposition of a dark residue on the inside of the quartz ampule directly above the coating as shown in Figure 7.7. EDS analysis of these deposits show that they are composed of CZTS elements and are likely ejected from the surface of the coating, presumably from the regions that are no longer covered by the coating.

Figure 7.8 shows the XRD patterns for each of the films shown in Figure 7.6. All patterns with the exception of the film annealed at 11.6 J/cm^2 for 10 flashes, are consistent with the expected kesterite CZTS XRD pattern (ICDD No. 00-026-0575). The coating annealed at 11.6 J/cm^2 for 10 flashes shows peaks expected from CZTS and SnS (ICDD No. 03-065-3812). The elemental compositions of the coatings in Figures 7.6 and 7.8 were determined using EDS and are presented in Figures 7.9, 7.10, and Table 7.2. Coatings exhibiting blisters and islands also show decomposition of the CZTS coating with loss of zinc and tin. The other coatings show no change in elemental composition after IPL annealing. Raman spectra of all coatings in Figures 7.6 and 7.8 are shown in Figure 7.11. The Raman

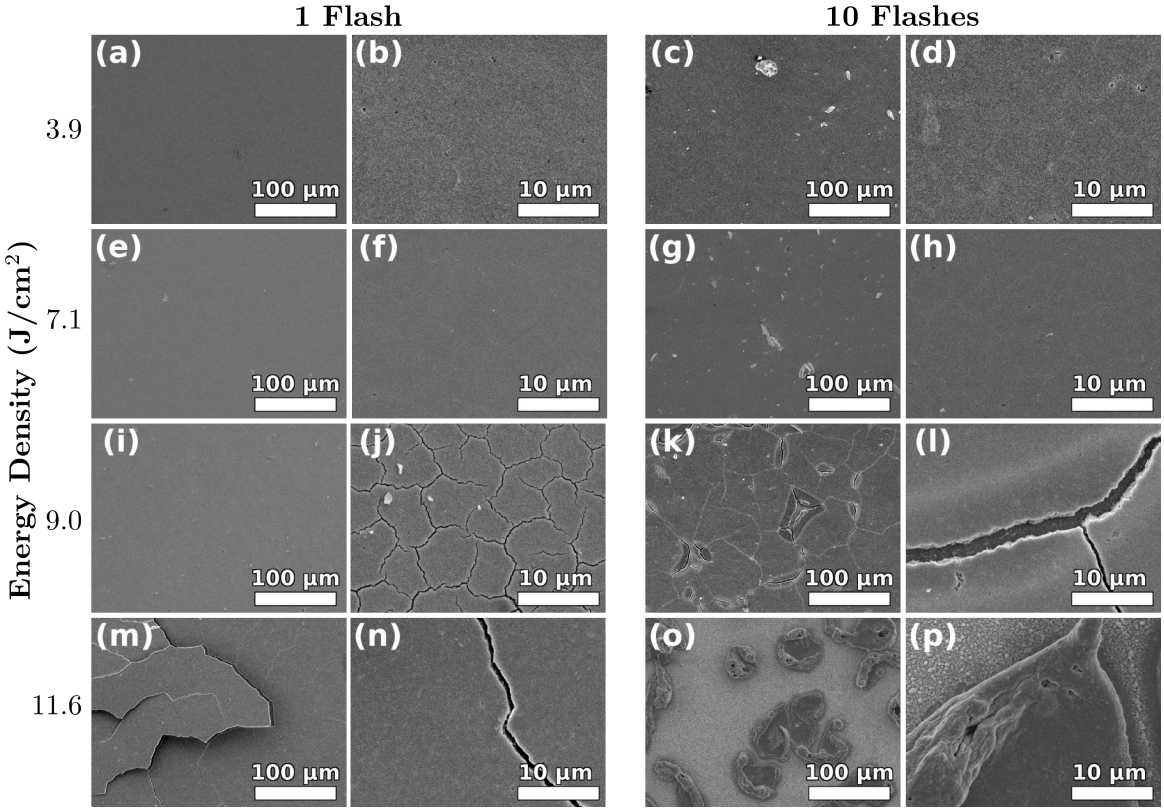

Figure 7.6 SEM images of CZTS nanocrystal coatings on Mo-coated SLG substrates after IPL annealing at flash energy densities ranging between 3.9 and 11.6 J/cm^2 for 1 and 10 flashes: (a & b) 3.9 J/cm^2 and 1 flash, (c & d) 3.9 J/cm^2 and 10 flashes, (e & f) 7.1 J/cm^2 and 1 flash, (g & h) 7.1 J/cm^2 and 10 flashes, (i & j) 9.0 J/cm^2 and 1 flash, (k & l) 9.0 J/cm^2 and 10 flashes, (m & n) 11.6 J/cm^2 and 1 flash, (k & l) 11.6 J/cm^2 and 10 flashes.

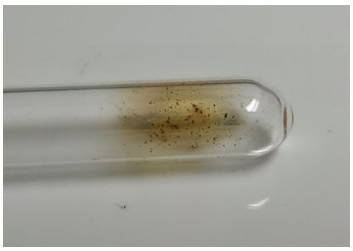

Figure 7.7 Photograph of quartz ampule with residue deposited from CZTS nanocrystal coating during IPL annealing at 11.6 J/cm^2 for 10 flashes.

spectra of all the coatings show the expected major CZTS Raman shift at 336-338 cm^{-1}. The coating annealed at 11.6 J/cm^2 for 10 flashes also exhibits peaks at 173, 184, and 228 cm^{-1} which are similar in location to those reported for nanocrystalline SnS.[203]

The two different cracking densities qualitatively observed in Figure 7.6 can be quantified by measuring the linear crack density as a function of cumulative IPL annealing energy density (product of number of flashes and energy density per flash) as shown in Figure 7.12. Coatings annealed at 3.9 J/cm^2 with a single flash and at 11.9 J/cm^2 with 10 flashes are not included since no discernible cracking was observed in the former and the latter was mostly vaporized and ablated. Crack densities measured on these samples cluster around two values, one at ~0.2 μm^{-1} (~5 μm spacing between cracks) and another at ~0.01 μm^{-1} (~100 μm spacing), henceforth referred to as high-density and low-density cracking, respectively. IPL annealing at low energies, 3.9 and 7.1 J/cm^2, for 1 and 10 flashes results in high-density cracking while IPL annealing at high energies, 10.3 and 11.6 J/cm^2 for 1 and 10 flashes results in low-density cracking. At the intermediate energy density of 9.0 J/cm^2, a change in cracking density from high-density cracking to low-density cracking occurs when the number of flashes is increased from 1 to 10. Crack spacing is correlated to the magnitude of stress relaxation in thin films, such that crack density increases with stress in the film.[204] The occurrence of two independent crack densities and the change in crack density with the number of flashes during IPL annealing at 9.0 J/cm^2 indicates two separate stress generation mechanisms responsible for the two cracking densities.

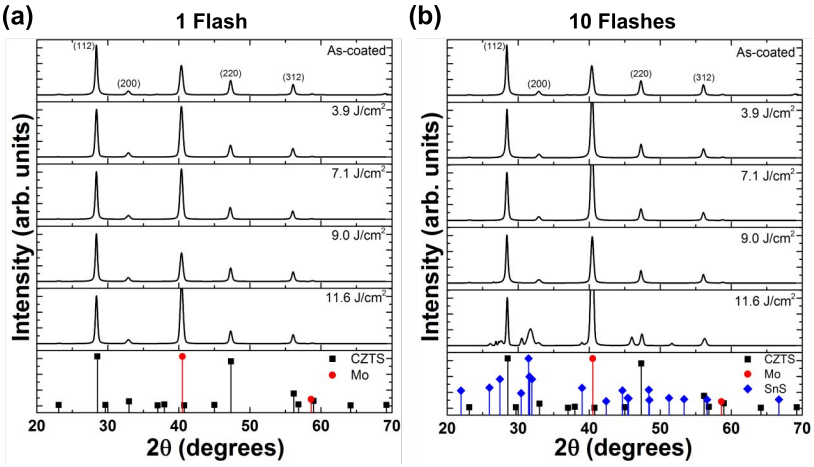

Figure 7.8 XRD patterns of CZTS nanocrystal coatings on Mo-coated SLG substrates before and after IPL annealing at flash energy densities ranging between 3.9 and 11.6 J/cm^2 for (a) 1 and (b) 10 flashes.

7.3.2 CZTS Decomposition and Blister Formation Mechanism

Low-density cracking coincides with the appearance of coating blisters as observed in Figure 7.6k,l. The bulging of the area under the blisters suggests that the blistering is initiated at the substrate-coating interface. High magnification SEM images of the interior of the blisters show nanocrystal deposits that appear distinct from the starting CZTS nanocrystals as shown in Figure 7.13. To examine these deposits, we used a piece of Scotch tape to liftoff the surrounding coating from the substrate, exposing the nanocrystals. Figure 7.14b

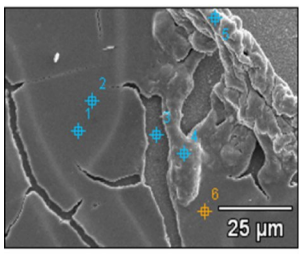

	Atomic Percent			
Location	Cu	Zn	Sn	S
1	25	12.1	12.7	50.2
2	23.5	13.9	12.7	50
3	5.4	1.8	4.5	88.2
4	26.7	16.9	9.2	47.2
5	28.7	18.9	6.7	45.7
6	30.1	10.9	11.7	47.4

Figure 7.9 SEM image and summary of EDS results from a CZTS nanocrystal coating on a Mo-SLG substrate annealed at 9.0 J/cm^2 for 10 flashes. Table locations correspond to numbered positions in SEM image.

Table 7.2 Summary of EDS results from IPL annealed CZTS nanocrystal coatings on Mo-SLG substrates at various energies and flashes. All atomic percentages are averages of three separate measurements. All coatings listed represented uniform coatings without large abnormalities.

		Atomic Percent			
Energy Density (J/cm^2)	**# of Flashes**	**Cu**	**Zn**	**Sn**	**S**
3.9	1	24.6	11.6	12.4	51.4
7.1	1	24.4	11.3	12.4	51.9
9	1	24	12.4	12.8	50.8
11.6	1	24.2	12.9	12	51.2
3.9	10	23.9	12.9	12	51.2
7.1	10	23	12.7	12.3	51.9

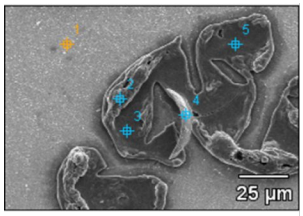

	Atomic Percent			
Location	**Cu**	**Zn**	**Sn**	**S**
1	2.6	–	13.0	84.5
2	76.0	–	–	24.1
3	33.6	14.6	14.6	43.2
5	33.8	11.9	11.9	44.7

Figure 7.10 SEM image and summary of EDS results from a CZTS nanocrystal coating on a Mo-SLG substrate annealed at 11.6 J/cm^2 for 10 flashes. Table locations correspond to numbered positions in SEM image. EDS data for location 4 was lost due to computer error and is absent from summary table.

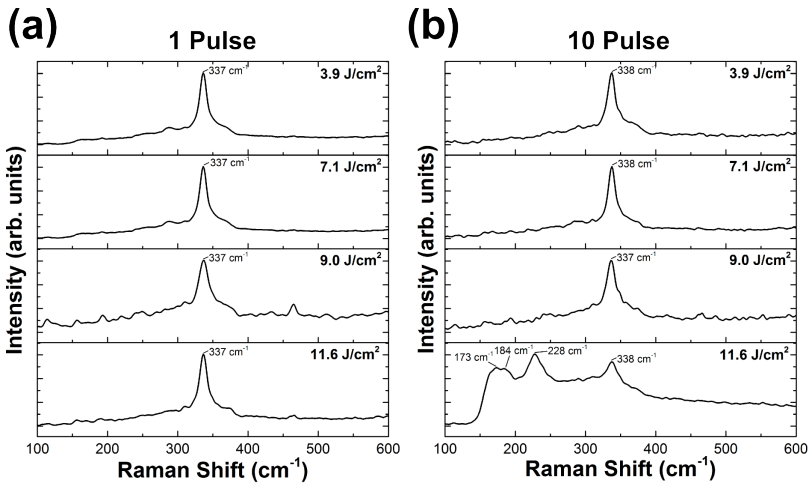

Figure 7.11 Representative Raman spectra from IPL annealed CZTS nanocrystal coatings on Mo-coated SLG substrates at varying energy densities for (a) 1 flash and (b) 10 flashes.

is an optical image of such a nanocrystal deposit isolated in this manner on the Mo-coated SLG substrate. The surrounding coating has been removed though remnants of the crack locations are still identifiable as faint lines of nanocrystals emanating from the deposit. 2-D Confocal Raman spectroscopy imaging was used to examine the phase composition of this nanocrystal deposit as a function of position. We find that this nanocrystal deposit is composed of both CZTS and SnS_2 nanocrystals. To illustrate this, we show two confocal Raman images produced by filtering all Raman scattering except for the major characteristic Raman peaks for CZTS (filter range 324 to 342 cm^{-1}) and SnS_2 (filter range 305 to 320 cm^{-1}) in Figures 7.14a and 7.14c, respectively.[202] Near the top edge of the deposit (marked by a red square), only CZTS is present and the Raman spectra collected from this region (Figure 7.14d) shows only the major CZTS peak at 336 cm^{-1}. Near the bottom edge of the deposit (marked by a blue dot), the SnS_2 peak (315 cm^{-1}) appears and increases in intensity towards the bottom-center of the deposit. The Raman spectra collected from this region (Figure 7.14e) shows the Raman scattering peaks for both SnS_2 and CZTS indicating that these phases coexist in this region (approximately 4 μm in diameter). A peak centered at 465 cm^{-1} was also present in varying intensities for all spectra over and is assigned to SiO_2, likely coming from contamination during breaking of the ampule. Neither CZTS nor any

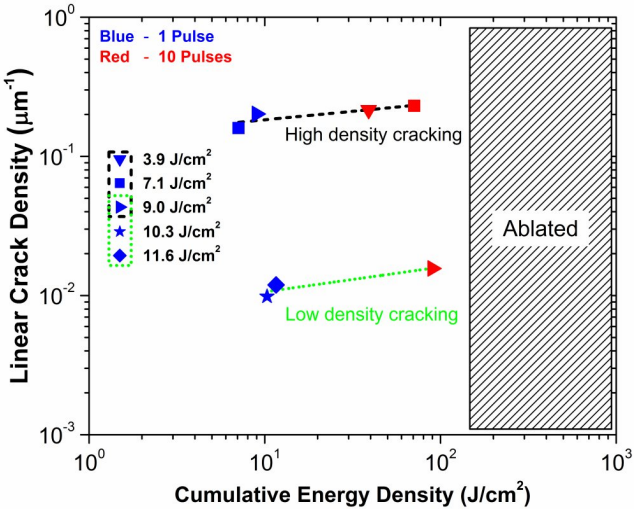

Figure 7.12 Plot of linear crack density of CZTS nanocrystal coatings on Mo-coated SLG after IPL annealing as a function of cumulative energy density. Cumulative energy density is the total energy per unit area that the coating is exposed to and is calculated by multiplying the number of flashes (1 or 10 flashes) with energy density of an individual flash, which ranged from 3.9 to 11.6 J/cm^2. Crack densities are clustered around two values, 0.2 and 0.01 μm^{-1}, referred to as high-density and low-density cracking, respectively.

of the expected decomposition products of CZTS exhibit Raman scattering at this wavelength.[202] It is also unlikely that the signal originates from the soda lime glass because the molybdenum is thick and the laser does not penetrate to the glass substrate.

Based on the data shown in Figure 7.14, we propose that the blistering and low density cracking during IPL annealing of CZTS nanocrystal coatings on Mo-coated SLG substrates is associated with localized decomposition of CZTS at the molybdenum-CZTS interface and subsequent evolution of vapor decomposition products to burst the coating. Figure 7.15 shows a schematic of the proposed blister formation mechanism that precedes low density cracking. CZTS may decompose through solid-state decomposition at the molybdenum-CZTS interface to form MoS_2 and solid binary sulfides. Scragg *et al.*[205,206] detailed this decomposition pathway during thermal annealing of sputtered CZTS coatings, but CZTS decomposition during IPL annealing has not been previously reported. In addition, the total annealing time for IPL annealing (< 30 s) conducted here is much shorter than the thermal

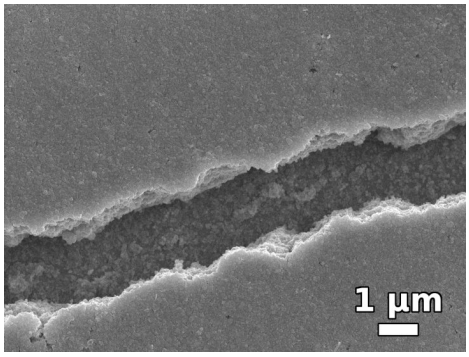

Figure 7.13 SEM image of blistered region of CZTS nanocrystal coating after IPL annealing at 9.0 J/cm^2 for 10 flashes. Center of blister shows small nanocrystal deposits.

annealing times (> 30 min) used for previous evaluations of CZTS decomposition.

Before IPL annealing, the CZTS nanocrystal coating has a uniform microstructure and chemical composition. As the annealing time (*i.e.*, number of flashes) increases, CZTS reacts with Mo locally to form MoS_2 and decomposes into binary sulfides (Cu_2S(s), ZnS(s), and SnS(s)). In particular, SnS(s) has high vapor pressure[205] and yields SnS(g) in equilibrium with the solid phase. If the SnS(g) formation rate is low (*i.e.*,, low energy density single flashes), it may be able to diffuse through the nanocrystal network to the surface. However, as the coating temperature increases with subsequent IPL flashes, the SnS(s) and SnS(g) formation rates increase. The larger volume of SnS(g) formed may not diffuse fast enough to the surface resulting in local high pressure pockets of SnS vapor under the coating. When these vapor pockets deform the coating forming blisters and may burst.

An important observation that supports this proposed blister formation mechanism is the presence of SnS_2(s) in the regions where blisters have formed. SnS_2 is observed during Raman spectroscopy of the nanocrystal deposits while the proposed pathway requires formation of a SnS(s) phase. Excess sulfur from the CZTS nanocrystals may exist within the blisters oxidizing the formed SnS(s) to SnS_2(s). Additionally, we detected SnS(s) by XRD in coatings cast on Mo-coated SLG substrates when IPL annealing was conducted using the highest IPL energy density (11.6 J/cm^2) and 10 flashes. EDS also shows high concentrations of Sn and S (Figure 7.10) on the textured areas surrounding the coating islands

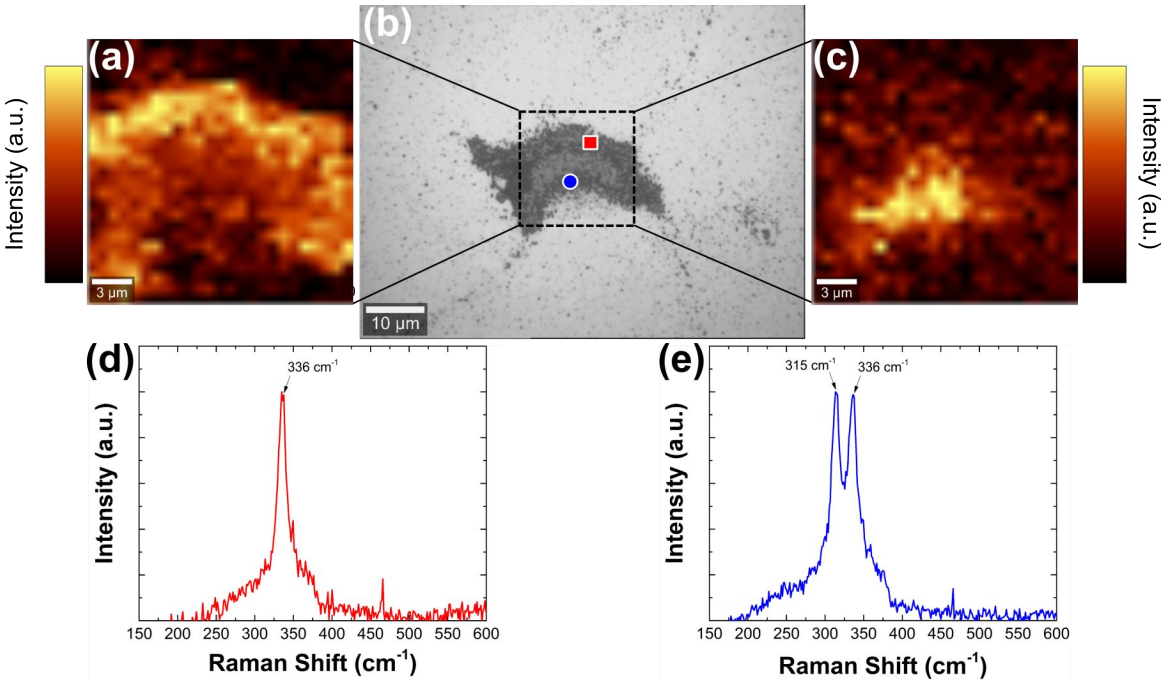

Figure 7.14 Summary of the analysis, using confocal Raman microscopy and imaging, of the Mo-CZTS interfacial region in a blister formed on the nanocrystal coating post IPL annealing with ten 9.0 J/cm^2 flashes. The surrounding CZTS nanocrystal coating was removed to reveal the region shown in the optical micrograph in (b). (a) and (c) show two dimensional (2-D) images created from the Raman spectra recorded from the region shown in the dashed box in (b). In (a), the 2-D Raman scattering map was created using an integrated intensity filter that selects high intensity scattering between 324 and 342 cm^{-1}, corresponding to the A1 mode of CZTS. In (c), the 2-D Raman scattering map was created using an integrated intensity filter that selects high intensity scattering between 305 and 320 cm^{-1}, corresponding to the A1g mode of SnS_2. (d) Raman spectrum of a CZTS rich region from the location indicated by the red dot in (b). (e) Raman spectrum of a SnS_2 rich region from the location indicated by the blue dot in (b).

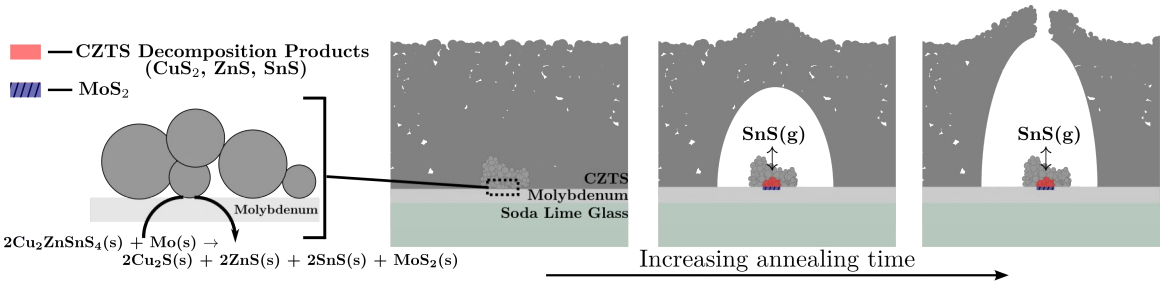

Figure 7.15 A schematic illustration of the proposed blister formation mechanism. CZTS decomposition at the CZTS-Mo interface during IPL annealing generates gases; blistering is caused by these product gases as they leave the film.

shown in Figure 7.6o,p, but the overlap of the Mo Lα peak (2.293 keV) with the S Kα peak (2.307 keV) obfuscates phase determination based on elemental composition in these areas. At high IPL energy densities, the decomposition is no longer localized to small regions of nanocrystals but occurs across the coating and the volume of SnS formed is significant enough to be detected by XRD.

The blistering mechanism, as proposed, is not inherently limited to occurring during IPL annealing and it may be expected to occur during thermal annealing as well. Figure 7.16a-d shows SEM images of a CZTS nanocrystal coating after thermally annealing at 600 °C for one hour without added sulfur and with 1 mg of sulfur added to the ampule, providing a vapor sulfur pressure of 50 Torr at 600 °C. XRD and Raman spectra of the films are presented in Figure 7.17. Small cracks are present in the film annealed without additional sulfur, but no blisters or raised regions of coatings are formed. The coating annealed with 1 mg of sulfur exhibits no cracking and forms a dense, continuous polycrystalline film. Figure 7.16e-h also shows SEM images of a CZTS nanocrystal coating after thermally annealing at 600 °C with and without added sulfur, but these coatings were IPL annealed at an energy density of 3.9 J/cm^2 for one flash prior to thermal annealing. These particular IPL annealing parameters generate neither cracking or blistering as evidenced in Figure 7.6a,b. However, large 100 μm blisters are formed throughout the coating after thermal annealing without sulfur (Figure 7.16e,f). The addition of 1 mg of sulfur to the annealing ampule reduces the size of the blisters and suppresses crack formation (Figure 7.16g,h).

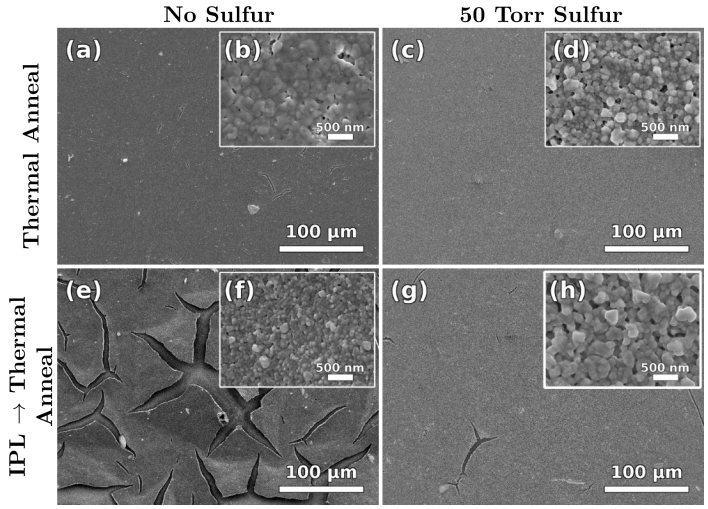

Figure 7.16 SEM images of CZTS nanocrystal coatings after thermal annealing in a conventional furnace at 600 °C for 1 hour with and without 1 mg of sulfur loaded into the ampule (50 Torr sulfur vapor pressure). The coatings shown in a-d were annealed after drying while the bottom coatings (e-h) were first annealed using IPL with a single 3.9 J/cm^2 flash and then annealed in a conventional oven. All films were in a quartz ampule as described in the experimental procedure.

Figure 7.16 reveals that blistering is a unique aspect of the rapid transient heating encountered during IPL annealing. Thermally annealed coatings do not show blistering unless they were first annealed using IPL. Remarkably, even a single low energy light pulse is enough to cause blistering when the coatings are annealed thermally following that pulse. A single pulse alone does not cause blistering without the subsequent thermal annealing (or continued IPL pulses). We surmise that a single light pulse is adequate to initiate decomposition reactions at the Mo-CZTS interface. Vaporization of the decomposition products (*e.g.*, SnS) during the subsequent thermal annealing creates the blisters *via* the mechanism shown in Figure 7.15. During thermal annealing, only the coatings that were previously subjected to IPL annealing developed blisters and only if there was no sulfur vapor in the tube. The addition of 1 mg of sulfur into the ampule reduces the severity of blistering during thermal annealing significantly, indicating that even coatings that do not blister during IPL annealing still undergo CZTS decomposition at the Mo-CZTS interface *via* the reactions proposed by Scragg *et al.*:[206]

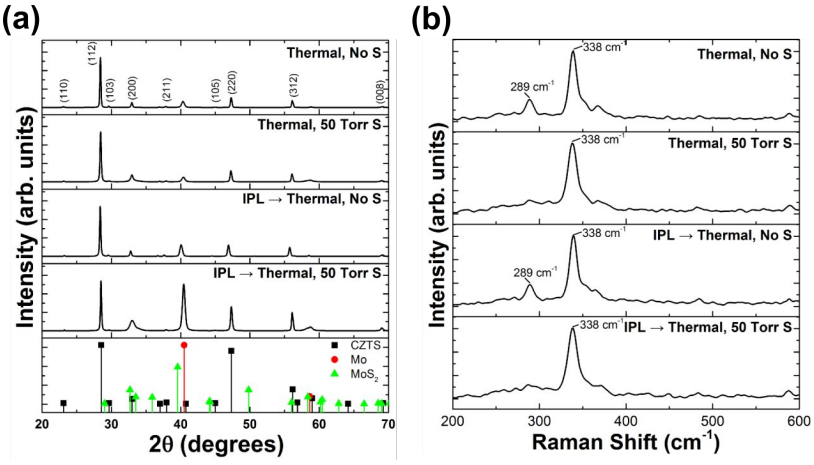

Figure 7.17 (a) XRD patterns and (b) Raman spectra for CZTS nanocrystal coatings on Mo-SLG substrates corresponding to Figure 4 for non-IPL-treated and IPL-treated CZTS coatings after thermal annealing.

$$2\,Cu_2ZnSnS_4(s) + Mo(s) \longrightarrow 2\,Cu_2S(s) + 2\,ZnS(s) + 2\,SnS(s) + MoS_2(s) \qquad (R3)$$

$$SnS(s) \longrightarrow SnS(g)\cdot \qquad (R4)$$

The addition of sulfur during thermal annealing prevents blister formation by reversing the IPL induced decomposition via

$$SnS(s) + S(g) \longrightarrow SnS_2(s) \qquad (R5)$$

$$Cu_2S(s) + SnS_2(s) \longrightarrow Cu_2SnS_3(s) \qquad (R6)$$

and

$$Cu_2SnS_3(s) + ZnS(s) \longrightarrow Cu_2ZnSnS_4(s)\cdot \qquad (R7)$$

To further test the proposed blistering mechanism, a CZTS nanocrystal coating cast on a bare quartz substrate (without Mo) was annealed with IPL under conditions that produced blistering in coatings cast on Mo-coated SLG (9.0 J/cm^2 for 10 flashes). Figure 7.18

displays an SEM image of this CZTS nanocrystal coating after IPL annealing; A representative XRD pattern and Raman spectrum collected from this coating are shown in Figure 7.19. While the coating is cracked, there is no blistering. This observation and lack of blisters in absence of Mo supports the proposed mechanism for blistering and the subsequent low density cracking initiated by decomposition of CZTS upon reaction with Mo. The coating cast on quartz without Mo coating exhibits high density cracking (0.2 μm^{-1}) similar to that observed by coatings annealed on Mo-coated SLG using IPL at low energy densities and single flashes (Figure 7.6d-j). The cracks in Figure 7.18 are not due to blistering and are in fact due to another mechanism that is discussed next.

7.4 Origin of High Density Cracking

The blistering mechanism leads to low-density cracking on a length scale similar to the distance between the blisters and is observed at IPL energy densities $\geq$ 9.0 J/cm^2. There is a second mechanism that leads to high-density cracking: we propose that this second mechanism is cracking to relax stresses generated due to thermal expansion mismatch between the coating and the underlying substrate. Rapid thermal transients, repeated heating and cooling cycles, and steep temperature gradients that develop during IPL exacerbate these stresses and consequently the cracking.[198,207]

Understanding the factors that affect the spatiotemporal temperature evolution of the nanocrystal coating during IPL annealing provides insight into the cause of high-density cracking and strategies that may help mitigate it. Towards this end, we determined the spatiotemporal evolution of the temperature of the coating and the substrate subjected to IPL annealing. Figure 7.20 shows the temporal evolution of the temperatures of the CZTS coating and substrate during IPL annealing (11.6 J/cm^2, 3.5 ms flash duration, 2.31 s flash period, 10 flashes) for the two model coating-substrate configurations shown in Figure 7.20c: in Case I the CZTS coating is on a Mo-coated SLG whereas in Case II the CZTS coating is on a Mo foil substrate. Figure 7.20a,b shows the temperature of the CZTS layer at the top center (red dotted line; $x = 0$, $z = 0$ μm in Case I and Case II) and the temperature of

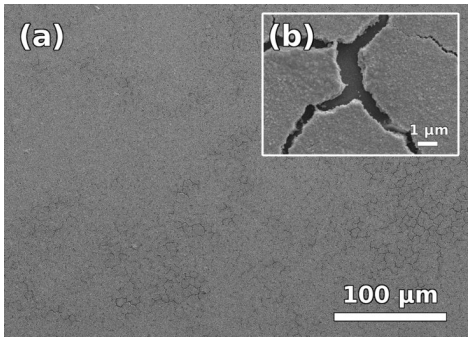

Figure 7.18 SEM images of a CZTS nanocrystal coating on quartz after IPL annealing with ten 9.0 J/cm^2 flashes at (a) low and (b) high magnification, showing lack of blistering but presence of high density cracking.

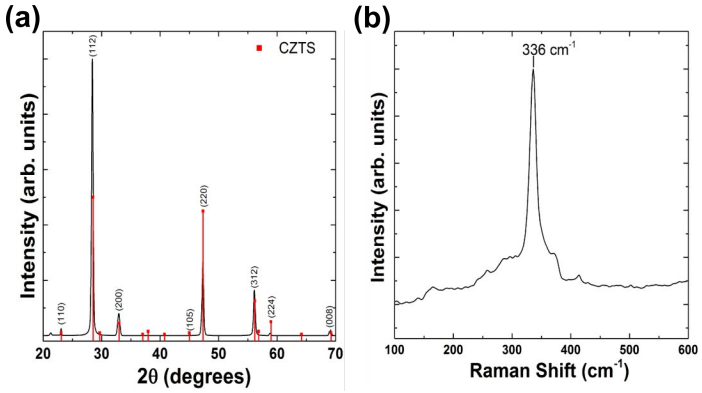

Figure 7.19 (a) XRD pattern and (b) Raman spectrum for CZTS nanocrystal coating on quartz substrate after IPL annealing at 9.0 J/cm^2 for 10 flashes.

the substrate at the bottom center (black solid line; $x = 0$, $z = 1004$ µm in Case I and $x = 0$, $z = 503$ µm in Case II). The difference in temperature, ΔT, between the CZTS (top center) and substrate (bottom center) is plotted below the corresponding temperature plot for both cases. The temperature of the CZTS nanocrystal coating in Case I exhibits large swings with time, sharply changing as the coating is heated and cooled rapidly with each light pulse. When the light flash is on the CZTS coating temperature rises rapidly while the SLG substrate only warms slightly and slowly as evidenced by the plot of ΔT which reaches a maximum of 450 K during flashes.

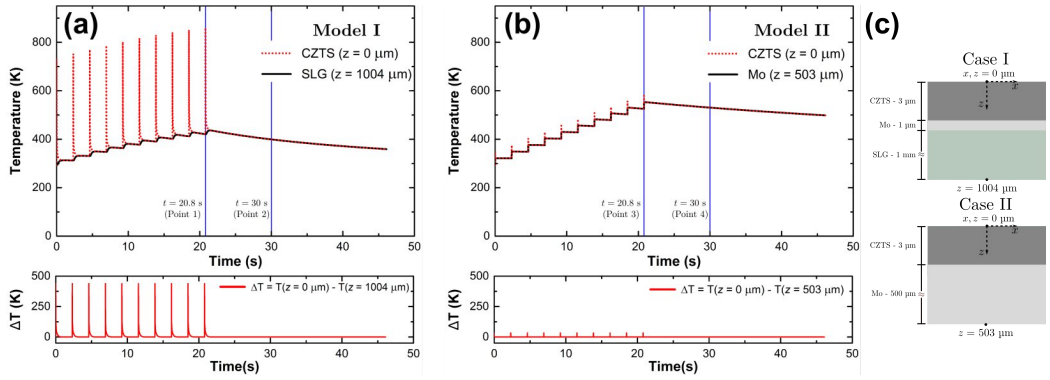

Figure 7.20 (a) Simulated temporal variation of the CZTS film (at $x = 0$, $z = 0$ μm) and the SLG substrate (at $x = 0$, $z = 1004$ μm) temperatures. The difference, ΔT, between these temperatures is plotted in the panel beneath (a). The locations ($x = 0$, $z = 0$) and ($x = 0$, $z = 1004$ μm) correspond to the center of the CZTS surface at the top and the center of the SLG surface at the bottom of the substrate, respectively, as illustrated in Case I shown in (c). (b) Simulated temporal variation of the CZTS film (at $x = 0$, $z = 0$ μm) and the Mo substrate (at $x = 0$, $z = 503$ μm) temperatures. The difference, ΔT, between these temperatures is plotted in the panel beneath (a).The locations ($x = 0$, $z = 0$ μm) and ($x = 0$, $z = 503$ μm) correspond to the center of the CZTS surface at the top and the center of the Mo surface at the bottom of the substrate, respectively, as illustrated in Case II shown in (c).

To better analyze the thermal development during IPL annealing it is useful to define the characteristic time for thermal diffusion, τ_i,

$$\tau_i = \frac{L_i^2}{\alpha_i} \tag{7.5}$$

where i denotes the properties of material i (*e.g.*, i=CZTS or Mo or SLG), α_i is the thermal diffusivity and L_i is the characteristic material length, assumed to be the z dimension of the relevant coating layer. For the characteristic times for thermal diffusion are 0.018, 1.81×10^{-5}, and $1,600$ ms for CZTS (3 μm), Mo (1 μm), and SLG (1 mm), respectively. Due to the large thickness and low thermal conductivity of the SLG layer, the characteristic time scale for thermal diffusion is much larger than the pulse length (3.5 ms) and is comparable to the pulse period (2.310 s). Heat generated in the CZTS layer due to absorption during flashes is slow to diffuse out of the CZTS and Mo layers. After each flash, heat generation

stops and the CZTS layer temperature decreases to reach an equilibrium temperature with the higher thermal density SLG layer resulting in a temperature drop of approximately 450 K.

The temperature evolution of the CZTS coating and the substrate suggests a possible reason for the high density cracking observed in Figures 7.6c-j. We surmise that a thermal expansion mismatch confounded by the large temperature difference between the CZTS and SLG layers during IPL annealing leads to cracking in the CZTS nanocrystal thin films. Specifically, the low thermal mass of the CZTS layer compared to SLG substrate and the low thermal conductivity of the SLG glass leads to differential heating of the CZTS coating with respect to the substrate. The SLG substrate does not heat significantly because it has low thermal conductivity and high heat capacity. This leads to a very large temperature differential between the CZTS layer and the SLG during each IPL flash. The mismatch in the thermal expansion coefficients, approximately 40-80 $\times$ 10^{-6} K^{-1} for CZTS based on values of the structurally similar CZTSe[208,209] and 9×10^{-6} K^{-1} for SLG,[210] ultimately causes stresses to build and crack the film. In addition, the repeated heating and cooling of the CZTS layer causes it to shrink through either sintering of the nanocrystal network due to the high coating temperature or constrained shrinkage during cooling after each pulse. Both effects would lead to a tensile stress within the coating which is relieved through cracking.

In addition, we have not observed low-density cracking accompanied by blister formation and the high-density cracking due to thermal expansion and contraction of the coating together on the same sample. Low-density cracking and blistering is accompanied by coating delamination, allowing the coating to expand and contract freely, eliminating the driving force for high density cracking. Consequently, high-density cracking due to thermal expansion and contraction is only observed under conditions where CZTS remains adhered to the substrate (*i.e.*, decomposition is slow and blistering is negligible).

The undesirable effects of temperature cycling during IPL annealing may be eliminated by replacing the SLG substrate with a high thermal diffusivity material. One attractive replacement is a metal foil (*e.g.*, stainless steel, Mo, etc.). We used a molybdenum substrate because it eliminated the need for Mo sputtering and CZTS solar cells with efficiencies of up to 3.8% have been made on Mo foil substrates.[211] Figure 7.20b plots the simulated tem-

perature at the top center of the CZTS layer and bottom center of the Mo layer, illustrated as Case II in Figure 7.20c, during IPL annealing under the same conditions as used for Case I (11.6 J/cm^2, 3.5 ms flash duration, 2.31 s flash period, 10 flashes). The temperature of the CZTS layer still spikes rapidly during the flashes, but the temperature differences between the CZTS layer and the Mo substrate are much smaller than those obtained when the substrate was SLG. In the case of a Mo foil substrate, the characteristic times for thermal diffusion are 0.018 and 4.5 ms for CZTS (3 μm) and Mo (500 μm), respectively. During flashes, heat generated in the CZTS layer is transported rapidly through the Mo layer reducing the size of the temperature gradient along the z-axis compared to the Mo-coat SLG configuration. In addition, the lower thermal mass of the Mo foil reduces the magnitude of cooling that occurs after the flash, allowing a high average temperature to be maintained during the entire IPL annealing time.

The difference in thermal behavior between Case I and Case II is even more evident when comparing 2-D temperature color maps at two separate time points during IPL annealing. Figure 7.21 shows the spatial variation of temperature in the $x - z$ plane of CZTS coatings on Mo-coated SLG and Mo foil during the final (10$^{\text{th}}$) IPL flash ($t = 20.8$ s) and after cooling for 9 seconds following the final flash ($t = 30$ s), as indicated in Figure 7.20a,b. At $t = 20.8$ s, Case I exhibits a severe temperature gradient ranging from approximately 860 K at the CZTS surface ($z = 0$ μm) to 420 K at the bottom of the SLG substrate ($z = 1003$ μm). At $t = 30$ s, the coating structure has cooled to a uniform temperature of 400 K. When the CZTS coating is on Mo foil rather than Mo-coated SLG, the thermal gradient is nearly non-existent during the flash at $t = 20.8$ s. Additionally, the Mo foil structure has a uniform temperature of 530 K at $t = 30$ s, significantly higher than that of the Mo-coated SLG structure. These simulations suggested that reduced thermal cycling and high average temperature during IPL annealing of CZTS on Mo layer may reduce thermal stresses and thus eliminate cracking. We tested this idea with annealing experiments conducted on CZTS nanocrystal coatings cast on Mo foil.

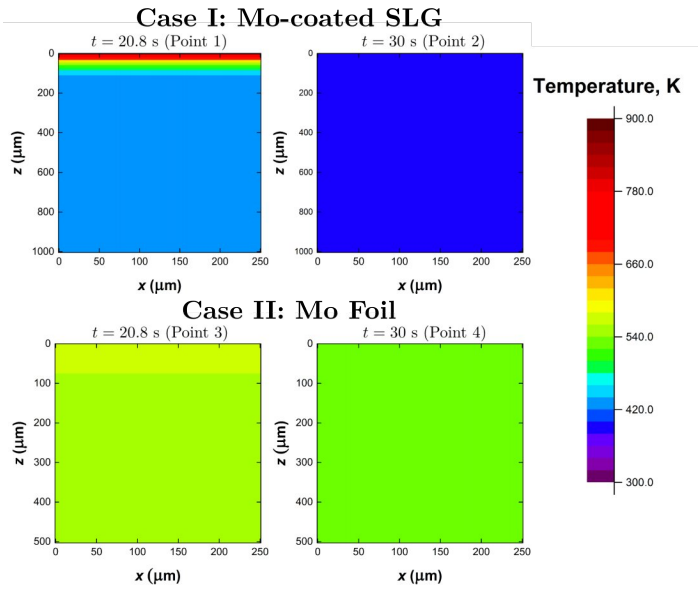

Figure 7.21 Spatial variation of the temperature in the x-z plane at times indicated in Figures 7.20a and 7.20b for the two models shown in Figure 7.20c. Typical temperature profiles are shown as snapshots during the last simulated flash at $t = 20.8$ s and after cooling for approximately 9 seconds following the last flash at $t = 30$ s. Steep spatial temperature gradients are created during the flash when SLG is used as the substrate. These gradients decay very rapidly causing film cracking due to thermal expansion mismatch between the film and the substrate. These gradients are virtually eliminated when SLG is replaced by a Mo foil substrate.

7.4.1 IPL Annealing of CZTS Nanocrystal Coatings on Molybdenum Foil

Figure 7.22 shows SEM images of CZTS nanocrystal coatings on (a,c) Mo-coated SLG and (b,d) Mo foil after IPL annealing at energy densities of (a,b) 9.0 J/cm^2 for 1 flash and (c,d) 11.6 J/cm^2 for 10 flashes. When the CZTS coating is on Mo-coated SLG, high density cracks are present after annealing at the lower energy density (9.0 J/cm^2, 1 flash) and low density cracks along with blisters are present after annealing at the higher energy density (11.6 J/cm^2, 10 flashes). Replacement of the Mo-coated SLG with Mo foil, prevents cracking at both IPL annealing energy densities and no blisters are present when annealing at 11.6 J/cm^2 for 10 flashes. The reduction in heating and cooling cycles and the lower maximum

CZTS temperature during IPL annealing are believed to be responsible for the absence of high- and low-density cracking, respectively.

At longer annealing times, it was found that the CZTS coatings began to blister and develop low density cracking, likely due to enhanced CZTS decomposition due to the higher cumulative energy densities. The addition of sulfur to the annealing ampules was investigated as a means to mitigate CZTS decomposition. Figure 7.23 shows SEM images of CZTS nanocrystal coatings cast on Mo foil after annealing with 10, 35, and 50 flashes in vacuum (no sulfur) (a-f) and in sulfur atmosphere (g-l). For the latter annealing conditions, 1 mg of sulfur was sealed in the ampule which if evaporated completely at 600 °C it would lead to sulfur vapor pressure of 50 Torr. The coating annealed for 50 flashes without added sulfur exhibits both CZTS and SnS characteristic peaks in XRD while all other coatings exhibit only CZTS peaks, as shown in Figure 7.24 along with Raman spectra of the coatings in Figure 7.23.

With 10 flashes, there is no discernible difference between the coatings annealed with (g,h) and without sulfur (a,b). Increasing the number of flashes to 35, the coating annealed in vacuum blistered and cracked (c,d) while the coating annealed with sulfur (i,j) shows no microstructural changes observable with SEM. Annealing in vacuum with 50 flashes causes the coating to decompose into mixed SnS and CZTS phases evidenced by XRD. The coating is cracked and isolated coating islands are formed, similar to that seen during IPL annealing on Mo-coated SLG substrates (Figure 7.6o,p). When annealing is conducted with sulfur in the ampule, the CZTS coating microstructure remains uniform and crack- free. In addition, no decomposition is observed in XRD or by Raman spectroscopy. It is clear, as expected from the proposed blistering mechanism above, sulfur is necessary to prevent CZTS decomposition and blistering during annealing of CZTS nanocrystal coatings on Mo foil when the number of flashes > 10. In addition, there is no low- or high-density cracking after IPL annealing of CZTS coatings on Mo foil in sulfur even with long annealing times (*i.e.*, high number of flashes). After 50 flashes, the coating annealed in sulfur is continuous with no signs of surface cracking. As speculated from the simulation studies, the reduction of heating and cooling cycles removes the driving force for crack formation. However, we do not observe any increase in nanocrystal grain sizes as measured from the width of the

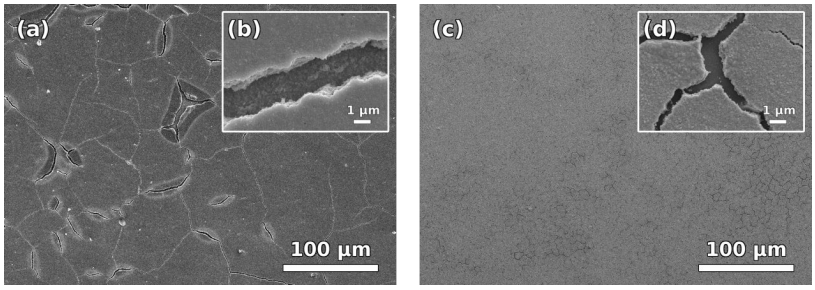

Figure 7.22 SEM images of CZTS nanocrystal coatings on (b & d) Mo foil and (a & c) Mo-coated SLG after IPL annealing with (a & b) one 9.0 J/cm^2 flash and (c & d) ten 11.6 J/cm^2 flashes. Use of Mo foil prevents (b,d) high density cracking at moderate IPL energy densities and (c,d) blistering at high IPL energy density.

CZTS XRD peak at 28.5° using the Scherrer's equation. Comparison of the SEM images before and after annealing in sulfur vapor using 10, 35, and 50 flashes confirms that grains do not grow substantially. It is important to note that the presence of sulfur vapor would reduce the intensity of the light reaching the CZTS coating since sulfur vapor absorbs in the relevant electromagnetic spectrum.[212] With 1 mg of sulfur in the annealing ampule, this absorption is likely insignificant but may be need to be considered at higher sulfur pressures.

While we eliminated cracking and blistering during IPL by annealing in sulfur and by using a metal foil as the substrate, none of our IPL annealing experiments led to CZTS grain growth. Three probable factors may be limiting grain; short annealing times, low sulfur pressure, and the lack of alkali-metals during annealing. The annealing studies shown in Figure 7.23 were limited to 50 or less flashes with total processing times of < 3 minutes. We increased the IPL annealing time by increasing the number of flashes. Figure 7.25 shows SEM images of a CZTS nanocrystal coating on Mo foil after IPL annealing with 10 mg sulfur in the ampule for 400 flashes (11.6 J/cm^2, 3.5 ms flash duration, 2.31 s flash period). Figure 7.26 displays the XRD pattern and Raman spectrum for the annealed coating. After 400 flashes, the grain size determined from the full-width half maximum of the (112) peak remains the same as that measured before annealing (~32 nm). Cracks and blistering could be seen in parts of the coating and are attributed to CZTS decomposition at the coating-substrate interface.

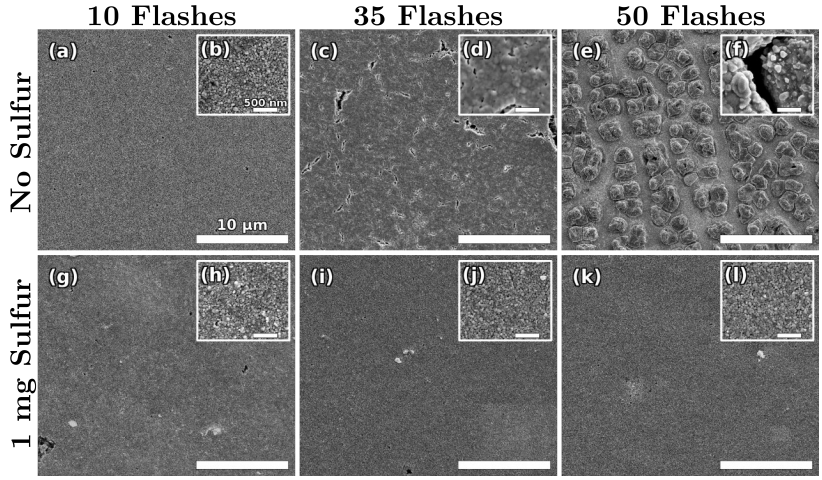

Figure 7.23 SEM images of CZTS nanocrystal coatings on Mo foil after IPL annealing at an energy density of 11.6 J/cm^2 without sulfur for (a,b) 10 flashes, (c,d) 35 flashes, and (e,f) 50 flashes and with 1 mg of sulfur loaded into the ampule for (g,h) 10 flashes, (i,j) 35 flashes, and (k,l) 50 flashes.

7.5 Outlook for CZTS Grain Growth During IPL Annealing

As reported by others, grain growth in CZTS nanocrystal coatings increases with sulfur vapor pressure during annealing.[60,213] From Figure 7.25, we attribute the lack of grain growth in our experiments to the low sulfur vapor pressure in the ampule during IPL annealing and the absence of alkali metals during annealing. Since only the coating and substrate are heated during IPL annealing, the quartz ampule remains close to room temperature. This leads to condensation of sulfur vapor onto the sides of the ampule. This condensation is observed visually. Consequently, the vapor pressure of the sulfur during annealing is much lower than those that we could maintain during thermal annealing. In thermal annealing the ampule is isothermal at a well-defined temperature and the sulfur vapor pressure can be precisely controlled. IPL annealing is not isothermal and maintaining sulfur vapor over the substrate without external heating is difficult. While the sulfur vapor present in the ampule is adequate to prevent CZTS decomposition, it is still too low to provide the necessary driving force for grain growth. In addition, the Mo foil contains no alkali metals (Na and K)

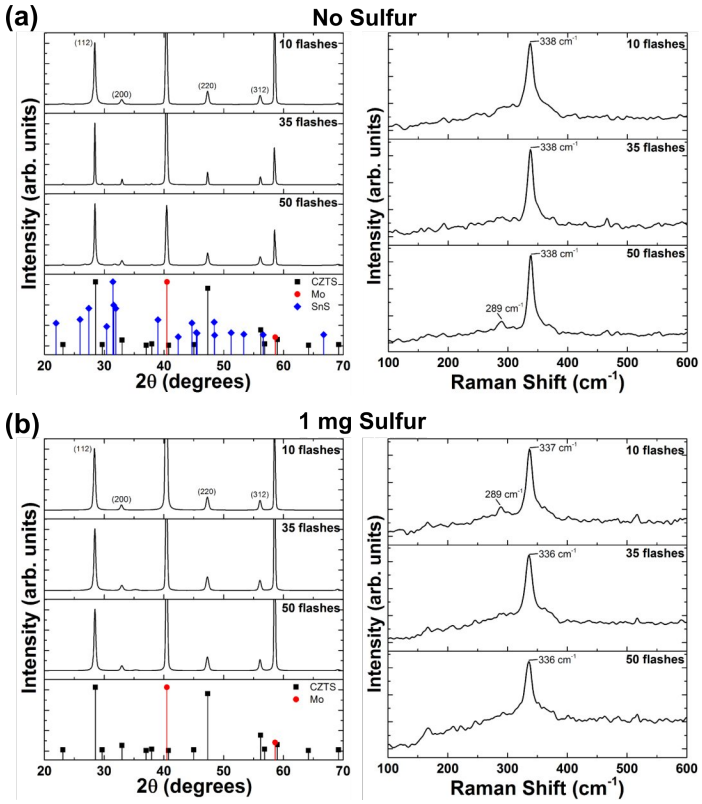

Figure 7.24 XRD patterns and Raman spectra of CZTS nanocrystal coatings on molybdenum foil substrates after IPL annealing at 11.6 J/cm^2 for 10, 35, and 50 flashes (a) with no additional sulfur and (b) 1 mg of sulfur in the quartz ampule.

as is the case with the commonly used Mo-coated SLG substrates. During thermal annealing, Na and K diffuse from the SLG substrate and aid grain growth.[106,124] This mechanism is absent during IPL annealing on Mo. The absence of an alkali-metals in the CZTS film during annealing has been shown to substantially reduce grain growth rates.[60,106] Methods to enhance the sulfur vapor pressure over the substrate and/or introduction of Na and K into the CZTS coating are necessary to achieve grain growth using IPL annealing. Achieving these in a practical cost effective manner are challenging but they are currently under study in our group.

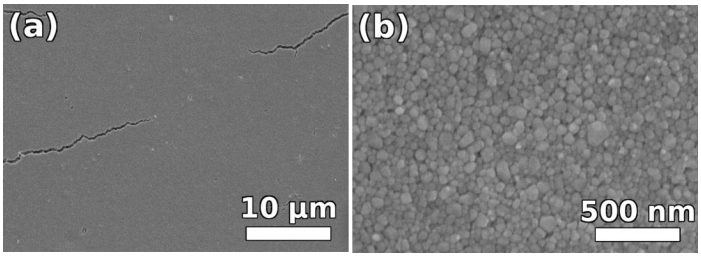

Figure 7.25 SEM images of CZTS nanocrystal coating on Mo foil after IPL annealing in sulfur with 400 flashes at an energy density of 11.7 J/cm^2. Annealing was conducted with 10 mg of sulfur loaded into the annealing ampule.

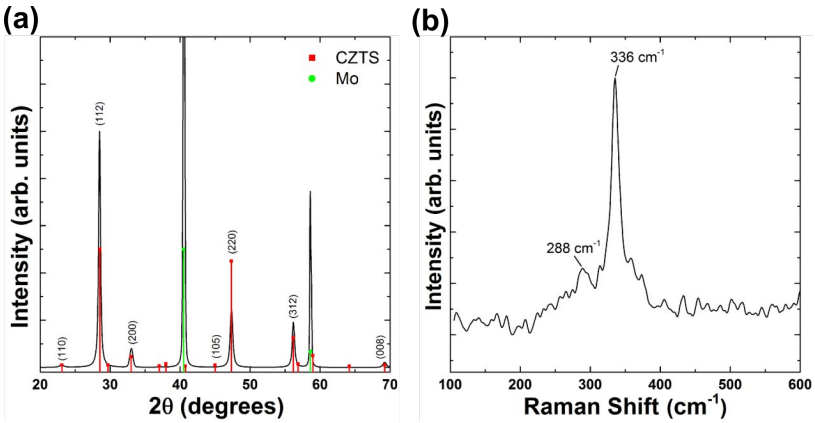

Figure 7.26 (a) XRD pattern and (b) Raman spectrum for CZTS nanocrystal coating on Mo foil after IPL annealing at 11.6 J/cm^2 for 400 flashes.

7.6 Conclusion

The effect of flash energy density (3.9 to 11.6 J/cm^2) and the number of flashes (1 and 10) on the microstructure of CZTS nanocrystal coatings cast on Mo-coated SLG substrates during IPL annealing was studied. It was found that coatings developed high-density cracks (linear crack density of ~0.2 µm^{-1}) even at low cumulative energy densities. Increasing the flash energy density and number of flashes lead to coating blister formation and low-density cracks (~0.01 µm^{-1}). Experiments revealed two distinct mechanisms for low-density and high-density cracking. Nanocrystal deposits that form inside the blisters during high energy density IPL annealing were analyzed and revealed the presence of CZTS and SnS_2.

We hypothesized that vapor formation at the CZTS-Mo interface upon reaction of CZTS with Mo caused the blistering and low-density cracking. This hypothesis was supported by absence of blistering after IPL annealing of CZTS nanocrystal coatings on quartz substrates. The high density cracking was found to be due to repeated thermal expansion and contraction of the CZTS coatings constrained laterally on the SLG substrate. The CZTS coating cracked, as it was heated and cooled differentially with respect to the SLG substrate that remained relatively cold. The spatiotemporal evolution of the temperatures of the CZTS nanocrystal coating and the substrate during IPL annealing was modeled using a 2-D finite element model. The simulations showed that the temperature of CZTS coatings on low thermal diffusivity substrates (e.g., SLG) increased and decreased rapidly with each light pulse. This rapid heating and cooling resulted in expansion and contraction that cracked the films. Replacing SLG with Mo foil, a high thermal diffusivity material, reduced the magnitude of this differential heating during IPL annealing and eliminated the high density cracking. Coatings annealed in vacuum decomposed and had low-density cracks while those annealed in presence of sulfur vapor and on Mo-foil showed no signs of cracking or decomposition. However, grain growth was negligible for all coatings annealed using IPL. The lack of grain growth was attributed to low sulfur vapor pressure and absence of grain growth enhancing alkali metals (e.g., Na, K) during IPL annealing.

Chapter 8

Future Directions

Two fundamental areas of research were explored in this thesis: continuous-amenable coating of nanoparticle dispersions and microstructure evolution of CZTS nanocrystals coatings during annealing. Interest in cost-efficient coating operations to form nanocrystal coatings is likely to increase as more uses for and methods to synthesize nanoparticles are discovered. Aerosol coating methods may find usefulness in operations that, like thin film solar cells, require > 1 μm thick coatings. With current techniques, surface roughness and the uniformity of thin (< 100 nm) coatings are unsuitable for most applications like semiconductor layers in printed electronics.

Successfully scaling spray coating methods to large production volumes will require reductions in material waste. The coating procedures utilized must generate as little waste as possible. In addition, the aerosol coating procedures investigated here, aerosol jet printing and ultrasonic spray coating, while inexpensive compared to vacuum deposition systems, require significant upfront capital costs and ongoing maintenance. Both processes would need numerous deposition systems or nozzle arrays to scale to appreciable economies of scale. Methods to improve upon these shortcomings especially those capable of increasing single-pass coating area and thickness while maintaining coating microstructure would be well worth further research.

CZTS as a thin film solar cell material has a more uncertain future. From the research presented here, it is clear that annealing and processing of CZTS is sensitive to a wide array

of variables that require precise control to produce high-quality films. The two biggest stumbling blocks are the relatively long annealing time (> 30 min at 550 °C or higher) and, more significantly, the high S/Se vapor required to induce grain growth. Implementation of a non-batch based annealing operation capable of providing consistent S/Se vapor would be difficult implement and operate continuously.

Beyond the processing difficulties involved in forming CZTS films, efforts to overcome its fundamental electrical deficiencies have been slowed with no improvement in record efficiencies since 2013.[29] CZTSSe solar cells have suffered from unexpectedly low open-circuit voltage (V_{OC}) compared to the structurally similar CIGS.[23,214–216] Recent work on the effects of post-annealing heat treatments have indicated the presence of surface-state traps that are removed upon oxidation in atmosphere.[50,217,218] Further research into deep level traps that are limiting the efficiency of CZTS is required.

Regardless of the CZTS's future in thin film solar cells, the observations and understanding of the film growth and sintering in CZTS nanocrystal coatings may find utility in other materials. The abnormal surface-oriented crystal growth and carbon content-dependent growth are unique phenomenon that have not yet been observed in other materials to our knowledge. These insights may prove useful for materials with similar growth behavior.

Bibliography

(1) *International Energy Outlook 2013*, U.S. Energy Information Agency, 2013, p. 312.

(2) M. Fay, S. Hallegatte, A. Vogt-Schilb, J. Rozenberg, U. Narloch and T. Kerr, *Decarbonizing Development*, The World Bank, 2015.

(3) *Fifth Assessment Report of the Intergovernmental Panel on Climate Change*, Cambridge University Press, Cambridge, UK, 2014.

(4) M. Frondel, N. Ritter and C. M. Schmidt, *Energy Policy*, 2008, **36**, 4198–4204.

(5) S. Borenstein, *The Private and Public Economics of Renewable Electricity Generation*, tech. rep., National Bureau of Economic Research, Cambridge, MA, 2011, p. 28.

(6) S. Hagerman, P. Jaramillo and M. G. Morgan, *Energy Policy*, 2016, **89**, 84–94.

(7) M. Green, J. Zhao, A. Wang and S. Wenham, *Sol. Energy Mater. Sol. Cells*, 2001, **65**, 9–16.

(8) M. A. Green, K. Emery, Y. Hishikawa, W. Warta and E. D. Dunlop, *Prog. Photovolt: Res. Appl.*, 2015, **23**, 1–9.

(9) *Photovoltaics Report*, tech. rep. August, Fraunhofer Institute for Solar Energy Systems (ISE), 2015, p. 43.

(10) J. Jean, P. R. Brown, R. L. Jaffe, T. Buonassisi and V. Bulović, *Energy Environ. Sci.*, 2015, **8**, 1200–1219.

(11) H. C. Kim, V. Fthenakis, J.-K. Choi and D. E. Turney, *J. Ind. Ecol.*, 2012, **16**, S110–S121.

(12) D. D. Hsu, P. O'Donoughue, V. Fthenakis, G. A. Heath, H. C. Kim, P. Sawyer, J.-K. Choi and D. E. Turney, *J. Ind. Ecol.*, 2012, **16**, S122–S135.

(13) V. Fthenakis and K. Zweibel, National Center for Photovoltaics Review Meeting, Denver, CO, Denver, 2003.

(14) *Critical Materials Strategy*, U.S. Department of Energy, 2011.

(15) R. L. Moss, E. Tzimas, H. Kara, P. Willis and J. Kooroshy, *Critical Metals in Strategic Energy Technologies*, European Commission Joint Research Centre Institute for Energy and Transport, 2011.

(16) M. Woodhouse, A. Goodrich, R. Margolis, T. L. James, M. Lokanc and R. Eggert, *IEEE J. Photovolt.*, 2013, **3**, 833–837.

(17) G. Kavlak, J. McNerney, R. L. Jaffe and J. E. Trancik, *Energy Environ. Sci.*, 2015, **8**, 1651–1659.

(18) M. Marwede and A. Reller, *J. Ind. Ecol.*, 2014, **18**, 254–267.

(19) M. Marwede, W. Berger, M. Schlummer, A. Maurer and A. Reller, *Renewable Energy*, 2013, **55**, 220–229.

(20) J. Nelson, A. Gambhir and N. Ekins-Daukes, Grantham Institute for Climate Change Briefing Paper No. 11, 2014.

(21) *Act Now to Handle The Coming Wave of Toxic PV Waste* (2015).

(22) L. G. Martinez, *Solar Photovoltaic Panels: The Other Side of The Story*, United Nations Industrial Development Organization, 2015.

(23) D. B. Mitzi, O. Gunawan, T. K. Todorov, K. Wang and S. Guha, *Sol. Energy Mater. Sol. Cells*, 2011, **95**, 1421–1436.

(24) K. Ito and T. Nakazawa, *Jpn. J. Appl. Phys.*, 1988, **27**, 2094–2097.

(25) T. M. Friedlmeier, N. Wieser, T. Walter, H. Dittrich and H.-W. Schock, Proceedings of the 14th European Photovoltaic Solar Energy Conference, 1997, pp. 1242–1245.

(26) T. Eguchi, T. Maki, S. Tajima, T. Ito and T. Fukano, Technical Digest, 21st International Photovoltaic Science and Engineering Conference, Fukuoka, 2011, 4D–3P–24.

(27) I. Repins, C. Beall, N. Vora, C. DeHart, D. Kuciauskas, P. Dippo, B. To, J. Mann, W.-C. Hsu, A. Goodrich and R. Noufi, *Sol. Energy Mater. Sol. Cells*, 2012, **101**, 154–159.

(28) B. Shin, O. Gunawan, Y. Zhu, N. A. Bojarczuk, S. J. Chey and S. Guha, *Prog. Photovolt: Res. Appl.*, 2013, **21**, 72–76.

(29) W. Wang, M. T. Winkler, O. Gunawan, T. Gokmen, T. K. Todorov, Y. Zhu and D. B. Mitzi, *Adv. Energy Mater.*, 2013, **4**, 1301465.

(30) C. K. Miskin, W.-C. Yang, C. J. Hages, N. J. Carter, C. S. Joglekar, E. A. Stach and R. Agrawal, *Prog. Photovolt: Res. Appl.*, 2015, **23**, 654–659.

(31) B. P. Rand, J. Genoe, P. Heremans and J. Poortmans, *Prog. Photovolt: Res. Appl.*, 2007, **15**, 659–676.

(32) T. P. Dhakal and S. Harve, Photovoltaic Specialist Conference (PVSC), 2015 IEEE 42nd, 2015, pp. 1–4.

(33) D. A. R. Barkhouse, O. Gunawan, T. Gokmen, T. K. Todorov and D. B. Mitzi, *Prog. Photovolt: Res. Appl.*, 2012, **20**, 6–11.

(34) S. G. Haass, M. Diethelm, M. Werner, B. Bissig, Y. E. Romanyuk and A. N. Tiwari, *Adv. Energy Mater.*, 2015, **5**, 1500712.

(35) J. van Embden, A. S. R. Chesman and J. J. Jasieniak, *Chem. Mater.*, 2015, **27**, 2246–2285.

(36) J. van Embden, A. S. R. Chesman, E. D. Gaspera, N. W. Du, S. E. Watkins and J. J. Jasieniak, *J. Am. Chem. Soc.*, 2014, **136**, 5237–5240.

(37) Q. Guo, H. W. Hillhouse and R. Agrawal, *J. Am. Chem. Soc.*, 2009, **131**, 11672–11673.

(38) S. C. Riha, B. a. Parkinson and A. L. Prieto, *J. Am. Chem. Soc.*, 2009, **131**, 12054–12055.

(39) B.-I. Park, Y. Hwang, S. Y. Lee, J.-S. Lee, J.-K. Park, J. Jeong, J. Y. Kim, B. Kim, S.-H. Cho and D.-K. Lee, *Nanoscale*, 2014, **6**, 11703–11711.

(40) R. Ma, F. Yang, S. Li, X. Zhang, X. Li, S. Cheng and Z. Liu, *Appl. Surf. Sci.*, 2016, **368**, 8–15.

(41) Y. Zhou, S. Xi, C. Sun and H. Wu, *Mater. Lett.*, 2016, **169**, 176–179.

(42) S. W. Shin, J. H. Han, C. Y. Park, A. V. Moholkar, J. Y. Lee and J. H. Kim, *J. Alloys Compd.*, 2012, **516**, 96–101.

(43) X. Yang, J. Xu, L. Xi, Y. Yao, Q. Yang, C. Y. Chung and C.-S. Lee, *J. Nanopart. Res.*, 2012, **14**, 931.

(44) H. Zhou, W.-C. Hsu, H.-S. Duan, B. Bob, W. Yang, T.-B. Song, C.-J. Hsu and Y. Yang, *Energy Environ. Sci.*, 2013, **6**, 2822–2838.

(45) S. Schorr, *Copper Zinc Tin Sulfide-Based Thin-Film Solar Cells*, ed. K. Ito, John Wiley & Sons Ltd, West Sussex, United Kingdom, 1st, 2014, pp. 53–74.

(46) X. Lu, Z. Zhuang, Q. Peng and Y. Li, *Chem. Commun.*, 2011, **47**, 3141–3143.

(47) M. Li, W.-h. Zhou, J. Guo, Y.-l. Zhou, Z.-l. Hou, J. Jiao, Z.-j. Zhou, Z.-l. Du and S.-x. Wu, *J. Phys. Chem. C*, 2012, **116**, 26507–26516.

(48) U. V. Ghorpade, M. Suryawanshi, S. W. Shin, C. W. Hong, I. Y. Kim, J. Moon, J. Yun, J. H. Kim and S. S. Kolekar, *Phys. Chem. Chem. Phys.*, 2015, **17**, 19777–19788.

(49) X. Lin, J. Kavalakkatt, K. Kornhuber, D. Abou-Ras, S. Schorr, M. C. Lux-Steiner and A. Ennaoui, *R. Soc. Chem. Adv.*, 2012, **2**, 9894–9898.

(50) Q. Guo, G. M. Ford, W.-C. Yang, B. C. Walker, E. A. Stach, H. W. Hillhouse and R. Agrawal, *J. Am. Chem. Soc.*, 2010, **132**, 17384–17386.

(51) C. Steinhagen, M. G. Panthani, V. Akhavan, B. Goodfellow, B. Koo and B. A. Korgel, *J. Am. Chem. Soc.*, 2009, **131**, 12554–12555.

(52) B. D. Chernomordik, A. E. Béland, N. D. Trejo, A. A. Gunawan, D. D. Deng, K. A. Mkhoyan and E. S. Aydil, *J. Mater. Chem. A*, 2014, **2**, 10389–10395.

(53) Y. Kim, K. Woo, I. Kim, Y. S. Cho, S. Jeong and J. Moon, *Nanoscale*, 2013, **5**, 10183–10188.

(54) S. C. Shei and P. Y. Lee, *IEEE Trans. Nanotechnol.*, 2013, **12**, 532–538.

(55) H. Wei, W. Guo, Y. Sun, Z. Yang and Y. Zhang, *Mater. Lett.*, 2010, **64**, 1424–1426.

(56) A. D. Collord and H. W. Hillhouse, *Sol. Energy Mater. Sol. Cells*, 2015, **141**, 383–390.

(57) C. Coughlan and K. M. Ryan, *CrystEngComm*, 2015, **17**, 6914–6922.

(58) S. Singh, P. Liu, A. Singh, C. Coughlan, J. Wang, M. Lusi and K. M. Ryan, *Chem. Mater.*, 2015, **27**, 4742–4748.

(59) A. Khare, A. W. Wills, L. M. Ammerman, D. J. Norris and E. S. Aydil, *Chem. Commun.*, 2011, **47**, 11721–11723.

(60) B. D. Chernomordik, A. E. Béland, D. D. Deng, L. F. Francis and E. S. Aydil, *Chem. Mater.*, 2014, **26**, 3191–3201.

(61) Y. Zou, X. Su and J. Jiang, *J. Am. Chem. Soc.*, 2013, **135**, 18377–18384.

(62) B. S. Tosun, B. D. Chernomordik, A. A. Gunawan, B. Williams, K. A. Mkhoyan, L. F. Francis and E. S. Aydil, *Chem. Commun.*, 2013, **49**, 3549–3551.

(63) C. Dun, W. Huang, H. Huang, J. Xu, N. Zhou, Y. Zheng, H. Tsai, W. Nie, D. R. Onken, Y. Li and D. L. Carrol, *J. Phys. Chem. C*, 2014, **118**, 30302–30308.

(64) K. K. Price, A. V. McCormick and L. F. Francis, *Langmuir*, 2012, **28**, 10329–10333.

(65) R. C. Chiu, T. J. Garino and M. J. Cima, *J. Am. Ceram. Soc.*, 1993, **76**, 2257–2264.

(66) M. Kaelin, D. Rudmann, F. Kurdesau, H. Zogg, T. Meyer and A. N. Tiwari, *Thin Solid Films*, 2005, **480-481**, 486–490.

(67) G. M. Ford, Q. Guo, R. Agrawal and H. W. Hillhouse, *Chem. Mater.*, 2011, **23**, 2626–2629.

(68) Q. Guo, G. M. Ford, R. Agrawal and H. W. Hillhouse, *Prog. Photovolt: Res. Appl.*, 2013, **21**, 64–71.

(69) V. T. Tiong, Y. Zhang, J. M. Bell and H. Wang, *R. Soc. Chem. Adv.*, 2015, **5**, 20178–20185.

(70) J. Jasieniak, B. I. MacDonald, S. E. Watkins and P. Mulvaney, *Nano Lett.*, 2011, **11**, 2856–2864.

(71) V. A. Akhavan, B. W. Goodfellow, M. G. Panthani, D. K. Reid, D. J. Hellebusch, T. Adachi and B. A. Korgel, *Energy Environ. Sci.*, 2010, **3**, 1600–1606.

(72) Y. Zhang, N. Suyama, M. Goto, J. Kuwana, K. Sugimoto and T. Satake, *Jpn. J. Appl. Phys.*, 2015, **54**, 08KC05.

(73) G. Larramona and S. Bourdais, *J. Phys. Chem. Lett.*, 2014, **5**, 3763–3767.

(74) S. Ahn, K. H. Kim, J. H. Yun and K. H. Yoon, *J. Appl. Phys.*, 2009, **105**, 113533.

(75) PAREXUSA, *Understanding Conventional & HVLP Spray Guns*, tech. rep., Parex USA General.

(76) R. J. Lang, *J. Acoust. Soc.*, 1962, **34**, 6–8.

(77) R. C. Chiu and M. J. Cima, *J. Am. Ceram. Soc.*, 1993, **76**, 2769–2777.

(78) J. J. Guo and J. A. Lewis, *J. Am. Ceram. Soc.*, 1999, **82**, 2345–2358.

(79) A. F. Routh and W. B. Russel, *AIChE J.*, 1998, **44**, 2088–2098.

(80) K. a. Shorlin, J. R. de Bruyn, M. Graham and S. W. Morris, *Physical Review. E*, 2000, **61**, 6950–6957.

(81) S. Bohn, J. Platkiewicz, B. Andreotti, M. Adda-Bedia and Y. Couder, *Phys. Rev. E: Stat. Phys., Plasmas, Fluids,* 2005, **71**, 046215.

(82) E. R. Dufresne, E. I. Corwin, N. A. Greenblatt, J. Ashmore, D. Y. Wang, A. D. Dinsmore, J. X. Cheng, X. S. Xie, J. W. Hutchinson and D. A. Weitz, *Phys. Rev. Lett.*, 2003, **91**, 224500.

(83) W. B. Russel, N. Wu and W. Man, *Langmuir*, 2008, **24**, 1721–1730.

(84) C. N. Bucherl, K. R. Oleson and H. W. Hillhouse, *Curr. Opin. Chem. Eng.*, 2013, **2**, 168–177.

(85) M. Law, J. M. Luther, Q. Song, B. K. Hughes, C. L. Perkins and A. J. Nozik, *J. Am. Chem. Soc.*, 2008, **130**, 5974–5985.

(86) M. G. Panthani, V. Akhavan, B. Goodfellow, J. P. Schmidtke, L. Dunn, A. Dodabalapur, P. F. Barbara and B. A. Korgel, *J. Am. Chem. Soc.*, 2008, **130**, 16770–16777.

(87) W. P. Lee and A. F. Routh, *Langmuir*, 2004, **20**, 9885–9888.

(88) K. Singh and M. Tirumkudulu, *Phys. Rev. Lett.*, 2007, **98**, 218302.

(89) J. C. Berg, *An Introduction to Interfaces and Colloids: The Bridge to Nanoscience*, World Scientific, Hackensack, NJ, 1st, 2009.

(90) M. I. Smith and J. S. Sharp, *Langmuir*, 2011, **27**, 8009–8017.

(91) J. H. Prosser, T. Brugarolas, S. Lee, A. J. Nolte and D. Lee, *Nano Lett.*, 2012, **12**, 5287–5291.

(92) K. B. Singh, L. R. Bhosale and M. S. Tirumkudulu, *Langmuir*, 2009, **25**, 4284–4287.

(93) D. M. Holmes, F. Tegeler and W. J. Clegg, *J. Eur. Ceram. Soc.*, 2008, **28**, 1381–1387.

(94) A. Sarkar and M. S. Tirumkudulu, *Soft Matter*, 2011, **7**, 8816–8822.

(95) M. S. Tirumkudulu and W. B. Russel, *Langmuir*, 2005, **21**, 4938–4948.

(96) T. Todorov, M. Kita, J. Carda and P. Escribano, *Thin Solid Films*, 2009, **517**, 2541–2544.

(97) J. J. Urban, D. V. Talapin, E. V. Shevchenko and C. B. Murray, *J. Am. Chem. Soc.*, 2006, **128**, 3248–3255.

(98) J. M. Luther, M. Law, M. C. Beard, Q. Song, M. O. Reese, R. J. Ellingson and A. J. Nozik, *Nano Lett.*, 2008, **8**, 3488–3492.

(99) S. C. Riha, S. J. Fredrick, J. B. Sambur, Y. Liu, A. L. Prieto and B. A. Parkinson, *Appl. Mater. Interfaces*, 2011, **3**, 58–66.

(100) Q. Guo, S. J. Kim, M. Kar, W. N. Shafarman, R. W. Birkmire, E. a. Stach, R. Agrawal and H. W. Hillhouse, *Nano Lett.*, 2008, **8**, 2982–2987.

(101) J. J. Scragg, P. J. Dale, D. Colombara and L. M. Peter, *ChemPhysChem*, 2012, **13**, 3035–3046.

(102) R. Mainz, B. C. Walker, S. S. Schmidt, O. Zander, A. Weber, H. Rodriguez-Alvarez, J. Just, M. Klaus, R. Agrawal and T. Unold, *Phys. Chem. Chem. Phys.*, 2013, **15**, 18281–18289.

(103) W. Wu, Y. Cao, J. V. Caspar, Q. Guo, L. K. Johnson, I. Malajovich, H. D. Rosenfeld and K. R. Choudhury, *J. Mater. Chem. C.*, 2014, **2**, 3777–3781.

(104) W. Ki and H. W. Hillhouse, *Adv. Energy Mater.*, 2011, **1**, 732–735.

(105) C. Platzer-Björkman, J. Scragg, H. Flammersberger, T. Kubart and M. Edoff, *Sol. Energy Mater. Sol. Cells*, 2012, **98**, 110–117.

(106) M. Johnson, M. Manno, X. Zhang, C. Leighton and E. S. Aydil, *J. Vac. Sci. Technol., A*, 2014, **32**, 061203.

(107) B. A. Williams, A. Mahajan, M. A. Smeaton, C. S. Holgate, E. S. Aydil and L. F. Francis, *ACS Applied Materials & Interfaces*, 2015, **7**, 11526–11535.

(108) C. J. Hages and R. Agrawal, *Copper Zinc Tin Sulfide-Based Thin Folm Colar Cells*, ed. K. Ito, John Wiley & Sons, Chichester, UK, 2014, vol. 1, ch. 11, pp. 239–270.

(109) J. J. Scragg, T. Kubart, J. T. Wätjen, T. Ericson, M. K. Linnarsson and C. Platzer-Björkman, *Chem. Mater.*, 2013, **25**, 3162–3171.

(110) Q. Guo, G. M. Ford, H. W. Hillhouse and R. Agrawal, *Nano Lett.*, 2009, **9**, 3060–3065.

(111) B. C. Walker, B. G. Negash, S. M. Szczepaniak, K. W. Brew and R. Agrawal, 39 th IEEE Photovoltaic Specialists Conference, Tampa, FL, 2013, pp. 2548–2551.

(112) S. C. Riha, B. A. Parkinson and A. L. Prieto, *J. Am. Chem. Soc.*, 2011, **133**, 15272–15275.

(113) K. E. Roelofs, Q. Guo, S. Subramoney and J. V. Caspar, *J. Mater. Chem. A*, 2014, **2**, 13464–13470.

(114) S. Ahn, S. Jung, J. Gwak, A. Cho, K. Shin, K. Yoon, D. Park, H. Cheong and J. H. Yun, *Appl. Phys. Lett.*, 2010, **97**, 021905.

(115) H. Katagiri, K. Jimbo, W. S. Maw, K. Oishi, M. Yamazaki, H. Araki and A. Takeuchi, *Thin Solid Films*, 2009, **517**, 2455–2460.

(116) Q. Tian, X. Xu, L. Han, M. Tang, R. Zou, Z. Chen, M. Yu, J. Yang and J. Hu, *CrystEngComm*, 2012, **14**, 3847–3850.

(117) M. Lu, Y. Cao, J. V. Caspar, I. Malajovich, D. Radu and H. D. Rosenfeld, 37th IEEE Photovoltaic Specialists Conference (PVSC), 2011, pp. 000402–000406.

(118) K. Ito, *Copper Zinc Tin Sulfide-Based Thin-Film Solar Cells*, ed. K. Ito, John Wiley & Sons, Chichester, UK, 2014, ch. 1, pp. 3–41.

(119) D. Braunger, D. Hariskos, G. Bilger, U. Rau and H. W. Schock, *Thin Solid Films*, 2000, **361**, 161–166.

(120) D. Rudmann, A. F. da Cunha, M. Kaelin, F. Kurdzesau, H. Zogg, A. N. Tiwari and G. Bilger, *Appl. Phys. Lett.*, 2004, **84**, 1129–1131.

(121) D. Rudmann, D. Brémaud, H. Zogg and A. N. Tiwari, *J. Appl. Phys.*, 2005, **97**, 084903.

(122) J. Granata, J. Sites, S. Asher and R. Matson, 26th IEEE Photovoltaic Specialists Conference (PVSC), 1997, pp. 387–390.

(123) P. Jackson, D. Hariskos, R. Wuerz, W. Wischmann and M. Powalla, *Phys. Status Solidi RRL*, 2014, **8**, 219–222.

(124) M. Johnson, S. V. Baryshev, E. Thimsen, M. Manno, X. Zhang, I. V. Veryovkin, C. Leighton and E. S. Aydil, *Energy Environ. Sci.*, 2014, **7**, 1931–1938.

(125) Y. Yang, X. Kang, L. Huang, S. Wei and D. Pan, *J. Phys. Chem. C*, 2015, **119**, 22797–22802.

(126) T. Gershon, Y. S. Lee, R. Mankad, O. Gunawan, T. Gokmen, D. Bishop, B. McCandless and S. Guha, *Appl. Phys. Lett.*, 2015, **106**, 123905.

(127) C. M. Sutter-Fella, J. A. Stückelberger, H. Hagendorfer, F. La Mattina, L. Kranz, S. Nishiwaki, A. R. Uhl, Y. E. Romanyuk and A. N. Tiwari, *Chem. Mater.*, 2014, **26**, 1420–1425.

(128) H. Zhou, T.-B. Song, W.-C. Hsu, S. Luo, S. Ye, H.-S. Duan, C.-J. Hsu, W. Yang and Y. Yang, *J. Am. Chem. Soc.*, 2013, **135**, 15998–16001.

(129) A. Schellenberger, R. Schlaf, C. Pettenkofer and W. Jaegermann, *Solid State Ionics*, 1993, **66**, 307–312.

(130) J. Sangster and A. Pelton, *J. Phase Equilib.*, 1997, **18**, 185–189.

(131) J. Sangster and A. D. Pelton, *J. Phase Equilib.*, 1997, **18**, 89–96.

(132) Y.-R. Lin, V. Tunuguntla, S.-Y. Wei, W.-C. Chen, D. Wong, C.-H. Lai, L.-K. Liu, L.-C. Chen and K.-H. Chen, *Nano Energy*, 2015, **16**, 438–445.

(133) L. Q. Phuong, M. Okano, Y. Yamada, A. Nagaoka, K. Yoshino, Y. Kanemitsu and T. Agency, 42nd Photovoltaic Specialist Conference (PVSC), IEEE, 2015, pp. 1–5.

(134) A. Nagaoka, H. Miyake, T. Taniyama, K. Kakimoto, Y. Nose, M. a. Scarpulla and K. Yoshino, *Appl. Phys. Lett.*, 2014, **104**, 152101.

(135) T. Maeda, A. Kawabata and T. Wada, *Phys. Status Solidi C*, 2015, **12**, 631–637.

(136) H. Xie, S. López-Marino, T. Olar, Y. Sánchez, M. Neuschitzer, F. Oliva, S. Giraldo, V. Izquierdo-Roca, I. Lauermann, A. Pérez-Rodríguez and E. Saucedo, *Appl. Mater. Interfaces*, 2016, **8**, 5017–5024.

(137) D. Aldakov, A. Lefrançois and P. Reiss, *J. Mater. Chem. C*, 2013, **1**, 3756.

(138) A. Khare, B. Himmetoglu, M. Johnson, D. J. Norris, M. Cococcioni and E. S. Aydil, *J. Appl. Phys.*, 2012, **111**, 083707.

(139) C. Jiang, J.-S. Lee and D. V. Talapin, *J. Am. Chem. Soc.*, 2012, **134**, 5010–5013.

(140) A. Nag, M. V. Kovalenko, J.-S. Lee, W. Liu, B. Spokoyny and D. V. Talapin, *J. Am. Chem. Soc.*, 2011, **133**, 10612–10620.

(141) M. Green, *J. Mater. Chem.*, 2010, **20**, 5797–5809.

(142) S. Levcenko, G. Gurieva, M. Guc and A. Nateprov, *Moldavian J. Phys. Sci.*, 2009, **8**.

(143) G. Socrates, *Infrared and Raman Characteristic Group Frequencies: Tables and Charts*, John Wiley & Sons, 3rd edn., 2004, p. 347.

(144) W. W. Yu, Y. A. Wang and X. Peng, *Chem. Mater.*, 2003, **15**, 4300–4308.

(145) S. Mourdikoudis and L. M. Liz-Marzán, *Chem. Mater.*, 2013, **25**, 1465–1476.

(146) Y. K. Jung, J. I. Kim and J.-K. Lee, *J. Am. Chem. Soc.*, 2010, **132**, 178–184.

(147) D. Pan, L. An, Z. Sun, W. Hou, Y. Yang, Z. Yang and Y. Lu, *Journal of American Chemical Society*, 2008, **130**, 5620–5621.

(148) P. J. Thistlethwaite and M. S. Hook, *Langmuir*, 2000, **16**, 4993–4998.

(149) L. Zhang, R. He and H.-C. Gu, *Appl. Surf. Sci.*, 2006, **253**, 2611–2617.

(150) P. R. Griffiths and J. A. De Haseth, *Fourier Transform Infrared Spectrometry*, John Wiley & Sons, 2nd edn., 2007, p. 704.

(151) J. M. Hoey, A. Lutfurakhmanov, D. L. Schulz and I. S. Akhatov, *Journal of Nanotechnology*, 2012, 324380.

(152) C. Werner, D. Godlinski, V. Zöllmer and M. Busse, *J. Mater. Sci.: Mater. Electron.*, 2013, **24**, 4367–4377.

(153) D. Zhao, T. Liu, J. G. Park, M. Zhang, J.-M. Chen and B. Wang, *Microelectron. Eng.*, 2012, **96**, 71–75.

(154) A. Mette, P. L. Richter and S. W. Glunz, *Prog. Photovolt: Res. Appl.*, 2007, **15**, 621–627.

(155) C. Yang, E. Zhou, S. Miyanishi, K. Hashimoto and K. Tajima, *Appl. Mater. Interfaces*, 2011, **3**, 4053–8.

(156) A. Mahajan, C. D. Frisbie and L. F. Francis, *Appl. Mater. Interfaces*, 2013, **5**, 4856–4864.

(157) D. Sen, S. Mazumder, J. S. Melo, A. Khan, S. Bhattyacharya and S. F. D'Souza, *Langmuir*, 2009, **25**, 6690–6695.

(158) J. Halme, J. Saarinen and P. Lund, *Sol. Energy Mater. Sol. Cells*, 2006, **90**, 887–899.

(159) M. Y. Valakh, V. M. Dzhagan, I. S. Babichuk, X. Fontane, A. Perez-Rodriquez and S. Schorr, *JETP Lett.*, 2013, **98**, 255–258.

(160) R. Caballero, E. Garcia-Llamas, J. M. Merino, M. León, I. Babichuk, V. Dzhagan, V. Strelchuk and M. Valakh, *Acta Mater.*, 2014, **65**, 412–417.

(161) E. Gu, C. Yan, F. Liu, Y. Liu, Z. Su, K. Zhang, Z. Chen, J. Li and Y. Liu, *J. Mater. Sci.: Mater. Electron.*, 2015, **26**, 1932–1939.

(162) G. Chen, C. Yuan, J. Liu, Z. Huang, S. Chen, W. Liu, G. Jiang and C. Zhu, *J. Power Sources*, 2015, **276**, 145–152.

(163) T. Prabhakar and N. Jampana, *Sol. Energy Mater. Sol. Cells*, 2011, **95**, 1001–1004.

(164) J. Goldstein, D. E. Newbury, P. Echlin, D. C. Joy, A. D. J. Roming, C. E. Lyman, C. Fiori and E. Lifshin, *Scanning Electron Microscopy and X-ray Microanalysis*, Springer, New York, NY, 3rd, 2007, p. 690.

(165) T. J. Huang, X. Yin, C. Tang, G. Qi and H. Gong, *ChemSusChem*, 2016, **9**, 1032–1041.

(166) A. de Kergommeaux, A. Fiore, N. Bruyant, F. Chandezon, P. Reiss, A. Pron, R. de Bettignies and J. Faure-Vincent, *Sol. Energy Mater. Sol. Cells*, 2011, **95**, 39–43.

(167) M. Zhou, Y. Gong, J. Xu, G. Fang, Q. Xu and J. Dong, *J. Alloys Compd.*, 2013, **574**, 272–277.

(168) X. Xin, M. He, W. Han, J. Jung and Z. Lin, *Angew. Chem. Int. Ed.*, 2011, **50**, 11739–11742.

(169) L. Li, N. Coates and D. Moses, *J. Am. Chem. Soc.*, 2010, **132**, 22–23.

(170) V. A. Akhavan, B. W. Goodfellow, M. G. Panthani, C. Steinhagen, T. B. Harvey, C. J. Stolle and B. A. Korgel, *J. Solid State Chem.*, 2012, **189**, 2–12.

(171) G. Larramona, S. Bourdais, A. Jacob, C. Choné, T. Muto, Y. Cuccaro, B. Delatouche, C. Moisan, D. Péré and G. Dennler, *R. Soc. Chem. Adv.*, 2014, **4**, 14655–14662.

(172) M. Werner, C. M. Sutter-Fella, H. Hagendorfer, Y. E. Romanyuk and A. N. Tiwari, *Phys. Status Solidi A*, 2015, **212**, 116–120.

(173) S. López-Marino et al., *J. Mater. Chem. A*, 2016, **4**, 1895–1907.

(174) W. M. Hlaing OO, J. L. Johnson, a. Bhatia, E. a. Lund, M. M. Nowell and M. a. Scarpulla, *J. Electron. Mater.*, 2011, **40**, 2214–2221.

(175) B. D. Chernomordik, P. M. Ketkar, A. K. Hunter, A. E. Béland, D. D. Deng and E. S. Aydil, *Chem. Mater.*, 2016, **28**, 1266–1276.

(176) C. A. Schneider, W. S. Rasband and K. W. Eliceiri, *Nat. Methods*, 2012, **9**, 671–675.

(177) J. Schindelin et al., *Nat. Methods*, 2012, **9**, 676–682.

(178) P. Ravindran and E. J. Davis, *J. Colloid Interface Sci.*, 1982, **85**, 278–288.

(179) J. Sears, K. Huang, S. Ray and H. Fairbanks, Ultrasonics Symposium Proceedings, 1977, pp. 131–133.

(180) L. Besley and G. Bottomley, *J. Chem. Thermodyn.*, 1974, **6**, 577–580.

(181) National Institute for Occupational Safety and Health (NIOSH), *Cyclohexanone*, eng, 2015.

(182) H. Y. Erbil and Y. Avci, *Langmuir*, 2002, **18**, 5113–5119.

(183) S. Uchiyama, S. Aoyagi and M. Ando, *Atmos. Environ.*, 2004, **38**, 6319–6326.

(184) S. Bose, S. S. Keller, T. S. Alstrøm, A. Boisen and K. Almdal, *Langmuir*, 2013, **29**, 6911–6919.

(185) Q. Zhang, M. Gao, R. Zhao and X. Cheng, *Phys. Rev. E: Stat. Phys., Plasmas, Fluids,* 2015, **92**, 1–8.

(186) T. Tanaka, T. Nagatomo, D. Kawasaki, M. Nishio, Q. Guo, A. Wakahara, A. Yoshida and H. Ogawa, *J. Phys. Chem. Solids*, 2005, **66**, 1978–1981.

(187) K. Ramasamy, M. A. Malik and P. O'Brien, *Chem. Sci.*, 2011, **2**, 1170–1172.

(188) S. Ahmed, K. B. Reuter, O. Gunawan, L. Guo, L. T. Romankiw and H. Deligianni, *Adv. Energy Mater.*, 2012, **2**, 253–259.

(189) H. Xin, J. K. Katahara, I. L. Braly and H. W. Hillhouse, *Adv. Energy Mater.*, 2014, **4**, 1301823.

(190) W.-C. Hsu, H. Zhou, S. Luo, T.-B. Song, Y.-T. Hsieh, H.-S. Duan, S. Ye, W. Yang, C.-J. Hsu, C. Jiang, B. Bob and Y. Yang, *ACS Nano*, 2014, **8**, 9164–9172.

(191) L. Vauche, J. Dubois, A. Laparre, M. Pasquinelli, S. Bodnar, P.-P. Grand and S. Jaime, *Phys. Status Solidi A*, 2015, **212**, 103–108.

(192) M. R. R. Menon, S. Ranjbar, M. G. Sousa, P. A. Fernandes and A. F. da Cunha, *Mater. Res. Express*, 2014, **1**, 045046.

(193) C. Munn, S. Haran and I. Seok, Proceedings of SPIE, ed. V. K. Varadan, 2013, vol. 8691, 86911A.

(194) M. Hösel and F. C. Krebs, *J. Mater. Chem.*, 2012, **22**, 15683.

(195) J. Perelaer, R. Abbel, S. Wünscher, R. Jani, T. van Lammeren and U. S. Schubert, *Adv. Mater.*, 2012, **24**, 2620–2625.

(196) R. Dharmadasa, I. Dharmadasa and T. Druffel, *Adv. Eng. Mater.*, 2014, **16**, 1351–1361.

(197) H. Colorado, S. Dhage and H. Hahn, *Mater. Sci. Eng., B*, 2011, **176**, 1161–1168.

(198) R. Dharmadasa, B. Lavery, I. M. Dharmadasa and T. L. Druffel, *Appl. Mater. Interfaces*, 2014, **6**, 5034–5040.

(199) S. R. Dhage, H.-S. Kim and H. T. Hahn, *J. Electron. Mater.*, 2011, **40**, 122–126.

(200) M. Singh, J. Jiu, T. Sugahara and K. Suganuma, *Thin Solid Films*, 2014, **565**, 11–18.

(201) E. C. Beder, C. D. Bass and W. L. Shackleford, *Appl. Opt.*, 1971, **10**, 2263–2268.

(202) A.-J. Cheng, M. Manno, A. Khare, C. Leighton, S. A. Campbell and E. S. Aydil, *J. Vac. Sci. Technol., A*, 2011, **29**, 051203.

(203) S. Sohila, M. Rajalakshmi, C. Ghosh, A. K. Arora and C. Muthamizhchelvan, *J. Alloys Compd.*, 2011, **509**, 5843–5847.

(204) D. H. Timm, B. B. Guzina and V. R. Voller, *Int. J. Solids Struct.*, 2003, **40**, 125–142.

(205) J. J. Scragg, T. Ericson, T. Kubart, M. Edoff and C. Platzer-Björkman, *Chem. Mater.*, 2011, **23**, 4625–4633.

(206) J. J. Scragg, J. T. Wätjen, M. Edoff, T. Ericson, T. Kubart and C. Platzer-Björkman, *J. Am. Chem. Soc.*, 2012, **134**, 19330–19333y.

(207) M. Huang, Z. Suo, Q. Ma and H. Fujimoto, *J. Mater. Res.*, 2000, **15**, 1239–1242.

(208) G. Kaune, S. Hartnauer and R. Scheer, *Phys. Status Solidi A*, 2014, **211**, 1991–1996.

(209) X. He and H. Shen, *Phys. Scr.*, 2012, **85**, 035302.

(210) *High temperature glass melt property database for process modeling*, ed. T. P. Seward III and T. Vascott, The American Ceramic Society, Westerville, Ohio, 1st, 2005.

(211) Y. Zhang, Q. Ye, J. Liu, H. Chen, X. He, C. Liao, J. Han, H. Wang, J. Mei and W. Lau, *R. Soc. Chem. Adv.*, 2014, **4**, 23666–23669.

(212) R. I. Billmers and A. L. Smith, *J. Phys. Chem.*, 1991, **95**, 4242–4245.

(213) M. G. Sousa, A. F. da Cunha, P. A. Fernandes, J. P. Teixeira, R. A. Sousa and J. P. Leitão, *Sol. Energy Mater. Sol. Cells*, 2014, **126**, 101–106.

(214) O. Gunawan, T. K. Todorov and D. B. Mitzi, *Appl. Phys. Lett.*, 2010, **97**, 233506.

(215) T. Gokmen, O. Gunawan and D. B. Mitzi, *Appl. Phys. Lett.*, 2014, **105**, 033903.

(216) D. W. Miller, C. W. Warren, O. Gunawan, T. Gokmen, D. B. Mitzi and J. D. Cohen, *Appl. Phys. Lett.*, 2012, **101**, 142106.

(217) K. Sardashti, R. Haight, T. Gokmen, W. Wang, L. Y. Chang, D. B. Mitzi and A. C. Kummel, *Adv. Energy Mater.*, 2015, **5**, 1–9.

(218) F. Zeng, Y. Lai, Z. Han, B. K. Ng, Z. Zhang, H. Zhang, L. Jiang and F. Liu, *RSC Adv.*, 2015, **6**, 6562–6570.

(219) A. R. Uhl et al., *Prog. Photovolt: Res. Appl.*, 2015, **23**, 1110–1119.

(220) D. H. Webber, J. J. Buckley, P. D. Antunez and R. L. Brutchey, *Chem. Sci.*, 2014, **5**, 2498–2502.

(221) S. Ji, T. Shi, X. Qiu, J. Zhang, G. Xu, C. Chen, Z. Jiang and C. Ye, *Scientific Reports*, 2013, **3**, 2733.

Appendix A

Effect of CZTS Nanocrystal Size on Coating Microstructure Using Ultrasonic Spray Coating, Aerosol Jet Printing, and Dropcasting Methods

In the preceding chapters, different coating operations were used to form the precursor CZTS nanocrystal coatings but little justification was provided for the choice of coating method. Here, the three coating operations used are compared in their capability to form coatings from dispersions comprising CZTS nanocrystals ranging in size from 5 to 35 nm. In each case, the coating uniformity and continuity are the primary comparison markers used to compare coatings. The three coating methods analyzed are dropcasting, aerosol jet printing, and ultrasonic spray coating.

A.1 Dropcasting

Figure A.1 shows SEM images of CZTS nanocrystal coatings formed *via* dropcasting of (a,b) 5 and (c,d) 35 nm CZTS nanocrystal dispersions. With 5 nm CZTS nanocrystals, the coating cracks extensively during drying resulting in a non-continuous coating. Isolated "islands" comprising CZTS nanocrystals are separted by approximately ~10 μm wide cracks. The crack formation is due to the high stress development during drying induced by the small nanocrystal size, as described in Section 2.5.2. With 35 nm CZTS nanocrystals, continuous crack-free coatings are formed by dropcasting (Figure A.1c,d). The increase in nanocrystal size decreases the capillary pressure induced by the liquid mensci during drying and in turn reduces the magnitude of stress. It was found that dropcasting was effective

for coating formation for CZTS nanocrystals with diameters ≥ 25 nm, but coatings formed from CZTS nanocrystals < 30 nm still resulted in cracked coatings at times. The variabilty in successful coating formation may be related to the nanocrystal size distribution that may result from differences in CZTS nanocrystal synthesis batches but are not measurable using XRD.

A.2 Ultrasonic Spray Coating

Figure A.2 displays SEM images of CZTS nanocrystal coatings formed by ultrasonic spray coating (a-d) 5 nm and (e-h) 15 nm CZTS nanocrystals using (a,b - 5 nm; e,f - 15 nm) 3 coating passes and (c,d - 5 nm; g,h - 15 nm) 6 coating passes. With 5 nm CZTS nanocrystals and 3 coating passes, the coating is cracked and non-uniform. The cracks are generally isolated and do not form an inter-connected network, likely due to an uneven coating thickness. Some regions of the coating are thicker than the critical cracking thickness (CCT) while others are below it causing the cracks to stop advancing in those regions. With 6 coating passes, the coating exhibits a continuous cracking network similar to that observed during dropcasting (Figure A.1a,b). In Figure A.2c,d, the coating seems to be a bilayer coating with a secondary cracked coating observed between the cracks of the uppermost coating. It seems that in this case, the coating cracked after application of the first couple of coating layers. Subsequent layers applied on top of the cracked coating did not fill in the voids but formed a secondary cracked coating above the first.

Increasing the CZTS nanocrystal size to 15 nm improves the coating microstructure and uniformity with both 3 and 6 coating passes. The surface of the coating formed with 3 spray passes (Figure A.2e,f) has distinct non-uniformities. The formation of these features is caused by the low liquid volume fraction of the aerosol droplets as discussed in Chapter 6. With 6 coating passes (Figure A.2g,h), the non-uniformities are less extreme with

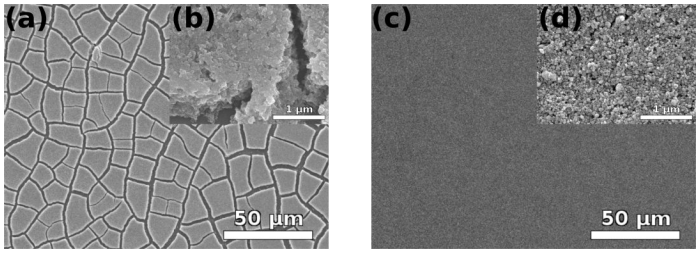

Figure A.1 SEM images of CZTS nanocrystal coatings formed by dropcasting CZTS nanocrystal dispersions containing (a,b) 5 and (c,d) 35 nm diameter nanocrystals.

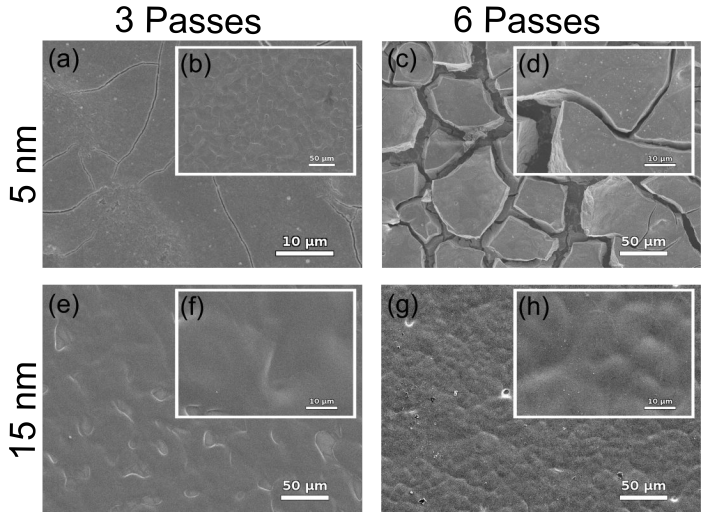

Figure A.2 SEM images of CZTS nanocrystal coatings formed by ultrasonic spray coating CZTS nanocrystal dispersions containing (a-d) 5 and (e-h) 15 nm nanocrystals formed with 3 coating passes and 6 coating passes.

"hilly" features replacing the craters observed with 3 coating passes, resulting in a more uniform coating. Similar coating morphologies were observed with coatings made from 35 nm CZTS nanocrystal dispersions.

A.3 Aerosol Jet Printing

Figure A.3 shows images of CZTS nanocrystal coatings formed through aerosol jet printing followed by compaction, as described in Section 4.2. Coatings from 5 nm CZTS nanocrystal dispersions are dense and uniform while those formed from 35 nm dispersions are filled with holes and have uneven coverage. Additionally, no individual nanocrystals are discernible in the coating where as other coatings using 35 nm nanocrystals do have identifiable nanocrystals (Figure A.1d). This brings into question what the coating is composed of and why its differs from the dropcasted coating.

Dispersions of the larger 35 nm nanocrystals are less stable than 5 nm nanocrystal dispersions, likely due to their higher volume to surface area ratio reducing the stabilizing ligand concentration and the increased van der Waals forces with the increased particle size. During aerosol jet printing, atomization occurs within a glass vial that is angled inside of ultrasonic water bath. A jet is generated at the top surface of the dispersion inside of the

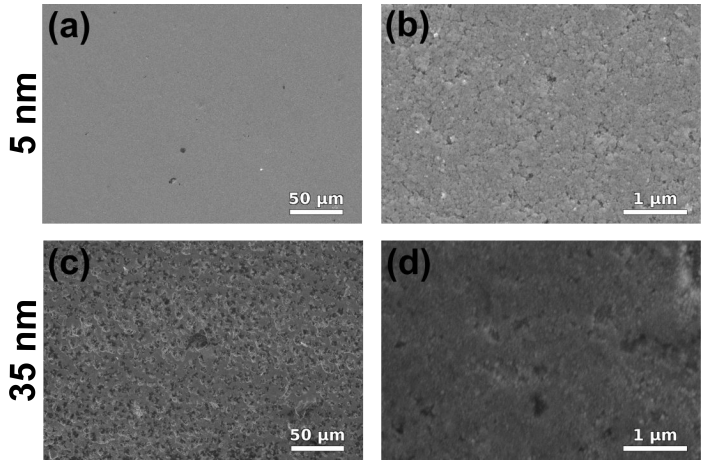

Figure A.3 SEM images of CZTS nanocrystal coatings formed aerosol jet printing followed by compaction *via* hydraulic press at 800 MPa for 15 seconds using (a,b) 5 nm and (c,d) 35 nm CZTS nanocrystal dispersions.

vial. Since the ultrasonic waves are focused at the jet location, the majority of the dispersion is only gently agitated. Larger nanocrystals may settle to the bottom of the vial and are no longer taken up within the droplets leading to a coating formed from smaller diameter nanocrystals.

Appendix B

Liquid Selenium Enhanced Sintering During Intense Pulsed Light Annealing of Cu_2ZnSnS_4 Nanocrystal Coatings

B.1 Introduction

Creation of a robust intense pulsed light (IPL) annealing method to form CZTS polycrystalline films from nanocrystal coatings would greatly improve the possiblity of inexpensive CZTS thin film solar cells produced by a continuous roll-to-roll process. Chapter 7 explored the use of IPL for annealing CZTS nanocrystal coatings in a sulfur vapor atmosphere. Due to the intermittent heating involved in IPL annealing, creation of a sulfur-rich atmosphere was not possible. Any solid sulfur that did vaporize condensed onto the cooler regions of the annealing ampule. This prompted exploration of an alternative annealing procedure to enhance grain growth during IPL annealing without requiring a chalcogenide vapor environment.

One possibility to improve IPL annealing of CZTS nanocrystal coatings is to utilize liquid phase sintering to enhance grain growth rates in CZTS nanocrystal coatings during IPL annealing. Chernmordik *et al.*[175] observed distinct film textures on CZTS nanocrystal coatings after selenization at 600 °C when the coating was hot-loaded (*i.e.*, loading annealing ampule directly into a preheated furnace). They attributed these distinct film textures to the condensation of selenium vapor onto the CZTS nanocrystal coating. The regions where selenium condensed exhibited enhanced CZTS grain growth as well as the absence of a fine-grain layer, unussal for a CZTSSe film from nanocrystals. Uhl *et al.*[219] utilized selenium liquid phase sintering to form $CuInSe_2$ solar absorber layers. In this case, 3 - 5 μm of Se was deliberately sputtered on top of the $CuInSe_2$ and the coating was annealed *via* rapid thermal processing at optimized temperatures to maintain a sufficient volume of liq-

uid selenium. Both works take advantage of the rapid sintering and grain growth imparted by the presence of the selenium liquid phase.

During IPL annealing, a liquid phase may aid in enhancing grain growth. A liquid phase would be able to minimize temperature differences throughout the coating that may arise due to uneven light exposure and/or absorption differences due to thickness variation. Additionally, lower temperatures in the range of the Se melting point may be used rather than the higher temperatures required for solid state growth or S/Se vapor-enhanced growth.

B.2 Materials and Methods

CZTS nanocrystal synthesis, coating formation on Mo foil substrates, and IPL annealing were performed in the manner described in Section 7.2. For all studies, 35 nm CZTS nanocrystals were used and coatings were dropcasted onto Mo foil substrates.

Selenium was applied to the coatings in two ways. In the first method solid selenium pellets (individual pellet weight of ~1 mg, total weight of 5 mg) were placed in the ampule along with the CZTS coating on Mo foil. After sealing and prior to IPL annealing, multiple pellets were arranged on top of the CZTS nanocrystal coating by gently shaking the ampule similar to the process used by Chernmorodik *et al.*.[175] Generally, 2-3 pellets were aligned on top of the CZTS coating with 1-2 additional pellets in the ampule but not successfully placed on top of the coating.

The second method utilized Se solutions produced in the manner described by Webber *et al.*[220] To create a selenium solution, 20 mg of Se pellets were dissolved in 1 ml of a 1:4 volume ratio ethanethiol and ethylenediamine solution by stirring at room temperature for 1 hour. Approximately 70 µL of the resulting Se-containing solution was deposited onto the nanocrystal coatings. The coatings were then placed in quartz ampules which were evacuated and sealed before IPL annealing.

The microstructure of the coatings was analyzed before and after annealing using a JEOL 6500 scanning electron microscope. Raman spectroscopy was conducted on a Witec Alpha300R confocal Raman microscope with a 532 nm wavelength source, a DV401 CCD detector, and a UHTS300 spectrometer. The spectra were collected with an 1800 lines/mm grating, providing a spectral resolution of 0.02 cm^{-1}.

B.3 Results and Discussion

Figure B.1 displays SEM images of a CZTS nanocrystal coating after IPL annealing at 11.6 J/cm^2 for 10 pulses. In Figure B.1a, solidified Se is observed on top of the CZTS nanocrystal coating. This morphology was formed after the Se pellet in the location melted during IPL annealing and solidified after heating was ceased. It is clear that the temperature achieved during IPL annealing is sufficient to melt Se (m.p. ~220 °C). Furthermore, condensation of Se on the quartz ampule was observed during IPL annealing with the formation of a red residue on the quartz, indicating temperatures above 220 °C to sufficiently vaporize Se in addition to melting. Figure B.1b is a zoomed in image of the space between the solidified Se mounds. CZTS nanocrystals are observed in between the solidified Se "puddles" showing that the coating is retained while the melting covers the top of the coating. The liquid Se present during IPL annealing indicate the potential of this annealing procedure, but lacks evidence of grain growth enhancement or CZTSSe alloy formation.

Figure B.2a shows Raman spectra collected f at the three locations (labeled A, B, C) in Figure B.2b. Raman spectra of locations A and B indicate pure CZTS phases with strong peaks occurring at ~336 cm^{-1}.[202] At location C, two additional peaks are clearly observed at Raman shifts of 193 and 238 cm^{-1} in addition to the peak at 336 cm^{-1}. These peaks are characteristic of CZTSe,[221] indicating the formation of CZTSe during IPL annealing. The dark region in Figure B.2b is assumed to be a solidified Se puddle as observed in Figure B.1. This would make location C a Se-rich region with heavy exposure to Se during IPL annealing. The Raman peaks shown in Figure B.2 conform well with other observations of CZTSSe alloys. Ji *et al.* reported gradually intensity increase in CZTS characteristic peaks accompanied with the increase in intensity of CZTSe characteristic peaks as the Se content of CZTSSe nanocrystals was increased (*i.e.*, $Cu_2ZnSn(S_{1-x}Se_x)$ for $x = 0 - 1$).

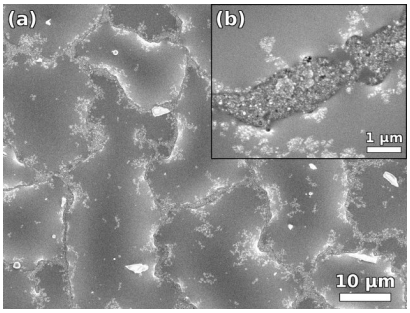

Figure B.1 (a) XRD pattern and (b) Raman spectrum for CZTS nanocrystal coating on quartz substrate after IPL annealing at 9.0 J/cm^2 for 10 flashes.

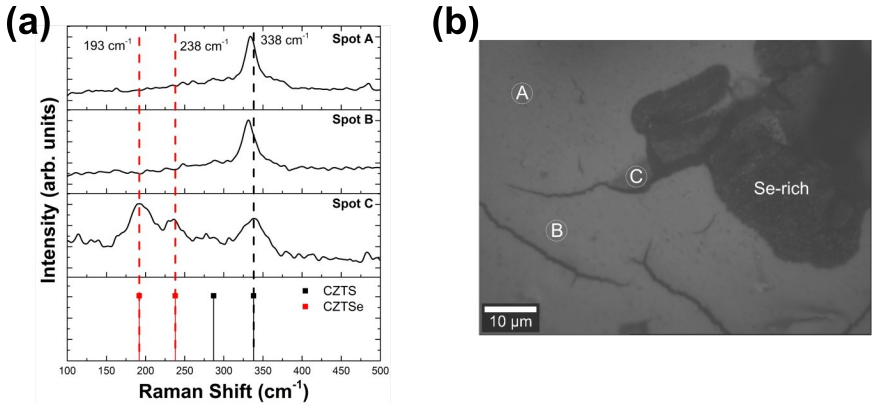

Figure B.2 (a) XRD pattern and (b) Raman spectrum for CZTS nanocrystal coating on quartz substrate after IPL annealing at 9.0 J/cm^2 for 10 flashes.

B.4 Outlook

In the context of the results reported by Chernomordik *et al.*[175] and Uhl *et al.*,[219] these initial observations show promising prospects for liquid Se enhanced growth during IPL annealing. There are a number of issues that must be addressed to successful produce IPL annealed films in this manner. The uniformity of the Se across the coating must be improved. Figure B.3 shows an alternative Se addition procedure that was investigated. In this case, a Se-containing solution was deposited onto the CZTS nanocrystal coatings and then allowed to dry. This increased the uniformity of Se coverage compared to individual Se pellets, but resulted in a high amount of carbon residue left on the coatings after drying the amine-thiol solution. Uhl *et al.* sputtered Se onto $CuInSe_2$ nanocrystal coatings.[219] This method improves uniformity over Se pellets but requires vacuum processing limiting its utility.

Figure B.3 Photographs of CZTS nanocrystal coatings on Mo foil after deposition of 70 µL of Se-containing ethanethiol and ethlyenediamine solution on top of coating. A significant amount of residual carbon was as the solution dried.

The removal of excess Se from the coating after successful IPL annealing is another possible complication. It is likely that the most successful annealing conditions require a large volume of liquid Se to effectively enhance CZTSSe grain growth. Any Se that is not incorporated into the film in the form of CZTSSe would remain at the film interfaces and grain boundaries. This would cause short-circuits in any solar cell devices constructed from these films. The most logical method to remove the excess Se is to vaporize it from the film and allow it to condense on a non-film surface. The use of quartz ampules would provide a non-film surface and allow the Se to condense on the interior of the quartz tube. The annealing operation would have to be devised to allow the solid Se to melt and maintain it in a liquid state for a long enough time period for the film to develop. After this period, the temperature would need to be increased above the vaporization temperature for a short period of time to remove any excessive Se from the film. It is possible that separate IPL annealing operations could be tuned to perform these desired transformations. However, it would likely require extensive trial and error since temperature measurement is difficult during IPL annealing.